ENERGY CONVERSION AND STORAGE CONTROL FOR SMALL WIND TURBINE SYSTEMS

Teză destinată obţinerii
titlului ştiinţific de doctor inginer
la
Universitatea "Politehnica" din Timişoara
în Domeniul Inginerie Electrică
de către

Ing. Diana Paula Petrila

Conducător ştiinţific: prof.univ.dr.ing. Nicolae MUNTEAN
Referenţi ştiinţifici: prof.univ.dr.ing. Mircea RĂDULESCU
                             prof.univ.dr.ing. Lorand SZABO
                             conf.univ.dr.ing. Lucian TUTELEA

Ziua susţinerii tezei: 08.02.2013

Seriile Teze de doctorat ale UPT sunt:

1. Automatică	7. Inginerie Electronică şi Telecomunicaţii
2. Chimie	8. Inginerie Industrială
3. Energetică	9. Inginerie Mecanică
4. Ingineria Chimică	10. Ştiinţa Calculatoarelor
5. Inginerie Civilă	11. Ştiinţa şi Ingineria Materialelor
6. Inginerie Electrică	

Acknowledgements

I wish to express my endless gratitude to my supervisor Professor Nicolae Muntean, for giving me the chance to be part of his research team, for his competent guidance, support and patience, without which this work would have not been possible.

I am grateful to Professor Frede Blaabjerg, for his support during the three months PhD internship at the Institute of Energy Technology, Aalborg University, Denmark.

I wish to thank the referents, Professor Mircea Radulescu and Professor Lorand Szabo, from Technical University of Cluj-Napoca and Associate Professor Lucian Tutelea, from "Politehnica" University of Timisoara, for their pertinent comments and relevant suggestions.

I am also thankful for their support, to all my colleagues from the Power Electronics and Motion Control research team.

Finally, I will always be thankful to my family for the unfailing support and encouragement throughout all my years of study.

Timişoara, February, 2013   Diana Paula Petrila

Abstract,
Nowadays, the wind power is one of the most promising renewable sources of energy. That is possible because of the fast development of the power electronics, variable speed drives and wind turbines. Wind energy conversion systems (WECS) are very studied because of their benefits and as a result a large variety of WECS are proposed in the literature.

In this thesis a small-scale wind energy conversion system (SWECS) structure is proposed. All main components are described in detail and modeled. Also a speed estimator for the permanent magnet synchronous generator is elaborated. The proposed SWECS is simulated in a simplified way, to better explain and motivate the role of a supercapacitor, as storage element for transients.

In order to study, test and implement SWECS and some control strategies for it, a direct torque control "hardware in the loop" wind turbine emulator is proposed, simulated, built, and tested.

Due to wind's unpredictable nature, maximum power point (MPP) control algorithm is the key component, necessary to extract the maximum available power from WECS. Two MPP controls are developed and validated by simulation and experimental results on the real time "hardware in the loop" wind turbine emulator. The first MPP strategy is based on wind turbine known characteristics, memorized in the control system. The second is a perturb and observe, maximum power point tracking fuzzy logic controller (MPPT-FLC) algorithm. Both strategies are tested under steps and real wind speed profile and are applied for two wind turbine types.

A comparison between the two MPP controllers is presented, to highlight the most efficient energy conversion strategy. It is concluded that for all studied cases, MPPT–FLC is superior.

Some results from the site, where a similar system was installed, are presented to prove that in real conditions the system works properly.

Finally, the experimental setup details are presented as a part of the work. Each theoretical consideration is validated through simulations and experiments.

TABLE OF CONTENTS

OBJECTIVES

The main objectives of the thesis are:

- To present an overview of state of the art regarding the configurations, generators types, power electronics, and storage elements used in wind energy conversion systems (WECS);
- To highlight the most suitable components for a small-scale WECS (SWECS) and the most efficient and cost effective control schemes for viable solutions of a SWECS;
- To propose, design, and build a structure of a conversion and storage system for a small off-grid wind turbine;
- To propose, design, and build a direct torque control "hardware in the loop" wind turbine emulator, useful for study and test a real equipment for wind energy systems;
- To implement and test simplified control strategies, for easy commissioning of SWECS;
- To implement and test a "fuzzy logic" maximum power point tracking (MPPT) strategy for SWECS, taking into account the transient regimes, within safety limits;
- To compare the implemented strategies in terms of energy conversion efficiency;
- To present and compare the test results obtained with a proposed structure of SWECS, installed in the field, compared with laboratory and simulations results, using equivalent equipment.

OUTLINE

The thesis is organized in 7 chapters:

- Chapter 1 presents the state of the art of the wind energy conversion systems (WECS). Different structures, generators types, power electronics topologies, and storage elements used in WECS are presented in a comparative analysis. Also some common control methods that are being used in most commercial available wind turbines in the market are presented. Small-scale WECS (SWECS) and their integration in hybrid energy generation systems are described. Finally, conclusions are drawn highlighting the advantages of SWECS and the suitable components for such a system.
- In Chapter 2 is proposed a SWECS structure, including storage elements. All main parts of the system are described and modeled, based on known or measured parameters, in order to be simulated in Matlab/Simulink.
- To study wind turbine systems, it is necessary to have a real time emulator, because a wind turbine may not always be available and neither a wind tunnel test. Chapter 3 presents a "hardware in the loop" direct torque control wind turbine emulator, built for study and testing real components and control strategies. Simulation and experimental results obtained with the emulator are compared in order to validate the proper functioning of this tool.
- In Chapter 4 two MPP algorithms are implemented in order to extract the maximum available power from the proposed SWECS. The first one uses the known static power characteristics of the wind turbine. The second is a fuzzy logic MPPT controller, based on a set of rules which is derived from the system behavior and from the designed control strategy.
  Both control strategies are implemented on two, different types, of wind turbines, and studied with digital simulations. Extended experimental results are obtained using the real time "hardware in the loop" wind turbine emulator.
- In Chapter 5, results obtained from a full-scale system installed on an experimental platform are presented.
- In Chapter 6 the experimental setup is described, including some details regarding the equipment used also in the experimental platform.
- In Chapter 7, the overall conclusions, the main contributions and some future work are presented.

NOMENCLATURE

Abbreviations

AC	Alternative current
AG	Asynchronous generator
Bat	Batteries
BCM	Boundary conduction mode
BDC	Buck DC–DC converter
CCM	Continuous current mode
Conv1, Conv2, Conv3	Converters
CSC	Current source converter
DBR	Diode bridge rectifier
DC	Direct current
DE	Diesel engine
DFIG	Doubly fed induction generator
DOD	Depth of discharge
DTC	Direct torque control
ECS	Energy conversion system
EMI	Electromagnetic interference
ES	Energy storage
EESG	Electrically excited synchronous generator
FC	Fuel cell
FL	Fuzzy logic
FLA	Flooded lead acid battery
FLPI	Feedback linearized proportional integral method
FSWECS	Fixed-speed wind energy conversion system
FW	Flywheels
GB	Gear-box
GDP	Gross domestic product
HAWT	Horizontal-axis wind turbine
HBDC	Hybrid Buck DC-DC converter
HC	Hysteresis comparators
HDC	Hybrid DC-DC converter
HVAWT	Horizontal-vertical-axis wind turbine
IEC 61400-2	Wind turbine safety certification
IM	Induction machine
Inv	Inverter
IPMSG	Interior permanent magnet synchronous generator
LA	Lead Acid battery
Li-on	Lithium Ion battery
MPP	Maximum power point
MPPT	Maximum power point tracking
MPPT-FLC	Maximum power point tracking fuzzy logic controller

Mtoe	Million Tons of Oil Equivalent
N	Negative
NaS	Sodium Sulphur battery
NiCd	Nickel Cadmium batteries
NS	Negative small
ORC	Optimum regimes curve
P	Positive
P&O	Perturb and observe
PFC	Power factor corrected
PM	Permanent magnet
PMSG	Permanent magnet synchronous generator
PS	Positive small
PV	Photovoltaic
PWM	Pulse with modulation
PWM-VSI	Pulse with modulation-Voltage source inverter
R, R1, R2	Resistors
RCP	Rapid control prototyping
RTI	Real-time interface
SC	Supercapacitor
SCIG	Squirrel cage induction generator
SG	Synchronous generator
SPMSG	Surface mounted permanent magnet synchronous generator
SWECS	Small-scale wind energy conversion system
T, T1, T2	Static switching devices
TR	Transformer
TSR_{opt}	Optimum Tip-speed ratio
UPS	Uninterruptible power supply
VRLA	Valve regulated lead acid battery
VSI	Voltage source inverter
VSWECS	Variable-speed wind energy conversion system
WECS	Wind energy conversion system
WRIG	Wound rotor induction generator
WT	Wind turbine
Z, Z1, Z2	Loads

Symbols

A	Blade swept area	m^2
a, b, C_{T0}	Constants wind turbine coefficients	-
C, C1, C2, C3, Cn	Capacitors	F
Cf	Filter Capacitor	F
C_P, C_{pmax}	Wind turbine Power coefficients	-
C_T	Wind turbine Torque coefficients	-
D	Duty-cycle	-
d	distance	m
D1, D2, D3, D4, D5, D6	Diodes	-
E_k	Kinetic energy	W·s

fn	Rated frequency	Hz
fs	Switching frequency	Hz
I_DB	Input HDC current (diode bridge output current)	A
$I_{Cout.ripple}$	Current ripple	A
Ifp	Peak phase current	A
IGBT	Insulated-gate bipolar transistor	-
Iin	Input current	A
$I_{L,lim}$	Average value of inductor current	A
Iout	Output current	A
$I_{T,rms}$	Transistor rms current	A
J	WECS inertia	kg·m^2
J_{WT}	Wind turbine inertia	kg·m^2
J_g	Generator inertia	kg·m^2
J_{em}	Emulator inertia	kg·m^2
J_{IM}	Induction machine inertia	kg·m^2
J_{GB}	Gear-box inertia	kg·m^2
J_c	Compensation inertia	kg·m^2
k	Wind turbine coefficient	-
Kbyp	Bypass contactor	-
k_{dc}	Estimator coefficient	-
KpFe	Core loss coefficient	kg·m^2/s
k_q	MPPT-FLC integrator gain	-
k_P, k_w	MPPT-FLC scaling coefficients	-
L, L1, L2	Inductances	H
Ld, Lq	d and q-axis inductances	H
Ldc	DC equivalent inductance	H
m	Air mass	kg/m^3
n	Rotating speed	rpm
Nc	Number of stator slots	
P(ω)	Power versus rotating speed characteristic	-
P_1, P_2, P_3	Maximum power points	W
$P_{gexperiment}$	Experimental obtained generator power	W
$P_{gsimulation}$	Simulation obtained generator power	W
P_m	WECS Mechanical power	W
Pp	Pole pairs	-
Pw, Pwt	Wind and wind turbine power	W
R	radius of the turbine blade	m
Ra, Rb, Rc	Measured phase resistances	Ω
Rdc	DC equivalent resistance	Ω
S	Switch	-
t	Time	s
T_{IM}	Induction machine torque	N·m
ton, toff	Switching periods	s
T_{wt}	Wind turbine torque	N·m
$T_{estimated}$	Estimated torque	N·m
T_{GB}	Gear-box torque	N·m
T_0	Initial torque	N·m
T_{gs}	Shaft-speed torque	N·m

12 Nomenclature

V	Volume	m^3
v, v1, v2, v3	Wind speeds	m/s
V_I*_IN	Prescribed Voltage for HDC Current	V
V_{dc}	Rectified voltage	V
Vdc0	No load rectified voltage	V
V_{don}	Diode voltage drop	V
Vrect	Rectified voltage	V
V_{SC}	SC voltage	V
W_{MPP}, $W_{MPPT-FLC}$	Energies and the energies difference	kWh
ΔW	Energies difference	-
Xs, Xd, Xq	Synchronous reactances	Ω
$ΔP_m$	Mechanica power derivative	-

Greek Symbols

α	Firing angle	degree
β	Rotor blade pitch angle	rad
Δω	Rotating speed derivative	-
$ε_ω$	Speed error	-
η	Efficiency	%
λ, λopt	Tip-speed ratio	-
π	pi	-
ρ	Specific density of air	kg/m^3
$Ψ_{PM}$	PM flux	Wb
ω	Rotor speed	rad/s
$ω_e$	Electrical speed	rad/s
$ω_{IM}$	IM rotating speed	rad/s

LIST OF FIGURES AND TABLES

Figures

Tables

1. INTRODUCTION

1.1. Wind Energy

The global warming and the increased global energy demand have become the most discussed problems in the society. The solution to these problems is the use of renewable energy sources, which are clean, free and endless. Until now, just a small part of the total global electrical energy is produced in this way.

The demand for renewable energy is expected to triple, creating new market opportunities, with EU, US and China as major players (Fig.1.1) [1].
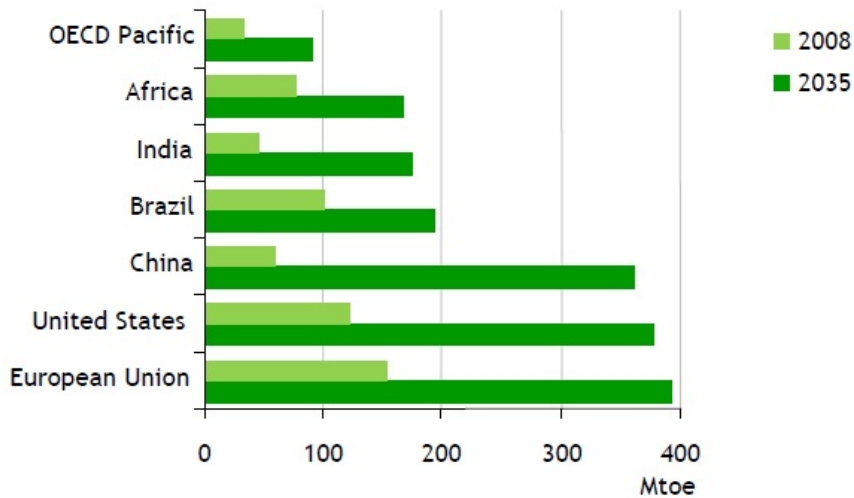
Fig.1.1. Global renewable energy demand evolution.

In EU, the share of renewables in the final energy consumption reached 10.3% compared to 9.7% in 2007. This increase is mainly due to the greater biomass and biofuel consumption (+7%) as well as hydroelectricity (+5%) and wind (+16%). The share of renewable electricity produced in the EU increased by 7.7% in 2008, compared to 6.1% in 2007. At this rate the EU is unlikely to reach its 20% target in 2020 [2].

Each EU member has a binding target - set as a combination of renewable potential and gross domestic product (GDP) - to increase its share of renewable energy by 2020 (Fig.1.2.) [1].
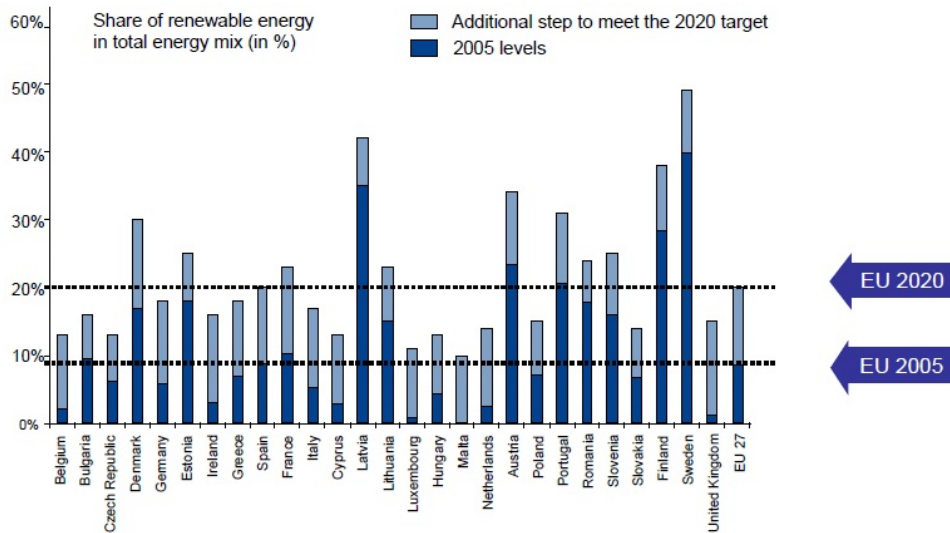
Fig.1.2. EU reneawable energy target.

One of the most promising renewable energy sources is the wind. This became possible due to the fast development of the power electronics, variable speed drives and wind turbines [3]. So, it is estimated that the wind energy produced until 2020 will reach 10% of the global demanded energy.

Europe remains in first place in terms of cumulated wind power capacity (almost 50% of the world's capacity); Asia has become the first market worldwide, with record numbers in China (over a third of the global market). Europe defended its place thanks to new markets in Central Europe (Poland: 254 MW installed in one year, +56% in capacity) [2].

On the other hand, distributed generation, consisted of a smattering of off-grid generation sources, industrial and commercial grid-connected generation—including backup supply and combined heat and power, and strategically located utility-placed generation for grid reliability, encouraged the small power renewable energy systems development [4]. Distributed generation is an approach that employs small-scale technologies (3 kW to 10 MW) to produce electricity close to the end users of power. In many cases, distributed generators can provide lower-cost electricity and higher power reliability and security.

In this chapter standard wind turbine configurations, commonly used power converters, storage elements, some power control strategies for wind energy conversion systems, and hybrid energy systems are presented, based on literature research. This part of the thesis was oriented the author in choosing the concrete work subjects and defining the research objectives.

1.2. Wind Energy Conversion Systems

The literature proposes a large variety of wind energy conversion systems (WECS). The main parts of WECS are: the wind turbine, the electric generator, the power electronic converter, the storage elements and the control system.

The wind kinetic energy is converted into mechanical energy by the wind turbine blades. The mechanical energy is converted into electrical energy by the generator and is delivered to the load through power electronic converters and storage elements (where needed). Also a gearbox and other components can be used if necessary. Even if many configurations are possible, WECS are frequently classified according to speed control or power control capabilities. According to the speed-control WECS are divided in two categories: fixed (FSWECS) and variable speed wind turbine systems (VSWECS). The power control ability divides WECS into three categories: stall-controlled, pitch-controlled and active-stall-controlled wind turbines [5].

FSWECS (Fig.1.3) are simple, robust and low cost; they operate at constant speed, regardless of the wind speed. They use induction generators directly connected to the grid. The power limitation can be done by stall, active stall or pitch control. As drawbacks they cannot convert the maximum power available from the wind because they operate at a constant speed for every value of the available wind speed. Another drawback is the stress which appears on the mechanical parts due to the torque pulsation produced by wind gusts. A soft-starter is also needed for limiting the starting currents. They are equipped with capacitor banks to limit the reactive power absorption from the grid. They cannot operate without a grid connection or in the case of a short term grid collapse.
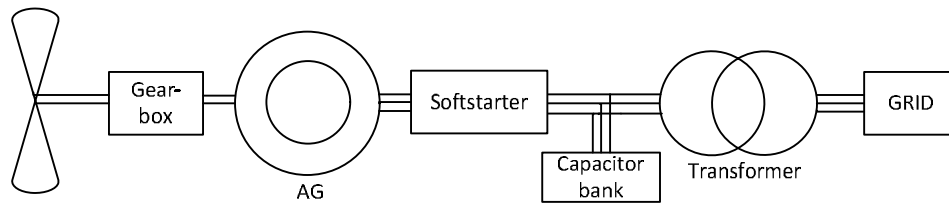
Fig.1.3. Fixed-speed WECS structure.

VSWECS (Fig.1.4) have many advantages compared to FSWECS, and they are the most used systems today. They can operate also as stand-alone systems. They offer the possibility to extract the maximum available power from the wind and so to increase the amount of captured energy. Also, because the captured energy is larger, the life-cycle cost is lower, in spite of the additional cost of power electronics and controllers required. The active and reactive power can be also controlled, and it can either inject or absorb active power from the grid. They are very flexible in terms of generator type: induction or synchronous generator with, or without a gearbox. While FSWECS are designed to achieve maximum aerodynamic efficiency for a single wind speed, VSWECS can be regulated to obtain this for a wide range of wind speeds. And finally, variable-speed operation allows the use of advanced control techniques.
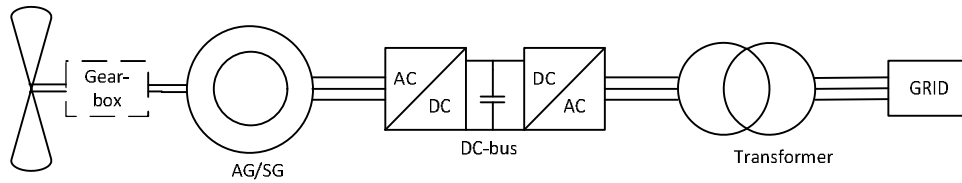
Fig.1.4. Variable-speed WECS structure.

1.3. Wind Turbine Systems Configurations

Standard wind turbine systems configurations using asynchronous generator (AG) and synchronous generator (SG) are presented next:

Configurations using Asynchronous Generator with cage rotor (AG):

a) The conventional configurations applied by many Danish wind turbine manufacturers during the 1980s and 1990s. This configuration was extended (Fig.1.3) with a capacitor bank (for reactive power compensation) and a soft-starter (for smoother grid connection) [6]-[15].

b) In the previous structure, the capacitor bank and the soft-starter are replaced by a full scale frequency converter or a low wind region sized frequency converter, with bypass (Fig.1.4), used e.g. by Wind World. This configuration uses a smaller frequency converter (20-30% of nominal generator power) compared to the full-scale configuration (approximately 120% of nominal generator power). The full-scale configuration enables variable speed operation at all wind speeds [6].

Configurations using Asynchronous Generator and wound rotor:

a) The structure from Fig.1.5 employs a wound rotor and it has been used by Vestas since the mid-1990's known as "OptiSlip". The basic idea is to control the total rotor resistance using a power electronic converter. With this converter, mounted on the rotor shaft, it is possible to control the slip over a 10% range. The slip control implies output power control in the system. An alternative configuration uses passive components instead of a power electronic converter, which also achieves a range of 10% slip variation [6]-[15].
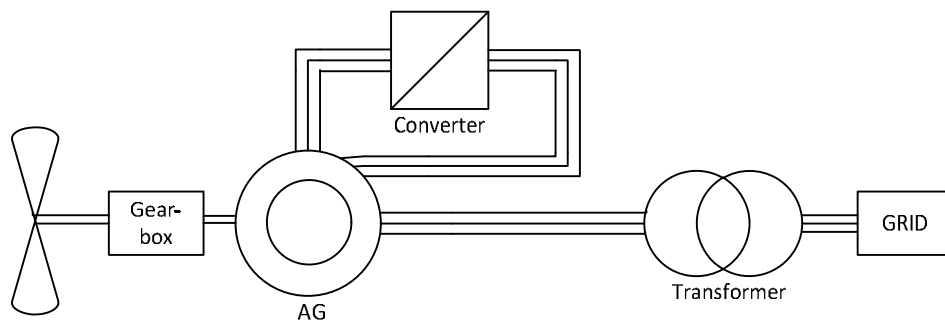
Fig.1.5. Configuration using AG with wound rotor.

b) Another configuration (Fig.1.6) uses a doubly fed AG (or DFIG). A frequency converter controls the currents in the rotor windings. This enables the whole generator output control, using a power electronic converter, rated at 20-30% of nominal generator power. This configuration is mainly motivated by two reasons:

- a wide speed range compared to the "OptiSlip" system;
- less expensive compared to the full power control configuration [6]-[15];
- lower losses in the power electronic converter.
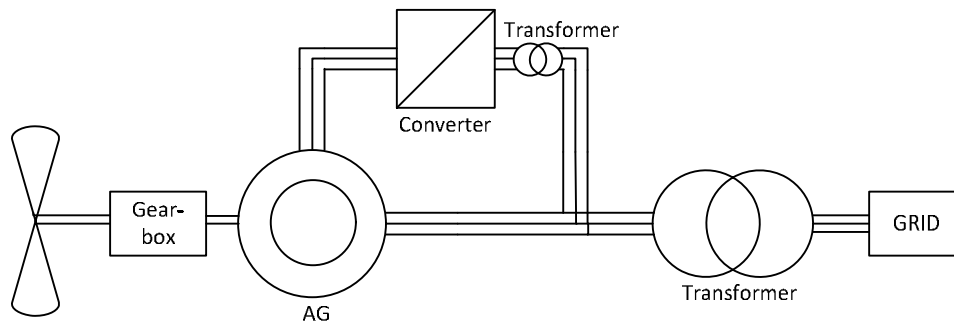
Fig.1.6. Configuration using doubly fed AG.

Configurations using Permanent Magnet Synchronous Generator (PMSG):

An alternative generator (Fig.1.4) that might replace doubly fed AG is PMSG with a full scale converter. Compared to the doubly fed AG this generator has the following advantages: better efficiency, less expensive, brushless, it can be used both in 50 Hz and 60 Hz grids, the grid-fault ride through capability is less complex etc. The decreasing cost of power electronics and the absence of brushes make this system attractive [6]-[15].

Configurations using Synchronous Generator (SG) with wound rotor:

a) The SG is externally excited, as shown in Fig.1.7, using a rectifier (the power converter). This configuration is not widely used in wind turbines systems. The disadvantages of this structure are:

- constant speed operation;
- the exciter circuit;
- the slip rings;
- a more complex wind turbine safely strategy.
  Also internally excited configurations exist [6].
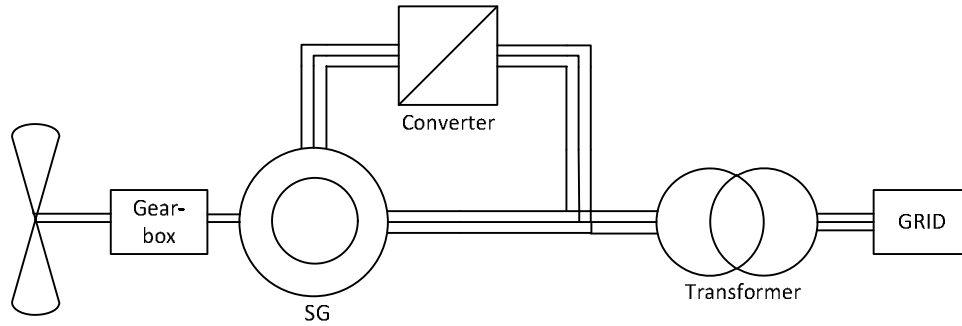
Fig.1.7. Configuration using SG with externally excited wound rotor.

b) A variable speed configuration with a full-scale power converter is presented in Fig. 1.8. [6].
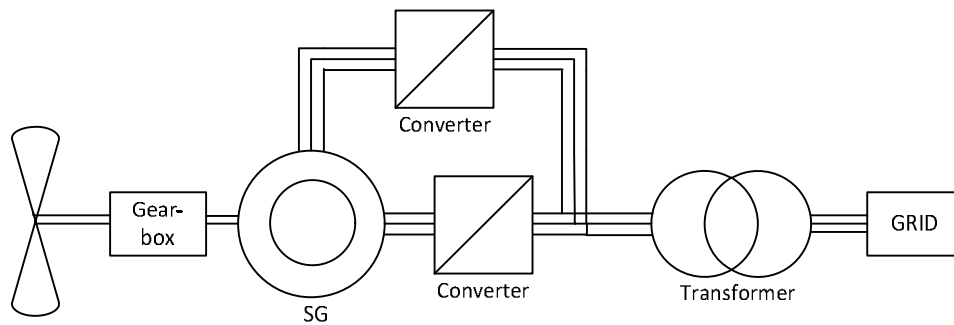
Fig.1.8. Configuration using SG and full-scale converter.

c) In Fig.1.9 a multi pole wound SG is used. In principle, it is the same configuration as the previous one, but no gearbox is needed. Enercon and Lagerwey use this type of generator [6]. It is possible to use this structure with multi pole PMSG also.
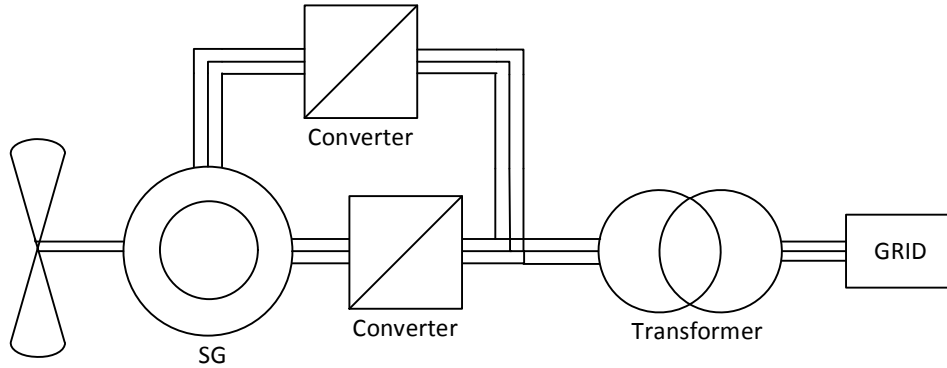
Fig.1.9. Configuration using multi pole SG and wound (or PM) rotor.

Table 1 presents the market penetration and share of the different wind turbine concepts based on recorded world supplier's market data [10].

Table 1.1. Market penetration and share of the different wind turbine concepts

Drive train	Generator Type	Power / Rotor diameter / Speed	Manufacturer
Multiple-stage gearbox	DFIG	4.5 MW / 120 m / 14.9 rpm	Vestas
		5 MW / 126 m / 12.1 rpm	Repower
		2.5 MW / 90 m / 14.85 rpm	Nordex
		3.6 MW / 104 m / 15.3 rpm	GE
		2 MW / 90 m / 19 rpm	Gamesa
		3 MW / 100 m / 14.25 rpm	Ecotecnia
		2 MW / 90 m / 20.7 rpm	DeWind
	SCIG	3.6 MW / 107 m / 13 rpm	Siemens
	WRIG	2 MW / 88 m / rpm	Suzlon
	PMSG	2.x MW / 88 m / 16.5 rpm	GE
Single-stage gearbox	PMSG	5 MW / 116 m / 14.8 rpm	Multibrid
		3 MW / 90 m / 16 rpm	Winwind
Hydro-controlled Multi-stage gearbox	EESG	2 MW / 90 m / 20.7 rpm	DeWind
Direct-drive	EESG	4.5 MW / 114 m / 13 rpm	Enercon
	PMSG	2 MW / 71 m / 23 rpm	Zephyros
	PMSG	2 MW / m / rpm	Mitsubishi

1.4. Power Converters in Wind Turbine Systems

Power converters are the most important parts of the WECS. Their structure, efficiency and controllability dictate the WECS performances.

Power converters structures can be classified regarding the conversion parameters (as the Chapter 1.3. has presented generally) in:
- constant frequency, variable voltage;
- variable frequency and voltage;
- single quadrant operation;
- four quadrant operation.

Power converters can also be rated:
- at full power;
- at small (partial) power.

Small-scale WECS (SWECS) have some dedicated structures, due to their low power and the imposed low prices.

In recent years, many power converter structures have been developed for electrical grid integration. The use of power electronic converters allows variable speed operation of the wind turbine, and enhanced power extraction. In variable speed operation, a control method, designed to extract maximum power from the turbine and provide constant grid voltage and frequency, is required. A wide range of control schemes, varying in cost and complexity, have been investigated for all considered conversion systems. In general, the power converter has to convert the electrical energy from variable voltage and frequency to a fixed voltage and frequency. Inverters for variable speed operation may be in general classified in two basic groups:
- VSI (voltage source inverter);
- CSC (current source converter).

While the VSI produces a switched voltage waveform at the terminals of the electrical machine, the CSC produces a switched current waveform. Both structure work using PWM strategies.

Different strategies exist to combine a rectifier and an inverter to form a frequency converter. Table 2 serves as a short introduction to five drive topologies applicable for adjustable speed in a WECS [6].

Table 1.2. Drive topologies applicable for adjustable speed in a WECS

Converter	Type	Technology
Back to back	VSI	PWM
Tandem	CSC + VSI	6 steps + PWM
Matrix	VSI	PWM
Multilevel	VSI	PWM
Resonant	VSI	PWM

A soft-starter is used during start up in order to limit the in-rush current and thereby reduce the disturbances to the grid. The soft starter is a power converter, which has been introduced for fixed-speed wind turbines to reduce the transient current during connection or disconnection of the generator to the grid. When the

generator speed exceeds the synchronous speed, the soft-starter is connected. Using firing angle control of the thyristors the generator is smoothly connected over a predefined number of grid periods. An example of connection diagram for the soft starter with a generator is presented in Fig.1.10 [5].
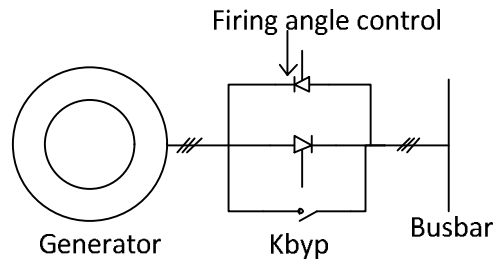
Fig.1.10. Connection diagram of soft starter with a generator.

The commutating devices are two thyristors, connected in anti-parallel, for each phase. The relationship between the firing angle (α) and the resulting amplification of the soft starter is non-linear and depends additionally on the power factor of the connected element. When the generator is completely connected to the grid a contactor (Kbyp) bypasses the soft-starter in order to reduce the losses during normal operation. The soft-starter is very inexpensive and it is a standard converter used in many wind turbine systems [5].

A capacitor bank (Fig.1.11) is used for power factor compensation. The generators are normally compensated into the whole power range. The capacitors switching is done as a function of the average value of measured reactive power during a certain period. The capacitor banks are usually mounted at the bottom of the tower, or in the nacelle. In order to reduce the current at connection of capacitors, an inductance (L) can be connected in series [5].
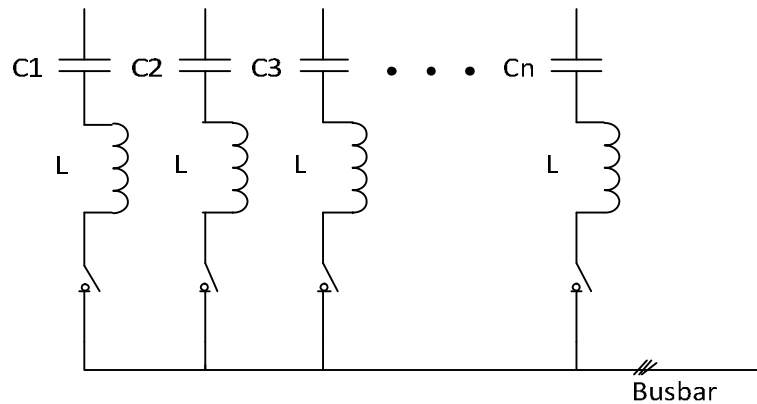
Fig.1.11. Capacitor bank configuration for power factor compensation.

The diode rectifier (Fig.1.12) is the most common used topology in power electronics. For a three-phase system it consists of six diodes. The diode rectifier can only be used in one quadrant, it is simple and inexpensive, and it could be used in some applications with a DC-bus, especially in small power systems [6].
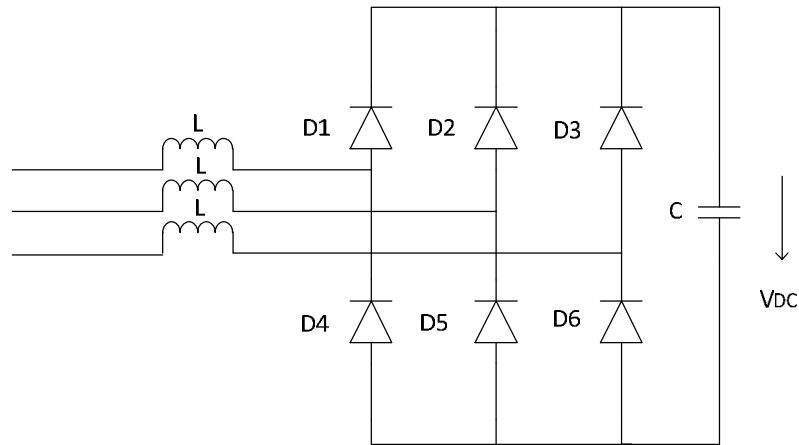
Fig.1.12. Diode rectifier for three-phase AC/DC conversion.

The three-phase boost rectifier, as shown in Fig.1.13, will be the most important converter topology in the three-phase unity power factor rectification for its continuous input currents, high efficiency, as well as the high output DC voltage needed by the voltage-source inverter (VSI).

The rectifiers do have their own properties which are different from those of the VSI. The rectifier operation is much simpler, since its only job is to provide power factor correction in most cases; in many applications, only unidirectional power flow is required, and the switching frequency should be as high as possible.

This topology is especially used for SWECS with AG and SG with PM. Some advantages of this configuration are: complete control of active or reactive power, proven technology, decoupling between grid and generator (compensation for non-symmetry and other power quality issues). Disadvantages in using this configuration could be: switching frequency limited because the converter is full-scale, need for major energy-storage in DC-link (reduced life-time and increased expenses) [16]-[17].
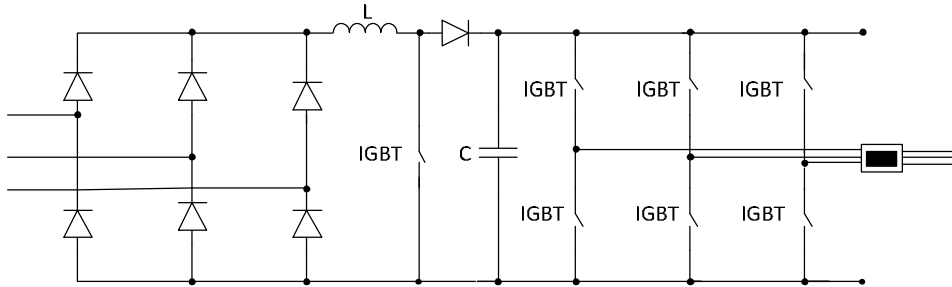
Fig.1.13. Boost–rectifier scheme.

VSI with IGBTs may transfer both active power and reactive power in both directions (AC–DC or DC–AC, four quadrant), and can be connected to the grid with an inductive filter. The reactive power demand can be supplied by the converter. The high-frequency switching of PWM converter may produce harmonics and interharmonics, which, in general, are in the range of some kilohertz. Due to the high frequencies, the harmonics are relatively easy to be removed by small-size filters. Fig.1.14 shows a typical power electronic converter consisting of self-commutated semiconductors such as IGBTs [10].
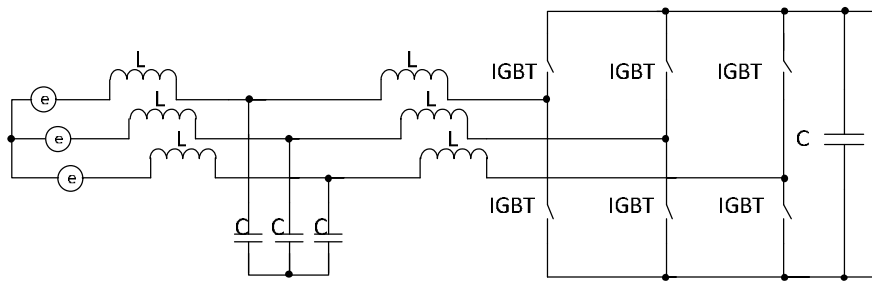
Fig.1.14. Circuit diagram of a VSI with IGBTs.

The general idea behind the multilevel converter technology is to create a sinusoidal voltage from several levels of voltages, typically obtained from capacitor voltage sources. The different proposed multilevel converter topologies can be classified in the following five categories (Fig.1.15):

- Multilevel configurations with diode clamps;
- Multilevel configurations with bi-directional switch interconnection;
- Multilevel configurations with flying capacitors;
- Multilevel configurations with multiple three-phase inverters;
- Multilevel configurations with cascaded single phase H-bridge inverters;
  Advantages of using a multilevel converter:

The main purpose of a multilevel converter was to achieve a higher voltage capability. As the ratings of the components increases and the switching and conducting properties improve, multilevel converters become more and more advantageous. The multilevel converter distinguishes with the lowest demands to

the input filters (or alternatively reduced number of switching). The low switching losses of the multilevel converter are another feature, which is often accentuated. For the same harmonic performance the switching frequency can be reduced to 25% compare with a two-level converter. Even though the conduction losses are higher, the overall efficiency for the diode clamped multilevel converter is higher compared with the two-level converter. This depends on the ratio between the switching losses and the conduction losses.
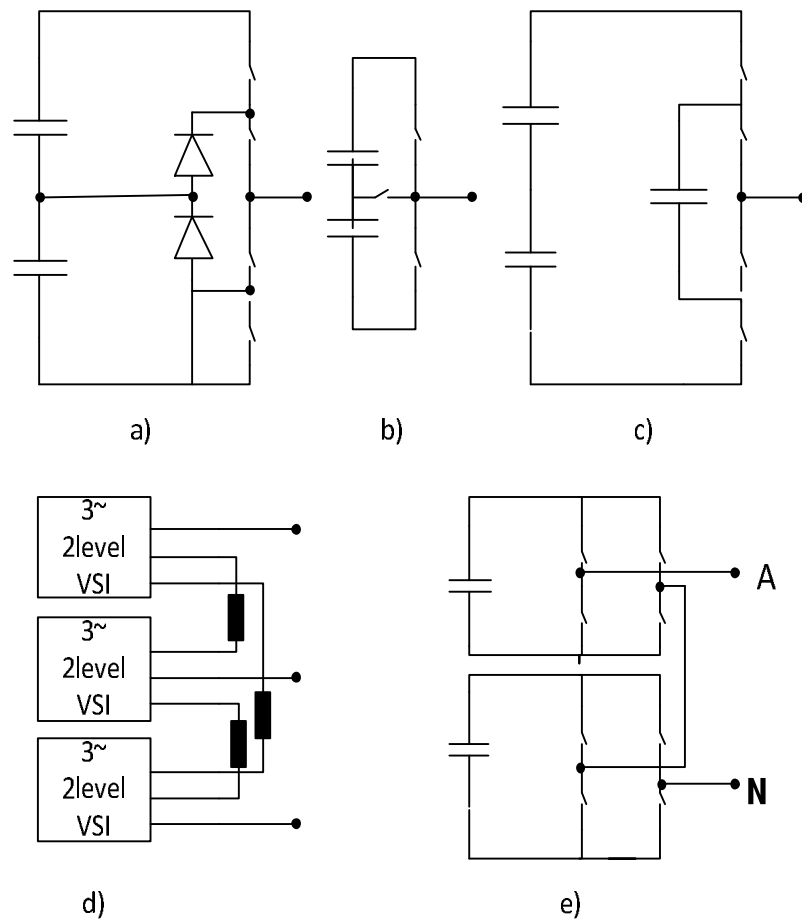
Fig.1.15. Multilevel topologies: a) One inverter leg of a three-level diode clamped multilevel converter; b) One inverter leg of a three-level multilevel converter with bidirectional switch interconnection; c) One inverter leg of a three level flying capacitor multilevel converter; d) Three-level converter consisting of three-phase inverters; e) One inverter leg of a three-level converter consisting of H-bridge inverters.

Disadvantages concerning the multilevel converter:

The most commonly disadvantage of the converters with split DC-link is the voltage unbalance between the upper and the lower DC-link capacitor. However, for a three-level converter this problem is not very serious, and is mainly caused by differences in the real capacitance of each capacitor, inaccuracies in the dead-time implementation or an unbalanced load. By a proper modulation control of the switches, the unbalance problem can be solved. For converters based on the topology from Fig.1.15.a-c, another problem is the unequal current stress on the semiconductors. It appears that the upper and lower switches in an inverter branch must be derated compared to the switches in the middle. For an appropriate design of the converter, different devices are required. For the topology in Fig.1.15.b it appears that both unequal current and voltage stress represents a design problem [6], [18].

The back-to-back PWM-VSI (Fig.1.16) is a bi-directional power converter consisting of two conventional PWM-VSIs. To achieve full control of the grid current, the DC-link voltage must be boosted to a higher level than the amplitude of the grid line-line voltage. The power flow of the grid side converter is controlled in order to keep the DC-link voltage constant, while the control of the generator side is set to suit the magnetization demand and the reference speed.

Advantages in using the back-to-back PWM-VSI:

The PWM-VSI is the most frequently used three-phase frequency converter. Many manufacturers produce components especially designed for use in this type of converter (e.g., a transistor-pack comprising six bridge coupled transistors and anti-paralleled diodes). The components costs can be low. A technical advantage of the PWM-VSI is the capacitor decoupling between the grid inverter and the generator inverter. Besides offering some protection, this decoupling offer separate control of the two inverters, allowing compensation of asymmetry both on the generator side and on the grid side, independently.

The inclusion of a boost inductance in the DC-link circuit has the advantage that the boost inductance reduces the demands on the performance of the grid side harmonic filter, and offers some protection of the converter against abnormal conditions on the grid.

Disadvantages of applying the back-to-back PWM-VSI:

The presence of the DC-link capacitor is mentioned as a drawback, since it is heavy and bulky, it increases the costs and maybe of most importance, it reduces the overall lifetime of the system. Another important drawback is the switching losses. Every commutation in both grid and generator inverter, between the upper and lower DC-link branch, is associated with a hard switching and a natural commutation. Since the back-to-back PWM-VSI consists of two inverters, the switching losses might be even more pronounced. The high switching speed on the grid side may also require extra EMI-filters [6], [19].
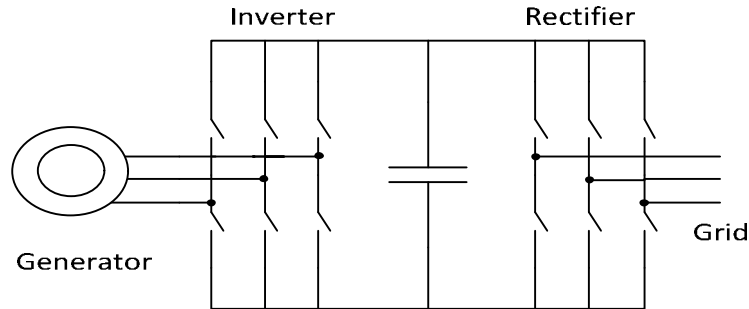
Fig.1.16. The back-to-back PWM-VSI converter topology.

The basic idea of the matrix converter (Fig.1.17) is that a desired input current (to/from the supply), a desired output voltage and a desired output frequency may be obtained by properly connecting the output terminals to the input terminals. In order to protect the converter, the following two control rules must be complied with: two (or three) switches in an output leg are never allowed to be on at the same time. All of the three output phases must be connected to an input phase at any instant of time. The actual combination of the switches depends on the modulation strategy.

Advantages of using the Matrix Converter:

For a low output frequency the thermal stresses of the semiconductors in a conventional inverter are higher than in a matrix converter. This arises from the fact that the semiconductors in a matrix converter are equally stressed, at least during every period of the grid voltage, while the period for the conventional inverter equals the output frequency. This reduces the thermal design problems for the matrix converter.

Although the matrix converter includes six additional power switches compared to the back-to-back PWM-VSI, the absence of the DC-link capacitor may increase the efficiency and the lifetime. Depending on the realization of the bi-directional switches, the switching losses may be lower compared with a PWM-VSI, because half of the switching became natural commutations (soft switching). Compared to converters with constant DC-link voltage and only two output levels, the output harmonic content is lower, due to the fact that it is composed of three levels.

Disadvantages and problems of the matrix converter:

A major disadvantage of the matrix converter is the intrinsic limitation of the output voltage. Without entering the over-modulation range, the maximum output voltage is 0.866 times the input voltage. To achieve the same output power as the back-to-back PWM-VSI, the output current has to be 1.15 times higher, giving higher conduction losses. The unavailability of a true bi-directional switch is mentioned as one of the major obstacles for the propagation of the matrix converter. In the literature, three proposals for a bi-directional switch exist: the diode embedded, which acts like a true bi-directional switch, the common emitter and the common collector switch. The latter two are able to control the current direction, which is preferable in the phase commutations. Since real switches do not have infinitesimal switching times (which are not desirable either) the commutation

between two input phases constitutes a contradiction between the two basic control rules of the matrix converter [6].
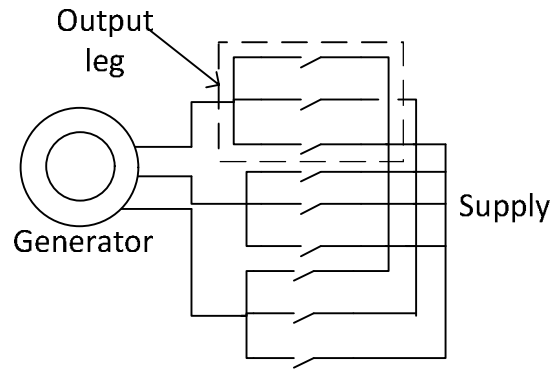
Fig.1.17. The matrix converter topology.

1.5. Control Strategies

Wind turbines are generally designed to extract maximum output from the wind speeds around 12-15 m/s, but in case of stronger winds it is necessary to waste a part of the excess energy in order to avoid damages [20].

So, one of the most important tasks of a control strategy is to limit the power input to the turbine to a level that the mechanical and electric components are able to handle. This must be achieved by reducing the power extracted from the wind. The common control methods that are being used in the most commercial available wind turbines in the market for their over speed and power control capability are:

- Stall-control
- Pitch-control
- Active-stall-control

Stall-controlled WECS, have a special design of the rotor blade profile. The power is controlled at high wind speeds, using the stall effect, creating turbulence on the side of the rotor blade which is not facing the wind. The stall prevents the lifting force from acting on the rotor [10]. The drawbacks of this power control method are: high mechanical stress caused by wind gusts, stall induced vibrations, variations in the maximum steady state power due to variations in the air density and grid frequency [7].

Pitch-controlled WECS implies modifying the pitch angle of the blade, turning them away or into the wind. When the output power is too high, the blade pitch mechanism turns the rotor blades out of the wind. The blades are turned back when the wind drops. The control will generally pitch the blades a few degrees every time the wind changes in order to keep the rotor blades at the optimum angle in order to maximize the output for all wind speeds. The pitch mechanics is usually operated using hydraulics [20]. The main advantages of controlling the pitch angle are power control performance, assisted start-up, and emergency stop power reduction. The pitch control mechanism is an additional cost to the WECS.

Active-stall WECS control moves the blades on the opposite direction from what a pitch control does. The attack angle of the rotor blades will be increased in order to make the blades to go into a deeper stall, wasting the excess energy in the wind. An advantage is that the output power can be controlled more precisely, avoiding overshooting the rated power of the turbine at the beginning of a wind gust. It is usually operated using hydraulics or electric motors. All of these add complexity and increase the operation and maintenance costs [7], [20].

Fixed-speed WECS can be energy conversion optimized by using one of these aerodynamic power controls.

Higher energy conversion efficiency for variable-speed WECS can be obtained by one or all of the following power control:
- aerodynamic power control by the pitch control method;
- generator control to capture maximum available power;
- grid power transfer control, through power electronics converter, which must ensure that the strict quality standards (frequency, power, factor, harmonics, flicker etc.) are met [7].

The role and objectives of WECS control are:
- limit the power and rotating speed at the rated values to protect all the components of the WECS;
- maximum power extraction to reach the goal of energy conversion optimization;
- realize a predictive energy management;
- create the possibility to disconnect a part of the load, if necessary;
- transfer the requested power quality to the grid;
- supervise and acquire data whenever it is desirable.

The latest WECS are equipped with control and supervision subsystems which realize supervision and data acquisition, e.g. SCADA.

1.6. Small-Scale Wind Turbine Systems

The IEC safety standard for wind turbines (IEC 61400-2) defines a small turbine having a rotor swept area less than 200 m^2, which corresponds roughly to P<50 kW [21].

Vertical axis wind turbines (VAWT) are more suitable for small-scale and home use because there is no need for a yaw system to deal with turbulence; operating commonly at a relative low speed eliminates the relative complicated overspeed protection for horizontal axis wind turbines (HAWT); it is appropriate for home use because it is much quieter than HAWT. Also horizontal vertical axes (HVAWT) are used because they combine the advantages of both HAWT and VAWT [21], [22].

All modern generators are three-phase; this increases the ratio of power to weight and produces a more constant shaft torque in comparison to fewer phases. Even for grid connected small turbines, it is usual to rectify the variable frequency and voltage generator output voltage and then invert it to produce AC power at constant voltage and frequency [21].

DFIG and PMSG are commonly used in wind energy systems. In recent years, direct-driven generators have been used, improving reliability and allowing the system to work without the gearbox [24].

PMSG became the most popular in small-scale wind systems due to the following reasons:

- PM poles take the place of excited circuits and reduce the complexity of manufacture and control;
- PMSGs with many poles perform efficiently at low speeds which usually mean they do not need a gearbox;
- They often have external PM arrays instead of the traditional inter rotor, so heat radiation is better than traditional generators topologies;
- They have higher power density because the active material weight of the generator for the same air-gap diameter is nearly halved, while the energy yield is a few percent higher;

The direct driven generators have these advantages [24]:

- reduce the complexity of the structure and improve reliability. Without the gearbox, the number of mechanical faults will definitely decrease;
- eliminate vibration and noise from gearbox;
- eliminate the cost of maintenance of the gearbox;

Circuits combining an AC-DC rectifier and a DC-DC converter are commonly used in small-scale off-grid wind turbines systems. The AC-DC diode rectifier is connected to the terminal of the generator and the controllable DC-DC converter is connected to the rectifier output to achieve a constant voltage. Another kind of converter system consists of only an AC-DC PWM rectifier, which is controlled to make the output DC voltage constant [25].

The Maximum Power Point Tracking (MPPT) is the basic method used below the rated speed. The MPPT aims to track the optimal operating point by controlling the rotational speed of the generator by the DC-DC converter. Some novel algorithms such as fuzzy logic or neural network are used to improve the control performances [25].

Many micro-turbines charge batteries and use a much simpler control system. Another solution is to combine a rectifier, a MPPT controller and an inverter for grid connection. Filtering is often used to reduce the harmonic distortion of the power injected to the grid. The inverter must also control the power factor. In addition the turbine output power must be synchronized with the grid. It is also becoming common for the turbine controller to have a major or exclusive role in over-speed protection. As with all forms of over-speed protection, there are potential problems with shorting the output. The current or heat generated may demagnetize the magnet and/or burn out the windings [21].

Fig. 1.18 shows a typical small-scale wind turbine system (SWECS) with basic elements and protection devices [21].
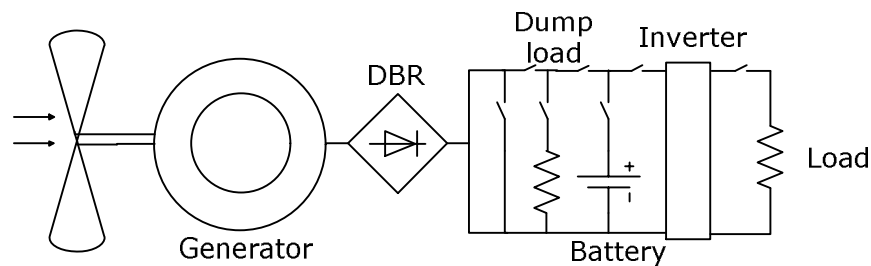
Fig.1.18. Small-scale wind turbine system.

According to the application characteristics of SWECS, they should present the following advantages [26]-[28]:
- simplicity;
- low cost;
- high efficiency;
- safety;
- low noise;
- high reliability;
- inexpensive maintenance.

1.6.1. Off-Grid Wind Turbine Systems

Most standalone systems can be integrated in three categories: micro systems (100 W or less), mini systems (100 W up to 10 kW) and small systems (10 kW up to 50 kW). Many energy sources are used in combination such as wind, solar panels, fuel cells, biomass, or a diesel engine generator (DG).

A standalone system may have a method for storing energy when wind conditions are poor. Usually batteries are used for storage. When the wind falls below the "cut in" speed, the batteries are used. When the wind is sufficient, the wind turbine charges the batteries [20].

A typical small-scale off-grid system consists essentially of a wind turbine, an electrical generator, an AC-DC converter, a DC-DC-AC converter, a control system and a battery bank.

The integration of renewable energies into an energy conversion system in addition to a storage unit gives the so called "hybrid supply system", which is actually used as a standard for electrical energy supply in many isolated regions in the world, especially in developing countries. The concept of hybrid supply system is based on combining two or more energy sources, mainly a photo-voltaic unit with a wind energy plant and biomass system to reduce the zero power intervals and optimize the global cost. It is a solution for the long power cut offs problems caused by DG maintenance and also by using just one type of renewable energy source, due to poor power capture resulting from bad atmospheric conditions (e. g. cloudy days or no wind) [29]. Stand-alone power systems with grid back-up capability are useful when homeowners want to become energy independent from the utility grid, but they want to have a back-up in case of a renewable power sources failure. Electronic controls are necessary to monitor continuously the performance of the battery bank. Also, an independent power source, like a DG, could be the back-up solutions in regions were the utility power service is not reliable.

Fig.1.19 illustrates a hybrid energy system configuration composed by a photo-voltaic unit (PV), a wind turbine (WT) coupled to a PM generator with a three phase diode bridge rectifier (DBR), as primary energy sources, and a fuel-cells (FC) stack as back up energy source. All three energy systems are connected in parallel to a common DC bus through three individual DC–DC boost converters. The diodes D1, D2 and D3 play an important role in the system. The diodes allow only unidirectional current flow from the sources to the DC bus. Therefore in the event of malfunctioning of any of the sources, the respective diode will automatically disconnect it from the overall system. The DC bus output voltage from all converters is set to be fixed and the output voltage from each source is controlled independently [30], [31].
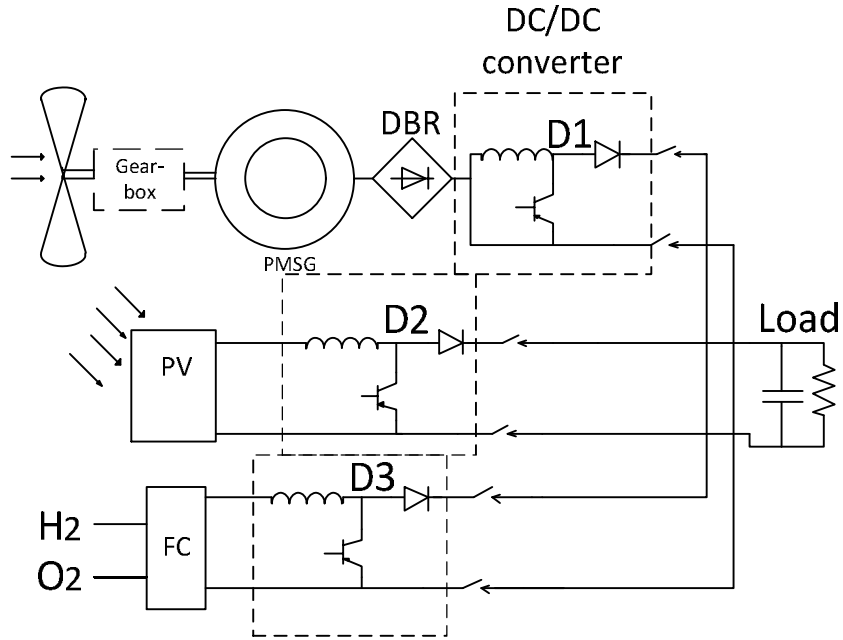
Fig.1.19. Hybrid wind/solar/fuel-cells energy system.

Another renewable hybrid energy system which can be seen in Fig.1.20, consists of a wind energy system, a solar power system, a battery bank for storage, a diesel generator or the grid for back up, power conditioning equipment, and a controller to maintain the grid power quality [32].
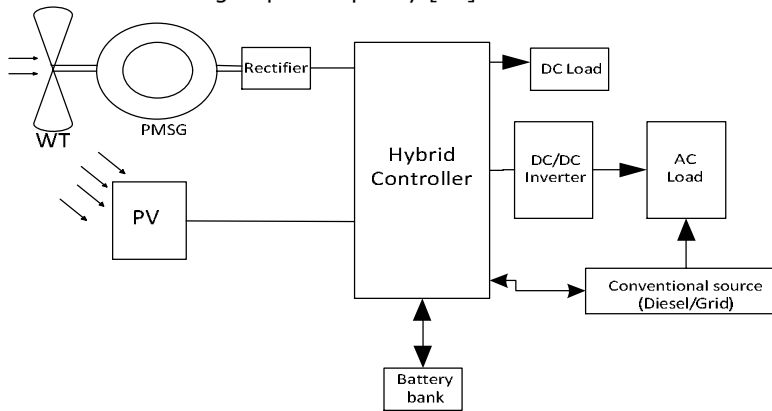
Fig.1.20. Hybrid wind/solar energy system.

Next, in Fig. 1.21, is presented the structure of a hybrid solar/wind/biomass electrical energy supply system. The idea proposed in [29] is that 50% of the

demand must be satisfied by the PV system since solar energy is abundant in the country, for which the system was designed. The rest should be shared between the wind energy conversion system (25% to 50%) and biomass plus battery at a maximum part of 25%. A power flow control strategy that would manage the power production units and their sharing is essential for the good operation of the hybrid system.

The system is also able to supply cooling resources that will be used to increase the solar panel efficiency which is negatively affected by any increase in the panel temperature.
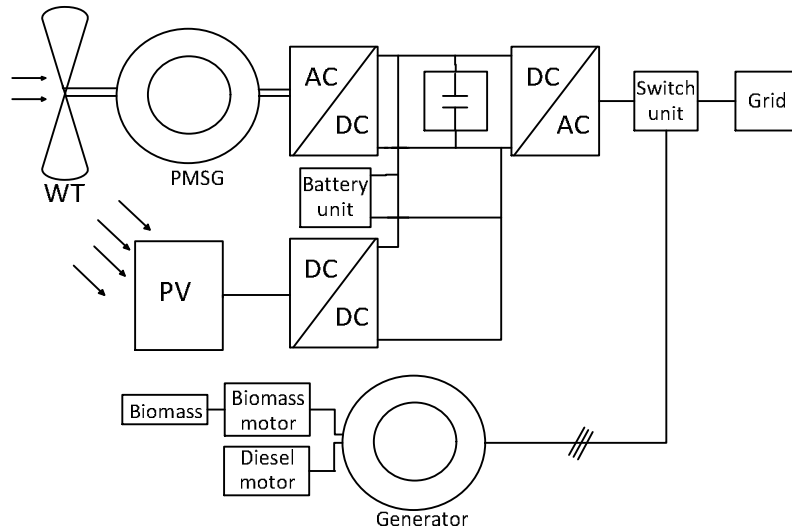
Fig.1.21. Hybrid wind/solar/biomass energy system.

In fig. 1.22 is presented a wind/DG composed of a stall regulated wind turbine with an AG connected to an AC bus-bar in parallel with a diesel-generator driving a SG. The generators serve the 40 kW electrical loads in parallel and the control of voltage and frequency is maintained by the diesel-generator. The electrical frequency is determined by the speed governor control of the diesel engine (DE), and the grid voltage is maintained by excitation of the SG field windings [33].

From the control point of view, the wind/diesel plant considered in [33] has an operating point that is continuously changing due to the natural fluctuation of available power from the renewable energy source. In addition, non-linearity exists in the models of the wind turbine and the electric generators. A linear controller designed to work optimally around a nominal operating point of a non-linear system may be degraded at other operating points. Therefore, a non-linear robust controller based on the feedback linearized proportional integral (FLPI) method was used.
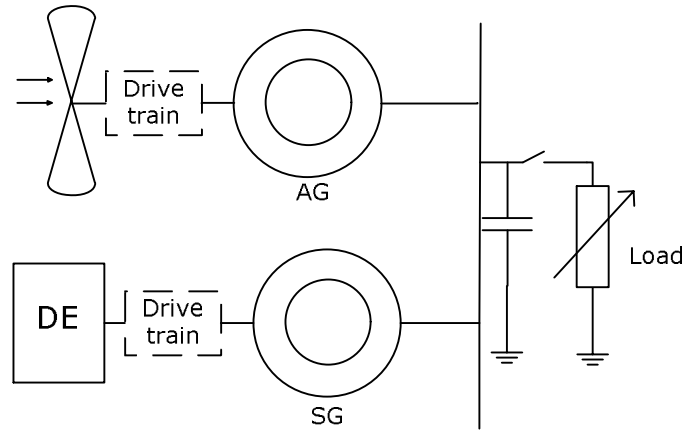
Fig.1.22. Hybrid wind/diesel energy system.

1.7. Storage Elements

Because the wind is intermittent, and not 100% predictable, and this can lead to power system instability, reliability, and power quality, storage elements are required, especially in off-grid regime [34]-[36].

There are many types of energy storage technologies available at the moment. Each of them has its own characteristics and is suitable for different grid-support or stand-alone applications [34].

The important requirements to be considered when choosing a storage element are:
 – cost option (capital and maintenance);
 – size;
 – energy density;
 – energy storage capacity;
 – cycling capability;
 – lifetime;
 – depth of discharge (DOD);
 – reliability and efficiency of the storage system;

Next, an overview of the state of the art regarding energy storage elements is presented.

Lead Acid battery (LA) is the oldest, cost effective option, and most mature energy storage technology that has been used in small to large-scale applications. There are several types of lead acid batteries, among which the most utilized are: the flooded lead acid (FLA) and the valve-regulated lead acid (VRLA). The lifetime of these storage elements varies significantly depending on its application, the number of charge/discharge cycles, how deeply it is recharged and discharged etc. They are characterized by relatively low prices, easy maintenance, efficiency between 72%-85% and fast time response. Because its low power density, limited lifetime, environmental unfriendliness due to lead-electrolyte leakage, marginal performance

at low temperature, they are considered less suitable for large-scale WECS applications [34], [37]-[39].

Sodium Sulphur battery (NaS) is a mature energy storage (ES) technology with a significant commercial experience. It is characterized by high round-trip ac-to-ac efficiency, between 75% and 90%. NaS have an estimated life-time of 15 years or 4500 cycle at 90% DOD. The major drawback of this ES technology is that a heat source is required, using the battery's own stored energy, since the operating temperature must be kept at around 300°C. Due to its characteristics, NaS are suitable for applications such as load leveling, voltage sag compensation, peak shaving and power quality [34], [39].

Lithium Ion battery (Li-ion) technology is relatively new since the first commercial unit was released by Sony in 1990. Li-ions are characterized by the highest efficiencies (around 95%) among the electrochemical energy storage technologies, and by high energy densities of about 200 Wh/kg. They represent an attractive solution for different applications since its life cycle is estimated to be about 3000-4500 cycles at 80% DOD, can operate over a wide range of temperatures, between - 30°C and 60°C, and has reduced self-discharge ratio of about 1% per month. Currently, the main drawback is their high cost due to their special packing and internal overcharge protection circuits [34]. They are predominant in small-scale applications such as in consumer electronic products. They are also a suitable solution for utility grid support applications, such as distributed energy storage, transportable systems for grid-support, commercial end-user energy management, home back-up, frequency regulation, wind power and photovoltaic power smoothing etc. [37], [39].

Nickel Cadmium batteries (NiCd) are together with LA the most mature battery technology available on the market. The efficiency of NiCd lies between 65% and 75%. Their estimated life cycle varies between 2500 and 3000 cycles at 100% DOD. A big advantage of this technology is its ability to operate over a large temperature range from - 40°C to 50 °C. Similar to the LA, the lifetime of NiCd can be significantly reduced by deep cycles. Moreover, NiCd suffer from "the memory effect" and have a high self-discharge rate between 2% and 5% per month. Another important drawback of the NiCd is related to their environmental impact since cadmium is a toxic material. Considering their characteristics, probably NiCd will not be used for grid support in wind power applications [34], [39].

Supercapacitors (SC) are compact in size and can store a much higher amount of energy than conventional capacitors while also being able to deliver at a much higher power than batteries. Maxwell Technologies offer "BOOSTCAP" SC on the market with capacitance ranges up to 2700 Farads [40]. According to [41] the SC can be rated up to 5000 F.

The advantages of SC, compared with batteries, are [39], [40]:

- they function well in cold weather, down to –40°C, without heating; they are extremely safe because a pack with equalization is discharged overnight;
- they have a long life cycle. This means that they are maintenance-free which ultimately results in costs-savings.
- they are more efficient than batteries; 84-95% as compared to an average of below 70% for batteries.
- they are very earth-friendly, as they are 70% recyclable, and do not include any heavy metals.
- they offer up to 10 times the power of batteries.

As is clearly seen in the above comparison, batteries have high energy capacity while the supercapacitors have high power capacity. In an optimal hybrid storage system, both technologies would be combined in a way to maximize the benefits [40].

SC is considered suitable for applications within the wind power industry, being able to suppress fast wind power fluctuations, but only for short periods of time [41], [42].

Flywheels (FW) are mechanical energy storage devices which store the energy in a kinetic form, in a spinning rotor which is charged and discharged through a generator. FW charges by accelerating the rotor to a very high speed. The energy is maintained in the system as kinetic energy until it is discharged as the wheel's rotation slows down [34], [39].

FW store power in direct relation to the mass of the rotor and to the square of their surface speed. Therefore, the most efficient way to store energy in a FW is to make it spin faster and not by making it heavier [34].

Two categories of FW can be distinguished: low-speed and high-speed. According to [41], the current research is focused on high-speed FW which are able to rotate with up to 100 000 rpm. This technology is able to provide a maximum power of 750 kW for one hour. FW technology is characterized by a very fast response time of 4 milliseconds or less, sizes between 100 kW and 1650 kW and efficiencies of about 93%. Moreover, FW may be used for short durations (up to one hour), require little maintenance and have a predicted life-time of approximately 20 years or 150000 cycles at 100% DOD [34].

FW are suitable for applications such as: UPS and frequency variation damping, making useful to smooth the irregular output of wind turbines [34].

It is unlikely that FW to be considered a suitable option as a sole storage provider for power generation applications [34].

There are many energy storage technologies available at this moment on the market. To identify the most relevant storage solution for a certain application, it is important to consider many relevant parameters such as: cost, energy storage capacity, size, lifetime, environmental impact etc.

1.8. Conclusion

The scope of this chapter was to present an overview of the state of the art regarding the configurations, electric generators, power electronic converters, storage elements and control principles used in WECS.

WECS were classified according to speed control or power control capabilities.

Induction machines, like DFIG, and AG have been proposed as generators for WECS in many research articles [43]. The advantage of a DFIG is that the speed is variable within a sufficient range with limited converter cost. The stator active and reactive power can be controlled independently by controlling the rotor currents with the converter. Furthermore, the grid-side converter can control its reactive power, independently of the generator operation. This allows the performance of voltage support towards the grid. AG enables variable speed operation at all wind speeds and does not need to have the same output frequency as the grid.

A major disadvantage of the AG is the need for excitation capacitors to self-excite before they can generate power. The AG drawback is the high cost of the full scale converter [10].

The PMSG seems to be attractive as a wind turbine generator. Advantages include self-excitation, high power factor, and high efficiency. In the PMSG, efficiency is higher compared with the induction machine. But PMs are expensive and are difficult to handle in manufacture. Additionally, the use of PM excitation requires the use of a full power converter [6].

In conclusion, the high efficiency wind turbine configurations are using PMSG and DFIG [44].

Converter topologies with different control schemes have been also described. The standard topologies, from the simplest converters for starting up the turbine, to the advanced full power topologies, were presented.

It is concluded that the back-to-back converter, the matrix converter and the multilevel converter are the most commercial used in different conversion topologies at high power [6].

In low power applications, PMSG with DBR, and a DC-DC converter that can regulate the power and can charge the storage elements, followed by a PWM-VSI (connected or not to the grid) is the most used solution.

All control methods described, attempt to obtain maximum energy transfer from the wind turbine to the load and to realize the grid interface conditions.

Wind turbine design objectives have changed a lot in the last 15 years. Modern wind turbine have become larger, of higher-power, they are preferred to be variable-speed, pitch controlled, drive train with or without gearbox, and fully controllable. The development of the components of a WECS depends on the controlled capabilities of every component.

SWECS have also been much studied and very used especially in stand-alone and hybrid power systems. Some typical applications are the hybrid wind-photovoltaic or wind turbines coupled with fuel-cell or diesel, all using batteries as storage elements. The main problem in a hybrid system is the designed control strategy for all the elements so that a power supply exists at any time and on the other hand it shouldn't be any waste of energy.

It can be expected that a very large number of small (5-10 kW) systems will be installed in households for combined power and heat production. The small-scale wind turbines will be in contrast to the big trend in wind energy, where the wind turbines are increasing in capacity and will be concentrated in the areas with the highest wind resources. The control of this distributed generation systems will be a serious challenge.

In the end, it is necessary to analyze these WECS based on some indicators as:

• Overall efficiency;
• Power flow capability;
• Range of speed operation;
• Machine weight;
• Reliability and maintenance.

Finally, the use of this alternative renewable source of energy has a positive impact on the environment. It reduces combustion of fossil fuels and consequently CO_2 emission which is the principal cause of the greenhouse-effect/global warming.

References

[1] "Background on Energy in Europe"- Information prepared for the European Council, 4 February 2011.

[2] C. Lewiner, "Sustainable Energy and Climate Change", European Energy Markets Observatory- Book, Springer Netherlands, 2012, pp. 79-88.

[3] M. Liserre, T. Sauter, J. Y. Hung, "Future Energy Systems - Integrating Renewable Energy Sources into the Smart Power Grid through Industrial Electronics", *IEEE Industrial Electronics Magazine*, vol. 4, no. 1, March 2010, pp. 18-37.

[4] B. L. Capehart, P. Mehta and W. Turner, "Distributed generation and your energy future", Cogeneration and Distributed Generation Journal, vol. 18 (4), 2003, pp.17-33.

[5] I. Munteanu, A. I. Bratcu, N. A. Cutululis, E. Ceanga, "Optimal Control of Wind Energy Systems", Springer, 2008.

[6] L. H. Hansen, L. Helle, F. Blaabjerg, E. Ritchie, S. Munk Nielsen, H. Bindner, P. Słrensen and B. Bak-Jensen, "Conceptual survey of Generators and Power Electronics for Wind Turbines", Riso National Laboratory, Roskilde, Denmark, December 2001.

[7] A. D. Hansen, F. Iov, F. Blaabjerg and L. H. Hansen, "Review of Contemporary Wind Turbine Concepts and their Market Penetration", *Wind Energy Volume*, vol. 28, no.3, 2004, pp.247–263.

[8] Z. Chen, J. M. Guerrero and F. Blaabjerg, "A Review of the State of the Art of Power Electronics for Wind Turbines", *IEEE Trans. on Power Electronics*, vol. 24, no.8, August 2009, pp.1859–1875.

[9] F. Blaabjerg, Z. Chen, R. Teodorescu, F. Iov, "Power Electronics in Wind Turbines Systems", *CES/IEEE 5th International Power Electronics and Motion Control Conference, IPEMC 2006*, 14-16 August, pp. 1–11.

[10] H. Polinder, D.-J. Bang, H. Li, Z. Chen, "Concept Report on Generator Topologies, Mechanical and Electromagnetic Optimization*"*, Integrated Wind Turbine Design, 6th Framework Programme, Delft University of Technology, Aalborg University, 2007.

[11] F. Blaabjerg and Z. Chen, "Power Electronics for Modern Wind Turbines", Morgan & Claypool Publishers, 2006.

[12] F. Blaabjerg, F. Iov, T. Terekes, R. Teodorescu, K. Ma, "Power Electronics – Key Technology for Renewable Energy Systems", *2th Power Electronics, Drive Systems and Technologies Conference,* Tehran, 16-17 Feb. 2011. pp. 445-466.

[13] N. A. Orlando, M. Liserre, V. G. Monopoli, R. A. Mastromauro, A. Dell'Aquila, "Comparison of power converter topologies for permanent magnet small wind turbine system", *International Symposium on Industrial Electronics, ISIE 2008*, June 30 -July 2, 2008, pp. 2359 - 2364.

[14] N. Milivojevic, I. Stamenkovic, N. Schofield and A. Emadi, "Electrical Machines and Power Electronic Drives for Wind Turbine Applications", *Industrial Electronics 34th Annual Conference of IEEE, IECON 2008*, Orlando, FL, 10-13 Nov. 2008. pp. 2326-2331.

[15] J. Yan, J. Chen, H. Ma, H. Liu, L Chen, " The survey of electrical control systems of wind turbine generators", *International Conference on Sustainable Power Generation and Supply, SUPERGEN '09*, Nanjing, 6-7 April 2009, pp. 1-5.

[16] F. Blaabjerg, F. Iov, Z. Chen, K. Ma, "Power Electronics and Controls for Wind Turbines Systems", *IEEE International Energy Conference, 2006. IPEMC 2006*, 14-16 August, pp. 1–11.

[17] F. Blaabjerg, "Wind Turbine Systems - 1A", Aalborg University Institute of Energy Technology.

[18] O. Bouhali, B. François, C. Saudemont, El Madjid Berkouk, "Practical power control design of a NPC multilevel inverter for grid connection of a renewable energy plant based on a FESS and a Wind generator", *32nd Annual IEEE Conference on Industrial Electronics, IECON 2006*, 6-10 November, Lille, pp. 4291-4296.

[19] J. A. Baroudi, V. Dinavahi, A. M. Knight, "A review of power converter topologies for wind generators", *Renewable Energy*, vol. 32, 2007, pp. 2369–2385.

[20] L. Mihet-Popa, "Wind Turbines Using Induction Generators Connected to the Grid", Ed. Politehnica, Timisoara 2007.

[21] D. Wood, "Small wind turbines - Analysis, Design, and Application", Springer 2011.

[22] D. Li, S. Wang, P. Yuan, "A Review of Micro Wind Turbines in the Built Environment", *Power and Energy Engineering Conference (APPEEC), 2010 Asia-Pacific*, Chengdu, 28-31 March 2010, pp. 1-4.

[23] J.H. Paulides, L. Encica, J.W. Jansen, E.A. Lomonova, D. van Wijck, "Small-scale Urban Venturi Wind Turbine: Direct-Drive Generator", *IEEE International Electric Machines and Drives Conference, 2009. IEMDC '09,* 3-6 May, 2009, pp. 1368-1373.

[24] H. Polinder, F. F.A. van der Pijl, G.-J. de Vilder, P. Tavner, "Comparison of direct-drive and geared generator concepts for wind turbines", *IEEE Transaction on Energy Conversion*, vol. 21, issue 3, Sept. 2006, pp. 725-733.

[25] W. Liang, W. Liu, "Key Technologies Analysis of Small Scale Non-Grid-Connected Wind Turbines: A Review", *World Non-Grid-Connected Wind Power and Energy Conference (WNWEC), 2010,* 5-7 November, 2010, pp. 1-6.

[26] Md. Arifujjaman, M. T. Iqbal, J. E. Quaicoe, "A comparative study of the reliability of the power electronics in grid connected small wind turbine systems", *Canadian Conference on Electrical and Computer Engineering, 2009. CCECE '09,* 3-6 May, 2009, pp. 394-397.

[27] H.-G. Park, S.-H. Jang, D.-C. Lee, H.-G. Kim, "Low-Cost Converters for Micro Wind Turbine Systems using PMSG", *The 7th International Conference on Power Electronics,* 22-26 October, 2007, EXCO, Daegu, Korea, pp. 483-487.

[28] M. Lopez, J.-C. Vannier, "Stand-alone Wind Energy Conversion System with Maximum Power Transfer Control", *Ingeniare, Revista chilena de ingineria, vol. 17, no. 3, 2009*, pp. 329-336.

[29] M. Kesraoui, "Designing a Wind/Solar/Biomass Electricity Supply System For an Algerian isolated Village", *13th European Conference on Power Electronics and Applications, 2009, EPE '09,* 8-10 Sept. 2009, Algeria, pp. 1-6.

[30] N. A. Ahmed, M. Miyatake, A.K. Al-Othman, "Power fluctuations suppression of stand-alone hybrid generation combining solar photovoltaic/wind turbine and fuel cell systems", *Energy Conversion and Management*, vol. 49, 2008, pp. 2711-2719.

[31] N.l A. Ahmed, A.K. Al-Othman, M.R. Al Rashidi, "Development of an efficient utility interactive combined wind/photovoltaic/fuel cell power system with MPPT and DC bus voltage regulation", *Electric Power System Research*, vol. 81, Issue 5, May 2011, pp. 1096-1106.

[32] P. Nema, R.K. Nema, S. Rangnekar, "A current and future state of art development of hybrid energy system using wind and PV-solar: A review", *Renewable and Sustainable Energy Reviews,* vol. 13, 2009, pp. 2096-2103.

[33] R. B. Chedid, S. H. Karaki, C. El-Chamali, "Adaptive Fuzzy Control for Wind-Diesel Weak Power Systems", *IEEE Transaction on Energy Conversion*, vol. 15, no.1, March 2000, pp. 71-78.

[34] D.-I. Stroe, A.-I. Stan, R. Diosi, R. Teodorescu, S. J. Andreasen, "Short Term Energy Storage for Grid Support in Wind Power Applications", 13th *International Conference of Electrical and Electronic Equipment, OPTIM 2012,* 24-26 May, Brasov, Romania, pp. 1012-1021.

[35] C. Abbey and G. Joos, "Supercapacitor Energy Storage for Wind Energy Applications", *IEEE Transaction on Industry Applications*, vol. 43, no. 3, May/June 2007, pp. 769-776.

[36] C. Abbey and G. Joos, "Energy Management Strategies for Optimization of Energy Storage in Wind Power Hybrid System", *IEEE 36th Power Electronics Specialists Conference, PESC '05*, Recife, Brazil, 16 June 2005, pp. 2066-2072.

[37] Z. O. Olaofe and K. A. Folly, "Energy Storage Technologies for Small Scale Wind Conversion System*", Power Electronics and Machines in Wind Applications (PEMWA), 2012,* 16-18 July 2012, pp. 1-5.

[38] L. Barote, C. Marinescu, "Storage Analysis for Stand-Alone Wind Energy Applications", 12th *International Conference of Electrical and Electronic Equipment, OPTIM 2010,* 20-21 May, Brasov, Romania, pp. 1180-1185.

[39] S. Vazquez, S. M. Lukic, E. Galvan, L. G. Franquelo and J. M. Carrasco, "Energy Storage Systems for Transport and Grid Applications*", IEEE TRANSACTIONS ON INDUSTRIAL ELECTRONICS,* vol. 57, no.12, December 2010, pp. 3881-3895.

[40] www.maxwell.com.

[41] ZM. Swierczynski, R. Teodorescu, C. Rasmussen, P. Rodriguez and H. Vikelgaard, "Overview of the energy storage systems for wind power integration enhacement*", 2010 IEEE International Symposium on Industrial Electronics (ISIE),* 4-7 July 2010, pp. 3749-3756.

[42] S. Breban, B. Robyns, M.M. Radulescu, "Study of a grid-connected hybrid wind/micro - hydropower system associated with a supercapacitor energy storage device*",* 12th *International Conference of Electrical and Electronic Equipment, OPTIM 2010,* 20-21 May, Brasov, Romania, pp. 1198-1203.

[43] L. Szabo, K. Á. Biro, C. Nicula, F. Jurca, "Useful Simulation Tool for Induction Generators Used In Wind Power Plants*", International Conference on Clean Electrical Power, ICCEP '07 ,* 2007, pp. 574-579.

[44] L.M. Fernandez, C.A. Garcia, F. Jurado, "Comparative study on the performance of control system for doubly fed induction generator (DFIG) wind turbines operating with power regulation*", Energy,* vol. 33, 2008, pp. 1438-1452.

2. THE PROPOSED WIND ENERGY CONVERSION SYSTEM STRUCTURE

2.1. Introduction

For SWECS (1…10kW), an important market exists for both on-grid and off-grid configurations. In off-grid systems the storage capacity and the system control are very important, because the input power, generated by a wind turbine, changes with the wind speed [1], [2].

The optimal operating point control of a wind turbine can be implemented with known of P(ω) characteristic, or with tracking algorithms (MPPT) [2], [3], through a power electronic converter (Conv1) and a permanent magnet synchronous generator (PMSG), usually used at this power level. Fig.2.1 shows a block diagram of a typical wind generation system with two DC busses and storage capability. The storage elements are usually rechargeable batteries (Bat), rated at (12 – 48)V_{dc}, depending on the PMSG nominal power.
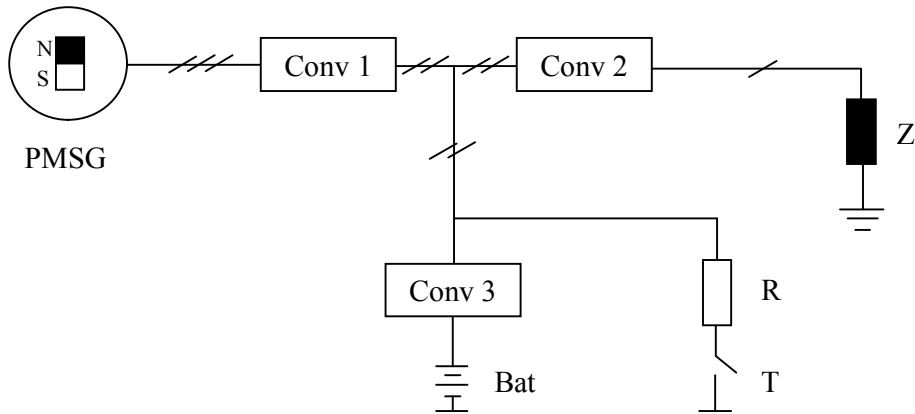
Fig.2.1. Off-grid wind system structure with two DC buses.

If the load (Z) nominal voltage is 240 V_{ef}, the power inverter (Conv2) needs a DC input voltage above 340 V_{dc}. For this reason, the power conversion has two DC buses, connected by a bidirectional DC–DC converter (Conv3). If the input power produced by the generator is higher than the output power plus the battery input (charge) power (in off-grid systems), a dumping resistor (R) is necessary to be connected on the high voltage DC bus with a static switching device (T).

The main problems of the presented configuration are:

If the inverter is implemented on the low voltage side [4], then the Conv3 is missing, but the system needs a step-up, low frequency (50 Hz) transformer (TR), as shown in Fig.2.2. This structure is used especially when the system can work both in off-grid and on-grid connections.
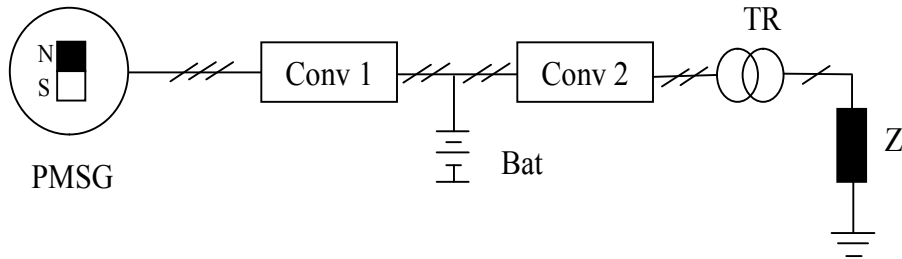
Fig.2.2. Off-grid wind system structure with step-up transformer.

In this chapter an architecture for SWECS, which uses a novel power converter and supercapacitors for short-term energy storage is proposed. The main components of the system are described in detail and modeled, for digital simulations and control implementation. Some simulation results are presented, in order to explain and analyze the system functionality.

2.2. The Proposed System Structure

The proposed conversion and control system for an off-grid SWECS is based on an intermediate, variable-voltage DC bus, implemented by means of a SC, connected between a hybrid DC–DC converter (HDC) on the PMSG side and a charge controller (Fig.2.3). The main role of the SC is to ensure the energy storage in transients, at higher current levels, in order to maintain the battery (Bat) in the rated charge/discharge regimes. The PMSG three phase voltages are rectified using a DBR.
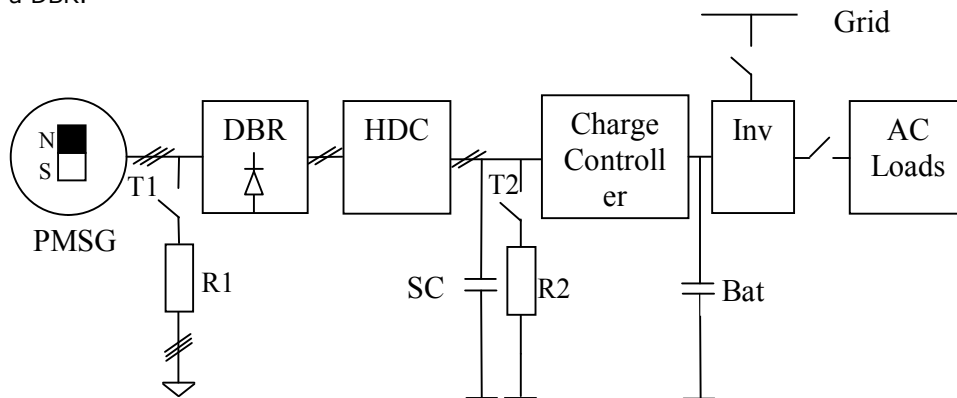
Fig.2.3. The proposed conversion structure.

Two resistors (R_1 and R_2) can be connected with two power switching devices (T_1 and T_2). The first one, which is a three phase resistor, is connected at the PMSG output and the second is in parallel with SC. Both R_1 and R_2 are used for protection.

In order to have relatively low currents in the PMSG windings, higher voltage is preferred, for efficiency reasons. Taking in consideration that the SC maximum voltage must be around (100 - 150) V (for price and technical reasons), and the SC voltage starts from 0 V when it is completely discharged, a hybrid configuration (described in the next sections) was chosen for HDC.

The charge controller regulates the output current based on the amount of DC power available and the state of charge of the battery. The inverter is a self-contained DC to AC inverter, battery charger and an integrated AC transfer switch. It can be used for stand-alone operation, grid-backup and grid-tie with battery energy storage.

2.3. Wind Turbine Characteristics and Model

Several wind turbines types have been proposed over the last years. Vertical axis wind turbines (VAWT) are more suitable for small-scale and home use because there is no need for a yaw system to deal with turbulence; operating commonly at a relative low speed eliminates the relative complicated over speed protection for horizontal axis wind turbines (HAWT). HAWT instead, can operate at higher wind speeds and are mounted at higher height. Today, the majority of manufactured wind turbines are HAWT, with either two or three blades [5], [6].

The principal components of a wind turbine are: the tower, the nacelle and the rotor. The nacelle is mounted on the tower and contains all the transmission mechanisms, the gearbox, the electrical generator, the control subsystems and some auxiliary elements (e.g., cooling and braking systems etc.). The rotor is composed of blades and turbine hub which is the blades support. The rotor is connected to the gearbox mechanism (if necessary). The gearbox converts low speed of the main shaft from about 15 - 60 rpm into high speed of the generator shaft around 900 - 1800 rpm. A disk brake is used in case of wind gusts, when there is no need for energy or in case of maintenance. It can be applied mechanically, electrically or hydraulically [6], [7].

The rotor blade of a wind turbine extracts the flow energy from air, convert it into rotational energy and then deliver it to the generator for power conversion in electrical energy.

The kinetic energy of an air mass travelling with a speed v is:

$$E_k = \frac{1}{2} \cdot m \cdot v^2 \tag{2.1}$$

where m is the air mass:

$$m = \rho \cdot V \tag{2.2}$$

V is the volume:

$$V = A \cdot d \tag{2.3}$$

and d is the distance:

$$d = v \cdot t \tag{2.4}$$

The power available from the wind (P_w) can be calculated by taking the derivative of the wind kinetic energy, equation (2.1). The wind speed v is assumed to be constant:

$$P_w = \frac{dE_k}{dt} = \frac{1}{2} \cdot \frac{dm}{dt} \cdot v^2 \tag{2.5}$$

$$P_w = \frac{1}{2} \cdot \rho \cdot A \cdot v^3 \tag{2.6}$$

where
A: blade swept area [m^2];
ρ: specific density of air [kg/m^3];
v: wind speed [m/s];
t: time.

The output power of a wind turbine is proportional with the cube of the wind speed. Larger rotors allow wind turbines to operate at higher wind speeds, increasing their output power. Because the area covered by the rotor is larger and so is the blades length, this leads to a large energy capture.

The aerodynamic efficiency of a wind turbine, while converting the power available from the wind into mechanical power is described by its power coefficient (C_P) curve. The physical meaning of the C_P is the ratio of the actual power delivered by the turbine to the theoretical power available from the wind:

$$C_P = \frac{P_{wt}}{P_w} \tag{2.7}$$

The theoretical maximum value of C_P is 0.59, known as the Betz limit and represents the maximum power extraction efficiency of a wind turbine [8], [9].

Fig.2.4 presents this C_P versus tip-speed ratio (λ) curve for a five-blade, fixed-pitch, variable-speed wind turbine, which is the first used wind turbine model in this thesis. From Fig.2.4 it is observed that the power conversion efficiency has a maximum for a specific λ, which is the optimal one, noted with TSR_{opt} (or λ_{opt}).
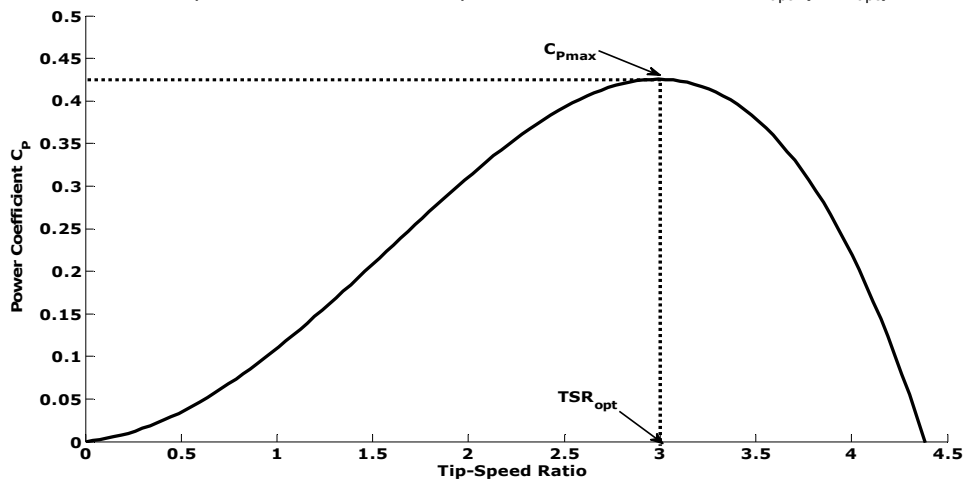
Fig.2.4. Power coefficient (C_P) versus the tip-speed ratio (λ) curve of the studied, five-blade fixed-pitch, wind turbine.

The mechanical power (P_{wt}) and torque (T_{wt}) of a wind turbine are given by the following equations:

$$P_{wt} = \frac{1}{2} \cdot \rho \cdot A \cdot C_P(\lambda, \beta) \cdot v^3 \tag{2.8}$$

$$T_{wt} = \frac{P_{wt}}{\omega} = \frac{1}{2 \cdot \omega} \cdot \rho \cdot A \cdot C_P(\lambda, \beta) \cdot v^3 \tag{2.9}$$

$$C_T = \frac{C_P}{\lambda} \tag{2.10}$$

where the rotor blade tip-speed ratio λ is defined as:

$$\lambda = \frac{\omega \cdot R}{v} \tag{2.11}$$

with:
R: radius of the turbine blade [m];
ω: rotor speed [rad/s];
β: rotor blade pitch angle [rad];
C_P: wind turbine power coefficient;
C_T: wind turbine torque coefficient.

$$T_{wt} = \frac{1}{2} \cdot \rho \cdot A \cdot R \cdot C_T(\lambda, \beta) \cdot v^2 \tag{2.12}$$

The first studied wind turbine has the following specifications:
- Rated power, P_n = 5.5 [kW];
- Rated wind speed, v_0 = 11 [m/s];
- Maximum speed, n = 126 [rpm];
- Turbine inertia, J_{wt} = 140 [kg·m^2];
- Blade swept area, A = 19.6 [m^2];
- Radius of the turbine blade, R = 2.5 [m];
- Maximum coefficient of power conversion, C_p = 0.42;
- Specific density of air, ρ =1.225 [kg/m^3] at 15 [$^\circ$C];

C_T is computed from [9]:

$$C_T = C_{T0} + a \cdot \lambda - b \cdot \lambda^{2.5} \tag{2.13}$$

where a, b, C_{T0} are the constants for the nominal tip-speed ratio λ_0 (λ_0 = 3):

$$\lambda_0 = \frac{\omega \cdot R}{v_0} \tag{2.14}$$

- a = 0.0986;
- b = 0.0113;
- C_{T0} = 0.0222.

The captured power versus the rotating speed characteristics, at constant wind speeds, have the allure as Fig.2.5 shows, and also have a maximum for every wind speed at an optimum rotor speed. The maximum torque has its optimum rotor speed (Fig.2.6).
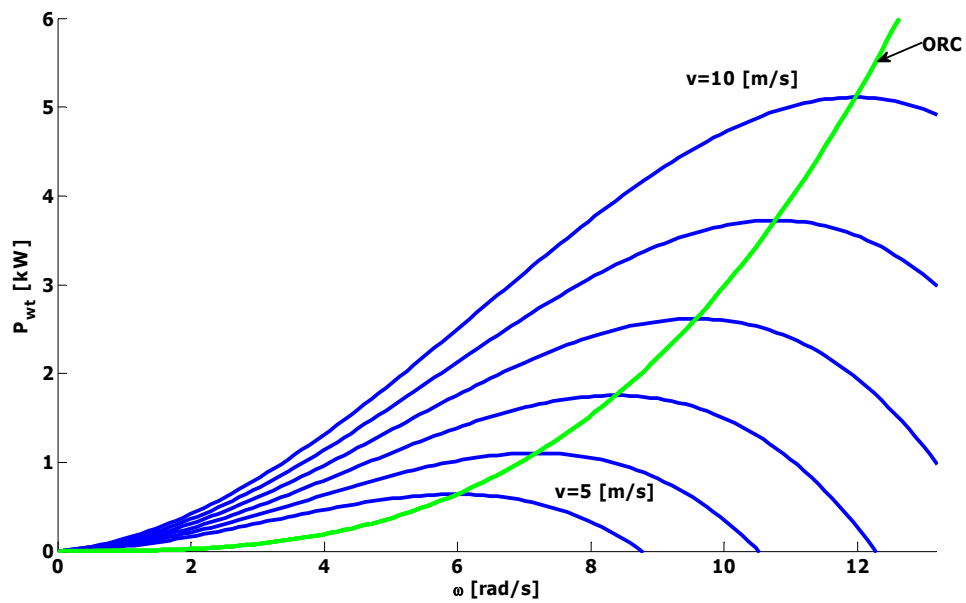
Fig.2.5. Wind turbine power versus rotating speed curves (in blue) and optimal regimes characteristic, ORC (in green) for different winds speeds.
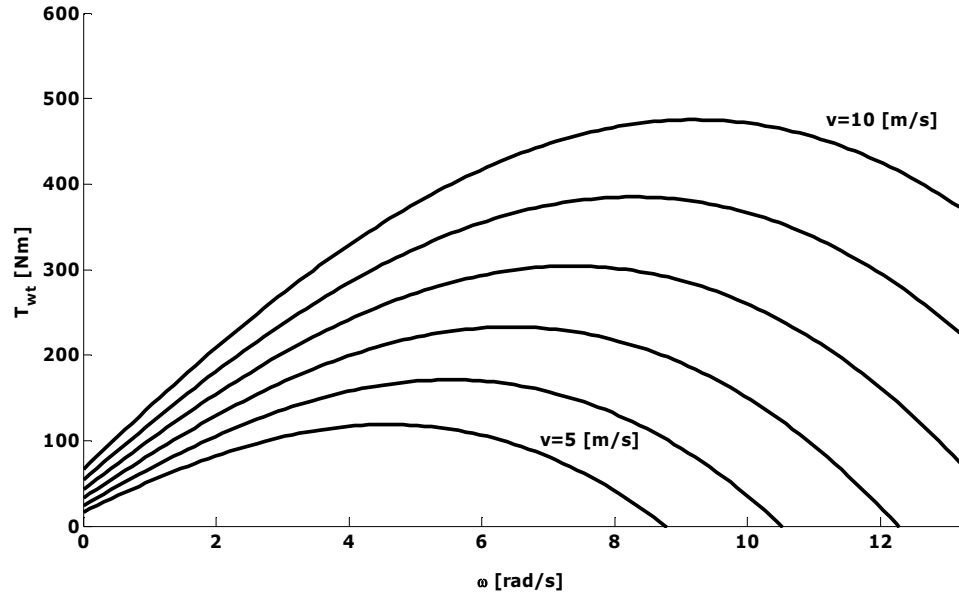
Fig.2.6. Wind turbine torque versus rotating speed curves for different wind speeds.

The wind turbine has different power levels at different wind speeds. The power curve of a wind turbine can be divided in four sections (Fig.2.7).
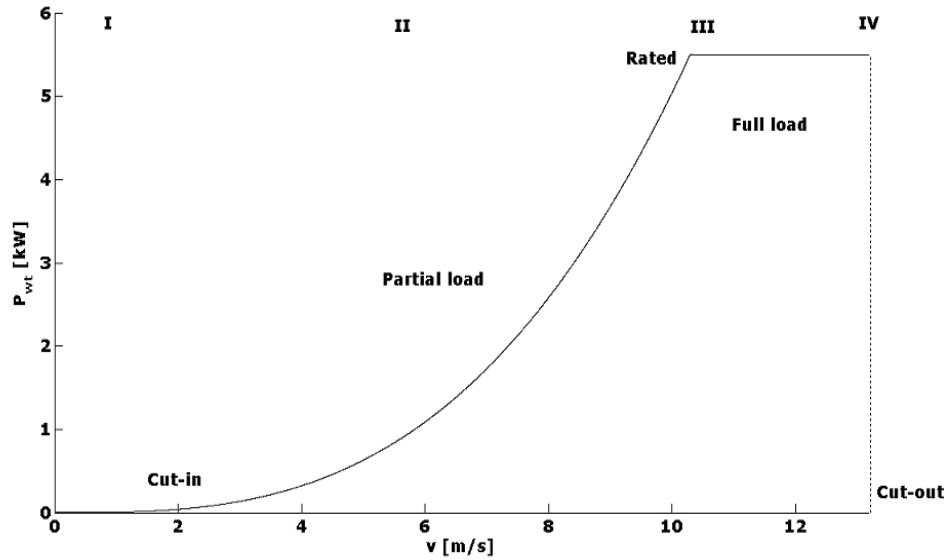
Fig.2.7. Wind turbine power levels.

In the first section the wind speed is smaller than the cut-in speed and so the extracted power is not enough to operate normally.

The second section is called partial load, the wind speed is higher than the cut-in speed and it is lower than the rated speed. The turbine starts to operate normally when the wind exceeds the cut-in speed. The tip-speed ratio is kept constant at the level which gives the maximum power coefficient, C_p, so the efficiency of the turbine is optimized.

In the third section the wind speed is lower than the safe range limit (cut-out speed) and higher than the rated speed. The objective is to maintain the rated output power by using one of the multiple power control solutions.

In the fourth section the wind speed is larger than the safe operation zone. The rotor will be braked and the extracted power will be zero.

Cut-in speed, rated speed and cut-out speed are part of the specifications of a wind turbine. There are different models that adapt these values in the area that they will operate, in order to extract the maximum available power.

The mathematical model for the wind kinetic energy transfer into mechanical energy on the shaft of the wind turbine was realized using equations 2.8 - 2.14. The block diagram of the model is shown in Fig.2.8.
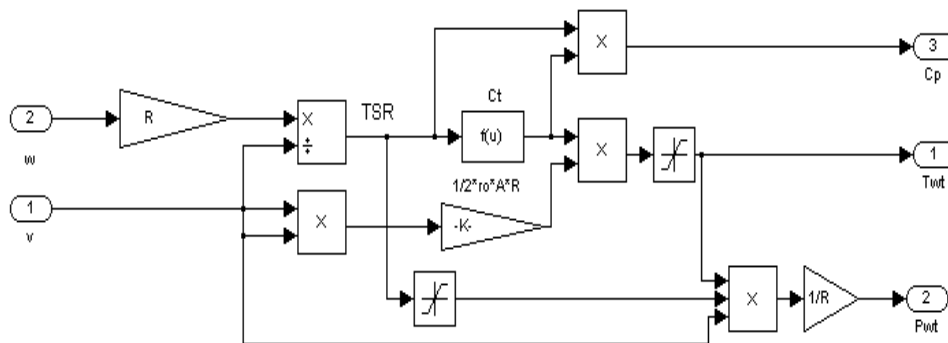
Fig.2.8. Matlab/Simulink block diagram of the wind turbine model.

In Fig.2.9 a picture with the five blades variable speed wind turbine described above, is presented.

Fig.2.9. The five blades variable-speed wind turbine.

The second wind turbine model is for a three blades fixed-pitch, and has the following specifications:
- Rated power, P_n = 5.5 [kW];

- Rated wind speed, $v_0 = 8$ [m/s];
- Rated rotor speed, $n = 85$ [rpm];
- Turbine inertia, $J_{wt} = 450$ [kg·m^2];
- Blade swept area, $A = 38.48$ [m^2];
- Radius of the turbine blade, $R = 3.5$ [m];
- Maximum coefficient of power conversion, $C_p = 0.46$;
- Specific density of air, $\rho = 1.225$ [kg/m^3] at 15 [$^\circ$C];
  The expression of C_T is the same as the first wind turbine, equation (2.14).
  The constants for the nominal tip speed ratio ($\lambda_0 = 4$) are:
- $a = 0.0626$,
- $b = 0.0046$,
- $C_{T0} = 0.0125$;

Fig.2.10 presents the C_P versus λ curve for the three-blade, fixed-pitch, variable speed wind turbine. From Fig.2.10 it is observed that the power conversion efficiency has a maximum for a specific, optimal, tip-speed ratio, TSR_{opt} (or λ_{opt}).

The captured power characteristics versus the rotating speed at different constant wind speeds have the allure presented in Fig.2.11 and also have a maximum for an optimum rotor speed. Fig.2.12 presents the torque versus the rotating speed.
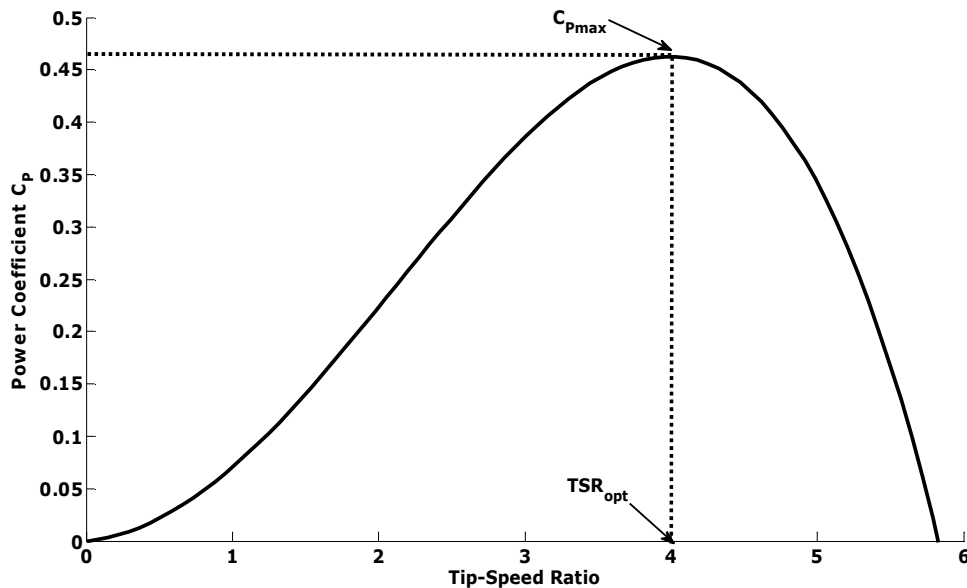
Fig.2.10. Power coefficient (CP) versus the tip-speed ratio (λ) curve of the three blades, fixed-pitch wind turbine.
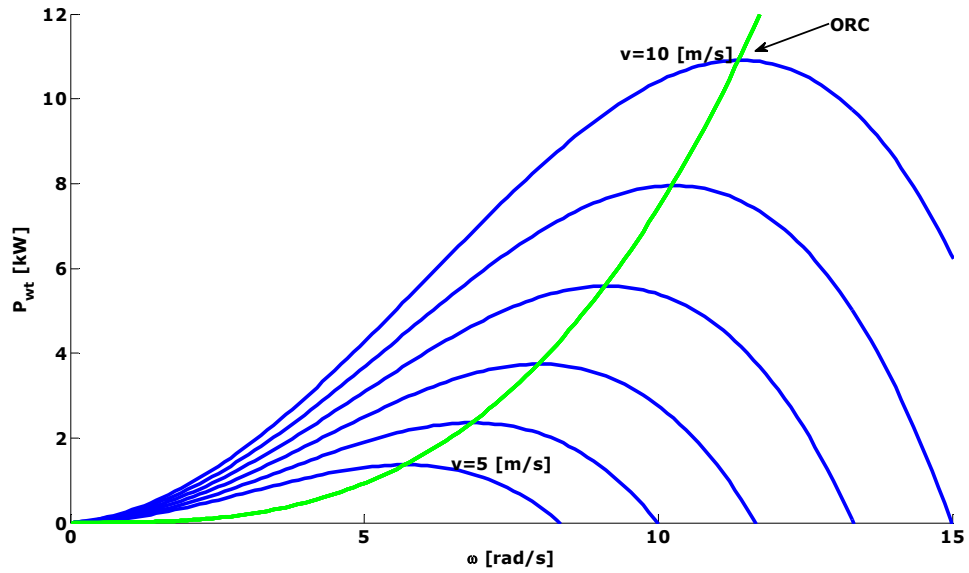
Fig.2.11. Wind turbine power versus rotating speed curves (in blue) and optimal regimes
characteristic, ORC (in green) for different wind speeds.
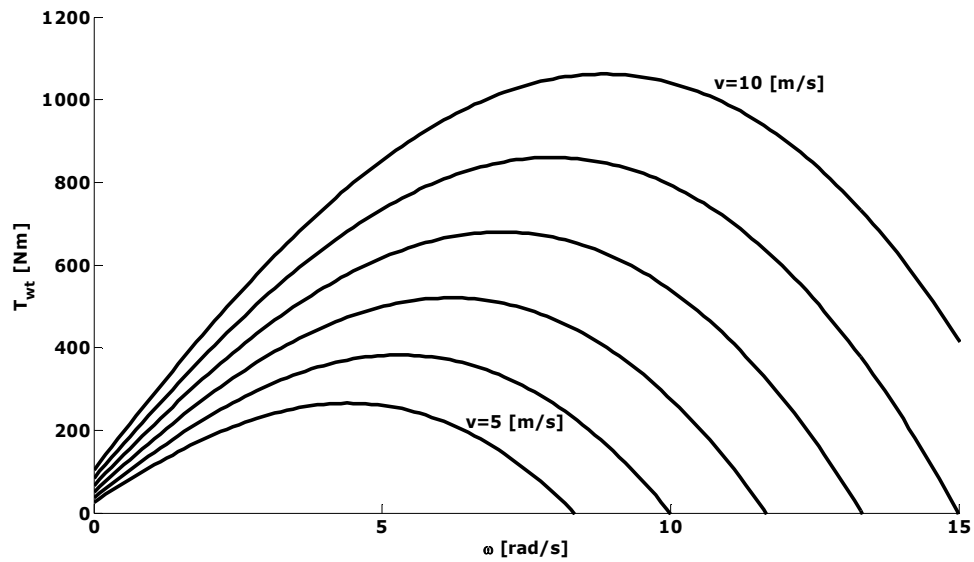
Fig.2.12. Wind turbine torque versus rotating speed curves for different wind speeds.

Fig.2.13. The three blades variable-speed wind turbine.

2.4. PMSG Characteristics and Model

The PMSG is a standard synchronous machine, where the DC excitation circuit is replaced with permanent magnets, placed on the rotor surface. Thus, the electrical losses in the rotor are eliminated and the thermal characteristics of the machine are improved. Also, the absence of the mechanical components such as brushes and slip rings makes the machine lighter, having a smaller physical size, a low moment of inertia leading to a higher power to weight ratio, which means a higher efficiency and reliability [10].

Due to the advantages mentioned above, the permanent magnet synchronous generator is an attractive solution for wind turbine applications.

The disadvantages of the permanent magnet excitation are: high costs for the permanent magnets and a fixed excitation.

Depending on the rotor configuration the PMSG can be classified in [11]:

- Surface mounted magnet type (SPMSG).

In this case the magnets are mounted on the surface of the rotor. The magnets can be regarded as air-gap because the permeability of the magnets is close to the air permeability. Thus, the inductances expressed in the d and q-axis are equal, $L_q = L_d$.

- Interior magnet type (IPMSG).

For this case the magnets are place inside the rotor. In this configuration, the saliency is present and the air gap of d-axis is increased compared with the q-axis, resulting that $L_d < L_q$.

The considered PMSG is a SPMSG with the following parameters [12]:

- Rated power: $S_n = 5$ [kVA];
- Rated current: $I_n = 12$ [A];
- Rated speed $n_n = 120$ [rpm];
- Rated frequency $f_n = 32$ [Hz];
- Number of stator slots $N_c = 33$;
- Pole pairs number, $p_p = 16$;
- PM flux, $\Psi_{PM} = 1.32$ [Wb];

The PMSG was tested using an AC variable speed DTC drive mechanically coupled with the generator.

Table 2.1 and Fig.2.14 show the no load PMSG phase voltage (U_0) versus speed characteristic.

Table 2.1. No load PMSG measured values

n [rpm]	U_0 [V]
0	0
47	71.02
60	78.77
80	116.98
93	134.01
109	161.57
117	170.32
122	178.45
131	187.16
136	197.98
144	207.25
152	224.06
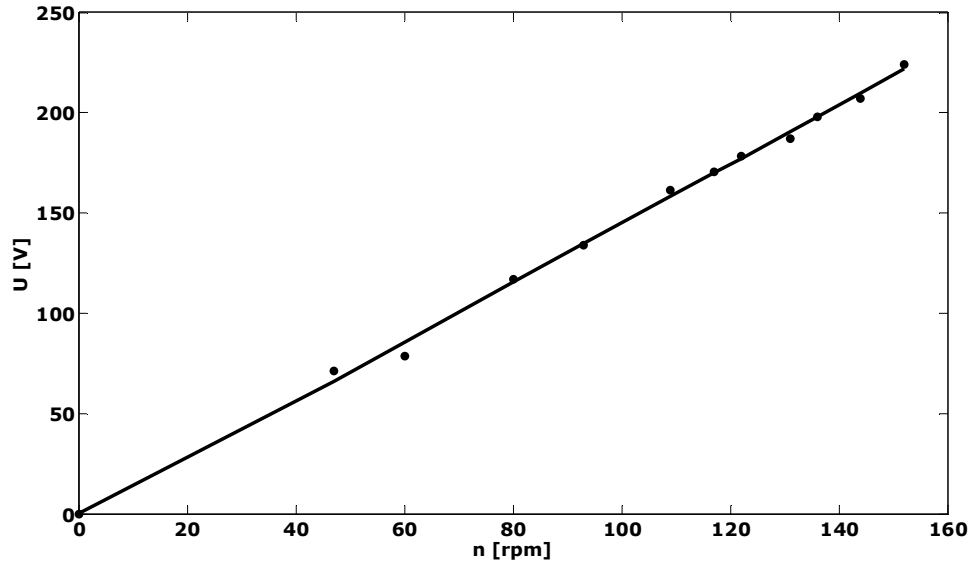
Fig.2.14. No load PMSG phase voltage versus speed.

For the PMSG load characteristic, a three-phase variable resistor as load was used. The speed was held constant at the nominal value of 120 [rpm]. The measured phase voltage (U), phase current (I) and output active power (P₂), measured with a power analyzer Norma LEM D4000, are presented in Table 2.2 and in Fig.2.15.

Table 2.2. Load PMSG measured values at rated speed n = 120 [rpm]

I [A]	U [V]	P₂ [W]
1.486	174.757	779.36
1.496	175.993	790.16
2.29	172.045	1231.36
2.867	167.966	1430.5
3.628	168.78	1837.14
5.035	164.76	2482.2
5.688	163.747	2786.73
6.346	160.643	3058.2
7.121	160.135	3490.7
7.77	157.564	3786.6
9.26	150.883	4126.6
9.852	150.973	4402
10.153	148.327	4485.3
10.76	148.34	4740
12.215	148.272	5446.7
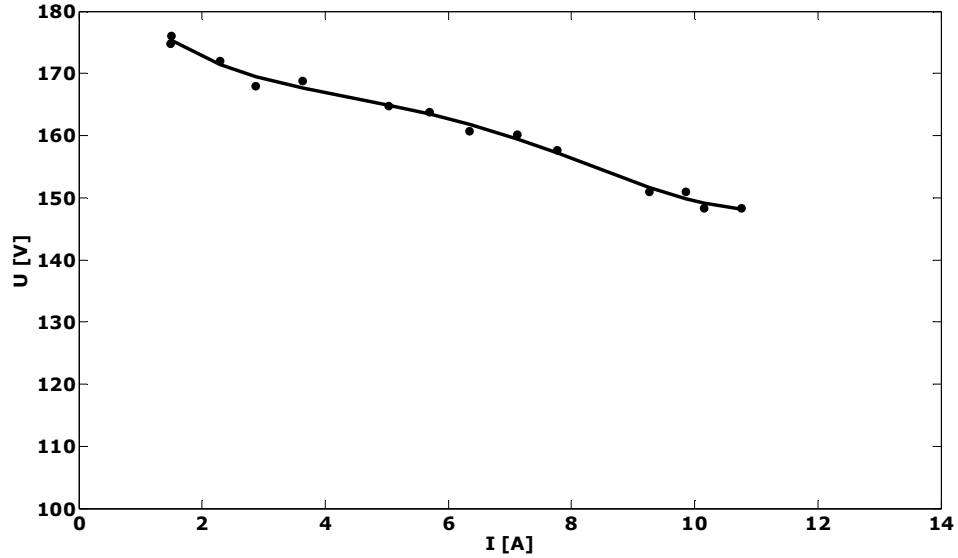
Fig.2.15. Voltage versus current at rated speed n = 120[rpm].

For the PMSG efficiency (η) versus phase current and output power characteristics, the phase current (I), the input power (P_1), and output electrical power (P_2), were measured. The values are presented in Table 2.3 and the characteristics are shown in Fig.2.16 and Fig.2.17. The input power was calculated using a torque meter (AEP transducer) and a speed transducer (Ebro DT 2236).

Table 2.3. PMSG measured values at rated speed n = 120 [rpm]

P_1 [W]	I[A]	P_2 [W]	η [%]
916.88	1.486	779.36	85
916.88	1.496	790.16	86.18
1403.64	2.29	1231.36	87.73
1624.76	2.867	1430.5	88.04
2009.6	3.628	1837.14	91.42
2763.2	5.035	2482.2	89.83
3140	5.688	2786.73	88.75
3454	6.346	3058.2	88.54
3945.72	7.121	3490.7	88.47
4289.87	7.77	3786.6	88.27
4738.89	9.26	4126.6	87.08
5086.8	9.852	4402	86.54
5212.4	10.153	4485.3	86.05
5463.6	10.76	4740	86.76
6330.24	12.215	5446.7	86.04
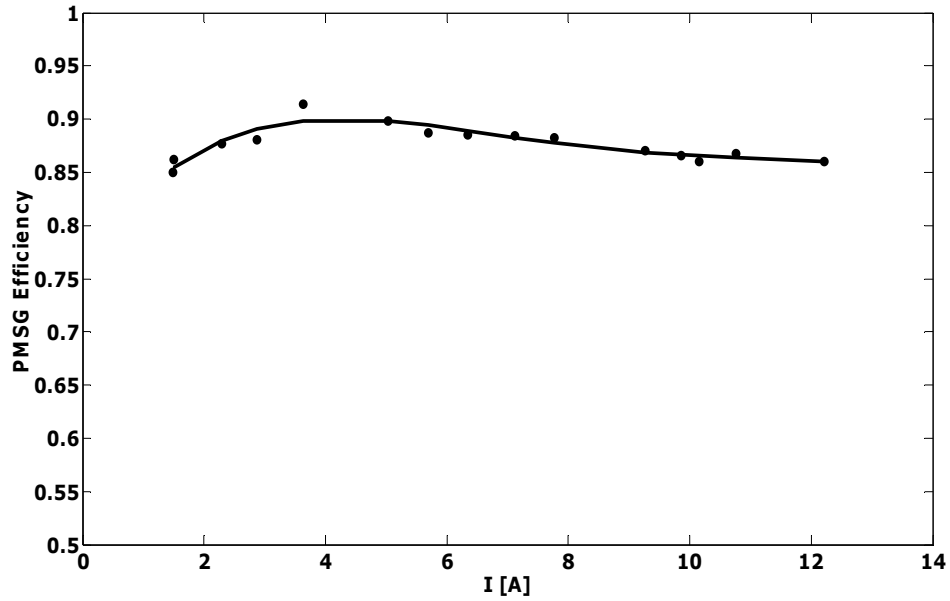
Fig.2.16. PMSG efficiency versus phase current at rated speed n = 120 [rpm].
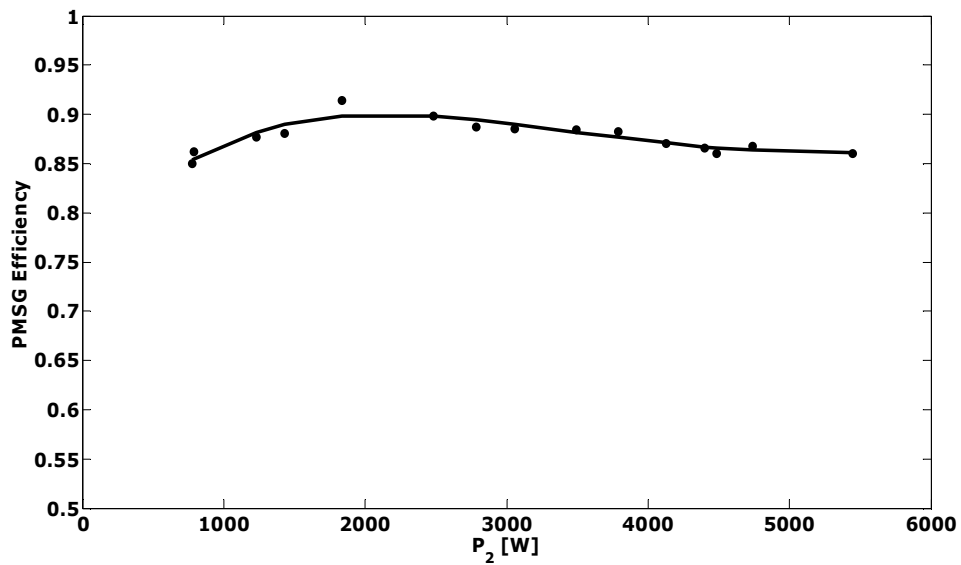
Fig.2.17. PMSG efficiency versus output power at rated speed n = 120 [rpm].

Because PMSG is a surface mounted magnet type generator, and the permeability of the magnets is close to the air permeability, the inductances expressed in the d and q-axis are equal and the synchronous inductance is defined, $L_q = L_d = L_s$.

The synchronous reactance ($X_s = X_q = X_d = 3.85$ [Ω]), was found based on the following measured parameters:

- U =148.27 [V];
- I = 12.21 [A];
- P_2 =5446 [W];
- n = 120 [rpm];
- the measured phase resistances at 21 [°C] are: $R_a = 0.95$ [Ω]; $R_b = 0.96$ [Ω]; $R_c = 0.96$ [Ω];

The synchronous inductance is equal with:

$$L_s = \frac{X_s}{2 \cdot \pi \cdot f_n} = 19.18mH \qquad (2.15)$$

Efficiency characteristics at different speeds, including DBR and HDC, are also illustrated in fig. 2.18 to 2.33. They were determined based on the measured parameters presented in tables 2.4 – 2.7, were:

n – PMSG rotating speed;
P_1 – PMSG input mechanical power;
P_2 – PMSG output electrical power;
I_2 – PMSG phase current;
P_3 – DC output power;
I_3 – DC current;
η_1 – PMSG efficiency;
η_2 – DBR and HDC efficiency;
η – PMSG, DBR, and HDC global efficiency.

Table 2.4. Efficiency measured values at n = 60 [rpm]

n	P_1	P_2	I_2	P_3	I_3	η_1	η_2	η
[rpm]	[W]	[W]	[A]	[W]	[A]			
60.07	516,787	473,53	1,87	460	7,66	0,916	0,971	0,890
60.07	755,691	697,53	2,80	674	11,19	0,923	0,966	0,892
60.02	942,260	878,6	3,53	835	13,89	0,932	0,950	0,886
60.00	1362,760	1245,49	5,10	1170	19,43	0,914	0,939	0,859
59.97	1528,962	1397,34	5,79	1317	21,85	0,914	0,943	0,861
59.93	1674,906	1523,8	6,39	1438	23,53	0,910	0,944	0,859
59.93	1899,482	1704,28	7,23	1620	24,75	0,897	0,951	0,853
59.93	2066,345	1837,29	7,86	1754	23,43	0,889	0,955	0,849
59.87	2374,857	2081,37	9,12	1990	24,18	0,876	0,956	0,838
59.78	2743,260	2362,45	10,71	2159	35,77	0,861	0,914	0,787
59.75	2935,610	2492,35	11,51	2270	37,65	0,849	0,911	0,773
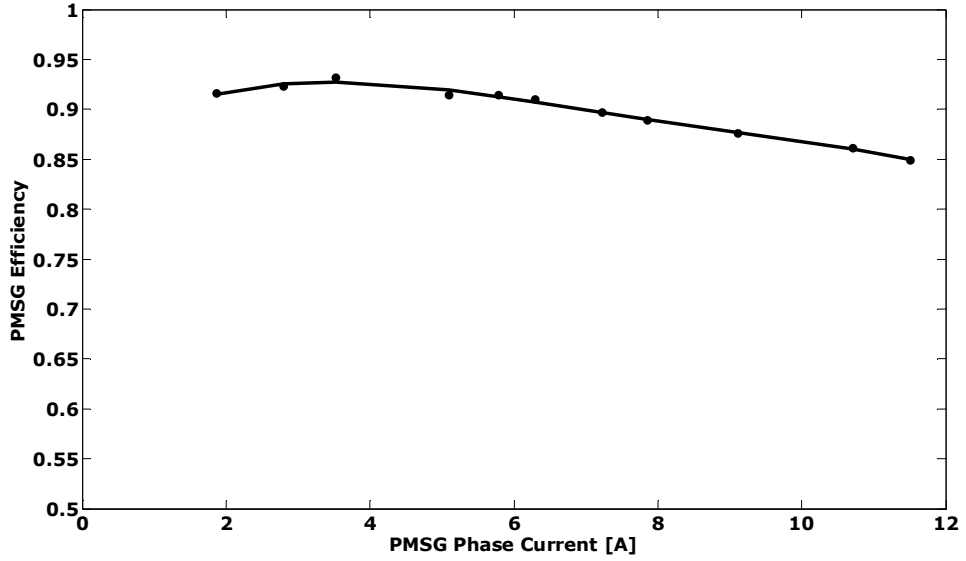
Fig.2.18. PMSG efficiency versus phase current characteristic at n = 60 [rpm].
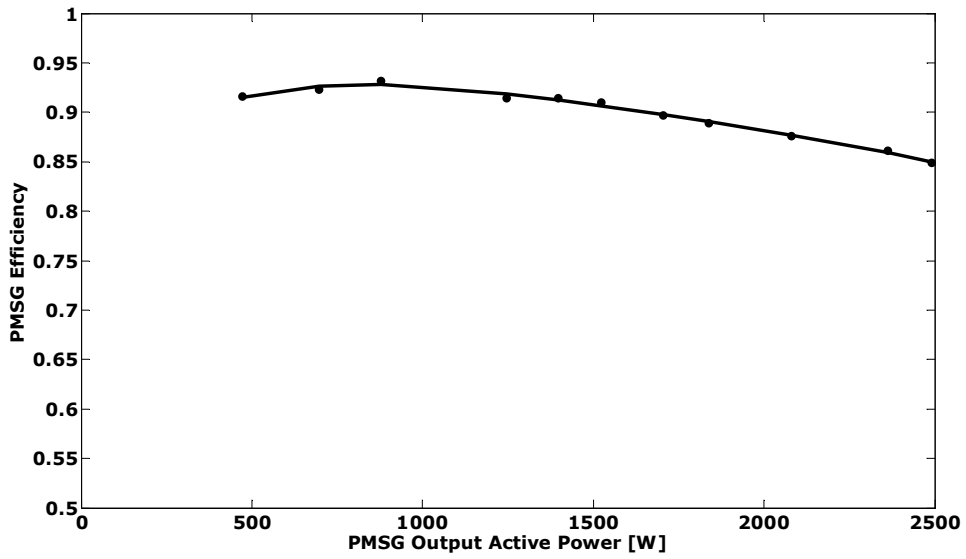
Fig.2.19. PMSG efficiency versus output power characteristic at n = 60 [rpm].
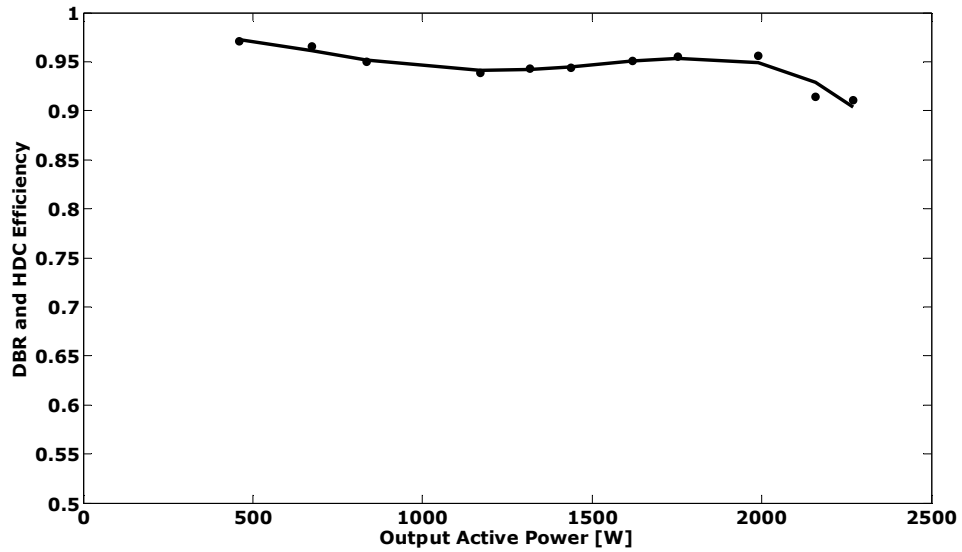
Fig.2.20. DBR and HDC efficiency versus output power characteristic at n =60 [rpm].
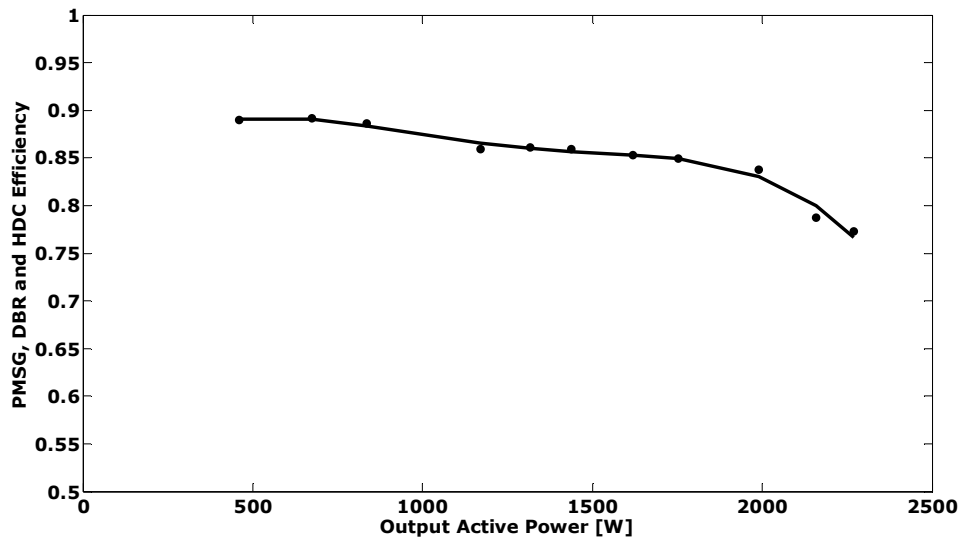
Fig.2.21. PMSG, DBR and HDC efficiency versus output power characteristic at n = 60 [rpm].

Table 2.5. Efficiency measured values at n = 80 [rpm]

n	P_1	P_2	I_2	P_3	I_3	η_1	η_2	η
[rpm]	[W]	[W]	[A]	[W]	[A]			
80	1004.8	918.83	3.8	852	2.77	0.914	0.927	0.848
79.93	1363.722	1256.39	4.72	1162	3.8	0.921	0.925	0.852
79.9	1689.31	1561.46	6.09	1455	4.72	0.924	0.932	0.861
79.85	2151.275	1988.94	7.54	1830	6.09	0.925	0.92	0.851
79.8	2631.039	2404.45	8.99	2220	7.54	0.914	0.923	0.844
79.73	3104.549	2794.92	11.23	2583	8.99	0.9	0.924	0.832
79.6	3835.903	3389.3	12	3126	11.2	0.884	0.922	0.815
79.54	4080.784	3570.5	0.16	3278	12	0.875	0.918	0.803
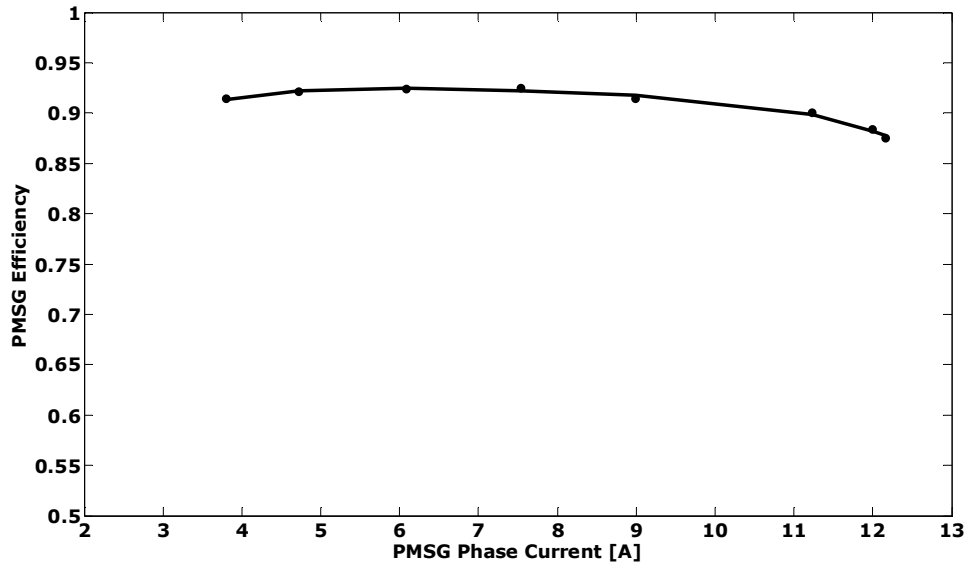
Fig.2.22. PMSG efficiency versus phase current characteristic at n = 80 [rpm].
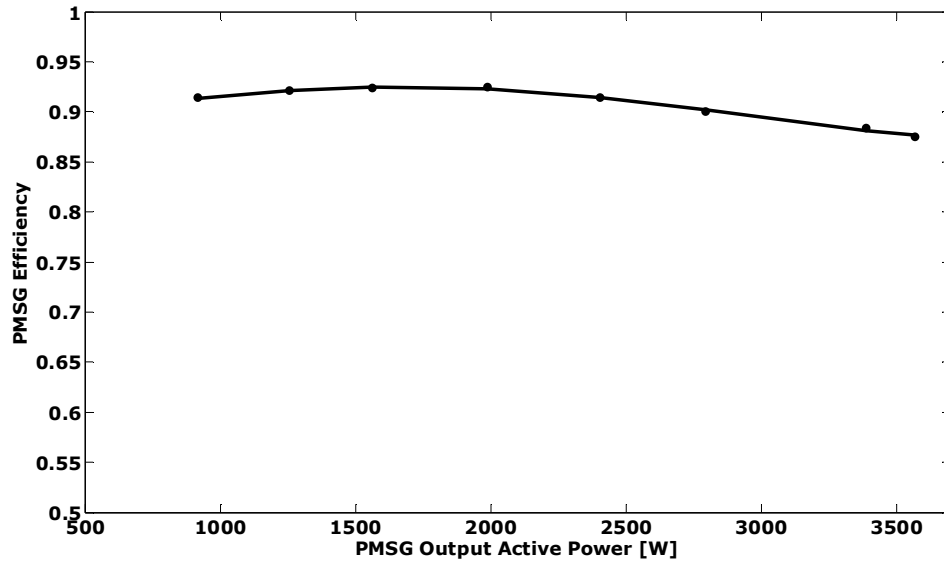
Fig.2.23. PMSG efficiency versus output power characteristic at n = 80 [rpm].
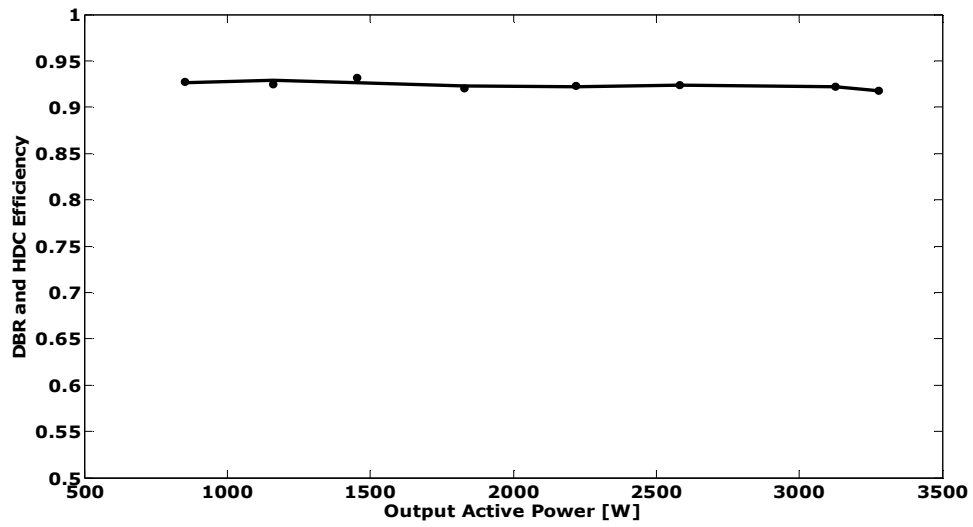
Fig.2.24. DBR and HDC efficiency versus output power characteristic at n = 80 [rpm].
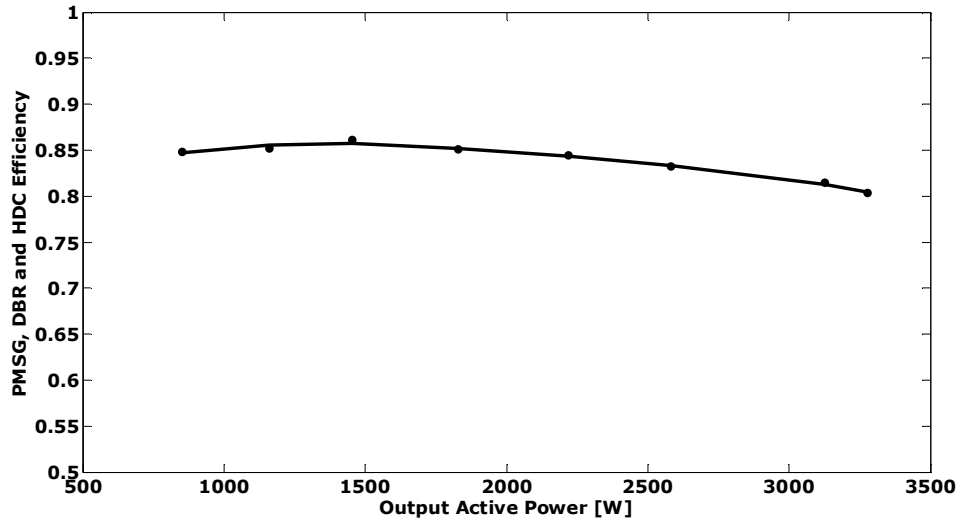
Fig.2.25. PMSG, DBR and HDC efficiency versus output power characteristic at n = 80 [rpm].

Table 2.6. Efficiency measured values at n = 100 [rpm]

n	P_1	P_2	I_2	P_3	I_3	η_1	η_2	η
[rpm]	[W]	[W]	[A]	[W]	[A]			
99.59	4942,716	4460,7	11,60	4085	11,6	0,902	0,916	0,826
99.5	4411,622	4025	10,26	3742	10,3	0,912	0,930	0,848
99.64	4085,878	3742,5	9,44	3485	9,44	0,916	0,931	0,853
99.62	3576,373	3311,7	8,27	3030	8,27	0,926	0,915	0,847
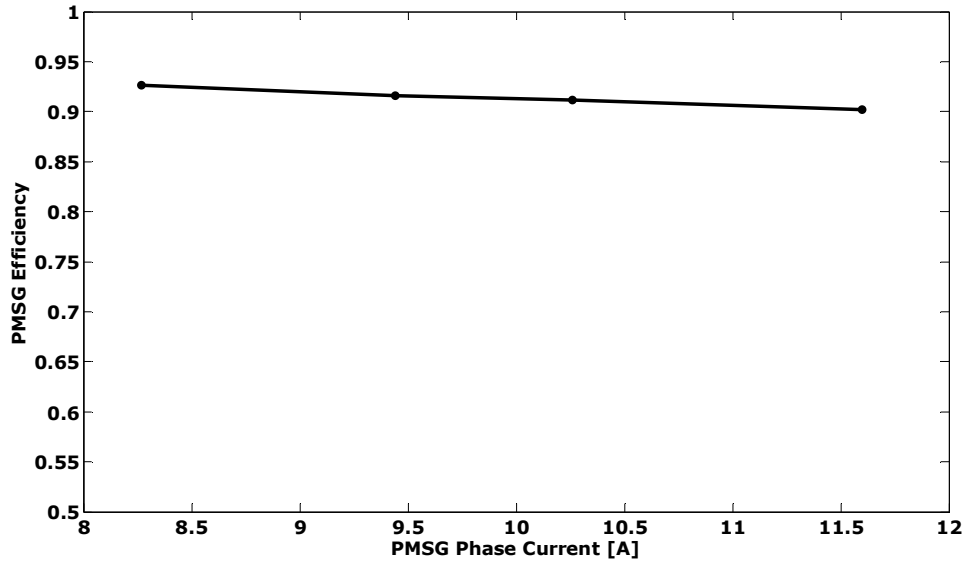
Fig.2.26. PMSG efficiency versus phase current at n = 100 [rpm].
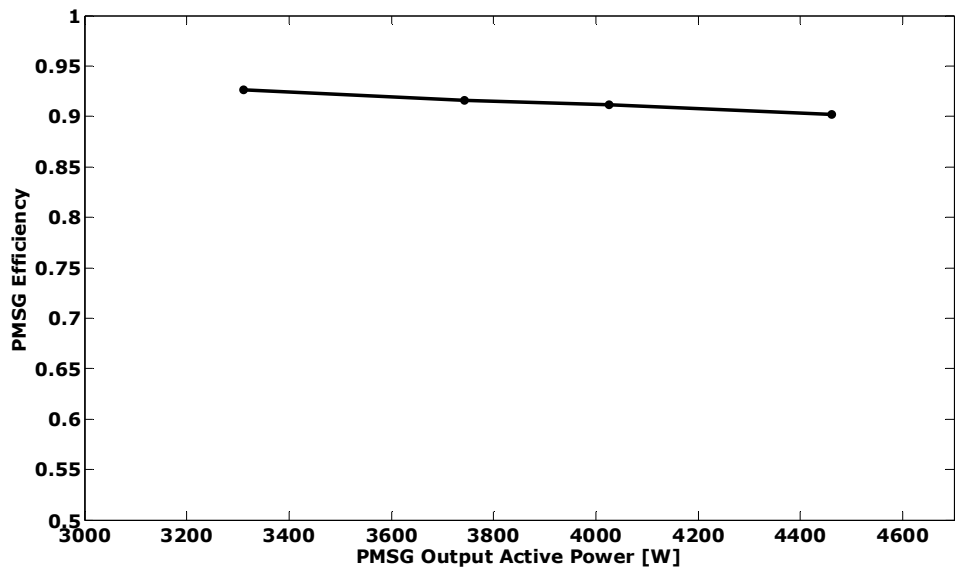
Fig.2.27. PMSG efficiency versus output power at n = 100 [rpm].
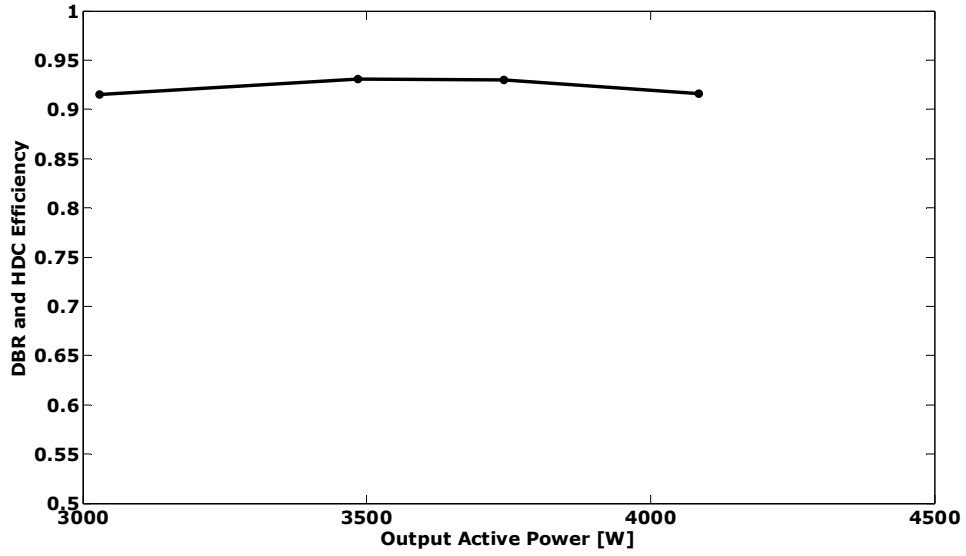
Fig.2.28. DBR and HDC efficiency versus output power at n = 100 [rpm].
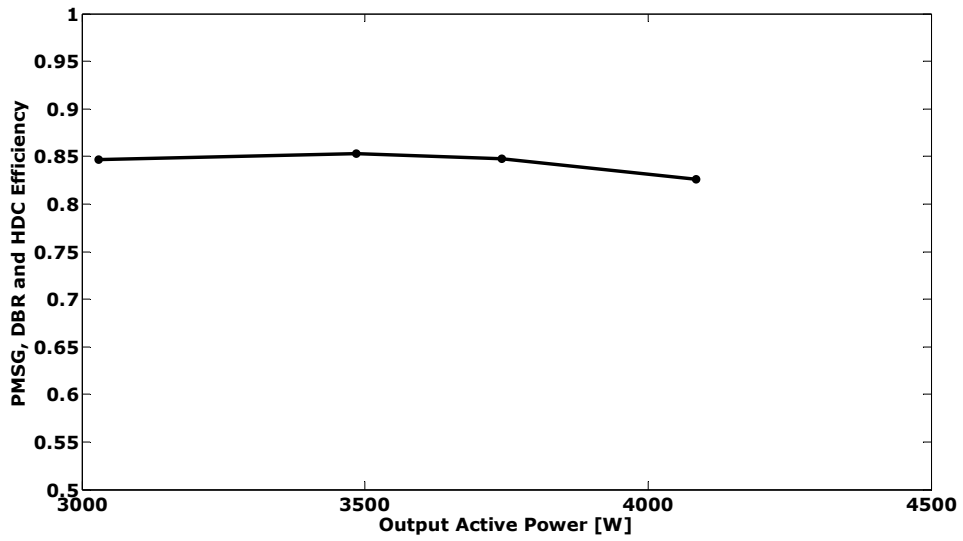
Fig.2.29. PMSG, DBR and HDC efficiency versus output power at n = 100 [rpm].

Table 2.7. Efficiency measured values at n = 109 [rpm]

n	P_1	P_2	I_2	P_3	I_3	η_1	η_2	η
[rpm]	[W]	[W]	[A]	[W]	[A]			
107.13	5480.937	4883.8	11.86	4420	0.891	0.905	0.806	107.13
109.12	5511.938	4981.2	11.85	4513	0.904	0.906	0.819	109.12
109.12	5756.354	5165.3	12.51	4679	0.897	0.906	0.853	109.12
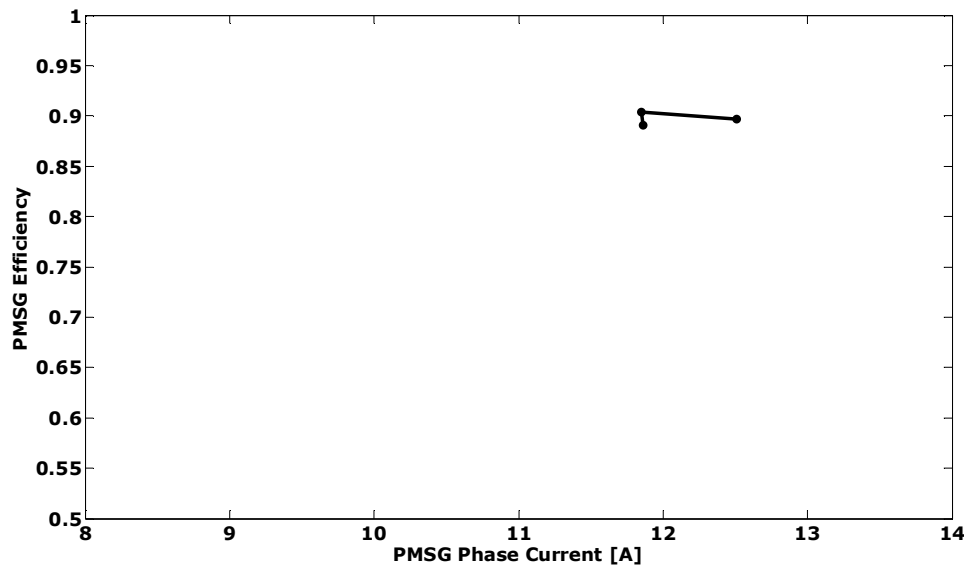
Fig.2.30. PMSG efficiency versus phase current at n = 109 [rpm].
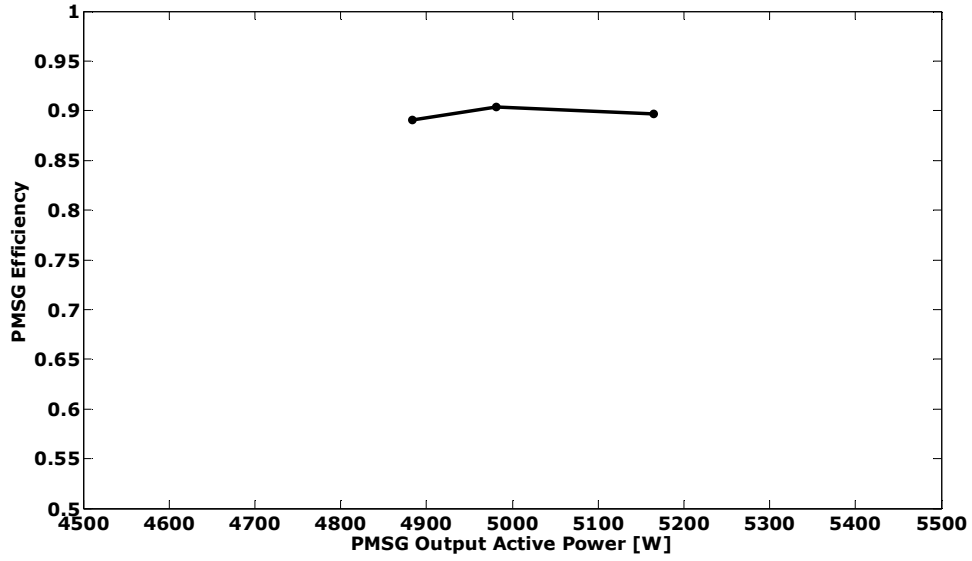
Fig.2.31. PMSG efficiency versus output power at n = 109 [rpm].
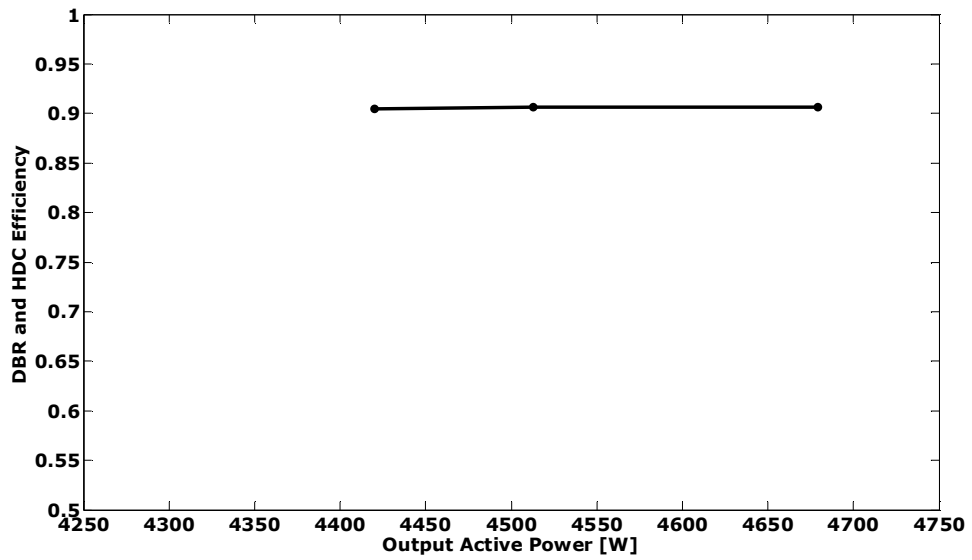
Fig.2.32. DBR and HDC efficiency versus output power at n = 109 [rpm].
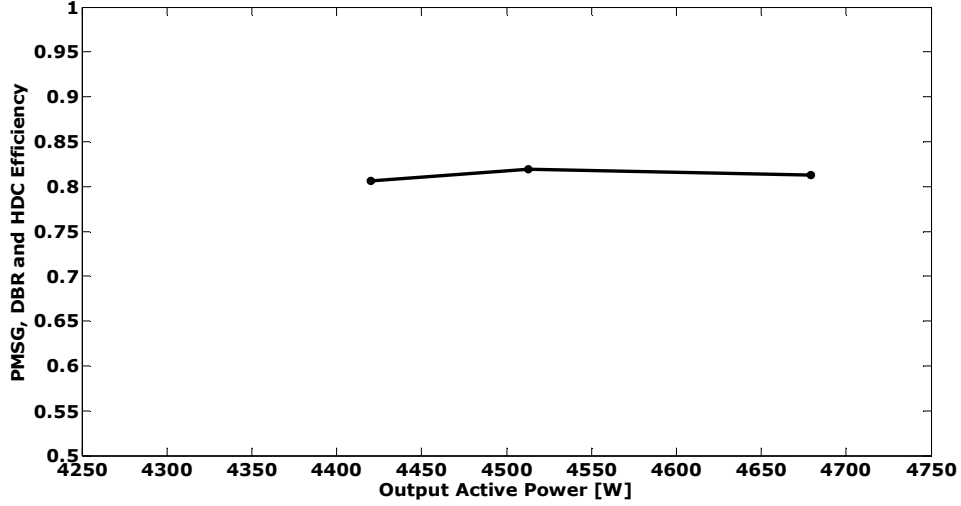
Fig.2.33. PMSG, DBR and HDC efficiency versus output power at n = 109 [rpm].

The PMSG Matlab/Simulink model created with equations 2.16 - 2.19, includes also the rectifier model:

In steady-state the following equation can be written [13]:

$$p_p \cdot \omega \cdot \sqrt{\psi_{PM}^2 - (L_s \cdot I_{fp})^2} - [R \cdot I_{fp} + k_v \cdot (V_{dc} + 2 \cdot V_{don})] = 0 \qquad (2.16)$$

The rectified current is:

$$I_{dc} = k_i \cdot I_{fp} \qquad (2.17)$$

The rectified voltage is:

$$V_{dc} = \frac{1}{C_f} \cdot \int (I_{dc} - I_{load}) \cdot dt \qquad (2.18)$$

The PMSG torque is:

$$T_g = 1.5 \cdot p_p \cdot I_{fp} \cdot \sqrt{\psi_{PM}^2 - (L_s \cdot I_{fp})^2} + \omega \cdot k_{pFe} \qquad (2.19)$$

where
- I_{fp}: peak phase current [A];
- $V_{don} = 0.8$ [V]: diode voltage drop;
- $C_f = 1e-3$ [F]: Filter capacitance;
- $k_v = 3/\pi$; $k_i = 2/\pi$;
- $k_{pFe} = 3.3$ [kg·m^2/s]: core loss coefficient.

The complete PMSG model, including DBR and the output filter is presented in Fig.2.34.

Fig.2.34. Matlab/Simulink block diagram of the PMSG model.

2.5. Speed Estimator for PMSG

To eliminate a speed sensor, needed for control and performances evaluation, a speed estimator is proposed in this section.

The estimator is based on the measured PMSG rectified DC voltage (V_{dc}) and current (I_{dc}).

Fig.2.35 shows a principle block diagram for the estimator equivalent circuit, were DBR is a diode bridge rectifier, C_f is the filter capacitance, R_{dc} and L_{dc} are the equivalent internal impedance components.
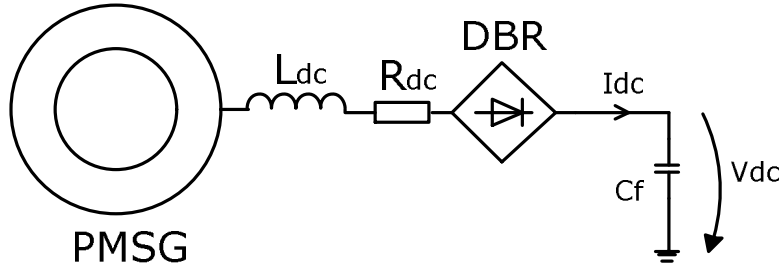
Fig.2.35. Block diagram for the estimator equivalent circuit.

The following equation can be written:

$$V_{dc} = V_{dc0} - \sqrt{R_{dc}^2 + (L_{dc} \cdot \omega_e)^2} \cdot I_{dc} \qquad (2.20)$$

where ω_e is:

$$\omega_e = p_p \cdot \omega \qquad (2.21)$$

and V_{dc0} is the no load voltage:

$$V_{dc0} = k_{dc} \cdot \omega \qquad (2.22)$$

k_{dc}, R_{dc} and L_{dc} were found with the minimum square deviation method, using the experimental results presented in Tab. 2.8.:
- no load voltage coefficient, $k_{dc} = 32.7$;
- DC equivalent resistance, $R_{dc} = 0.1$ [Ω];
- DC equivalent inductance, $L_{dc} = 0.03$ [H].
  With these parameters ω can be evaluated from:

$$\omega = \frac{65.4 \cdot V_{dc} + I_{dc} \cdot \sqrt{42.7716 + 0.9216 \cdot V_{dc}^2 - 0.009216 \cdot I_{dc}^2}}{2138.58 - 0.4608 \cdot I_{dc}^2} \qquad (2.23)$$

Fig.2.36 illustrates the rotating speed (measured and calculated) as a function of rectified voltage, for three different currents.

Table 2.8. Experimental/estimated results

I_{dc} [A]	V_{dc} [V]					
	$\omega=5$ [rad/s]		$\omega=7.5$ [rad/s]		$\omega=10$ [rad/s]	
0	**169**	163.5	**245**	245.25	**325**	327
2	**163**	158.9	**238**	238	**316**	317.3
3	**160**	156.2	**234**	234.4	**311**	312.5
4	**157**	153.8	**230**	230.8	**307**	307.7
5	**154**	151.4	**226**	227.2	**302**	302.9
6	**151**	149	**223**	223.6	**298**	298.1
7	**148**	146.6	**219**	220	**293**	293.3
8	**145**	144.2	**215**	216.4	**288**	288.5
9	**142**	141.8	**212**	212.8	**284**	283.7
10	**139**	139.4	**208**	209.2	**279**	278.9
Measured voltage values in bold and the calculated ones						
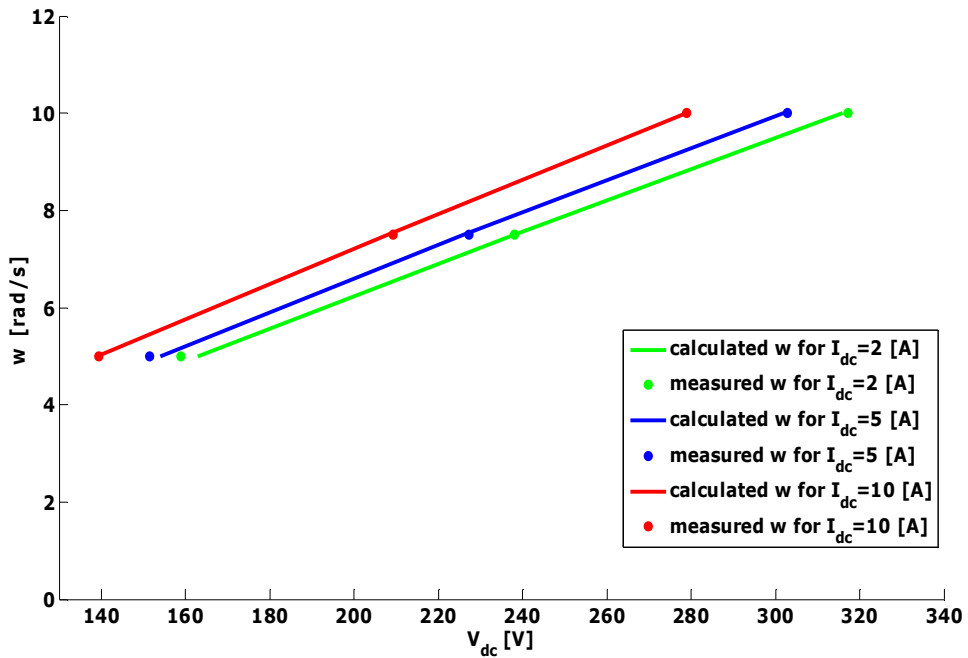
Fig.2.36. Rotating speed (measured and estimated) as a function of the rectified voltage, for three output DC currents.

2.6. The Mechanical Model

The mechanical part (Fig.2.37) is considered as a two-mass model, consisting of a large mass (corresponding to the wind turbine inertia J_{wt}) and a small mass (corresponding to the generator rotor inertia J_g).

The dynamic equation of motion is:

$$T_{wt} - T_g = J \cdot \frac{d\omega}{dt} \tag{2.24}$$

where
T_{wt}: wind turbine torque [N·m];
T_g: generator torque [N·m];
J: inertia of the wind turbine system [kg·m^2]:

$$J = J_{wt} + J_g \tag{2.25}$$
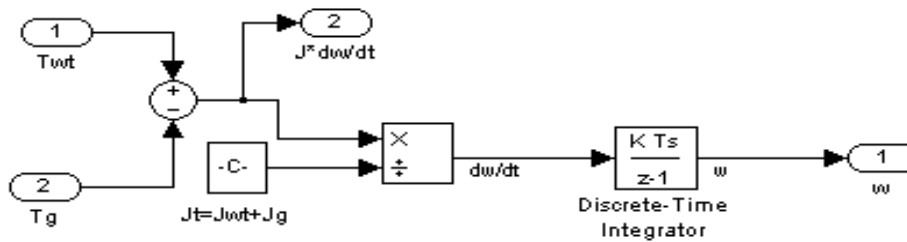
Fig.2.37. Matlab/Simulink block diagram of the mechanical model.

2.7. The Hybrid Buck DC-DC Converter

In the field of power electronics, in the last few years, many authors proposed new structures of DC–DC and DC–AC converters, with high input / output voltage gain, e.g. the hybrid and Z configurations [14], [15], adequate for this purpose.

The hybrid Buck DC–DC converter (HBDC) circuit diagram, studied and built as prototype for this application, is presented in Fig.2.38 [15], [16]. It is used to transfer the PMSG power (at rated voltage of 400V) to the SC, at (0-90) V.
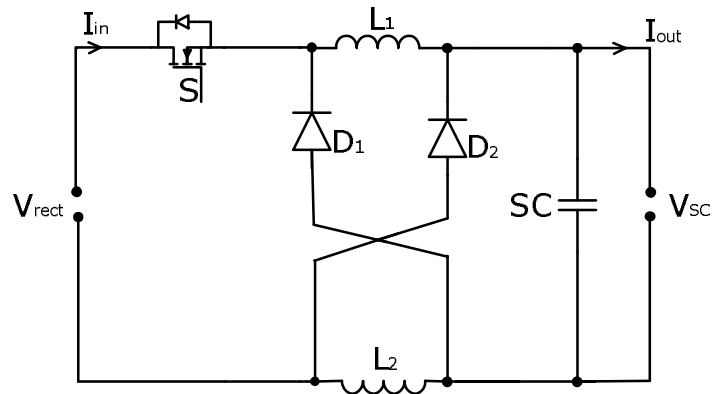
Fig.2.38. Hybrid Buck DC – DC converter.

HBDC has a higher step-down voltage ratio compared with the classical buck DC–DC converter (BDC) but, in order to have a complete description it is necessary to consider more aspects regarding the operation modes and component selection [17].

Fig.2.39 and Fig.2.40, show the two states of the HBDC during t_{on} and t_{off} switching time intervals. The inductors are connected in series while the power switch S is on, during t_{on}, and they are connected in parallel, during t_{off}.
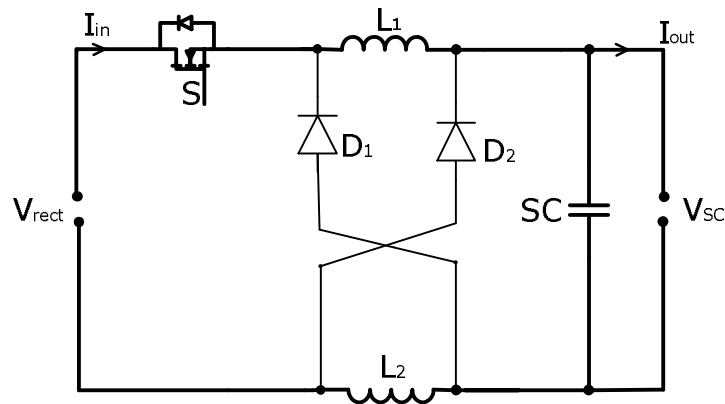
Fig.2.39. HBDC topology during t_{on}.
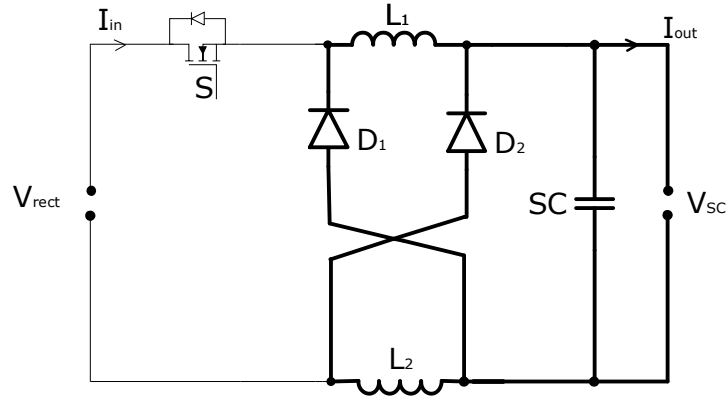
Fig.2.40. HBDC topology during t_{off}.

If the input voltage V_{rect} and the output voltage V_{SC} are considered constant during one switching period and L1=L2=L, the following equations can be written:

$$V_{rect} - V_{SC} = 2 \cdot L \cdot \frac{di_L}{dt} \qquad (2.26)$$

during t_{on}, and:

$$-L \cdot \frac{di_L}{dt} = V_{SC} \qquad (2.27)$$

during t_{off}.

The duty cycle D, in continuous current mode (CCM), and boundary condition mode (BCM), is:

$$D = \frac{t_{on}}{T} = \frac{2 \cdot V_{SC}}{V_{rect} + V_{SC}} \qquad (2.28)$$

and the output to input voltage ratio is defined by:

$$\frac{V_{SC}}{V_{rect}} = \frac{D}{2 - D} \qquad (2.29)$$

The voltage stress of the HBDC transistor is given by:

$$\hat{V}_T = V_{rect} + V_{SC} \qquad (2.30)$$

The approximate value of the transistor rms current is given in equation 2.31; I_{out} is the load (output) current.

$$I_{T,rms} \cong \frac{\sqrt{D}}{2-D} \cdot I_{out} \tag{2.31}$$

The HBDC current ripple, $I_{Cout,ripple}$, depends on the load, as the following equation shows:

$$I_{C_{out,ripple}} = 3 \cdot \frac{V_{SC}}{2 \cdot L_1 \cdot f_s} \cdot (1-D) + \frac{I_{out}}{2-D} \tag{2.32}$$

where f_s is the switching frequency.

When HBDC operates at the BCM, the average value of each inductor current, $I_{L,lim}$, is:

$$I_{L,lim} = \frac{V_{SC}}{2 \cdot L_1 \cdot f_s} \cdot (1-D) \tag{2.33}$$

if V_{SC} is kept constant.

The maximum value of equation 2.33 is obtained for D —›0 and is given by:

$$I_{L,lim,max} = \frac{V_{SC}}{2 \cdot L_1 \cdot f_s} \tag{2.34}$$

When V_{rect} is kept constant, $I_{L,lim}$ and $I_{L,lim,max}$ for HBDC can be obtained from:

$$I_{L,lim} = \frac{V_{rect}}{2 \cdot L_1 \cdot f_s} \cdot D \cdot \frac{1-D}{2-D} \tag{2.35}$$

The peak inductor current $\hat{I}_L$ and the corresponding p.u. expression (relative to $I_{L,lim,max}$ at BCM) are presented in (2.36), (2.37):

$$\hat{I}_L = \frac{V_{SC}}{2 \cdot L_1 \cdot f_s} \cdot (1-D) + \frac{I_{SC}}{2-D} \tag{2.36}$$

$$\frac{\hat{I}_L}{I_{L,lim,max}} = \frac{1 - \frac{V_{SC}}{V_{rect}}}{1 + \frac{V_{SC}}{V_{rect}}} + \frac{I_{SC}}{I_{L,lim,max}} \cdot \frac{1 + \frac{V_{SC}}{V_{rect}}}{2} \tag{2.37}$$

Using HBDC, the output voltage is reduced by (2-D) times compared with BDC, or the same output voltage is obtained for a higher value of D, which results in smaller peak transistor current.

The voltage stress of the HBDC transistor is bigger, but in applications that require a high conversion ratio, the maximum voltage across the transistor of HBDC is not drastically increased.

Smaller rms current values of HBDC give reduced conduction losses in transistor for this converter. In addition, the peak transistor current is lower due to the bigger value of HBDC duty cycle. This leads to smaller commutation losses if the hard switching is used. The HBDC output capacitor current ripple depends on the load [17].

The specifications of the considered DC–DC hybrid buck converter are:

- Rated power, P = 5 [kW];
- Input rectified voltage, V_{rect} = 130 - 400 [V];
- Output voltage, V_{SC} = (0 -)50 - 120 [V];
- Inductors, $L_1 = L_2$ = 200 [μH];
- Switching frequency, f_s = 9 [kHz];

Fig.2.41 presents the measured input current step response of the considered HBDC.
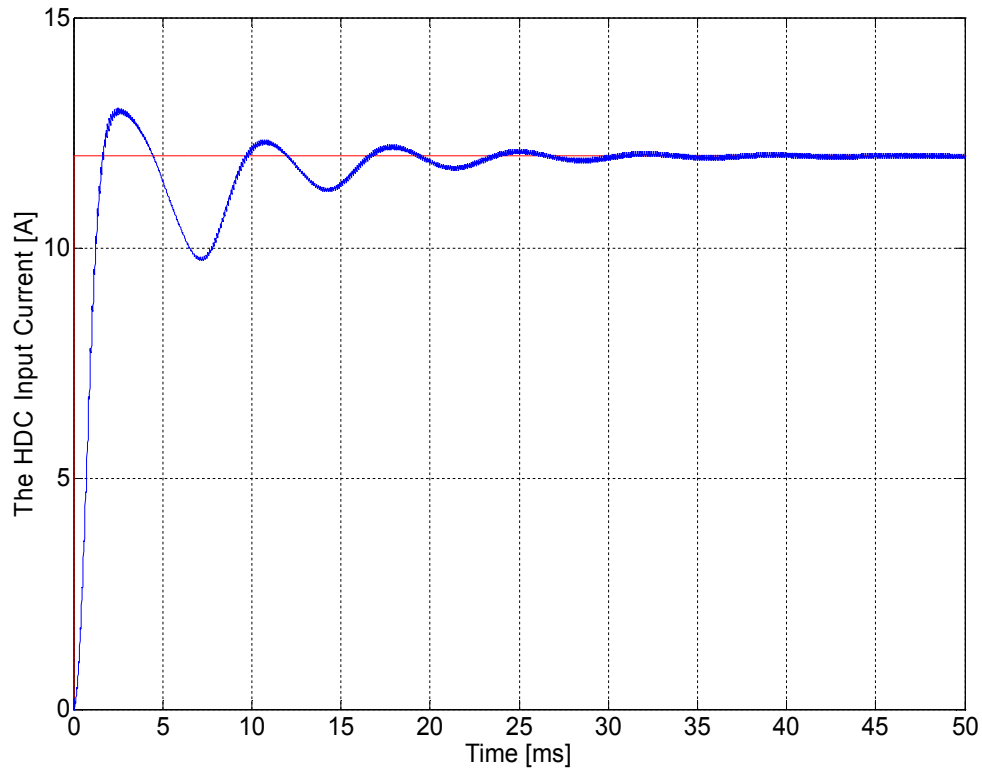
Fig.2.41. HDC input current step response.

2.8. The Storage Elements

In the last years, the supercapacitors (SC) have become an attractive storage solution [18]. The manufacturing technology is in continuous improvement,

and the price will decrease as the application area expands (which is expected). The charge/discharge currents of the SC can be much higher (comparing with batteries) and the life cycle is about 10 to 20 years.

The SC voltage, V_{SC}, is a measure of the stored energy W_{SC}:

$$W_{SC} = C \cdot \frac{V_{SC}^2}{2} \qquad (2.38)$$

From equation (2.38) it is evident that if V_{SC} drops to 50% of the initial value, we extract 75% of the stored energy.

Another possibility to store energy is in a water tank (boiler), the warmed water can be then used as thermal agent in the utilities. In many cases, the energy necessary for heating or for hot water producing represents about 80% of the total consumption, because the lighting and other electrical consumers are now much more efficient.

In this applications it is required a combination of energy, power density, cost, and life cycle specifications that cannot be met by a single energy storage device. In such case hybrid energy storage sources are used, they combine two or more energy storage technologies [19]. For the proposed wind energy conversion system supercapacitors were chosen as short term energy storage, in tandem with rechargeable batteries.

The supercapacitors need to ensure the transients in energy storage, when the currents from the PMSG and to the load are higher than the batteries rated charging and discharging currents.

The supercapacitors parameters are:
- nominal SC capacitance, C = 63 [F];
- rated SC voltage, V_{SC} = 125 [V];
- SC maxim continuous current, I_{max} = 150 [A];

For a long term energy storage source, batteries were also used in the proposed system. Four Valve regulated rechargeable batteries have been chosen with 12V/100AH/10AH specifications.

Also, the dumping resistors included in the system configuration (R1 and R2) can be used for warm water in a boiler, in order to avoid losses.

2.9. The Inverter and Charge Controller

The inverter needs to convert, supply, control, clean and distribute electrical power. For this application industrial equipment was used. It is a true sine wave inverter that can be used for residential and commercial applications: stand-alone, grid-backup and grid-tie with battery energy storage. Capable of being grid-interactive or grid-independent, the inverter will operate with generators and renewable energy sources to provide full-time or backup power.

Inverter features:
- High efficiency true sine wave output.
- Building block power levels – Up to three inverters can be installed together in a 230 volt, single-phase, two-wire configuration to produce up to 18 kilowatts. Multiple units can also be connected to create a three-phase

system. At least one inverter per phase is required, and up to two inverters can be connected in parallel on each phase.

- Surge capacity to start difficult loads like well pumps, refrigerators or A./C. compressors.
- Power factor corrected (PFC) input minimizes AC input current required for charging, increasing AC pass-through capacity.
- High DC output current and multi-stage chargers minimize charging time.
- Optional Automatic Generator Start allows operation with a wide range of generators, supported through a dedicated generator input.
- Supports multi-mode grid-tie operation.
- Integrated transfer switch.
- Temperature-controlled, variable-speed internal cooling fan. The fan turns on when the internal temperatures reaches 45 °C and reaches maximum speed at 70 °C. The fan turns off when the internal temperature falls to 40 °C.
- Housing design promotes vertical air flow through the inverter. This natural "chimney effect" provides convection cooling at lower power levels, and reduces the fan run time.
- Designed for reliability and field serviceability.

The Inverter uses a network communications protocol to communicate its settings and activity to other enabled devices. The Inverter and every enabled device in the system can be configured and monitored using a System Control Panel.

The Inverter is a self-contained DC to AC inverter, battery charger and integrated AC transfer switch. All configurations must comply with local and national electrical codes.

Whenever AC is present on the Inverter input, the unit can operate as a battery charger. Different battery types and chemistries require different charging voltage levels. Not charging batteries at the required levels can shorten battery life or damage the batteries.

The inverter can be programmed to control how and when to use utility power. Advanced features allow management of peak loads and time-of-use biling.

The "grid support" feature allows the Inverter to support local loads by converting excess capacity from external DC sources connected to its battery bank. Examples of external DC sources are charge controllers, micro-hydro and wind turbines. There are two modes of operation within Grid Support.

In the mode "grid support enabled, sell disabled", the available DC power is converted and used to power local loads. No power is exported to the utility. If the local load demand exceeds the available power from the external DC sources, power is then drawn from the utility to support the load. If the local load demand is less than the power available from external DC sources, the next excess power from the external DC sources is not converted and hence not used. In the mode "grid support enabled, sell enabled", all available excess power is first used to power local loads. Any remaining power is exported to the utility grid.

Generator support allows power to be automatically drawn from the batteries to assist an AC generator to support heavy loads (loads that exceed the available current from the generator). Generators have a limited output current and it is possible to reach this limit when operating heavy loads. The Inverter is designed to assist the generator when heavy current demands load down the generator by supplying additional power from the batteries. The battery charger can back off its charging current to the batteries so the combined load of the charger

and load support does not exceed that of the generator, or trip its output breakers or fuses.

A Battery Temperature Sensor is also included with the Inverter. The Battery Temperature Sensor monitors the temperature of the battery bank and adjusts the charging accordingly [20], [21].

The Charge Controller is designed to work with DC sources and deliver the maximum available current for charging batteries. It can be used with 12-, 24-, 36-, 48-, and 60-volt DC battery systems. However, the Inverter can only work at 24 or 48 volts. When the Charge Controller is used with the Inverter, it is limited to 24-or 48-volt battery banks. The Charge Controller features are:

- Two or three stage charging process;
- Convection cooled (no internal or external fan) using aluminum die-cast chasing and heat sink.
- 60 A capacity;
- 150 Volt open circuit voltage;
- Configurable auxiliary output;
- Input over-voltage and under-voltage protection, output over-current protection and back-feed (reverse current) protection.
- Over-temperature protection and power derating when output power and ambient temperature are high.
- Battery Temperature sensor to provide automatically temperature-compensated battery charging.

The Battery Temperature Sensor automatically adjust the charging process of the Charge Controller, which increases or decreases the battery charging voltage depending on the temperature of the battery to optimize the charge to the battery and to protect it from over-charge or damage. Using the temperature sensor can extend battery life and improve overall charging.

For inverter applications, the batteries must be deep discharge types and the same type from the same lot and date for all the batteries in the bank. The DC voltage of the inverter must match the nominal voltage of the system and all battery-connected devices. The minimum recommended battery bank is 100 Ah. The inverter is designed to operate with batteries and should not be operated without them [21], [22].

2.10. Simulation Results

In order to validate the previous design models, the proposed conversion and control system have been simulated using Matlab/Simulink software.

The loads (charger, battery, inverter an AC loads) were equated with two resistive components connected at the SC:

- Z_1 = 1.5 [Ω];
- Z_2 = 0.5 [Ω].

For a 100 [Wh] necessary energy storage, a "BMOD0063P125" supercapacitor module has been chosen, with the following specifications [23]:

- nominal capacitance, C = 63 [F];
- rated voltage, V_{SCn} = 125 [V];
- maxim continuous current, $I_{iHDCmax}$ = 150 [A];
- lifetime 100,000 [h].

It is possible to realize a predictive energy management around the DC variable voltage of the *SC*. This can be easily realized using hysteresis comparators (HC), as shown in Fig.2.42, in hardware or software implementation. Five SC voltage steps, V_{SCi} (*i=1…5*), are defined as follows:

- V_{SC1} = 60 [V], minimum working voltage level;
- V_{SC2} = 61 [V], load connection level;
- V_{SC3} = 70 [V], R_2 disconnection level;
- V_{SC4} = 90 [V], R_2 connection level;
- V_{SC5} = 100 [V], maximum working voltage level;

The working strategy of the proposed V_{SC} control is presented synthetically in Table 2.9, in a logical sequence. In order to complete the above consideration, a preliminary design procedure was elaborated and validated with digital simulations.
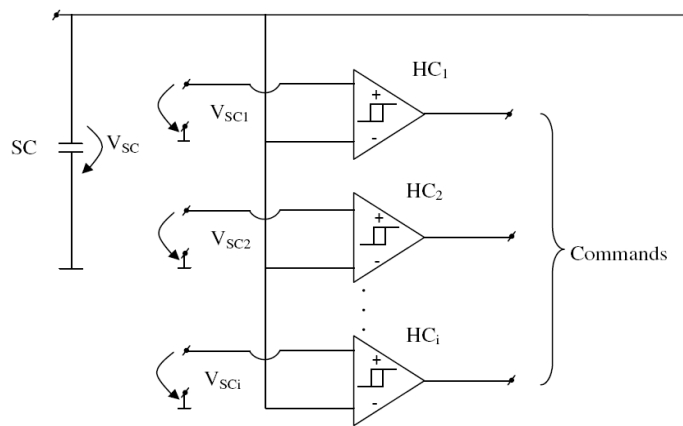
Fig.2.42. V_{SC}.control method.

Table 2.9. The working strategy of the proposed V_{SC} control

V_{SC}	Control commands
$V_{SC} > V_{SC2}$	SC starts to deliver energy to the charger.
$V_{SC} > V_{SC4}$	The maximum working SC voltage was achieved.
$V_{SC} > V_{SC5}$	The maximum admissible SC voltage was achieved. HDC stops functioning. Thus, SC is disconnected. This situation is possible when the loads aren't connected or the system works improperly.
$V_{SC} < V_{SC1}$	The energy produced by the PMSG is too low, and the charger stops.
$V_{SC} < V_{SC4}$	The SC was discharged by R_2. The resistor is disconnected.

If no load is connected, when the SC is fully charged, the system needs to connect the protection resistor R with P = 5 [kW] total power dissipation.

$$R = \frac{V_{SC5}^2}{P} \approx 2\Omega \tag{2.39}$$

Figs.2.43-2.45 show the system responses in three cases. In the first case (Fig.2.43), no load is connected to the system and the SC voltage reaches the V_{sc4} level, were the protection resistor R is connected. R limits the SC voltage at the admissible value.

In the second case (Fig.2.44), the load is equated with Z_1 and it can be seen that the SC voltage cannot rise as much as in the first case. SC ensures the storage for transients, when the charger does not need the entire energy delivered for the PMSG.

In the third case (Fig.2.45), the Z_2 load is connected and the entire energy is transferred; the SC voltage is kept constant.
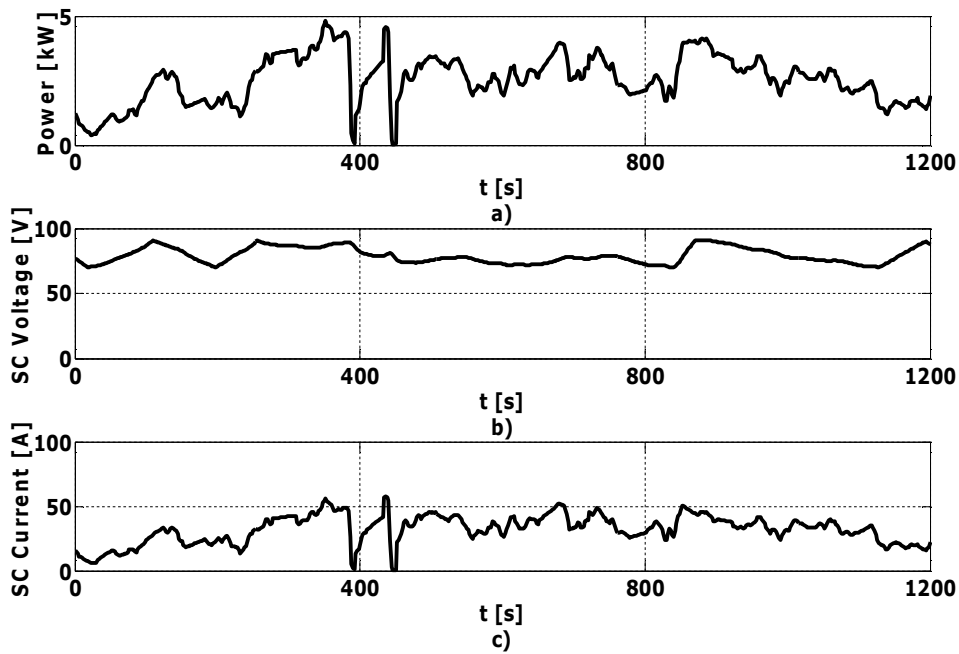
Fig.2.43. System response in the case of no AC load connected in the system: a) System power; b) SC voltage; c) SC current.
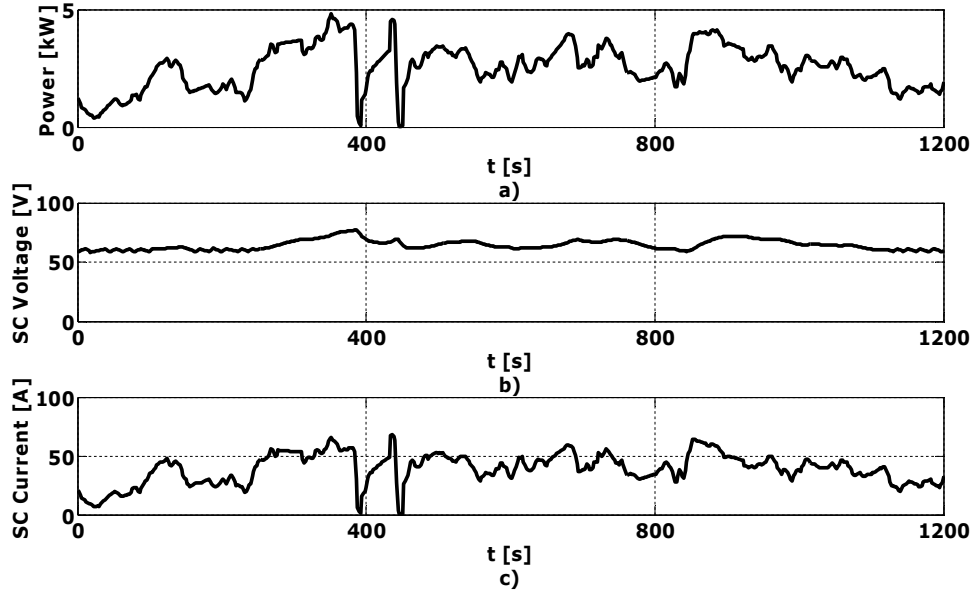
Fig.2.44. System response with a 1.5 Ω load connected in the system: a) System power; b)
SC voltage c) SC current.
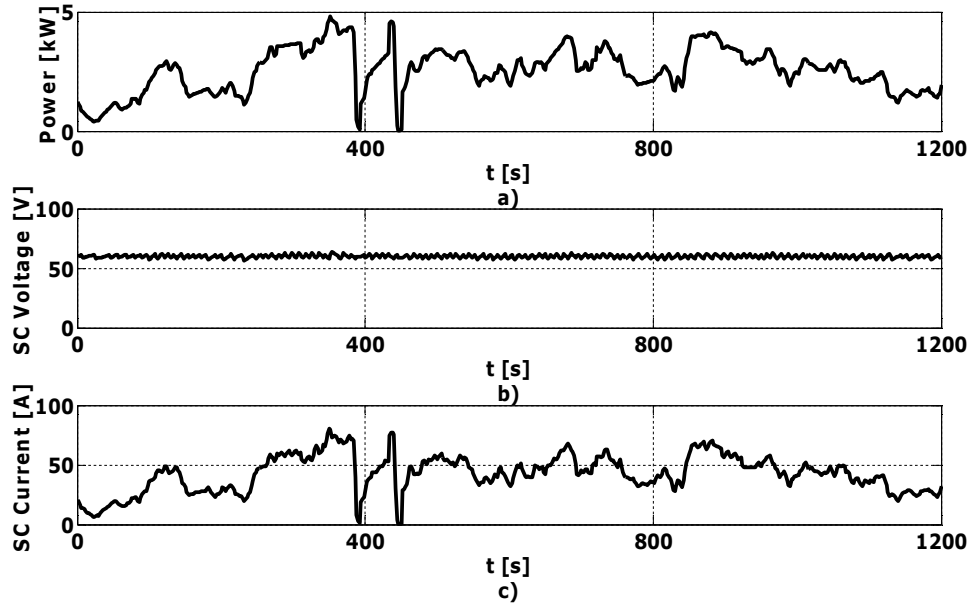
Fig.2.45. System response with a 0.5 Ω load connected in the system: a) System power; b)
SC voltage c) SC current.

2.11. Conclusion

This chapter presented the proposed SWECS structure using a hybrid DC-DC converter, a mixing (SC+batteries) storage elements. All WECS main components were described in detail and modeled.

A speed estimator was elaborated in order to eliminate the need of a speed sensor.

A new class of hybrid, high gain power converter was used as interface between the PMSG and SC.

The Inverter and the Charge Controller were used to convert, supply, control, clean and distribute electrical power and also to control the battery charging.

For protection two resistors were used: R_1 and R_2 connected to the PMSG output and respectively in parallel with SC, to dissipate the excess of energy when is needed. They can be also used in a boiler for hot water in order to eliminate the energy losses.

The system uses both supercapacitors and batteries, as hybrid electrical energy storage. The storage elements parameters must be designed taking into account the transient regimes and the needed back-up energy.

The supercapacitors offer higher power density, higher voltage levels, high charge / discharge currents and increased life-cycle compared to batteries.

The supercapacitor voltage level is a very precise measure of the stored energy and can be used as input for the control system and for energy management. The control structure is very simple, based on hysteresis comparators and implemented with inexpensive hardware components (e.g. programmable relays).

Five SC voltage steps were chosen (V_{SCi}) to define the output commands for the supercapacitor voltage control, and two equivalent loads have been used in order to study the SC behavior, by digital simulations.

References

[1]   Z. Chen, J. M. Guerrero, F. Blaabjerg, "A review of the state of the art of power electronics for wind turbines", *IEEE Trans. Power Electr.,* vol. 24, no. 8, August 2009, pp.1859-1875.

[2]   Md. Arifujjaman, M. Tariq Iqbal, J. E. Quaicoe and M Jahangir Khan, "Modelling and control of a small wind turbine", *Proc. of 18th Annual Canadian Conference on Electrical and Computer Engineering "CCECE05"*, Saskatchewan Canada, pp. 778-781, May 2005.

[3]   B. Ni, C. Sourkounis, "Influence of wind-energy-converter control methods on the output frequency components", *IEEE Trans. Ind. Applic.,* vol. 45, no.6, November – December, 2009, pp. 2116-2122.

[4]   www.schneider-electric.com/corporate/en/products-services/renewable

[5]   J. Hui, "An Adaptive Control Algorithm for Maximum Power Point Tracking for Wind Energy Conversion Systems", PhD. Thesis, Queen's University Kingston, Ontario, Canada, December 2008.

[6]   L. Mihet-Popa, " Wind Turbines Using Induction Generators Connected to the Grid", Ed. Politehnica, Timisoara 2007.

[7]   I. Munteanu, A. I. Bratcu, N. A. Cutululis, E. Ceanga, "Optimal Control of Wind Energy Systems", Springer, 2008.

[8]   S. M. Barakati, "Modeling and Controller Design of a Wind Energy Conversion System Including a Matrix Converter", PhD. Thesis, Waterloo, Ontario, Canada, 2008.

[9]   M. Barglazan, T. Milos, "Analytical models for characteristic curves of wind turbines", *WSEAS International Conference,* Timisoara, Romania, October 21-23, 2010, ISBN 978-960-474-237-0, pp. 298-300.

[10] N. Milivojevic, I. Stamenkovic, N. Schofield and A. Emadi, "Electrical Machines and Power Electronic Drives for Wind Turbine Applications", *34th Annual Conference of the IEEE Industrial Electronics Society (IECON 2008)*, Orlando, Florida, U.S.A, 10 - 13 November, pp. 2326 – 2331.

[11] M. O. Mora, "Sensorless vector control of PMSG for wind turbine applications" - Master Thesis, Aalborg University, Institute of Energy Technology, June 2009.

[12] G. Madescu, M. Mot, M. Biriescu, M. Gregonici, C. Koch, "Low speed PM generator for direct-drive wind applications", *International Conference on computer as a tool joint with CONFTELE 2011, EUROCON 2011*, pp. 1-4, April 2011.

[13] V. Caliskan, D. J. Perreault, T. M. Jahns and J. G. Kassakian, "Analysis of three-phase rectifiers with constant-voltage loads", *IEEE Trans. On Circuits and Systems, vol. 50, no. 9, September 2003, pp. 1220-1226.*

[14] F. Z. Peng, "Z-source inverter", *IEEE Tran. Ind. Applic.*, Vol. 39, March-April 2003, pp.504-510.

[15] B. Axelrod, Y. Berkovich, A. Ioinovici, "Switched-capacitor/switched-inductor structures for getting transformerless hybrid dc-dc PWM converters", *IEEE Trans. Circ. and Syst.,* vol.55, no. 2, March 2008, pp. 687-696.

[16] I. Rezaei, M. Akhbari, "Transformerless Hybrid Buck Converter with WideConversion Ratio, "*Power Electronics, Drive Systems and Technologies Conference"*, Teheran, Iran, February 16-17, 2011, pp. 599-603.

[17] O. Cornea, O. Pelan, N. Muntean, "Comparative Study of Buck and Hybrid Buck "Switched-Inductor" DC – DC Converters", *OPTIM 2012 - 13th International Conference on Optimization of Electrical and Electronic Equipment*, May 24-26, 2012, Brasov, Romania, pp. 853-858.

[18] J. H. Lee, S. H. Lee, S. K. Sul, "Variable – speed engine generator with supercapacitor: isolated power generation system and fuel efficiency", *IEEE Trans. Ind. Appl.,* vol. 45, no.6, nov.-dec. 2009, pp. 2130-2135.

[19] S. Vazquez, S. M. Lukic, E. Galvan, L. G. Franquelo and J. M. Carrasco, "Energy Storage Systems for Transport and Grid Applications*", IEEE TRANSACTIONS ON INDUSTRIAL ELECTRONICS,* vol. 57, no.12, December 2010, pp. 3881-3895.

[20] "XW Hybrid Inverter/Charger- Operation Guide".

[21] www.xantrex.com

[22] "XW Charge Controller Series Solar- Owner's Manual".

[23] www.maxwell.com, "HTM heavy transportation series 125V module", Datasheet.

3. HARDWARE IN THE LOOP WIND TURBINE EMULATOR

3.1. Introduction

In order to study and test wind turbine systems, it is necessary to have a real time emulator, because a wind turbine may not always be available and neither a wind tunnel test.

Another motivation of using a physical simulator for wind energy applications is the simple fact that it can provide controllable wind velocity [1].

The emulator is able to produce the same behavior as real wind turbine can do, in a real environment.

The basic requirement for a wind simulator is that its static and dynamic characteristics must be as close as possible to a real wind turbine. The advantage of the emulator is that various wind profiles and wind turbines can be incorporated as desired through software system [2]-[11]. Complex testing of the generator control for grid and stand-alone regimes [12]-[15] also need such a tool.

A wind turbine emulator shown in Fig.3.1 consists essentially of:
- A software part which implements the mathematical model of the wind turbine;
- A physical part that provides the similar static and dynamic characteristics as the real studied system.

Being in a close loop, the two systems communicate with each other. The real time software sends reference signals to the physical system which responds during the real time simulation [16].
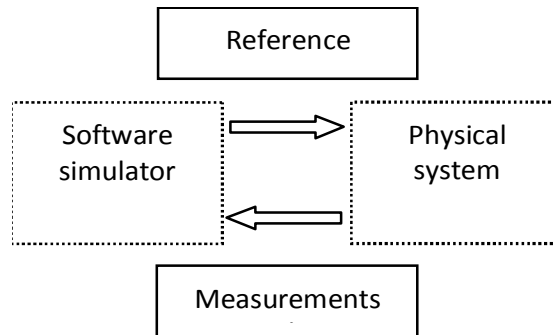
Fig.3.1. General diagram for a hardware in the loop wind turbine emulator.

In the beginning, a digital simulation wind turbine system, including the wind turbine and electrical generator models, was implemented in Matlab/Simulink [17].

The block diagram in Fig.3.2 contains a variable wind speed profile generator, a wind turbine aerodynamic model (presented in Chapter 2.3), and a PMSG model with the corresponding load (presented in Chapter 2.4).

Then, a hardware emulator for the wind turbine is proposed. The emulator structure, presented in Fig.3.3, contains: a dSPACE control board, a voltage source inverter with direct torque control (DTC), a three phase induction machine *(IM)* with GB) – the wind turbine equivalent, and a PMSG with resistive load.

The emulator control was implemented in Matlab/Simulink and it runs in real time on dSPACE board. The control output signal (torque reference T_{IMref}) is send to the DTC inverter, which returns the real (estimated) IM torque (T_{IM}) and the drive (estimated) rotating speed (ω_{IM}). The complete block diagram is shown in Fig.3.4.

In steady-state (neglecting the gearbox efficiency):

$$\frac{T_{IM}}{T_{wt}} = \frac{\omega}{\omega_{IM}} \tag{3.1}$$

The dynamic equation is:

$$T_{wt} - T_g = J \cdot \frac{d\omega}{dt} \tag{3.2}$$

where
T_{wt}: wind turbine torque [N·m];
T_g: generator torque [N·m];
J: inertia of the wind turbine system [kg·m^2].

The wind turbine torque and power result from the wind turbine characteristics, presented in Chapter 2.3 [17]:

$$T_{wt} = \frac{1}{2} \cdot C_M \cdot \rho \cdot v^2 \cdot A \cdot R \tag{3.3}$$

where
C_M is the wind turbine torque coefficient; expression (3.4) was obtained from the wind turbine test:

$$C_M = C_{M0} + a \cdot \lambda - b \cdot \lambda^{2.5} \tag{3.4}$$

where
a, b, C_{M0} are the constants for the nominal tip-speed ratio λ_0;

$$P_{wt} = T_{wt} \cdot \omega \tag{3.5}$$

The inertia of the wind turbine system is composed by:

$$J = J_{wt} + J_g \tag{3.6}$$

where
J_{wt}: inertia of the wind turbine [kg·m^2];
J_g: inertia of the PMSG [kg·m^2];

The hardware part of the emulator has itself the inertia J_{em}, composed by:

$$J_{em} = J_{IM} + J_{GB} + J_g \tag{3.7}$$

or

$$J_{em} = n^2 \cdot J_{IM} + J_g \tag{3.8}$$

where
J_{IM} : inertia of the IM [kg·m^2];
J_{GB} : inertia of the gearbox [kg·m^2];
n: gearbox coefficient;
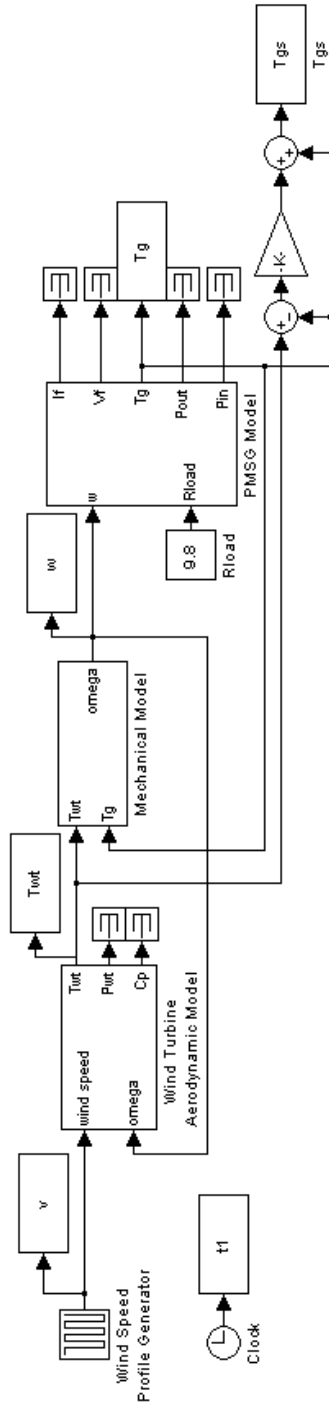
Fig.3.2. Wind turbine Matlab/Simulink simulation scheme.
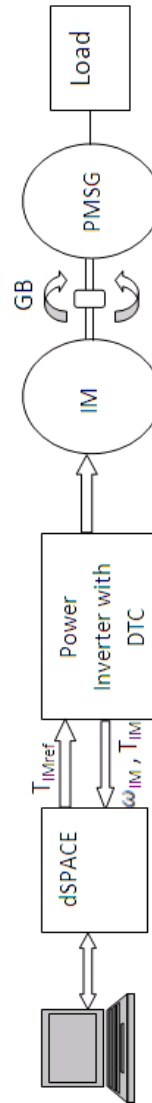
Fig.3.3. Wind turbine hardware emulator configuration.
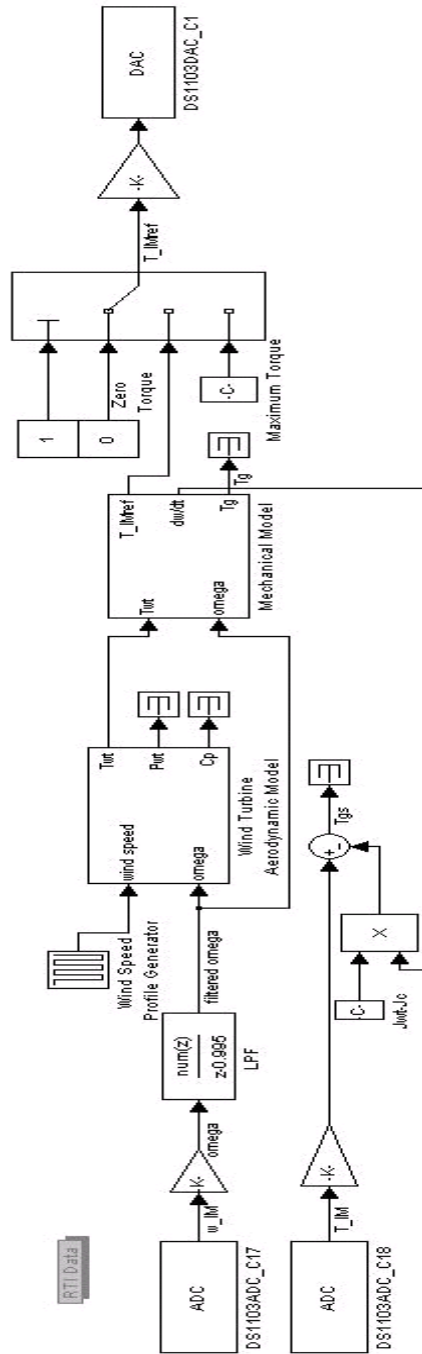
Fig.3.4. Wind turbine dSPACE implementation scheme.

Because J_{em} is different than J, it is necessary to introduce a compensation inertia in the emulator control J_c:

$$J_c = J - J_{em} \tag{3.9}$$

The speed derivative was computed using a close loop observer in order to reject the speed noise (Fig. 3.5). Direct speed derivative would have introduced noise that would have been passed as a reference torque to the IM. Noise filtering would have introduced delays, and because of the reverse reaction would have negatively affect the stability of the system.

$$T_{wt} - T_{estimated} = J \cdot \frac{d\omega}{dt} \tag{3.10}$$

$$T_{GB} = T_0 + k_t \cdot T_g + k_\omega \cdot \omega \tag{3.11}$$

$$T_{wt} - T_{IMref} + T_{GB} = J_c \cdot \frac{d\omega}{dt} \tag{3.12}$$

$$T_{wt} - T_g = (J_c + J_{IM}) \cdot \frac{d\omega}{dt} \tag{3.13}$$

where:
T_{GB} is the gearbox friction torque [N·m];
T_0 , k_t , k_ω , have been experimentally identified, observing the control output signal and the generator torque for different speeds and loads.

The estimated torque ($T_{estimated}$) was found with a PI controller, by minimizing the speed error (ε_ω). The PI coefficients, k_p and k_i were deducted by experimental attempts. From equation 3.10 results:

$$\frac{d\omega_{estimated}}{dt} = \frac{T_{wt} - T_{estimated}}{J} \tag{3.14}$$

$$\omega_{estimated} = \int \frac{d\omega}{dt} \cdot dt \tag{3.15}$$

$$\varepsilon_\omega = \omega_{estimated} - \omega \tag{3.16}$$

$$T_{estimated} = k_p \cdot \varepsilon_\omega + k_i \cdot \int \varepsilon_\omega \cdot dt \tag{3.17}$$

The PMSG shaft torque, as emulator output, is:

$$T_{gs} = T_{IM} \cdot \frac{\omega_{IM}}{\omega} - (J_{wt} - J_c) \cdot \frac{d\omega}{dt} \tag{3.18}$$
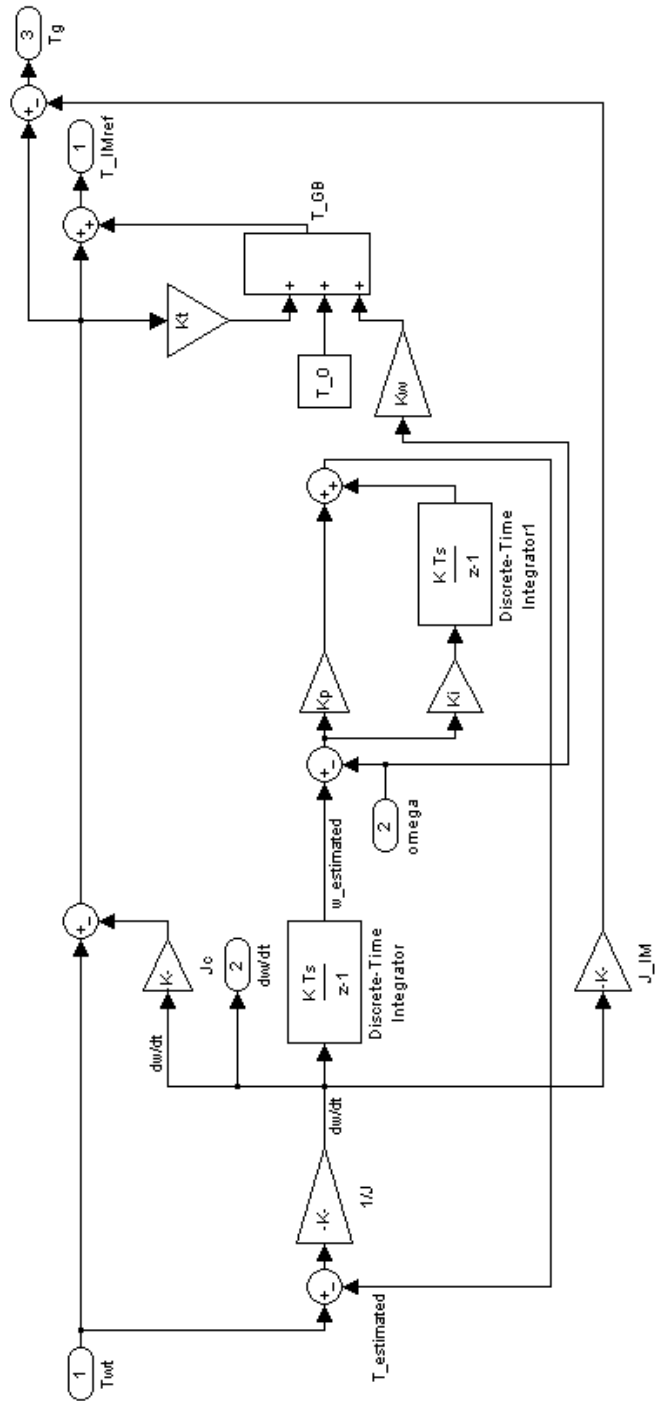
Fig.3.5. Torque observer Matlab/Simulink scheme.

3.2. Simulation and Experimental Results

The emulator test bench parameters are:
- PMSG Rated power, P_n = 5 [kW];
- Rated speed, n = 120 [rpm];
- Rated power of the IM, P_{IM} = 7.5 [kW];
- Rated IM speed, n_{IM} = 715 [rpm];
- PMSG inertia, J_g = 1.05 [kg·m^2];
- IM inertia, J_{IM} = 0.156 [kg·m^2];
- Hardware part of the emulator inertia, J_{em} = 6.68 [kg·m^2];
- Gearbox coefficient, n = 6.03;
- k_t = 0.05, k_ω = 3.08, T_0 = 17.66 [N·m];
- k_i = 10 [N/rad], k_p = 100 [N·s/rad].
- The wind turbine parameters, considered to validate the emulator were described in Chapter 2.3.
- The PMSG parameters, considered in the emulator structure, were described in Chapter 2.4.

A T_f = 0.02 sec. time constant first order low pass filter was used to reduce the speed measured noise.

The behavior of the wind power system was studied by simulation and emulation, considering a step variation of the wind speed between 9 and 10 [m/s], with a time period of 40 sec., as it is shown in Fig.3.6.a. The corresponding shaft speed (Fig. 3.6.b), wind turbine torque and generator torque (Figs. 3.7. a, b) are presented, for simulation study (left column) and for emulation process (right column).

Also the wind turbine energy is illustrated in Fig.3.8, simulation results in Fig. 3.8.a and the experimental (emulation) results in Fig.3.8.b. Good similarities can be observed between simulation and experiments, which validate the good accuracy of the emulator. The system responses were tested considering a rectangular wind speed shape which is the most difficult regime and is never meet in real situations.

The experimental setup, containing the dSPACE control board, the DTC inverter and the induction machine coupled with the PMSG, is presented in Fig.3.9-3.11.
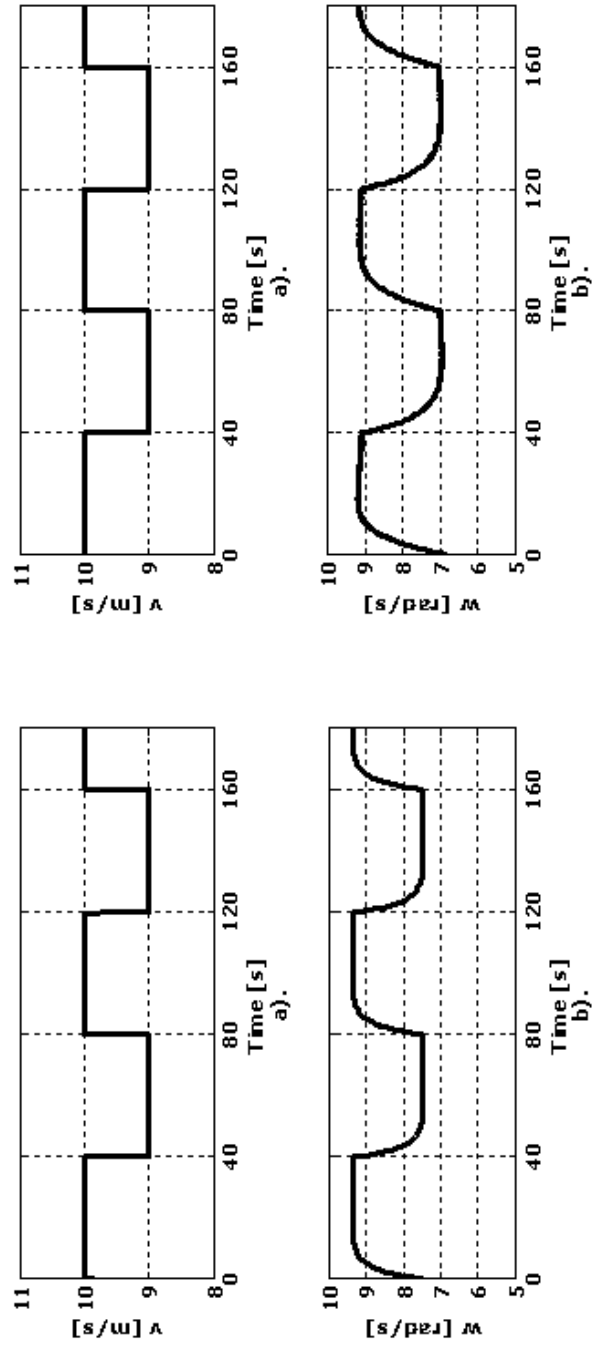
Fig.3.6. Simulation (left column) and experimental (right column) results: a) Wind speed; b) Rotating speed.
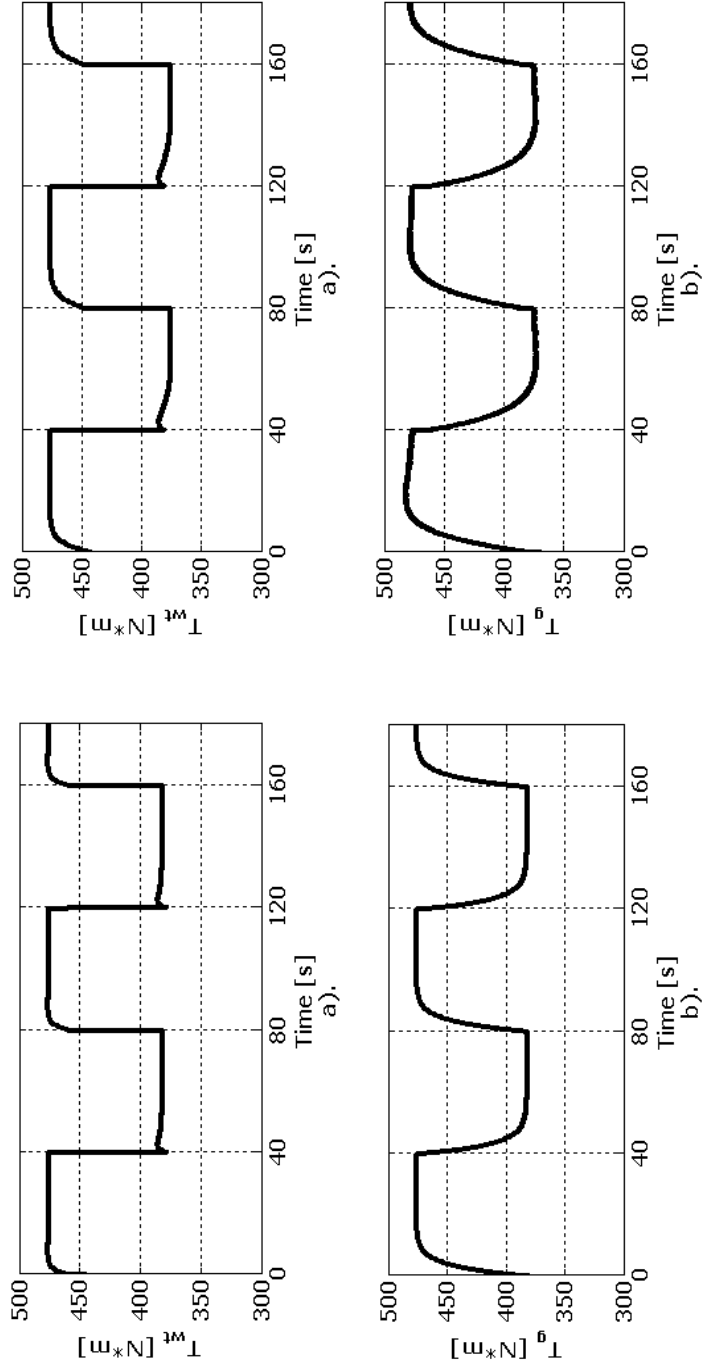
Fig.3.7. Simulation (left column) and experimental (right column) results: a) Wind turbine torque; b) PMSG torque.
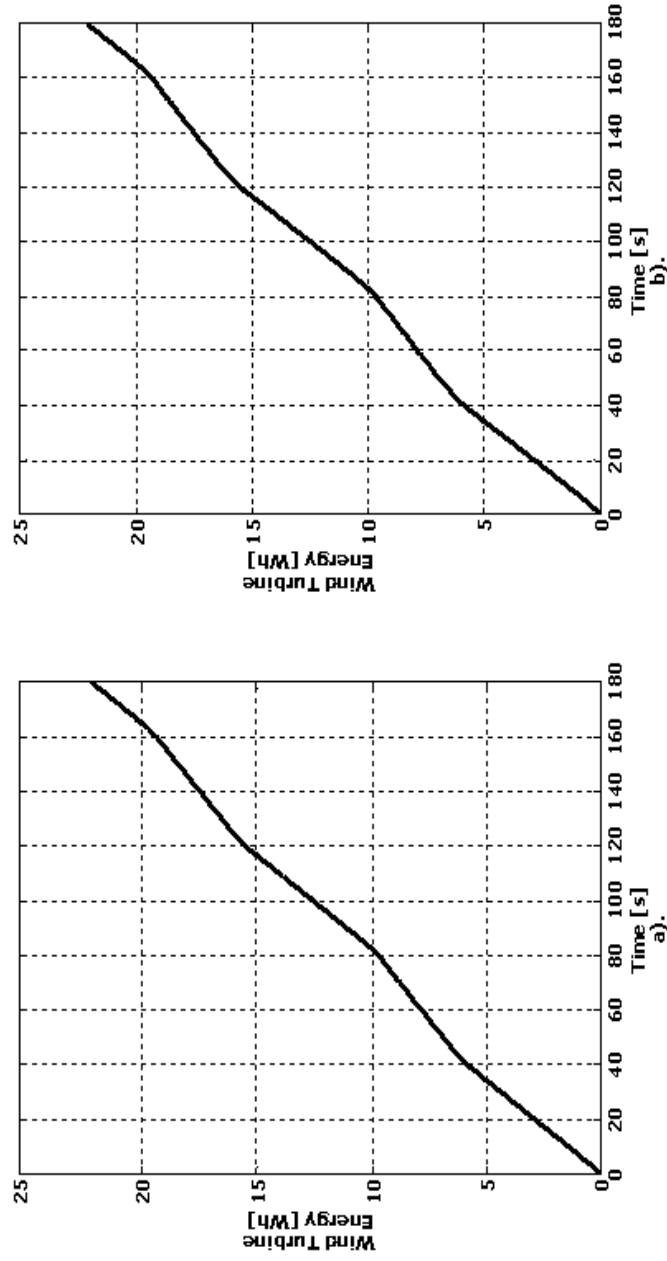
Fig.3.8. Wind turbine energy: a) Simulation result; b) Emulation result.
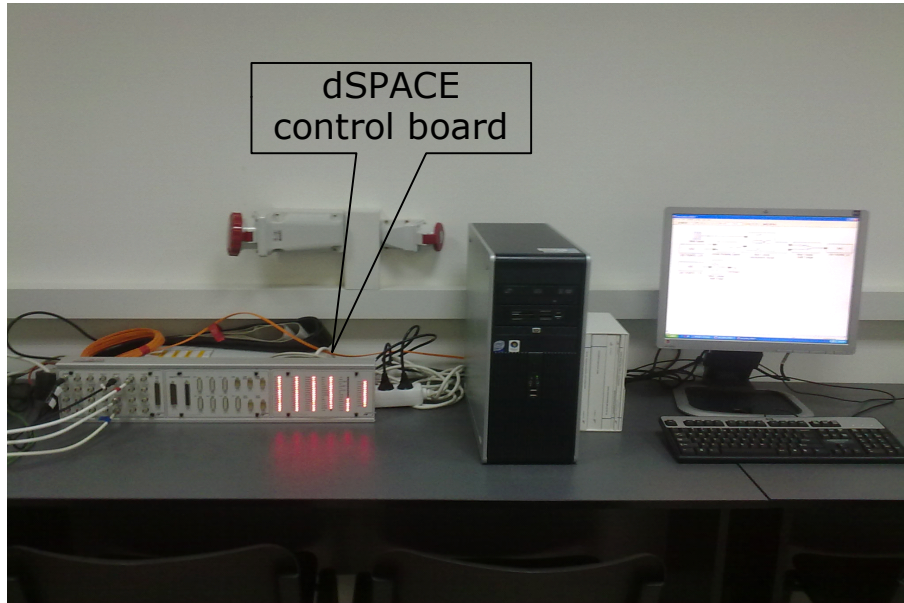
Fig.3.9. Experimental Setup: dSPACE control board.
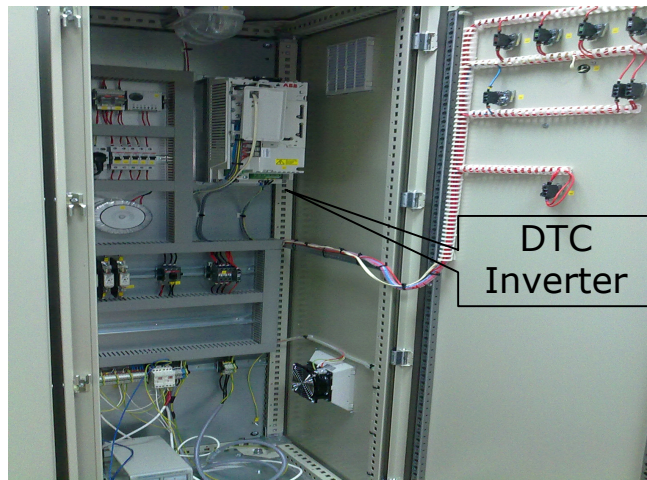
Fig.3.10. Experimental Setup: DTC Inverter.
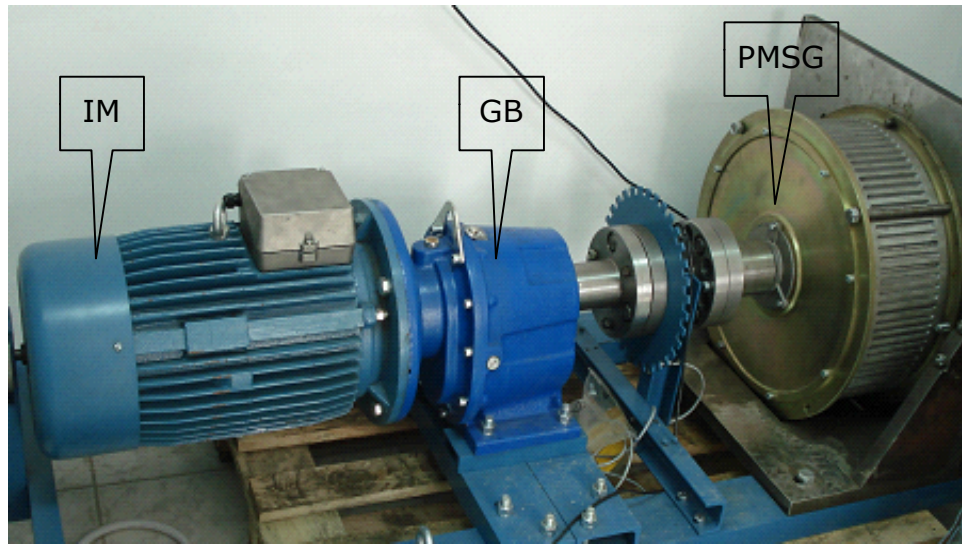
Fig.3.11. Experimental Setup: IM, GB and PMSG.

3.3. Conclusion

In this chapter a laboratory tool, useful for study and testing real equipment for wind energy systems, without a real wind turbine, was described. The hardware in the loop proposed configuration includes, as a main parts, a variable speed, DTC, drive, which can generate the same torque to the PMSG shaft, as a real wind turbine can do, and a dSPACE system. All necessaries software parts were also developed.

The digital simulations and experimental results are in good agreement, validating the wind turbine emulator.

The advantages of the proposed system are:
- flexibility (large range of wind turbine and generators can be tested without investments in aerodynamic tunnels and wind turbines);
- the energy produced by the wind system at different wind speed profiles can be easily estimated;
- possibility to test different control loops, power converters, storage elements, electrical loads, the connection to the utility grid etc.;
- universality (the emulator can be used at different powers; it is necessary to have the proper DTC drive and the corresponding IM and GB in terms of torque and power);
- rapid prototyping.

References

[1] I. Munteanu, A. I. Bratcu, N. A. Cutululis, E. Ceanga, "Optimal Control of Wind Energy Systems", Springer, 2008.

[2] B. Neammanee, S. Sirisumrannukul and S. Chatratana, "Development of a Wind Turbine Simulator for Wind Generator Testing", *International Energy Journal*, Volume 8, 2007, pp.21-28.

[3] Md. Arifujjaman, M. Tariq Iqbal, J. E. Quaicoe and M Jahangir Khan, Modelling and control of a small wind turbine, *Proc. of 18th Annual Canadian Conference on Electrical and Computer Engineering "CCECE05"*, Saskatchewan Canada, pp. 778-781, May 2005.

[4] L. A. C. Lopes, J. Lhuilier, A. Mukherjee and M. F. Khokhar, "A Wind Turbine Emulator that Represents the Dynamics of the Wind Turbine Rotor and Drive Train", *IEEE 36th Power Electronics Specialists Conference, PESC '05,* 16 June 2005, Recife, Brazil, pp. 2092 - 2097.

[5] S. Kumsup and C. Tarasantisuk, "Real-time wind turbine emulator for testing wind energy conversion systems", *IEEE International Energy Conference and Exhibition (EnergyCon), 2010,* 18-22 Dec. 2010, Manama, pp. 7 - 9.

[6] S. H. Song, B. C. Jeong, J. H. Oh, G. Venkataramanan, "Emulation of output characteristics of rotor blades using a hardware-in-loop wind turbine simulator", *Twentieth Annual IEEE Applied Power Electronics Conference and Exposition, APEC 2005,* 6-10 March 2005, pp. 1791 - 1796 Vol. 3.

[7] B. Gong and D. Xu, "Real time wind turbine simulator for wind energy conversion system", *IEEE Power Electronics Specialists Conference, PESC 2008,* 15-19 June 2008, Rhodes, pp. 1110 - 1114.

[8] Y. Jia, Z. Wang, Z. Yang "Experimental Study of Control Strategy for Wind Generation System", *IEEE Power Electronics Specialists Conference, PESC 2007,* 17-21 June 2007, Orlando, FL, pp. 1202 - 1207.

[9] M. Monfared, H. M. Kojabadi, H. Rastegar, "Static and dynamic wind turbine simulator using a converter controlled dc motor", *Renewable Energy, vol. 33, 2008,* pp. 906 - 913.

[10] H. Guo, B. Zhou, J. Li, F. Cheng, L. Zhang, "Real-time simulation of BLDC-based wind turbine emulator using RT-LAB", *International Conference on Electrical Machines and Systems, ICEMS 2009,* 15-18 Nov. 2009, Tokyo, pp. 1 - 6.

[11] W. Li, G. Joos and J. Belanger, "Real-Time Simulation of a Wind Turbine Generator Coupled With a Battery Supercapacitor Energy Storage System", *IEEE Transactions on Industrial Electronics, Vol. 54, Issue 4,* April 2010, pp. 1137 - 1145.

[12] A. G. Abo-Khalil, D. C. Lee, "Dynamic Modeling and Control of Wind Turbines for Grid-Connected Wind Generation System", *37th IEEE Power Electronics Specialists Conference, PESC '06,* 18-22 June 2006, Jeju, pp. 1 - 6.

[13] M. Fatu, C. Lascu, G.-D. Andreescu, R. Teodorescu, F. Blaabjerg, I. Boldea, "Voltage Sags Ride-Through of Motion Sensorless Controlled PMSG for Wind Turbines", *Power Electronics Specialists Conference,* 2007, pp. 1239 - 1244.

[14] M. Fatu, L. Tutelea, R. Teodorescu, F. Blaabjerg, I. Boldea, "Motion Sensorless Bidirectional PWM Converter Control with Seamless Switching from Power Grid to Stand Alone and Back," *Industry Applications Conference,* 2007, pp. 171 – 178.

[15] C. Saudemont, G. Cimuca, B. Robyns, M.M. Radulescu, "Grid Connected or Stand-Alone Real-Time Variable Speed Wind Generator Emulator Associated to a Flywheel Energy Storage System", *European Conference on Power Electronics and Applications, EPE 2005*, pp.1-10.

[16] G. Caraiman, C. Nichita, V. Mînzu, B. Dakyo, "Marine current Turbine Emulator Design Based on Hardware in the Loop Simulator Structure", *14th International Power Electronics and Motion Control Conference,* EPE – PEMC 2010, pp.101-107.

[17] N. Muntean, O. Cornea and D. Petrila, "A new conversion and control system for a small off – grid wind turbine", *Optim 2010 - 12th International Conference of Electrical and Electronic Equipment,* 20-22 may, Romania.

4. VARIABLE-SPEED SWECS CONTROL

4.1. Introduction

The configuration/architecture of a wind turbine system and the control strategies for tracking the maximum power points are the most important elements in achieving the goal of higher energy efficiency. To capture the maximum energy from an available wind potential, a maximum power point (MPP) control is necessary in order to adjust the turbine rotating speed according to the change of the wind speed, so that the tip speed ratio can be maintained at its optimal value [1]-[8].

P_1, P_2 and P_3 in Fig.4.1 are the maximum power operating points at the corresponding ω_1, ω_2 and ω_3 rotating speeds for three different wind speeds v_1, v_2 and v_3 in steady state regime [9].
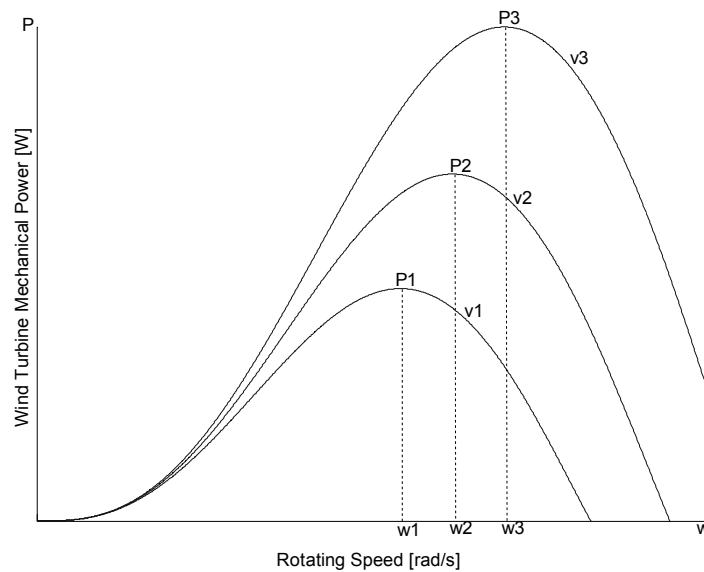
Fig.4.1. Wind turbine characteristics illustrated for three wind speeds.

MPP can be obtained by knowing the turbine characteristics, memorized in the controller, or by using maximum power point tracking (MPPT) algorithms.

Several studies have been focused on finding the better maximization power control strategy. For example, in [10] two types of MPP strategies have been studied, whether the turbine characteristics are supposed to be known or not. For the first type, the knowledge of the optimal characteristics allows to maximize the energy transfer by optimally controlling the torque, speed, or power. For the second type, a MPP algorithm has to be implemented, which could be a perturb-and-

observe (P&O) strategy [11]-[13]. Another MPPT algorithm could be implemented as a fuzzy logic controller based on a set of rules which is derived from the system behavior or from the designed control strategy [14]-[21].

MPPT is a superior control technique, because in all conditions the system reaches the optimum working point. MPP has some major disadvantages: the wind turbine characteristics can vary depending on technological aspects or due to external perturbations. Fig.4.2 shows the power versus rotating speed characteristics for three air densities. It can be seen that the maximum power points curve moves at different air densities. This fact can affect the optimal regimes characteristics (ORC) achievement [22].
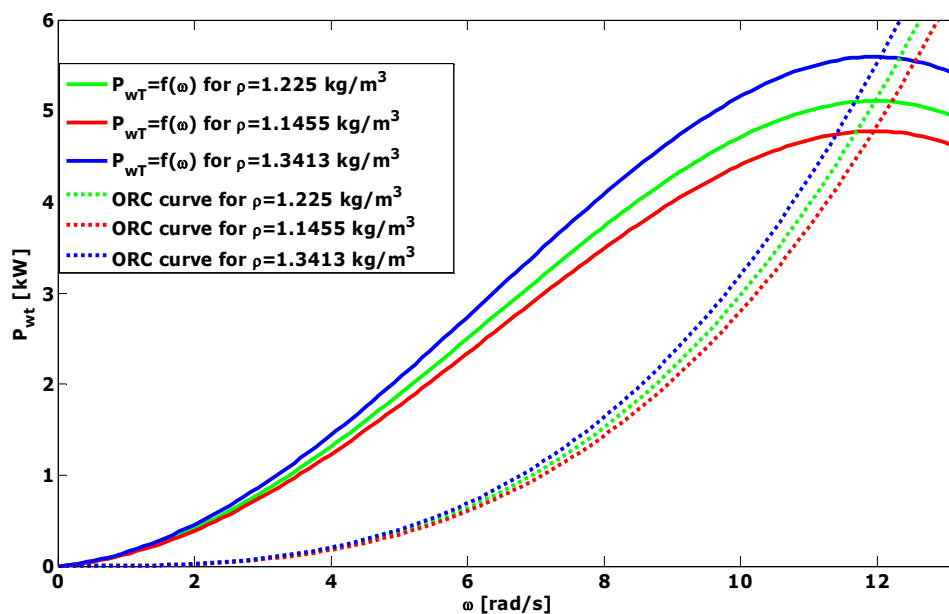
Fig.4.2. Wind turbine power versus rotating speed, and ORC, for different air densities at 10 [m/s] wind speed.

This chapter content is focused on theory, digital simulations and experimental results regarding the following control strategies for SWECS:
- MPP control, knowing the wind turbine characteristic;
- Fuzzy Logic, robust MPPT control, with P&O algorithm;
Both control strategies take into account the dynamic regime of SWECS.
Finally, a comparative evaluation of the above presented control systems is made.

4.2. MPP Control Algorithms

4.2.1. General Aspects

The control of variable-speed fixed-pitch WECS is made in general by modifying the electrical generator speed in order to maximize the available power captured from the wind. For each wind speed, a different optimal rotating speed at which the power has a maximum, needs to be considered. The right control strategy depends on the structure of the whole system, the known characteristics, the available parameters and the control goal.

MPP can be achieved in many ways, by knowing the wind turbine characteristics like: λ_{opt}, C_{pmax}, P_{wt}, T_{wt} curves and the wind speed, or by knowing and controlling other WECS parameters.

A simple method for extracting the maximum available power can be applied if the optimal value of the tip speed ratio λ_{opt} is known. The turbine operates on the optimal regime characteristics when:

$$\lambda(t) = \lambda_{opt} \tag{4.1}$$

Thus:

$$\omega_{opt}(t) = \frac{\lambda_{opt}}{R} \cdot v(t) \tag{4.2}$$

This approach has some disadvantages, because it needs the wind speed, measured by an anemometer mounted on the nacelle [23]. Also in [24] it is related that keeping λ_{opt} in wind gusts it is possible only with large generator torque variations, which means significantly high mechanical stress. An optimal control structure for this problem was proposed in [25].

Another method using λ_{opt} and C_{pmax}, can be simply implemented with the expression of the wind turbine power:

$$P_{wt} = \frac{1}{2} \cdot \rho \cdot A \cdot C_P(\lambda) \cdot v^3 \tag{4.3}$$

$$P_{wt} = \frac{1}{2} \cdot \rho \cdot A \cdot C_P(\lambda) \cdot \frac{\omega^3 \cdot R^3}{\lambda^3} \tag{4.4}$$

Substituting $\lambda(t) = \lambda_{opt}$ and $C_P = C_P(\lambda_{opt})$ the optimum wind turbine power can be obtained by:

$$P_{wt_{opt}} = k \cdot \omega_{opt}^3 \tag{4.5}$$

where

$$k = \frac{1}{2} \cdot \rho \cdot A \cdot R^3 \cdot \frac{C_P(\lambda_{opt})}{\lambda_{opt}^3} \tag{4.6}$$

This approach supposes that an active power control loop is being used, whose reference is determined based on equation 4.6.

Knowing the wind turbine coefficient k and measuring the transferred power it can be calculated the steady-state speed reference, which is able to seek the optimal operation without knowing the wind speeds [8].

A torque control can also be implemented knowing the wind turbine characteristic $C_P (\lambda_{opt})$. The optimal torque is obtained from the rotating speed value given by:

$$T_{wt} = \frac{1}{2} \cdot \rho \cdot A \cdot C_P(\lambda_{opt}) \cdot \frac{\omega^2 \cdot R^3}{\lambda_{opt}^3} \tag{4.7}$$

The following load torque has to be imposed to reach an optimal operation:

$$T_{wt_{opt}} = k \cdot \omega_{opt}^2 \tag{4.8}$$

Thus, the rotating speed directly gives the optimal reference torque, in steady-state.

In some papers only the steady state operation is described and analyzed. This approximation works if the inertia of the turbine is relatively large, and the wind speed changes slowly [2], [20].

For SWECS, working almost continuously in transient regimes, the energy stored by the rotor inertia is considerable and the controller must be able to correctly manage the dynamic operation.

The considered mechanical power (P_m) it is composed by:

$$P_m = P_g + J \cdot \omega \cdot \frac{d\omega}{dt} \tag{4.9}$$

where P_g is the PMSG mechanical (input) power.

4.2.2. Control System Description

In order to illustrate the MPP control a SWECS, with the structure presented in Fig.4.3 is considered. It consists of a PMSG driven by a fixed pitch wind turbine, DBR, HDC - the element that regulates the turbine speed through the controlled PMSG current, and the load [26].
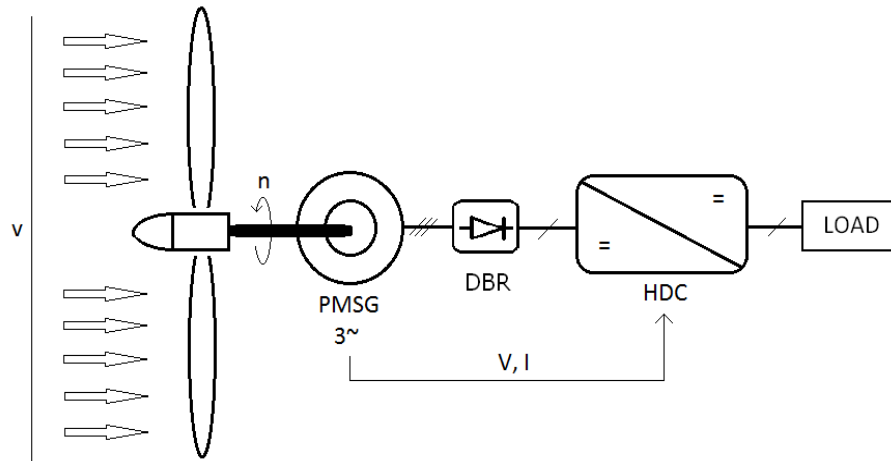
Fig.4.3. SWECS structure.

To obtain the desired rotating speed of the wind turbine, the generator torque must be changed. HDC works as a current controller, i.e. the converter controls the PMSG output current through the DBR, in order to change the PMSG torque T_g.

The converter is implemented as an ideal, fast current source (the measured current will be considered equal with the reference current).

The SWECS model was presented in Chapter 2 and in Fig.4.4 the Matlab/Simulink block diagram of his structure, including the MPP control is illustrated.
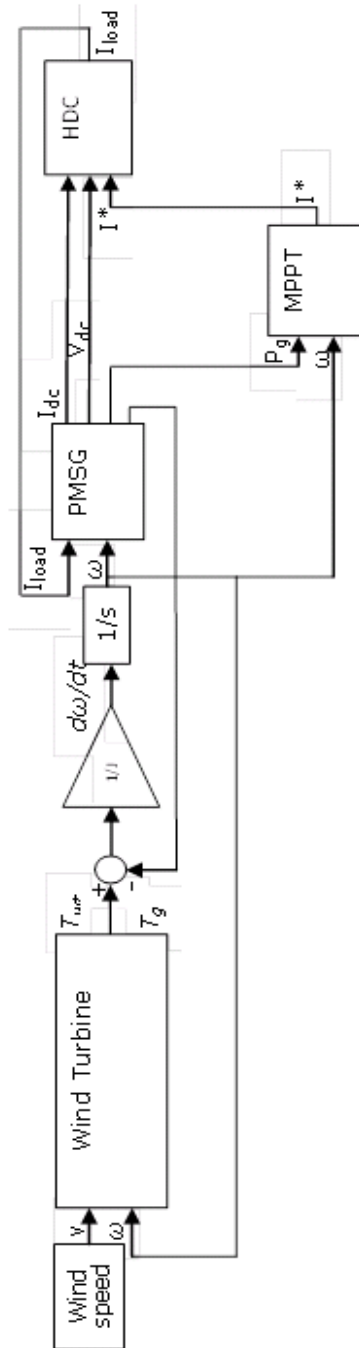
Fig.4.4. SWECS block diagram.

A current controller was realized as in Fig.4.5, using the estimated rotating speed (Chapter 2.5), the active power and the HDC reference current. The reference power was given by equation 4.5 and the constant coefficient k was found with equation 4.6. A classical PI controller was used to impose the power, as a function of the rotating speed, at the PMSG output, on the DC side.
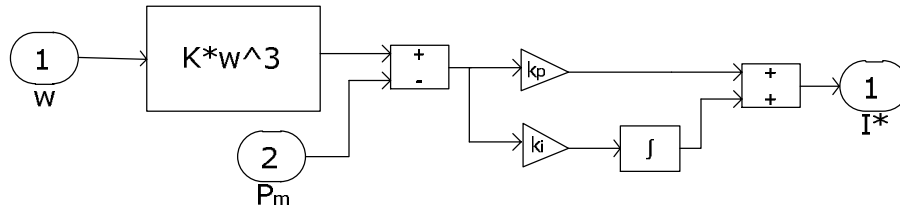
Fig.4.5. The current controller.

4.2.3. Simulation and Experimental Results with the Five Blades Wind Turbine

To test the designed MPP strategy, the "hardware in the loop" wind turbine emulator, presented in Chapter 3, was used [27].

The complete system, with the components described in Chapter 2, is illustrated in Fig. 4.6.
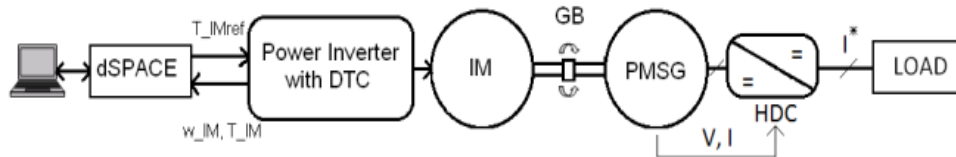
Fig.4.6. The complete system under study.

Knowing the wind turbine characteristics, presented in Chapter 2.3, the optimum constant coefficient from equation 4.6 is k = 2.98, for the five blades wind turbine.

The system simulation sample time was set to 1 [ms]. A comparative analysis is presented next, based on simulation and experimental results obtained with the above described MPP controller.

The experiment interface was designed with Control Desk® dSPACE experiment software (Fig. 4.7). It provides access to simulation platforms, read parameters values from the simulation, displays acquisition signals, and the control parameters can be changed in real time.

Fig,4.7. Control Desk experiment interface.

The step response of the controller simulation (in green) and experimental results (in black), for wind speed steps variation between 7 and 5 [m/s] are presented in Fig. 4.8.
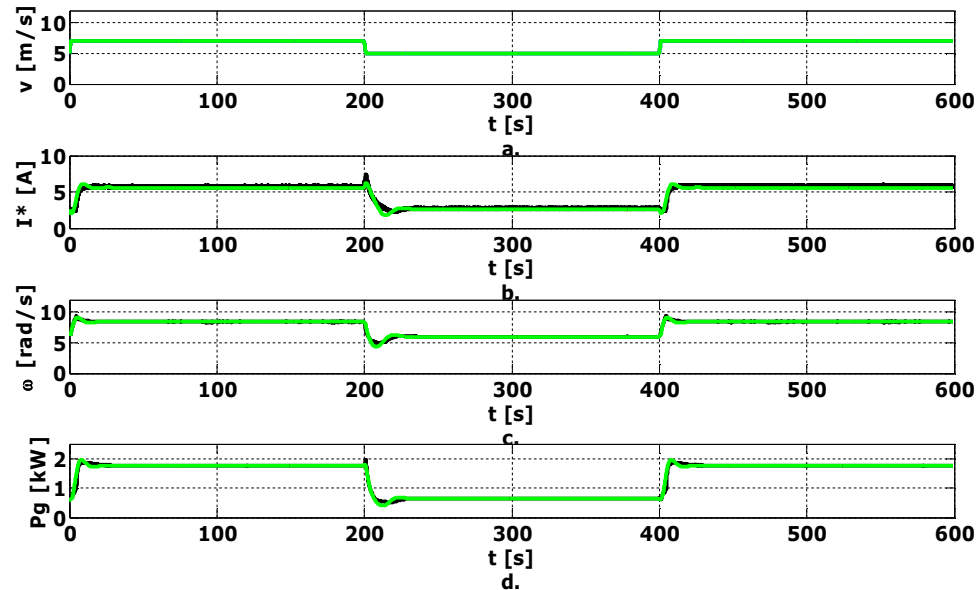
Fig.4.8. System response (simulations in green and experimental results in black) for wind speed steps of 7-5-7 [m/s]: a) Wind speed; b) Reference current; c) Rotating speed; d) PMSG mechanical power.

Fig.4.9 shows the power versus rotating speed response and illustrates how the control algorithm works.

The trajectories on the power curves are: in red the mechanical power (P_m), in green the simulated PMSG input mechanical power ($P_{gsimulation}$) and in black the experimentally obtained PMSG input mechanical power ($P_{gexperiment}$). Initially, for a wind speed step of 7 [m/s] the operation climbs the power curve until it reaches MPP, in an almost steady state regime. Experimentally, the start period is not showed on the graphic because the physical system needs a longer period of time for start and work in similar parameters as the simulation. When the wind velocity suddenly changes to 5 [m/s] the wind turbine power will jump on the lower power curve while the rotating speed cannot change instantaneously. Subsequently, the operation reaches the MPP on the 5 [m/s] wind speed curve. When the wind speed increases back to 7 [m/s] the P_g and the rotating speed increase until the system reaches again the MPP. It can be noticed that for some time intervals P_g is bigger or smaller than P_m due to the transients, when a part of energy is stored or released in/from the mechanical components.

Fig.4.10 illustrates the simulated step response of the MPP controller (in green) and experimental results (in black) for a real wind speed profile.

Good similarities can be observed between simulation and experiments, which validates the controller.
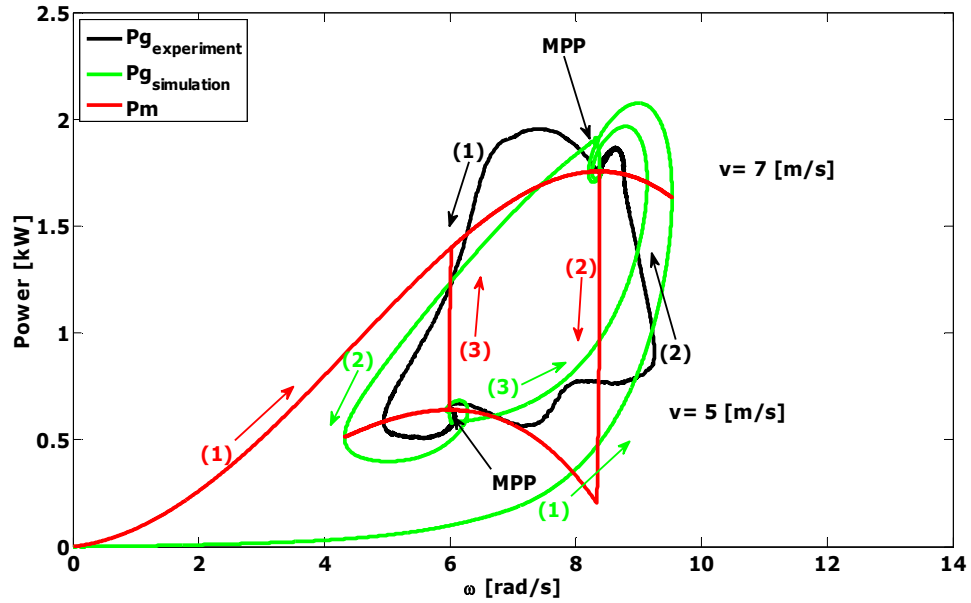
Fig.4.9. Steady-state turbine mechanical power (Pm), simulated and experimental PMSG mechanical power (P_g) versus rotating speed (ω), for wind speed steps of 7-5-7 [m/s].
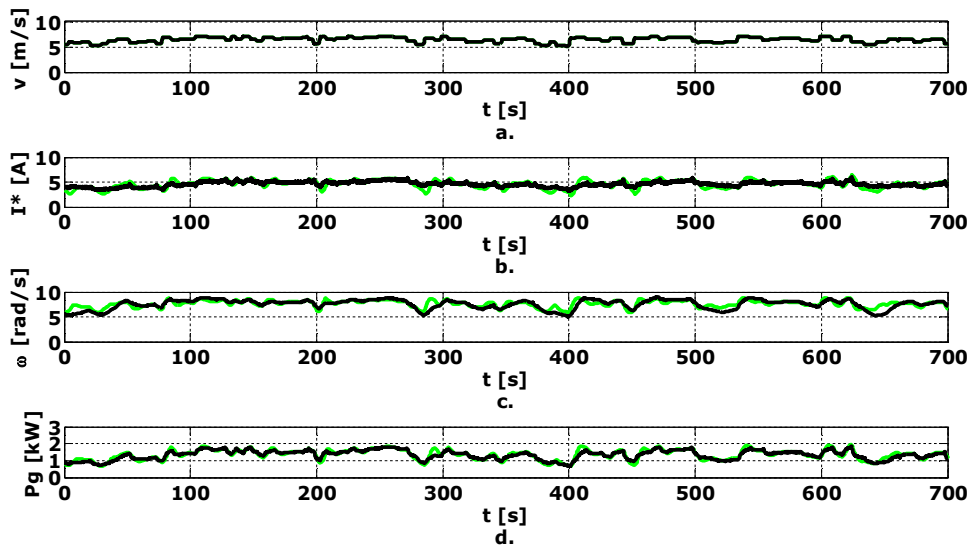
Fig.4.10. System response (simulations in green and experimental results in black) for a real wind speed profile: a) Wind speed; b) Reference current; c) Rotating speed; d) PMSG mechanical power.

4.2.4. Simulation and Experimental Results with the Three Blades Wind Turbine

Knowing the three blades wind turbine characteristics (Chapter 2.3), the optimum constant coefficient, from equation 4.6, is k=7.4.

In Fig.4.11 the step response of the MPP controller simulated (in green), and experimental results (in black) for wind speed steps variation between 7-6-7 [m/s] are presented.

Fig.4.12 shows the power versus rotating speed response and illustrates how the control algorithm works.

Fig.4.13 presents the step response of the MPP controller simulated (in green) and experimental results (in black) for a real wind speed profile.

Good similarities can be observed between simulation and experimental results, which validates again the controller.
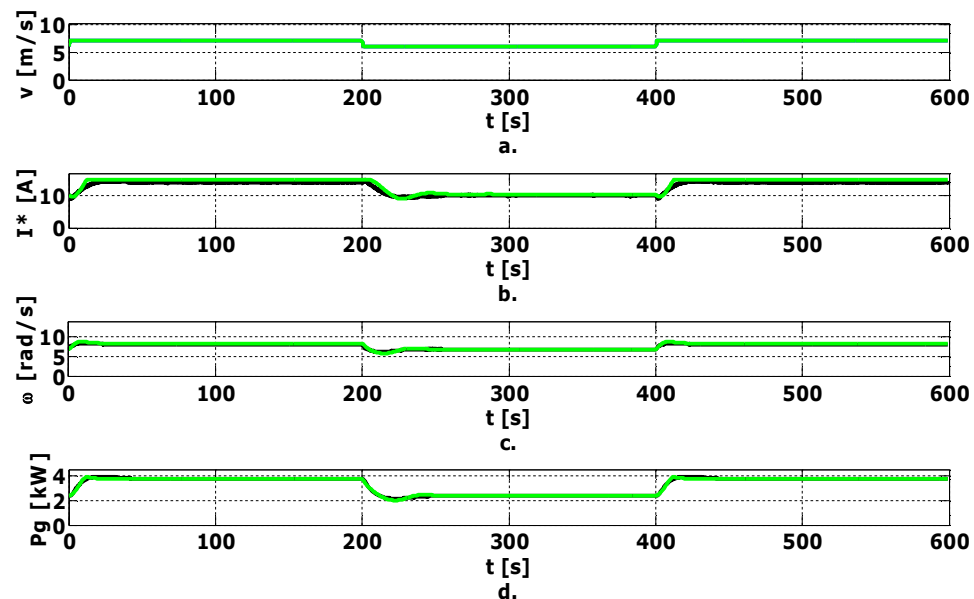
Fig.4.11. System response (simulations in green and experimental results in black) for wind speed steps of 7-6-7 [m/s]: a) Wind speed; b) Reference current; c) Rotating speed; d) PMSG mechanical power.
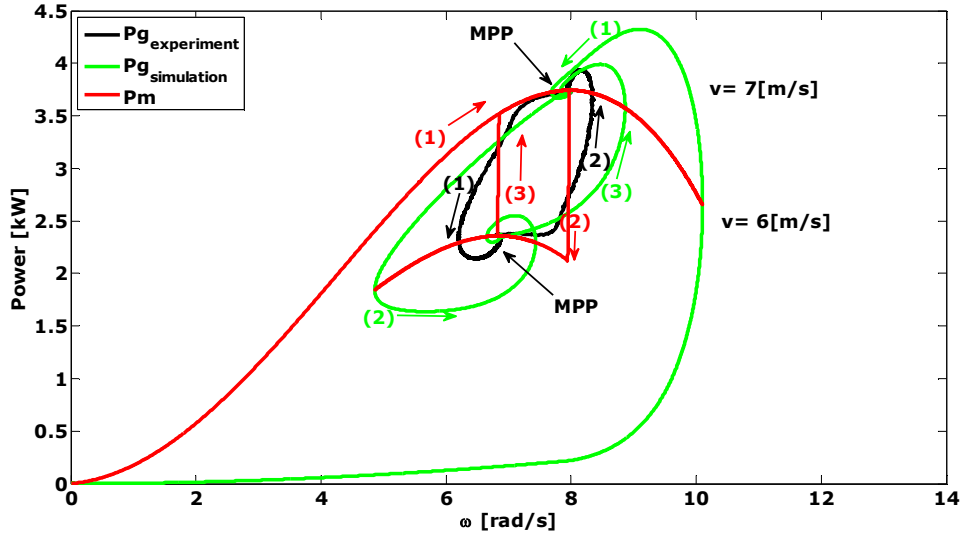
Fig.4.12. Steady-state turbine mechanical power (Pm), simulated and experimental PMSG mechanical power (P$_g$) versus rotating speed (ω), for wind speed steps of 7-6-7 [m/s].
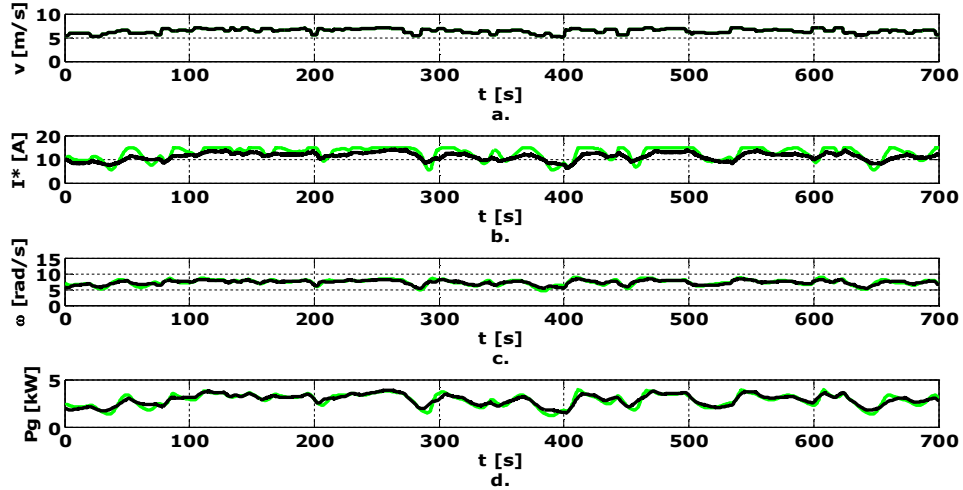
Fig.4.13. System response (simulations in green and experimental results in black) for a real wind speed profile: a) Wind speed; b) Reference current; c) Rotating speed; d) PMSG mechanical power.

Another MPP control method can be simply implemented, knowing the wind turbine characteristic C$_P$ (λ_{opt}) and using the speed estimator, described in Chapter 2.5. The maximum power can be expressed with equation 4.5 and the rotating

speed is depending on the rectified voltage and current (equation 2.23). In fig.4.14 was drawn the maximum electrical power versus the rectified voltage curve. Approximating this curve by two straight lines, the maximum power can be easily estimated especially in an industrial WECS for easy commissioning. The curve starts from 100 V, the point where SWECS can deliver power.
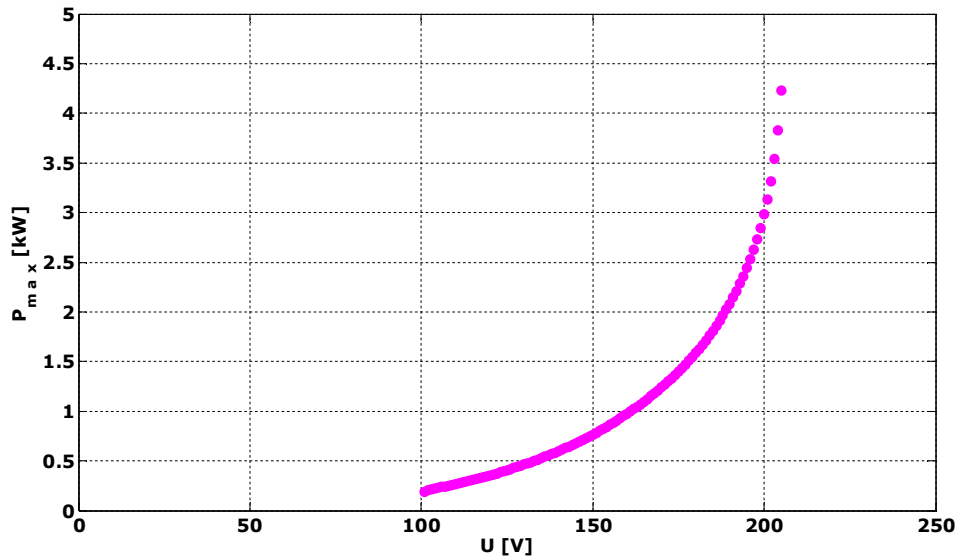
Fig.4.14. Maximum electrical power versus rectified voltage curve.

4.3. Fuzzy Logic Based MPPT Controller

In this section a fuzzy logic (FL) based MPPT controller (MPPT-FLC), designed in a simple and robust structure is proposed. The MPPT-FLC structure and working procedure are presented first. The theoretical aspects are validated with experimental results obtained with the proposed controller.

Digital simulations with MPPT-FLC and MPP (presented in Chapter 4.2) are compared in terms of robustness and energy conversion efficiency.

4.3.1. MPPT-FLC Description

The principle of the MPPT-FLC is to perturb the prescribed HDC current (I^*), which controls the PMSG output current through the DBR, in order to change the PMSG torque (T_g), and observe the corresponding change of mechanical power (ΔP_m) and the change of rotating speed ($\Delta \omega$).

MPPT-FLC extracts the maximum available power from the wind by increasing or decreasing the rectified PMSG current. Changing the PMSG current

changes the PMSG torque, which will modify the rotating speed according to the dynamic equation of motion (equation 2.24). In the steady state, if the turbine operates on the left side of the maximum power point (Fig.4.1), the controller has to decrease the reference current and, as a result, the rotating speed increases. In the same manner, when the operating point is on the right side of the maximum power point, the reference current needs to be increased.

The proposed MPPT-FLC schematic is shown in Fig.4.15. Its input variables are: rotating speed derivative ($\Delta\omega$), mechanical power derivative (ΔP_m) and the sign of $\Delta P_m/\Delta\omega$, which provides information on the power curve side, where the operating point is found. The output variable is the DC reference current derivative (ΔI^*).
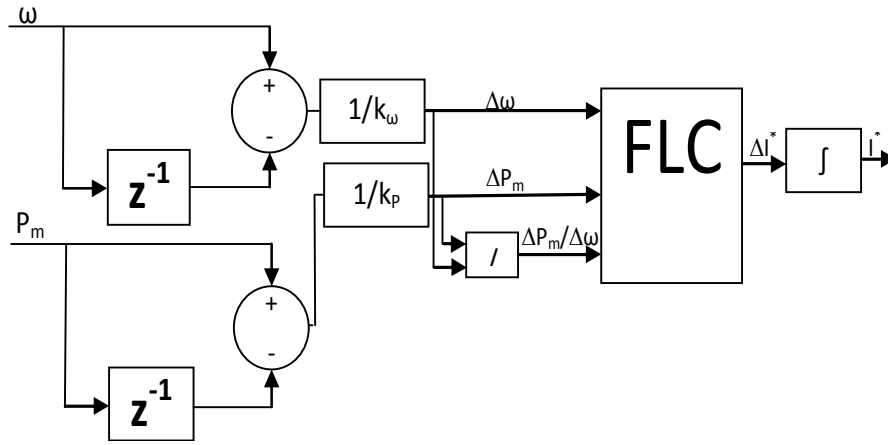
Fig.4.15. MPPT-FLC control system.

These input and output variables are normalized in the range of [-1 1], according to the system behavior in order that FLC block to be universal for all wind turbine characteristics. The scale coefficients used are k_w, k_P and the integrator gain is k_g. Thus:

$$\Delta\omega = \frac{1}{k_\omega} \cdot \left[\omega(t) - \omega(t-1)\right]$$ (4.10)

where t is the sampling instant;

$$\Delta P_m = \frac{1}{k_P} \cdot \left[P_m(t) - P_m(t-1)\right]$$ (4.11)

$$I^* = k_g \cdot \int \Delta I^*$$ (4.12)

The MPPT-FLC algorithm is characterized by "if then" rules as shown in Table 1. The fuzzy basic rules, which associate the fuzzy output to the fuzzy inputs, are

derived from the desired system behavior and the designed control strategy. The rules are designed so that the controller always seeks a MPP, without stopping.

Before the rules can be evaluated and after the input variables are transposed into the corresponding universe of discourse, they are fuzzified and converted into suitable linguistic values. The fuzzy values are: N (negative), NS (negative small), Z (zero), PS (positive small) and P (positive), characterized by membership grade. The triangular and trapezoidal membership functions of the FLC are used. The membership grade determines the degree to which the fuzzy inputs belong to each of the appropriate fuzzy set via membership function. The fuzzy degree of membership is always in the interval [0, 1].

After the inputs are fuzzified and the membership degree for each fuzzy input is established, the fuzzy operator AND is applied, which is a MIN (minimum) method. The fuzzy operator is applied if the antecedent of a given rule has more than one part, to obtain one number that represents the result of the antecedent on that rule. Evaluating rule 1 from Table 1, the antecedent has three parts: ΔP_m is N and $\Delta \omega$ is N and $\Delta P_m / \Delta \omega$ is P. The fuzzy AND operator, selects the minimum of the three membership values corresponding for each part. Thus, the fuzzy operation for rule 1 is complete.

Before applying the implication method (from the antecedent to the consequent) it must be determined the rules weight, which is a number between 0 and 1, applied to the number given by the antecedent. In this case all the weight rules are set to 1.

A consequent is a fuzzy set represented by a membership function. It is reshaped using a function associated with the antecedent, which is a single number. Thus, the input for the implication process is a single number and the output is a fuzzy set. The output fuzzy sets are identified using a fuzzy implication, MIN method, which truncates the output fuzzy set. Implication is implemented for each rule.

Aggregation is the process by which the fuzzy sets that represent the outputs of each rule are combined into a single fuzzy set. The input of the aggregation process is the list of truncated output functions returned by the implication process for each rule. The output of the aggregation process is one fuzzy set for each output variable. As long as the aggregation method is commutative, the order in which the rules are executed is unimportant. The MAX (maximum) aggregation method was used.

The input for the defuzzification process is a fuzzy set   (the   aggregate output fuzzy set) and the output is a single number. The center of gravity (or centroid) defuzzification method was implemented and returns the center of area under the curve. [28]

The fuzzy inference system created for MPPT-FLC, which includes the membership function, the logical operations and the "if-then" rules, is presented in Annex 3.

Table 4.1. MPPT-FLC Basic Rules

ΔI^{*} ($\Delta\omega$ \ ΔP_m)	N	NS	Z	PS	P
N	**N**	**N**	**N** / N	N	N
NS	**N**	**NS**	**N** / N	N	N
Z	**N** / N	**NS** / NS	**NS** / PS	**P** / N	N
PS	P	PS	**P** / PS	**P**	
P	P	P	**P** / PS	**P**	

Fuzzy values in bold are for $\Delta P_m/\Delta\omega > 0$ (P) and the other ones are for $\Delta P_m/\Delta\omega < 0$ (N)

4.3.2. Simulation and Experimental Results with the Five Blades Wind Turbine

The designed MPPT-FLC strategy was also tested with the "hardware in the loop" emulator, presented in Chapter 3. The used scale coefficients and the integrator gain k are:

- $k_w = 4$;
- $k_P = 2500$;
- $k_g = 2$.

First, some simulations were made using Matlab/Simulink and compared with experimental results.

The sample time of the system simulation was set to 1 [ms] and the sample time of the fuzzy logic controller was set to 100 [ms].

Fig.4.16 shows the simulation step response of the MPPT-FLC for a wind speed steps from 7 to 10 [m/s].

The controller power response (in blue) was compared with steady-state optimum points (in green) obtained with equation 4.5, knowing the wind turbine characteristics (Chapter 4.2 and [10]). The MPPT-FLC response shows that the controller can seek and track the maximum power value for every wind speed.

Fig.4.16. Simulation results for wind speed steps between 7-10-7 [m/s]: a) Wind speed; b) Reference current; c) Rotating speed; d) PMSG mechanical power.

Fig.4.17 shows the power versus rotating speed characteristics for a wind speed steps of 7–10–7 [m/s]. The trajectories on the power curves are: in red the mechanical power curve (P_m) and in blue the PMSG input mechanical power curve (P_g). Initially, for a wind speed step of 7 [m/s] the operation climbs the power curve until it reaches MPP, where the operation almost reaches the steady state regime. When the wind velocity suddenly changes to 10 [m/s] the wind turbine power will jump on the higher power curve while the rotating speed cannot change instantaneously. Subsequently, the operation reaches MPP on the 10 [m/s] wind speed curve. When the wind speed decreases back to 7 [m/s] the P_g decreases, and the rotating speed reaches again MPP. It can be noticed that for some instants P_g is bigger or smaller than P_m, due to the transients.
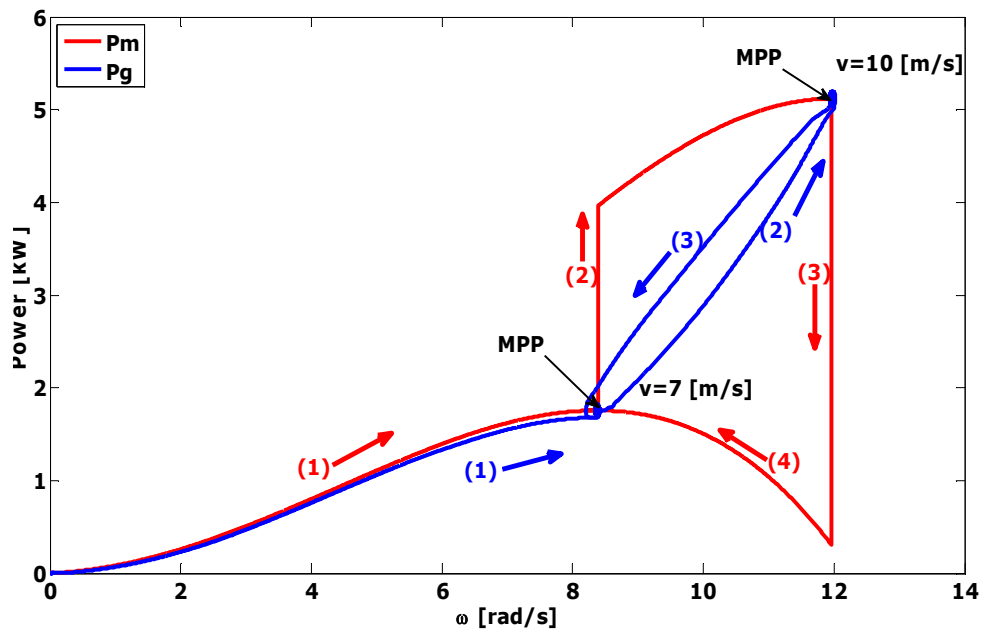
Fig.4.17. Mechanical power (P_m) and PMSG input mechanical power (P_g) versus rotating speed (ω) for wind speed steps of 7-10-7 [m/s] (simulation results).

For testing the controller immunity, the inertia was decreased and increased with 50% of the initial value. Fig.4.18 and fig 4.19 show the corresponding simulation results.

Fig.4.18. Mechanical power (P_m) and PMSG input mechanical power (P_g) versus rotating speed (ω) for wind speed steps of 7-10-7 [m/s], with J decreased with 50% of the initial value.

Fig.4.19. Mechanical power (P_m) and PMSG input mechanical power (P_g) versus rotating speed (ω) for wind speed steps of 7-10-7 [m/s], with J was increased with 50% of the initial value.

Fig.4.20 shows the power versus rotating speed curves obtained with MPPT-FLC for different values of the C_T for a wind speed of 10 [m/s]. The value of C_T was increased (C_{T1}) and decreased (C_{T2}) with 20% of the wind turbine rated C_T. The results prove that the proposed MPPT-FLC is robust with respect to the changes in wind turbine system parameters and air density.
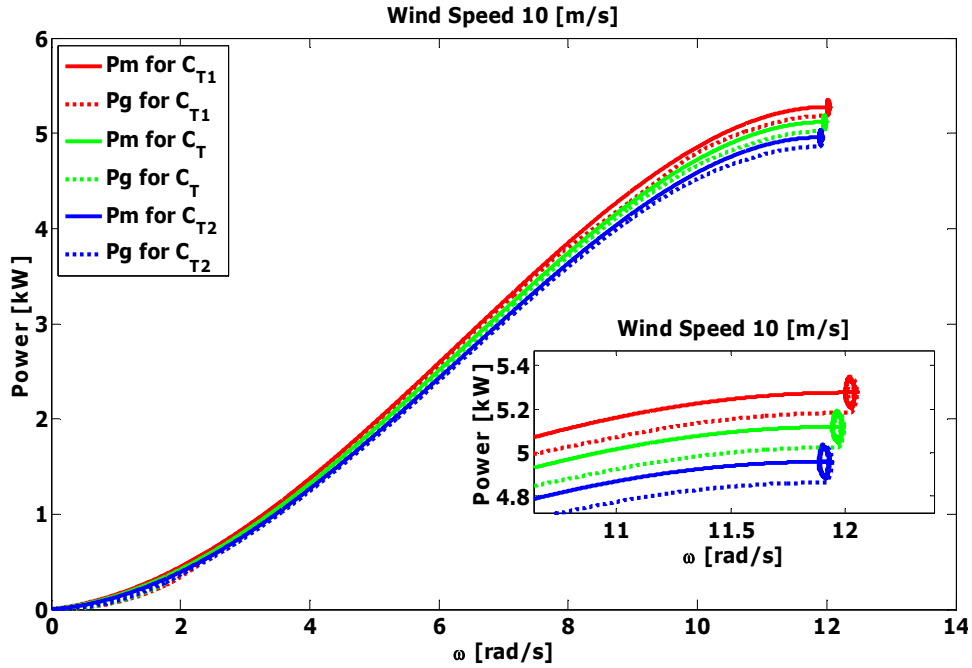
Fig.4.20. Mechanical power (P_m) and PMSG input mechanical power (P_g) versus rotating speed (ω) for different values of C_T at a wind speed of 10 [m/s].

In Fig.4.21 and 4.22 the simulation results (in blue) are compared with experiments (in magenta) for wind speed steps variation from 7-5-7 [m/s].

Fig.4.22 shows the power versus rotating speed characteristic for a wind speed step of 7-5-7 [m/s]: in red is the mechanical power (P_m), in blue the simulation PMSG input mechanical power ($P_{gsimulation}$), and in magenta the experimentally PMSG input mechanical power ($P_{gexperiment}$).

Fig.4.23 illustrates the step response of the MPPT-FLC simulation (in blue) and experimental results (in magenta) for a real wind speed profile.

Good similarities can be observed between simulation and experimental results, which validates the proposed MPPT- FLC.
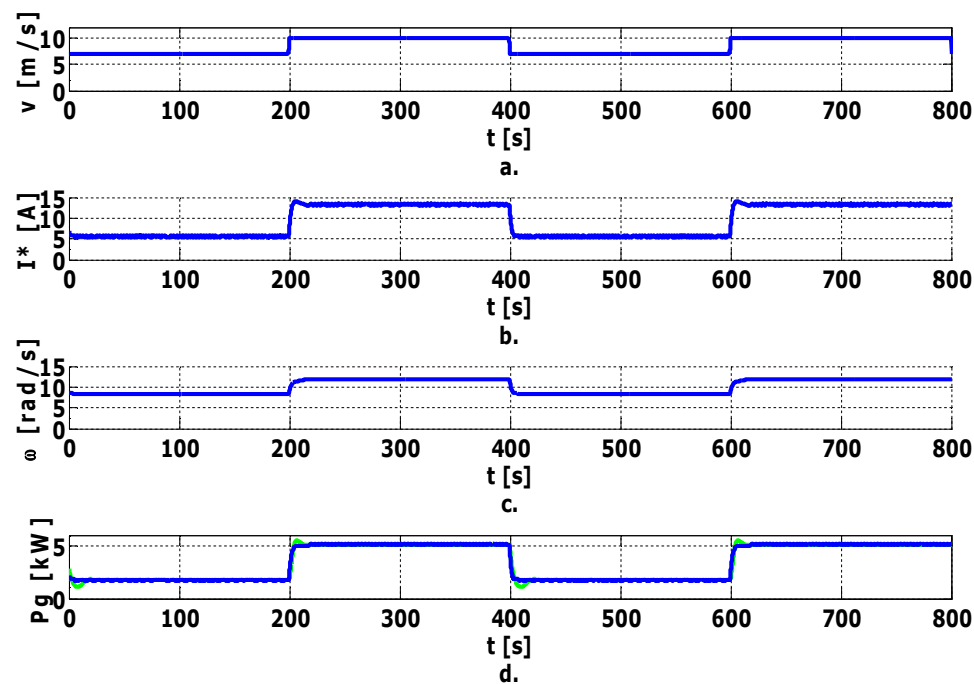
Fig.4.21. System response (simulation in blue and experimental results in magenta) for wind speed steps of 7-5-7 [m/s]: a) Wind speed; b) Reference current; c) Rotating speed; d) PMSG mechanical power.

Fig.4.22. Turbine mechanical power (Pm), simulated and experimental PMSG mechanical power (P$_g$) versus rotating speed (ω), for wind speed steps of 7-5-7 [m/s].

Fig.4.23. System response (simulation in blue and experimental results in magenta) for a real wind speed profile: a) Wind speed; b) Reference current; c) Rotating speed; d) PMSG mechanical power.

4.3.3. Simulation and Experimental Results with the Three Blades Wind Turbine

The parameters of the three blades wind turbine are specified in Chapter 2.3.

The used scale coefficients and the integrator gain k are:

- $k_w = 5$;
- $k_P = 3500$;
- $k_g = 2$.

The sample time of the wind turbine system simulation is set to 1 [ms] and the sample time of the MPPT-FLC is set to 100 [ms].

Fig.4.24 shows the simulation step response of the MPPT - FLC for wind speed steps variation between 5 and 7 [m/s].

The controller power response (in blue) was compared with steady-state optimum power points (in green) obtained with equation 4.6, knowing the wind turbine characteristics (Chapter 4.2 and [8]). The MPPT - FLC response shows that the controller can seek and track the MPP for every wind speed even the wind turbine was changed.
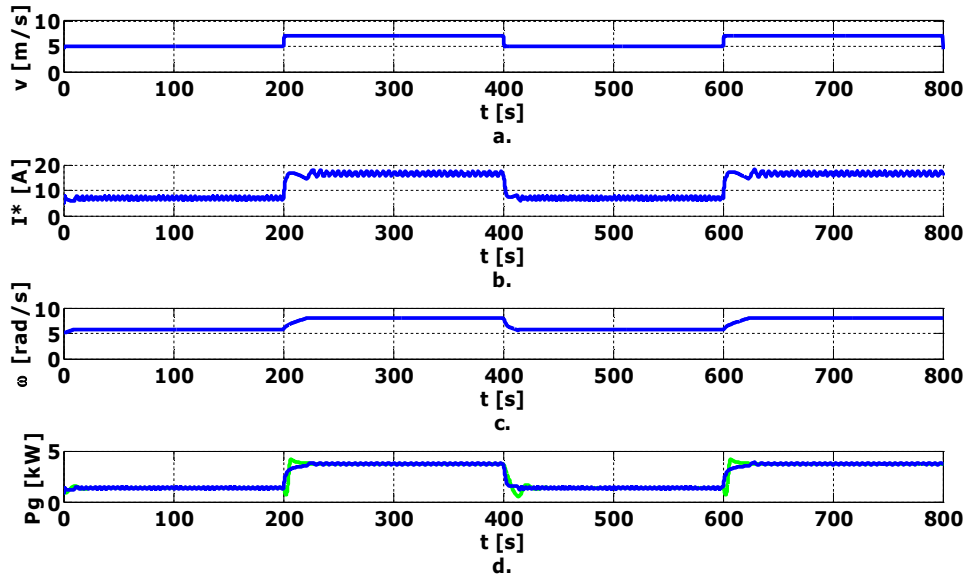
Fig.4.24. Simulation results for wind speed steps between 7-5-7 [m/s]: a) Wind speed; b) Reference current; c) Rotating speed; d) PMSG mechanical power.

Fig.4.25 shows the power versus rotating speed characteristics for a wind speed step of 5–7–5 [m/s]: in red is represented the mechanical power (P_m), and in blue the PMSG input mechanical power (P_g). The MPP is reached for every wind speed.
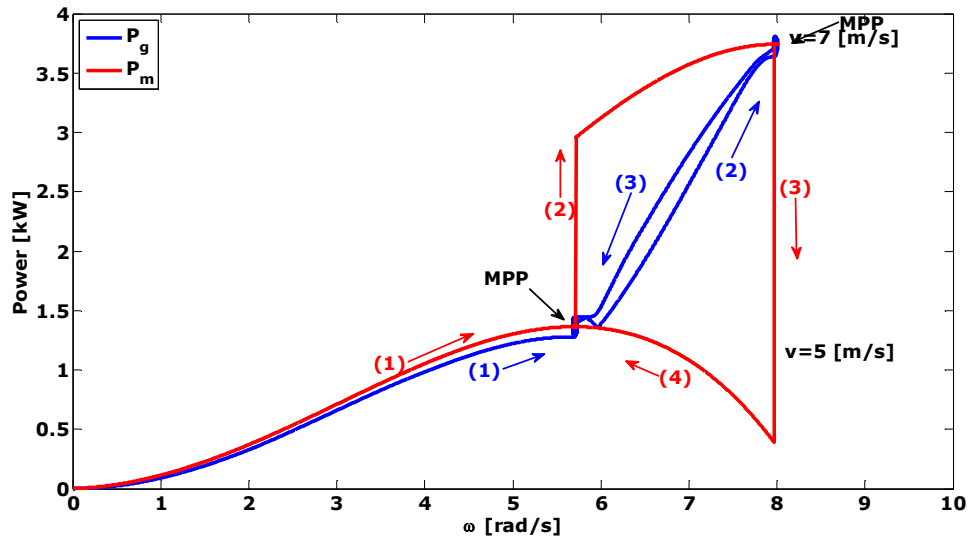
Fig.4.25. Mechanical power (P_m) and PMSG input mechanical power (P_g) versus rotating speed (ω) for wind speed steps of 5-7-5 [m/s] (simulation results).

For testing the controller immunity, the inertia was decreased and increased with 50% of the initial value. Fig.4.26 and Fig.4.27 show the corresponding simulation results for these cases.
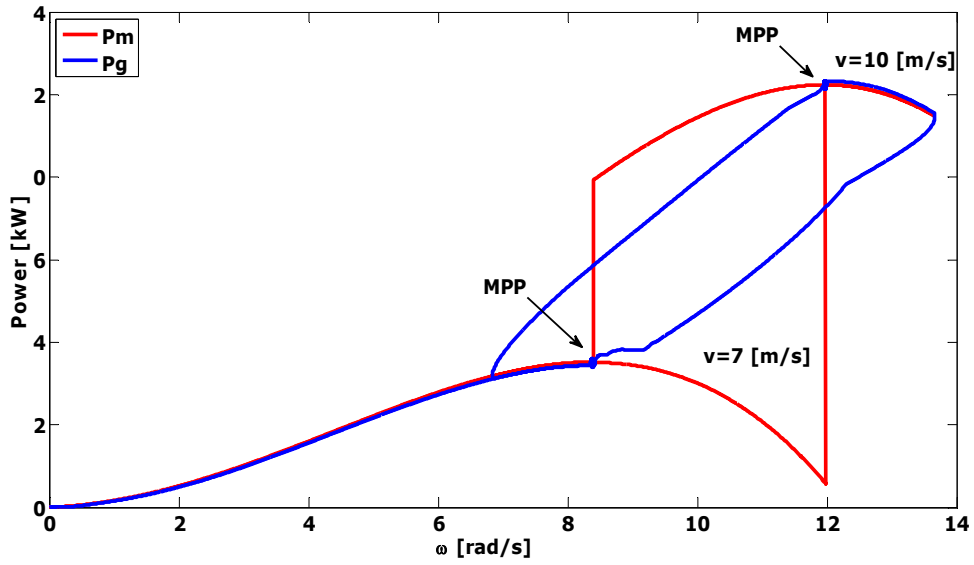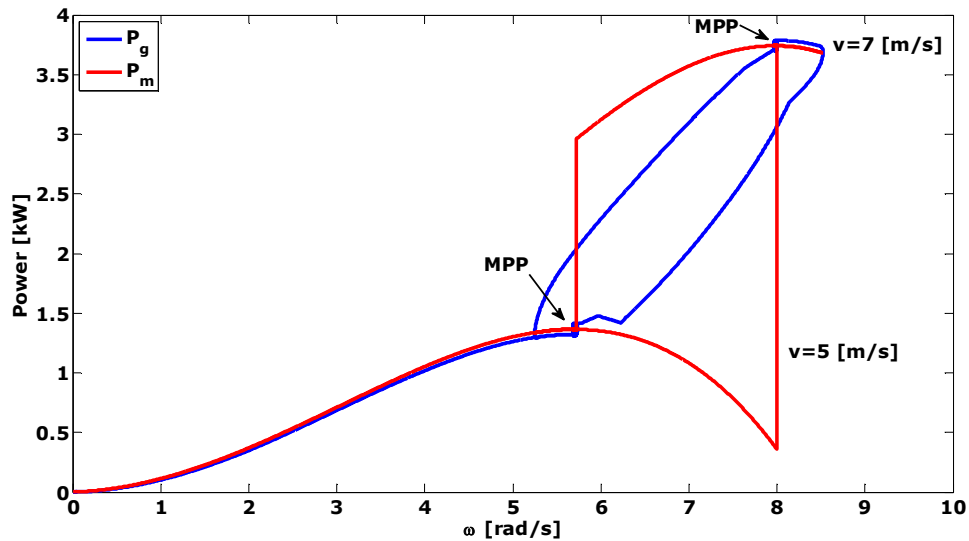

Fig.4.26. Mechanical power (P_m) and PMSG input mechanical power (P_g) versus rotating speed (ω) for wind speed steps of 5-7-5 [m/s], with J decreased with 50% of the initial inertia.
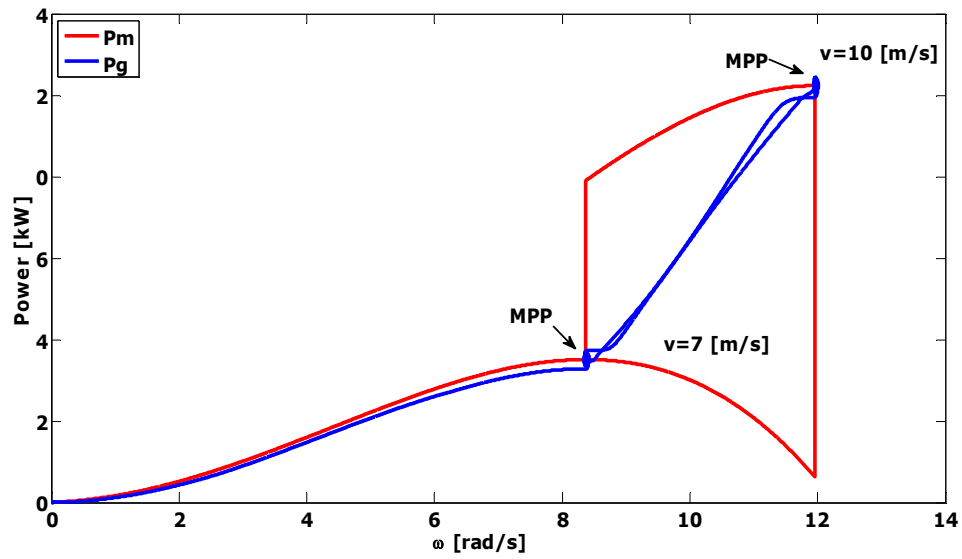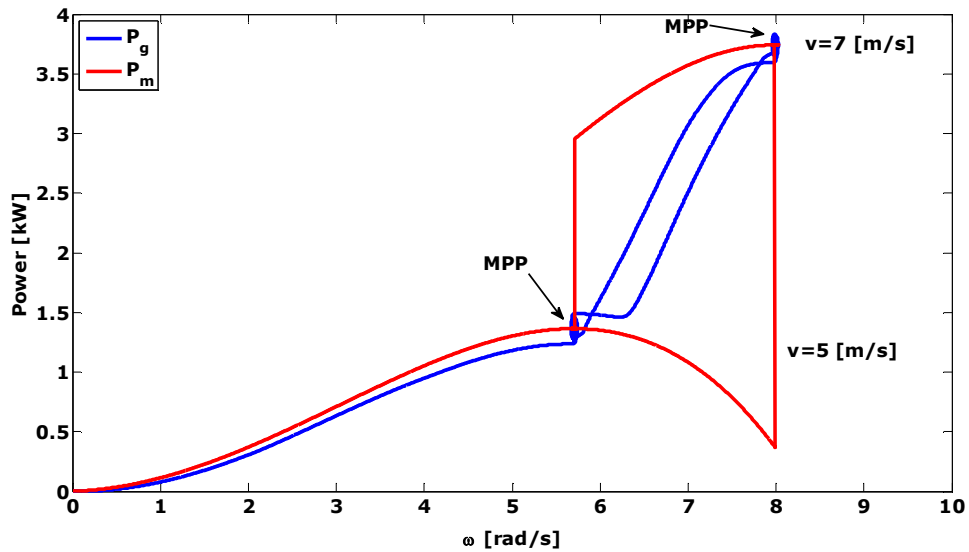

Fig.4.27. Mechanical power (P_m) and PMSG input mechanical power (P_g) versus rotating speed (ω) for wind speed steps of 5-7-5 [m/s], with J increased with 50% of the initial inertia.

Fig.4.28 shows the power versus rotating speed curves obtained with MPPT-FLC for different values of the C_T for a wind speed of 5 [m/s]. The value of C_T was increased (C_{T1}) and decreased (C_{T2}) with 20% of the wind turbine specific C_T. The results prove that the fuzzy logic based control strategy is robust with respect to changes in wind turbine system parameters and air density.
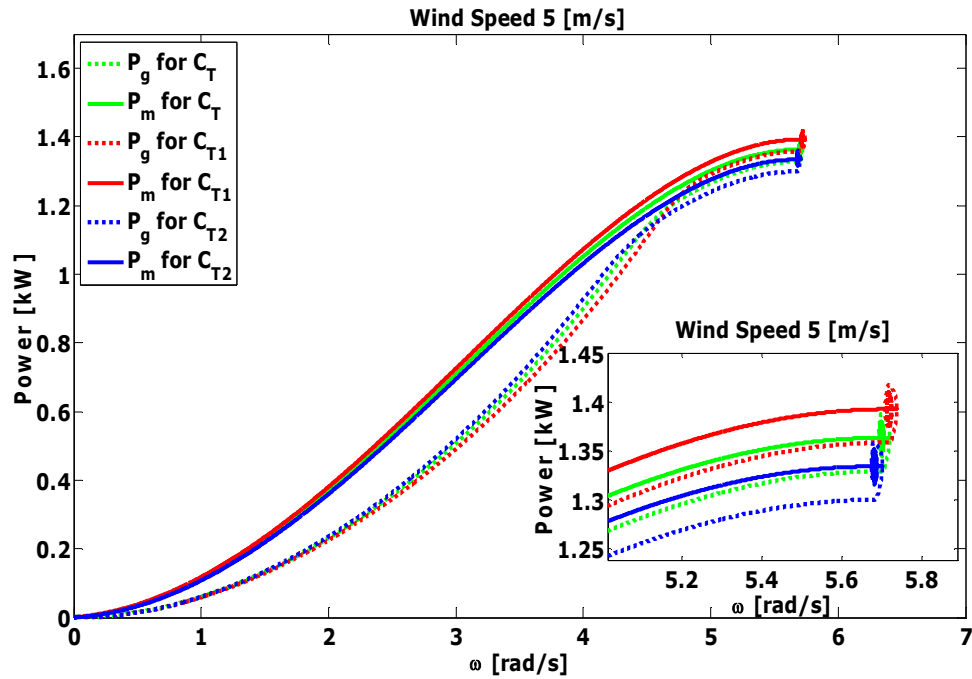
Fig.4.28. Mechanical power (P_m) and PMSG input mechanical power (P_g) versus rotating speed (ω) for different values of C_T for at a wind speed of 5 [m/s].

In Fig.4.28 and Fig.4.29 the simulation results are compared with experiments for wind speed steps variation from 7 to 5 [m/s].

Fig.4.30 illustrates the step response of the MPPT-FLC simulation (in green) and experimental results (in black) for a real wind speed profile.

Good similarities can be observed between simulation and experimental results, which validates the proposed MPPT-FLC.
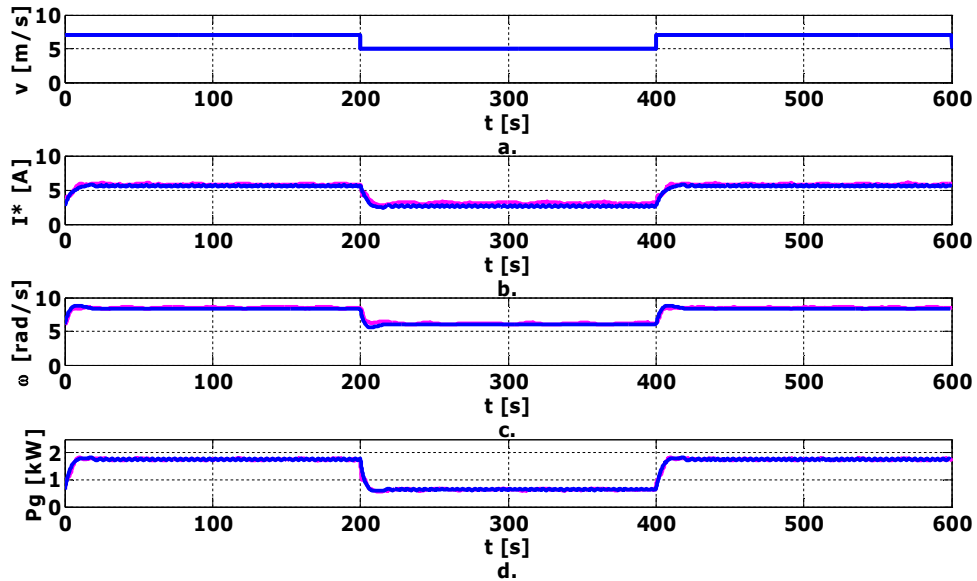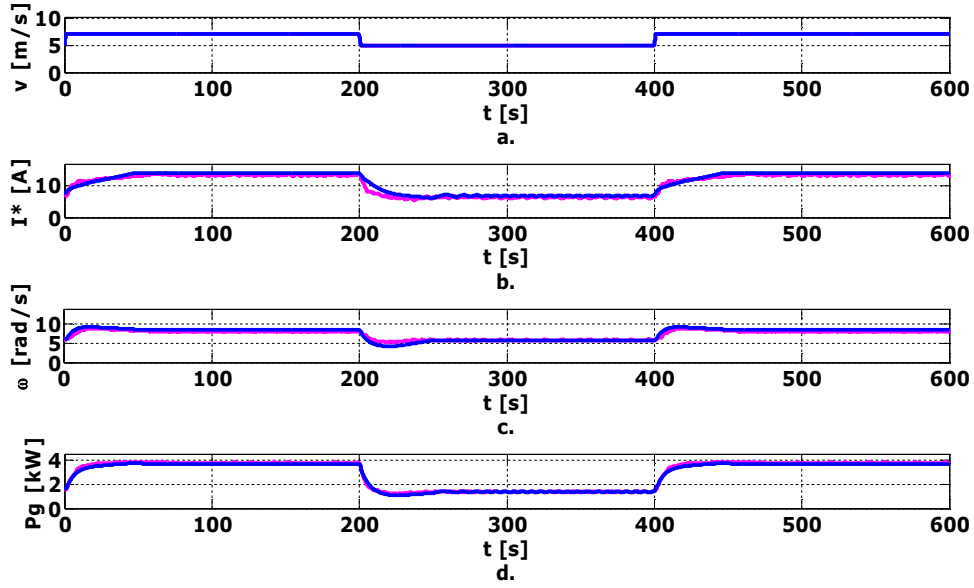
Fig.4.29. Simulation and experimental results for wind speed steps between 7-5-7 [m/s]: a) Wind speed; b) Reference current; c) Rotating speed; d) PMSG mechanical power.
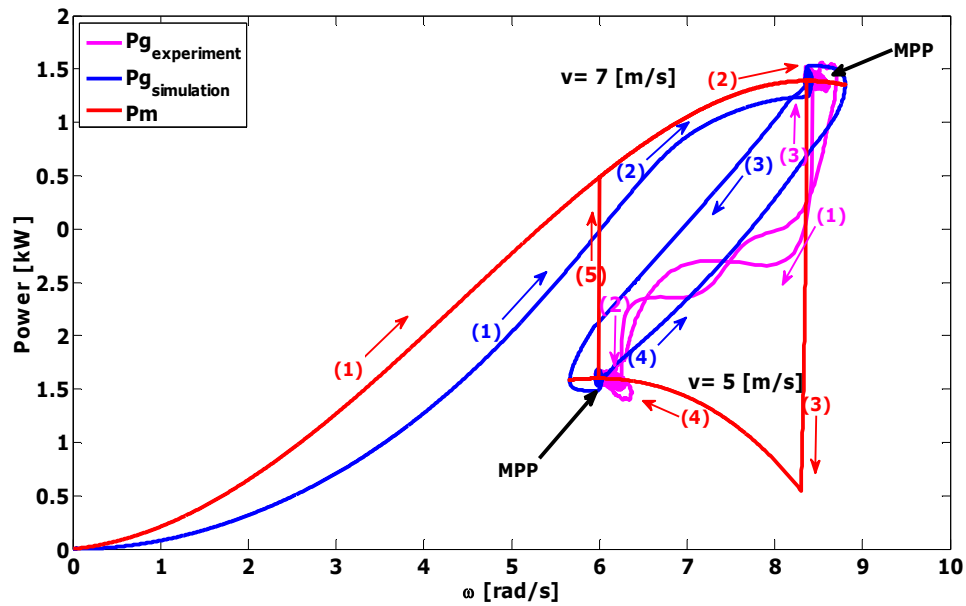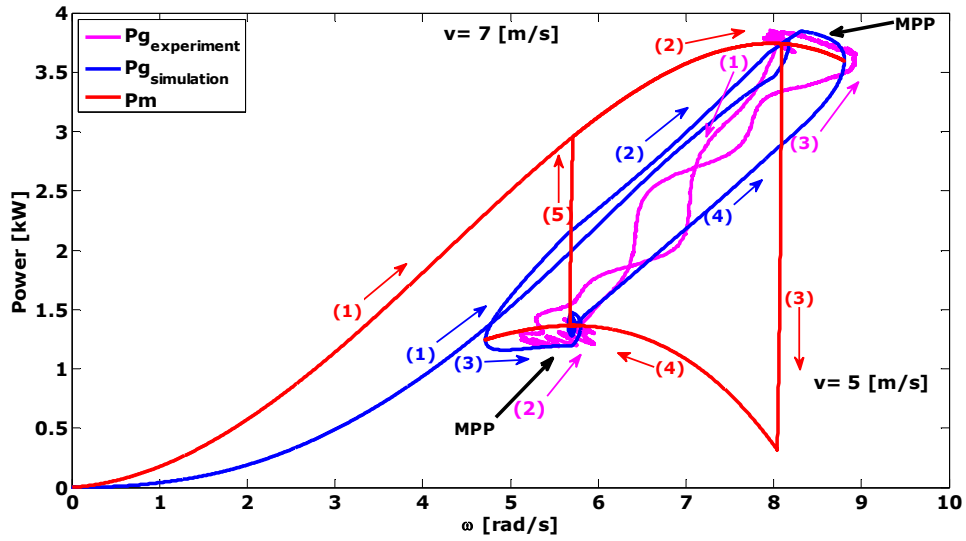

Fig.4.30. Mechanical power (Pm), simulated and experimental PMSG mechanical power (P_g) versus rotating speed (ω) for wind speed steps of 7-5-7 [m/s].
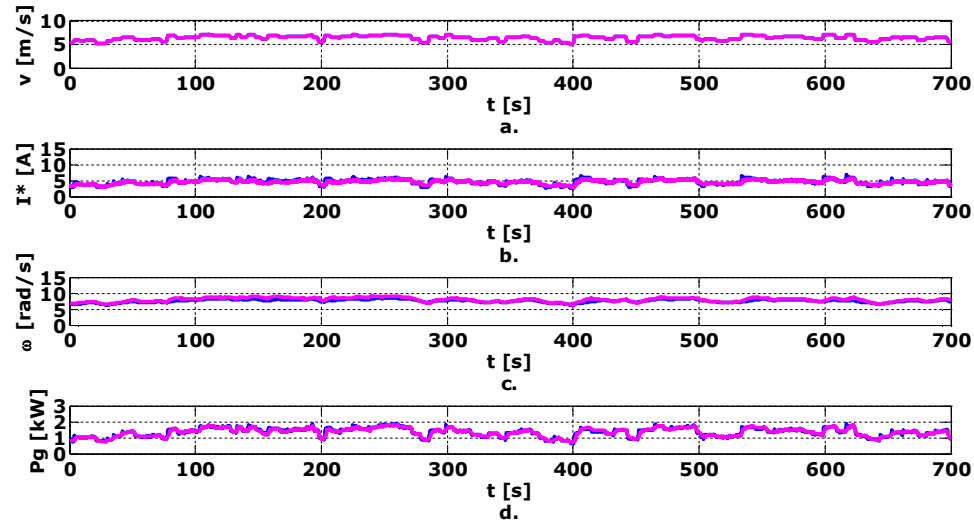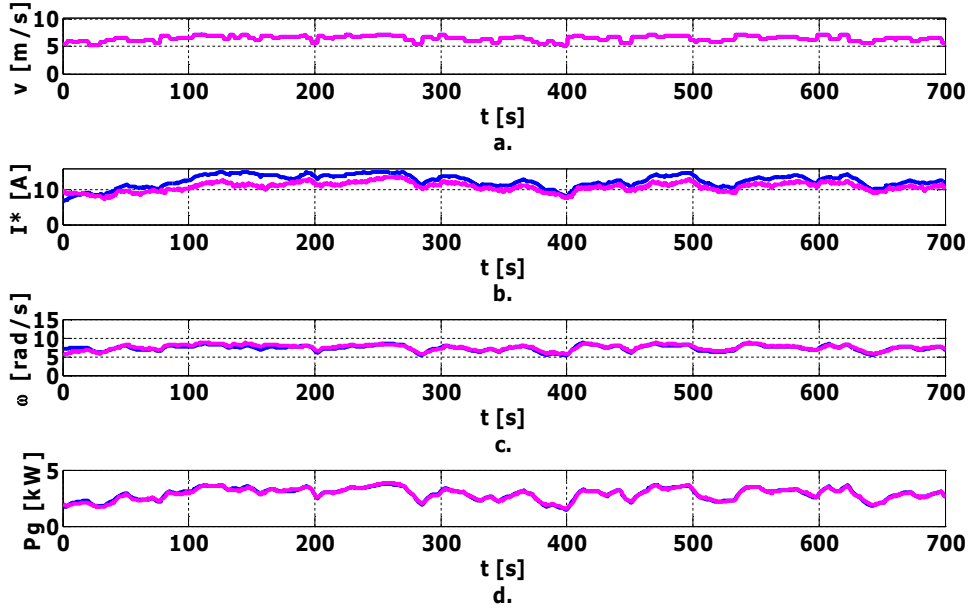
Fig.4.31. Simulation and experimental results for a real wind speed profile: a) Wind speed; b) Reference current; c) Rotating speed; d) PMSG mechanical power.

4.4. Comparative Evaluation of the MPP and MPPT-FLC Controllers

The control efficiency was analyzed comparing the WECS energies extracted from the wind for the same wind profile, using the presented control strategies.

In order to have a reference for this comparison, a global efficiency (η) of the conversion system, is introduced:

$$\eta = \frac{W_{control}}{Ww} \tag{4.13}$$

where $W_{control}$ is the electrical energy obtained with the presented controllers and W_w is a theoretical (maximum) obtainable mechanical energy from the turbine, considering the instantaneous achievement of the optimal rotating speed value (the maximum power point).

Fig. 4.32 shows a comparison of the electrical energy produced by the five blades wind turbine, using the two controllers for a step wind speeds between 7-6 [m/s]. In green is the electrical energy obtained using MPP controller (W_{MPP}) , in blue is the electrical energy obtained using MPPT-FLC ($W_{MPPT-FLC}$) and in red is W_W .

From Fig. 4.32 and equation 4.13, η≈0.82, closed to the electrical components (PMSG, DBR and HDC) efficiency, which proves that the two controllers can extract the maximum energy available from the wind.

For better interpretation, Fig. 4.33 shows the electrical energy difference ΔW:

$$\Delta W = W_{MPPT - FLC} - W_{MPP} \qquad (4.11)$$

It can be observed that the energies difference is slightly negative, but decreases in time.

Figs 4.34-4.42 show the simulation results with five blades wind turbine for a real wind speed profile.

Fig. 4.34 shows the system response and figs. 4.35, 4.36, show W_{MPP}, $W_{MPPT-FLC}$, W_W and ΔW.

From Fig. 4.35 and equation 4.13, $\eta \approx 0.8$, close again to the conversion efficiency.

Figs. 4.37 - 4.42, show W_{MPP}, $W_{MPPT-FLC}$, ΔW with modified wind turbine parameters and air density. First, Ct was decreased and increased with 20% of the initial value. Then the air density was increased. In all cases the MPPT–FLC extracted a higher energy than the MPP controller.

Fig. 4.43 shows a comparison between W_{MPP}, $W_{MPPT-FLC}$, W_W and Fig. 4.44 shows ΔW, for step wind speeds between 7-6 [m/s] with the three blades wind turbine.

From Fig. 4.43 and equation 4.13, $\eta \approx 0.81$, again close to the conversion efficiency.

It can be observed that in this case the ΔW is slightly negative, but decreases in time.

Figs. 4.45 - 4.53 show the simulation results with the three blades wind turbine for a real wind speed profile.

Fig. 4.45 shows the system response and Figs. 4.46, 4.47 show W_{MPP}, $W_{MPPT-FLC}$, W_W and ΔW. $\eta \approx 0.77$, smaller than the previous cases values.

Figs. 4.48 - 4.53 show the energies and ΔW when the wind turbine parameters and air density are modified. First Ct was decreased and increased with 20% of the initial value. Then the air density was increased. In all cases MPPT–FLC extracted a higher energy than the MPP controller.

It can be concluded that MPPT–FLC has higher efficiency and immunity to the wind turbine parameters or air density changes.
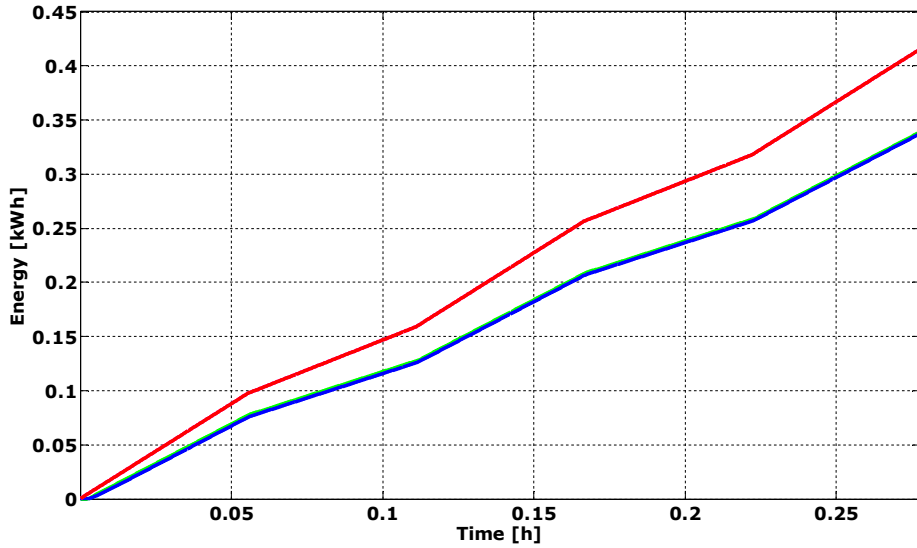
Fig.4.32. Energy simulation results (in red the maximum mechanical obtainable energy, in green with the MPP controller and in blue with the MPPT–FLC) for wind speed steps between 7-6 [m/s] with the five blades wind turbine.
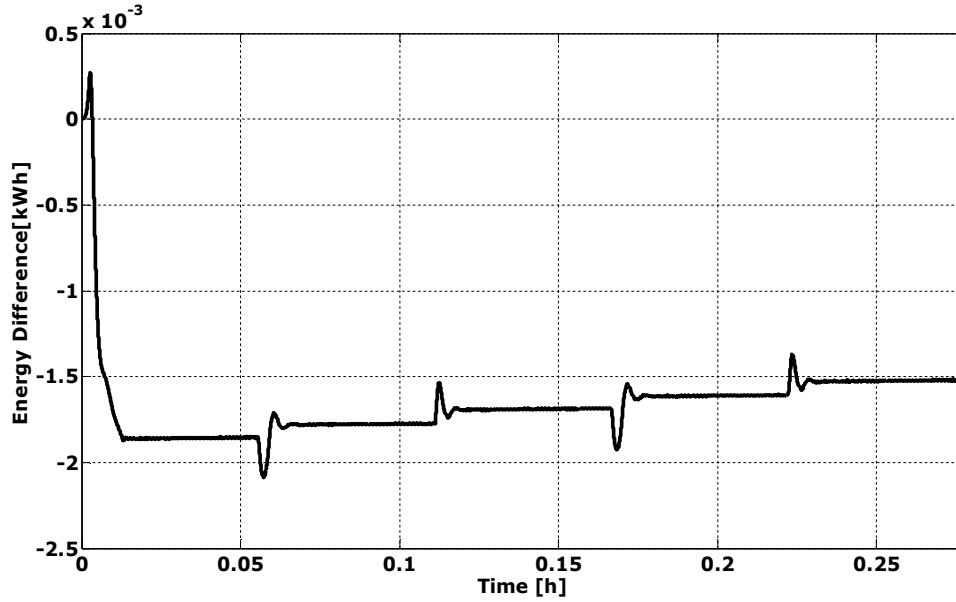
Fig.4.33. Energy difference simulation results for wind speed steps between 7-6 [m/s] with the five blades wind turbine.
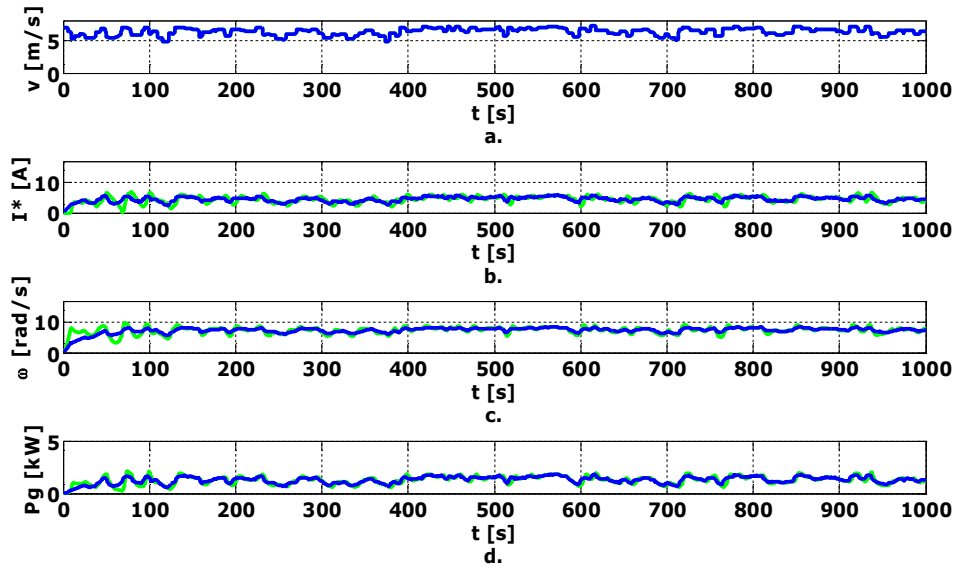
Fig.4.34. Simulation results (in green with the MPP controller and in blue with the MPPT–FLC) for a real wind speed profile with the five blades wind turbine: a) Wind speed; b) Reference current; c) Rotating speed; d) PMSG mechanical power.
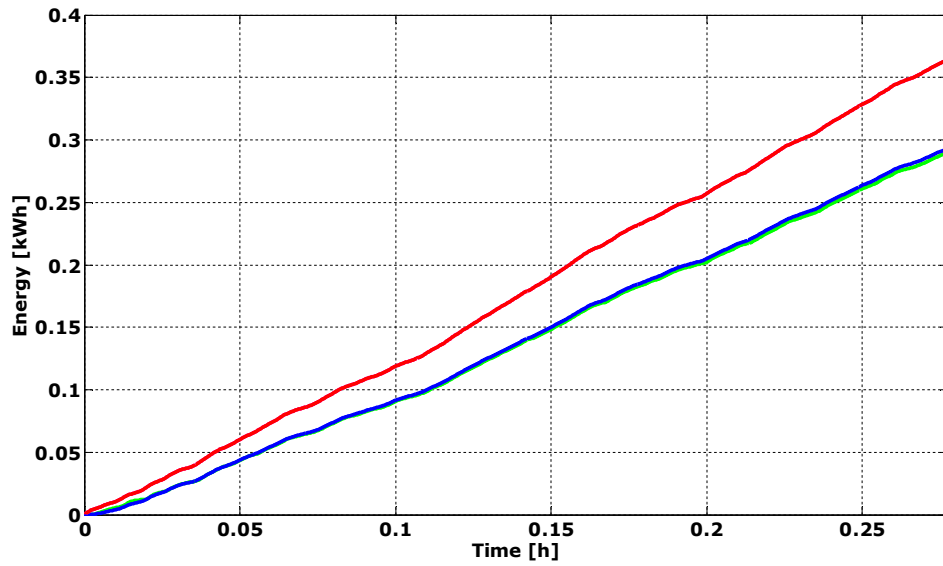
Fig.4.35. Energy simulation results (in red the maximum mechanical obtainable energy, in green with the MPP controller and in blue with the MPPT–FLC) for a real wind speed profile with the five blades wind turbine.

Fig.4.36. Energy difference simulation results for real wind speed profile with the five blades wind turbine.

Fig.4.37. Energy simulation results (in green with the MPP controller and in blue with the MPPT–FLC) for a real wind speed profile with the five blades wind turbine and Ct decreased with 20%.

Fig.4.38. Energy difference simulation results for real wind speed profile with the five blades wind turbine and Ct decreased with 20%.

Fig.4.39. Energy simulation results (in green with the MPP controller and in blue with the MPPT–FLC) for a real wind speed profile with the five blades wind turbine and Ct increased with 20%.

Fig.4.40. Energy difference simulation results for real wind speed profile with the five blades wind turbine and Ct increased with 20%.

Fig.4.41. Energy simulation results (in green with the MPP controller and in blue with the MPPT–FLC) for a real wind speed profile with the five blades wind turbine and ρ=1.3413.

Fig.4.42. Energy difference simulation results for real wind speed profile with the five blades wind turbine and ρ=1.3413.
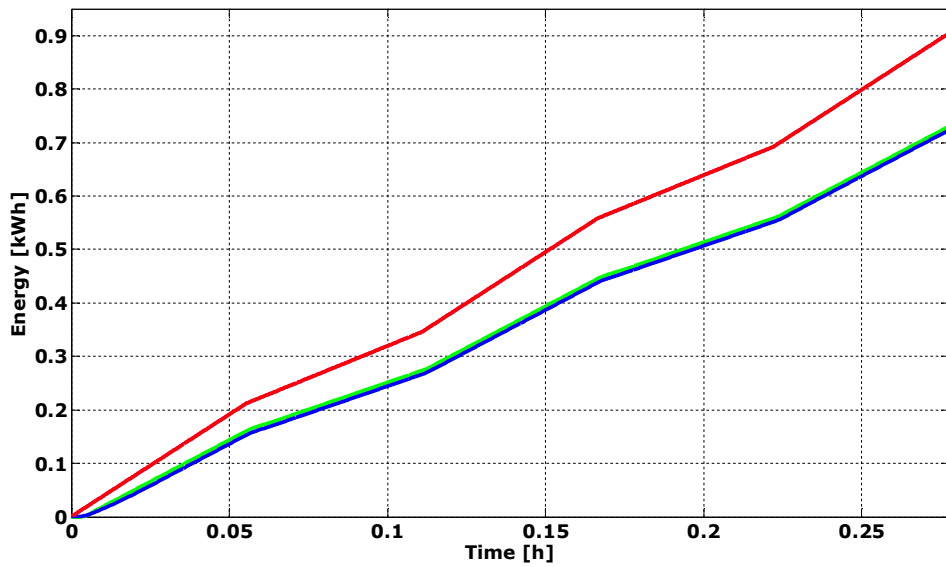
Fig.4.43. Energy simulation results (in red the maximum mechanical obtainable energy, in green with the MPP controller and in blue with the MPPT–FLC) for wind speed steps between 7-6-7 [m/s] with the three blades wind turbine.
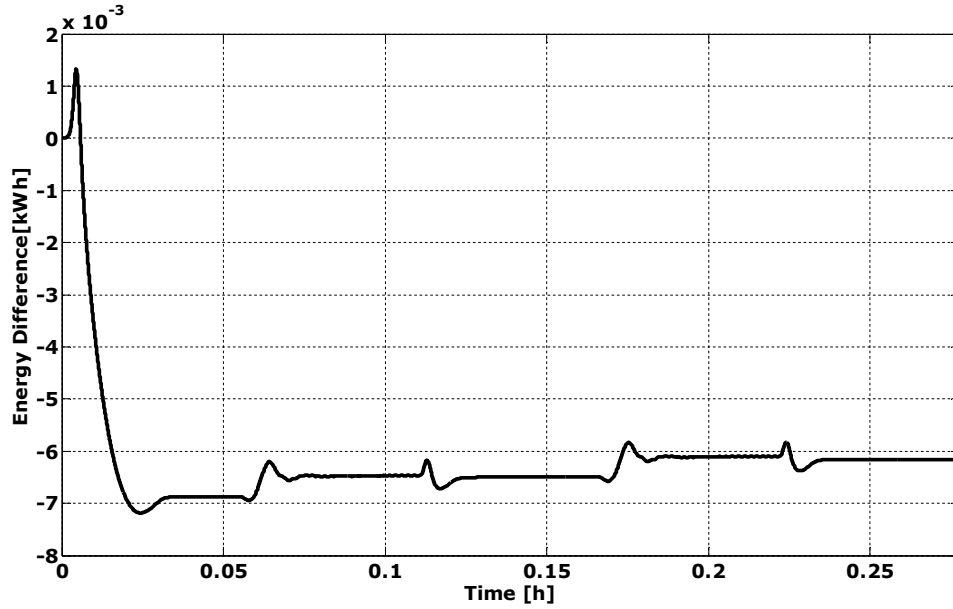
Fig.4.44. Energy difference simulation results for wind speed steps between 7-6-7 [m/s] with the three blades wind turbine.
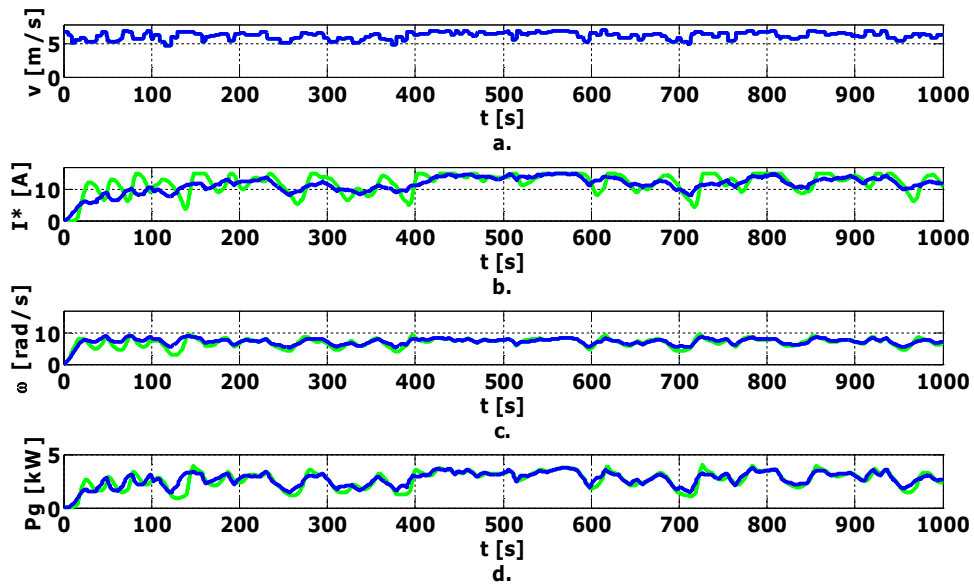
Fig.4.45. Simulation results (in green with the MPP controller and in blue with the MPPT–FLC) for a real wind speed profile with the three blades wind turbine: a) Wind speed; b) Reference current; c) Rotating speed; d) PMSG mechanical power.
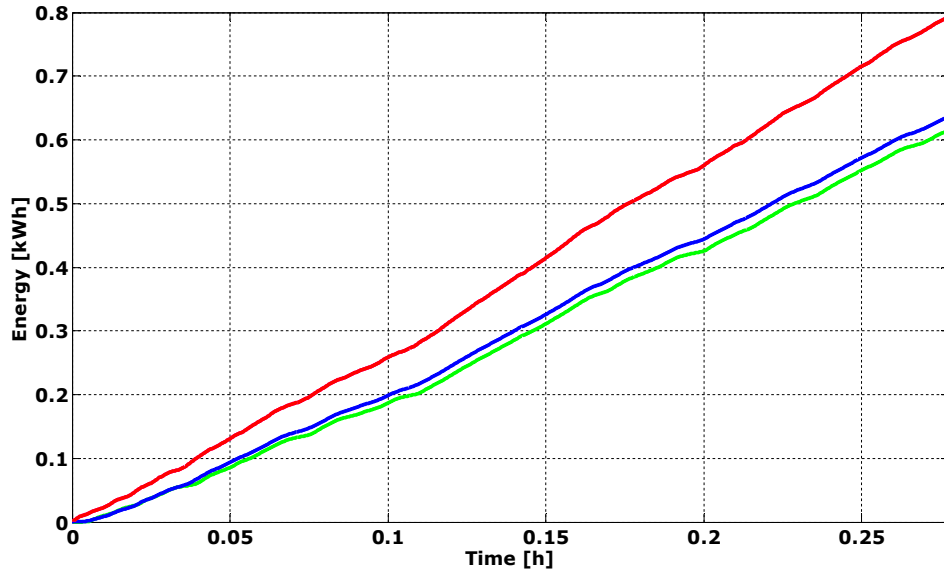
Fig.4.46. Energy simulation results (in red the maximum mechanical obtainable energy, in green with the MPP controller and in blue with the MPPT–FLC) for a real wind speed profile with the three blades wind turbine.
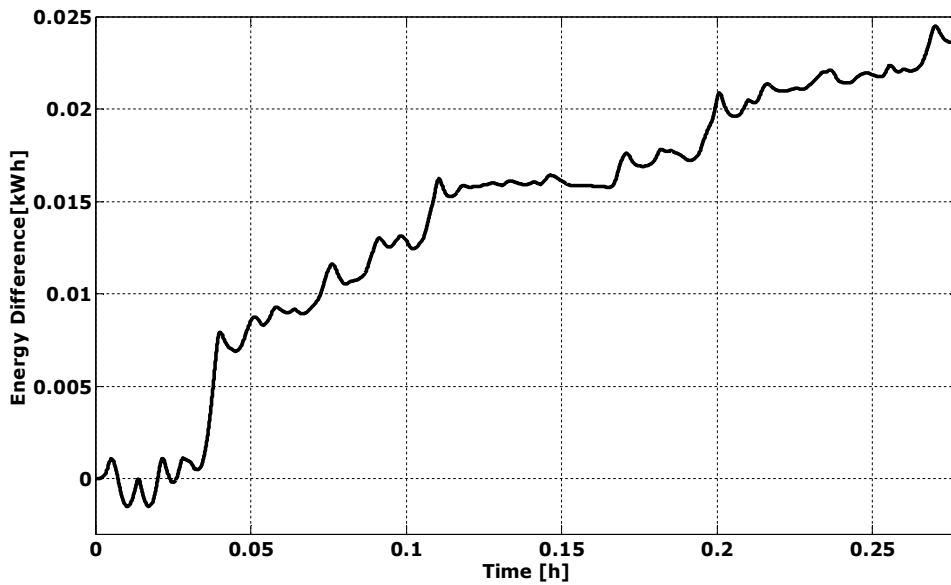
Fig.4.47. Energy difference simulation results for real wind speed profile with the three blades wind turbine.
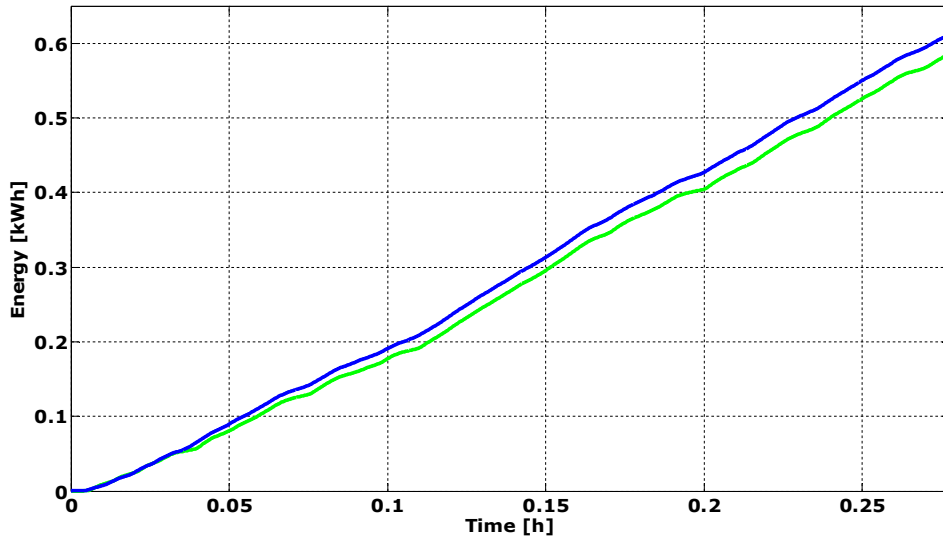
Fig.4.48. Energy simulation results (in green with the MPP controller and in blue with the MPPT–FLC) for a real wind speed profile with the three blades wind turbine and Ct decreased with 20%.
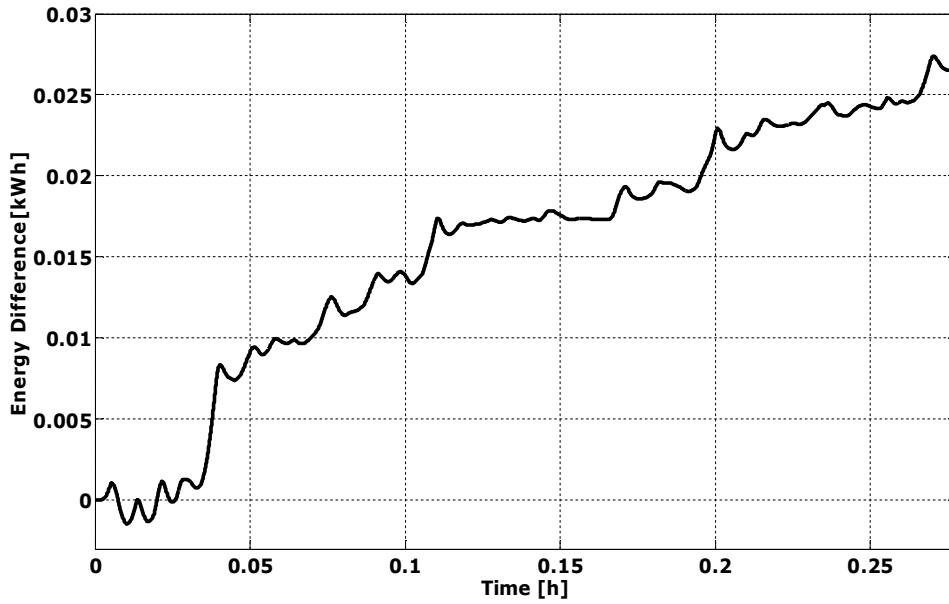
Fig.4.49. Energy difference simulation results for real wind speed profile with the three blades wind turbine and Ct decreased with 20%.
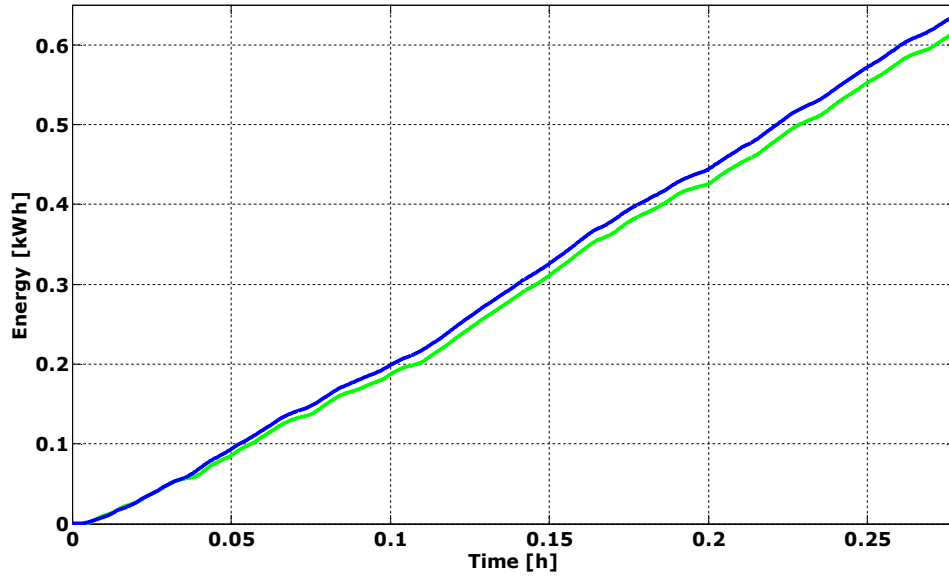
Fig.4.50. Energy simulation results (in green with the MPP controller and in blue with the MPPT–FLC) for a real wind speed profile with the three blades wind turbine and Ct increased with 20%.
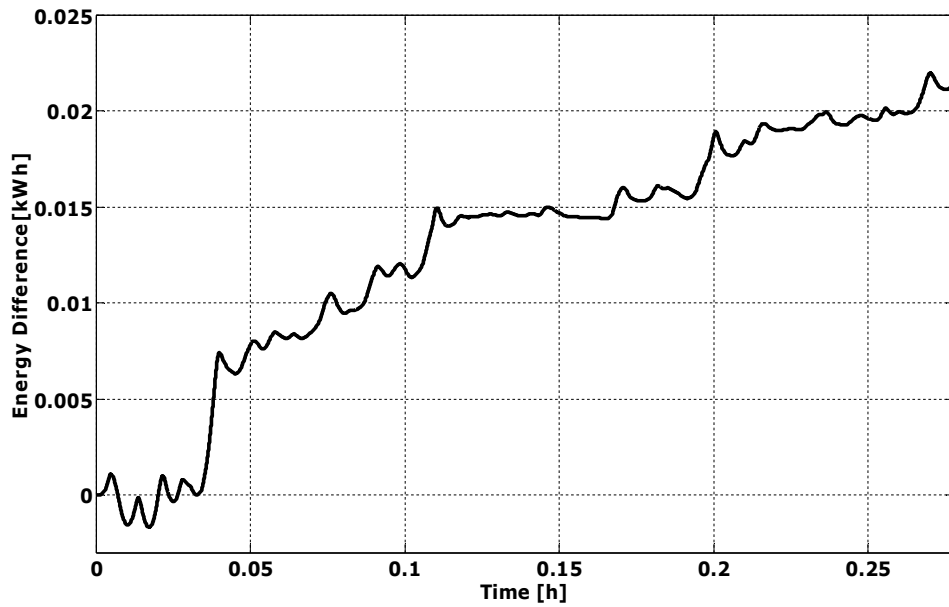
Fig.4.51. Energy difference simulation results for real wind speed profile with the three blades wind turbine and Ct increased with 20%.
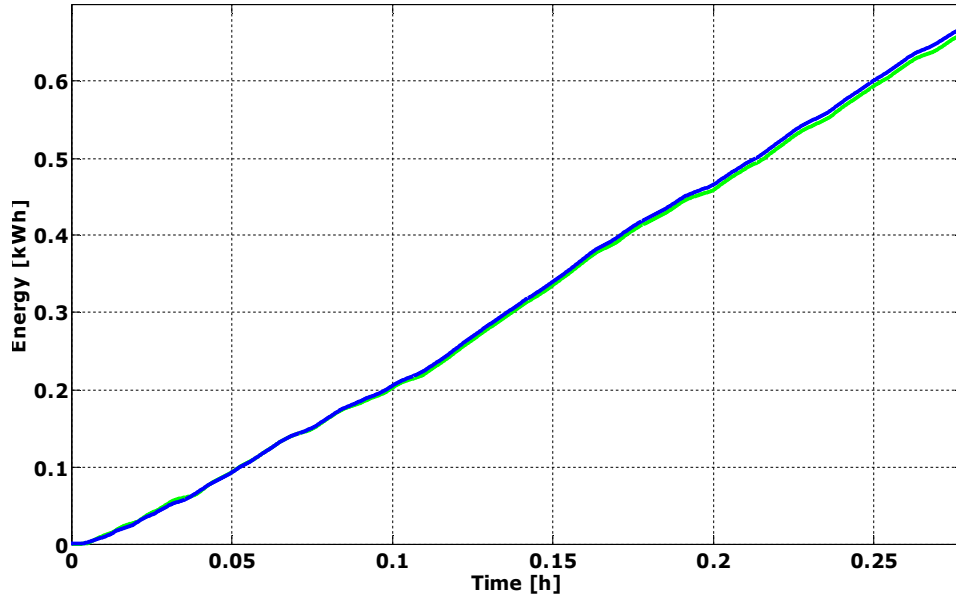
Fig.4.52. Energy simulation results (in green with the MPP controller and in blue with the MPPT–FLC) for a real wind speed profile with the three blades wind turbine and ρ=1.3413.

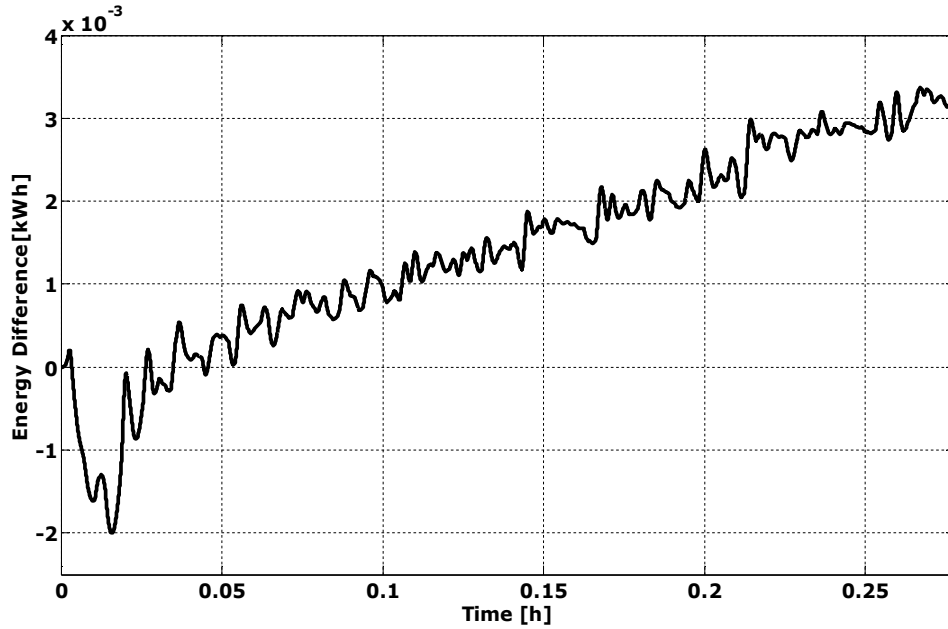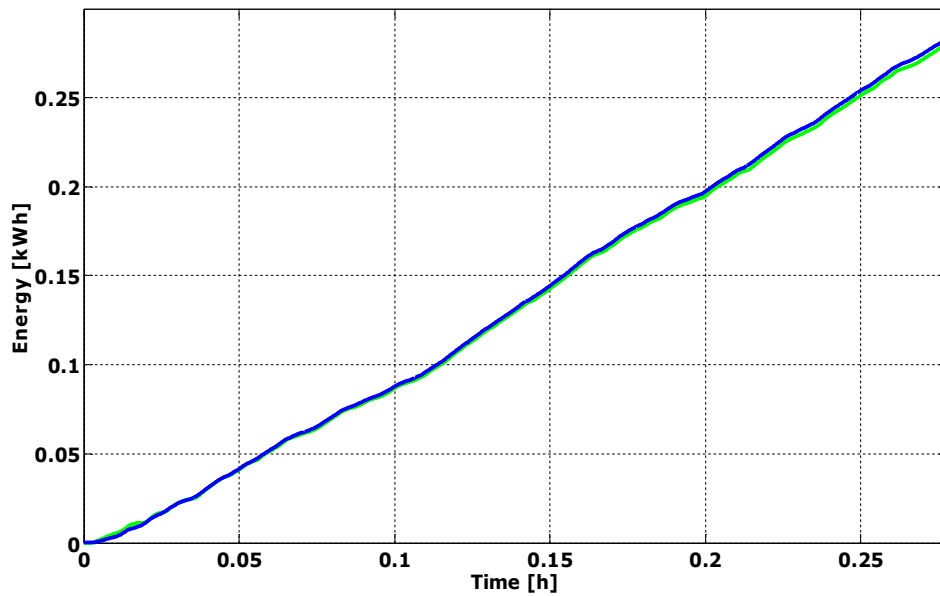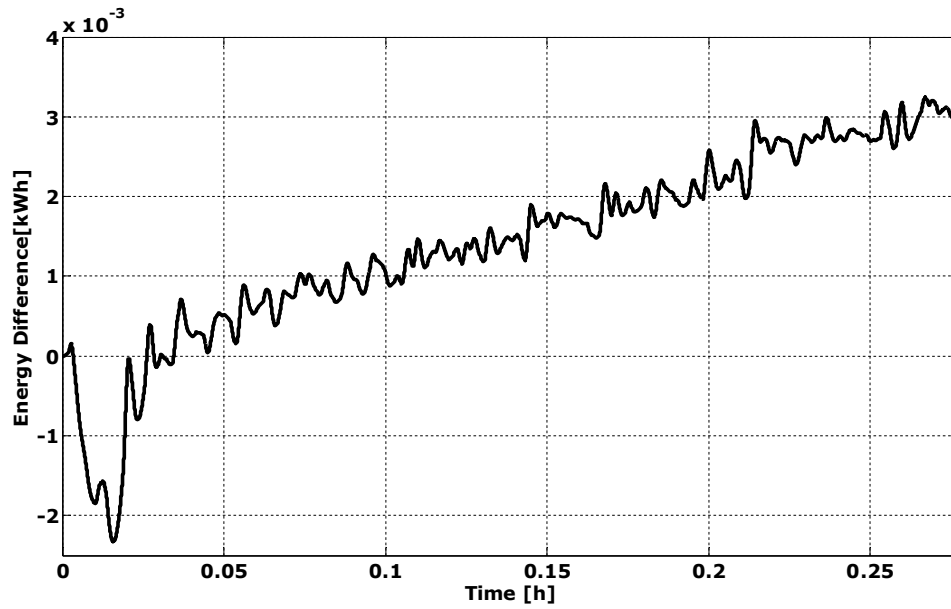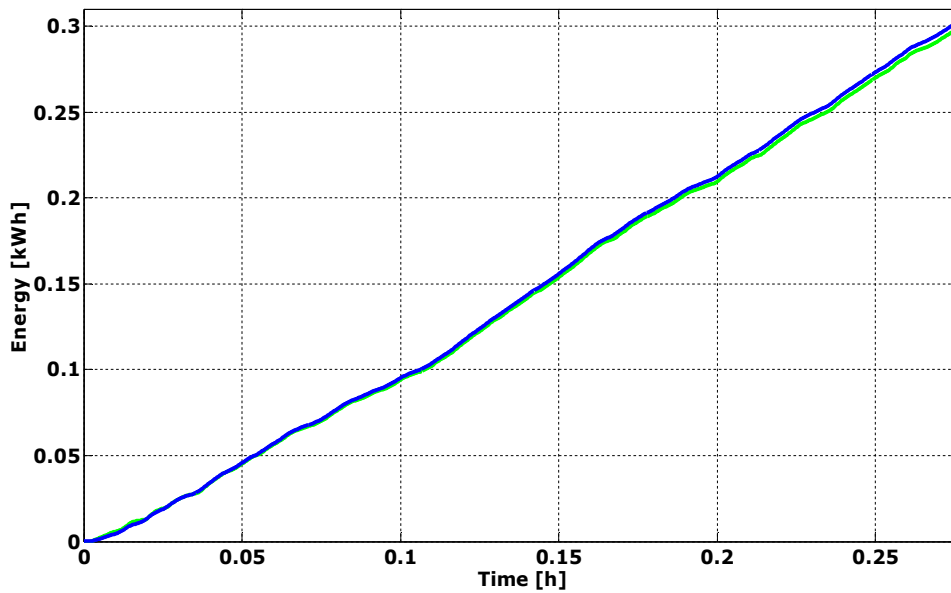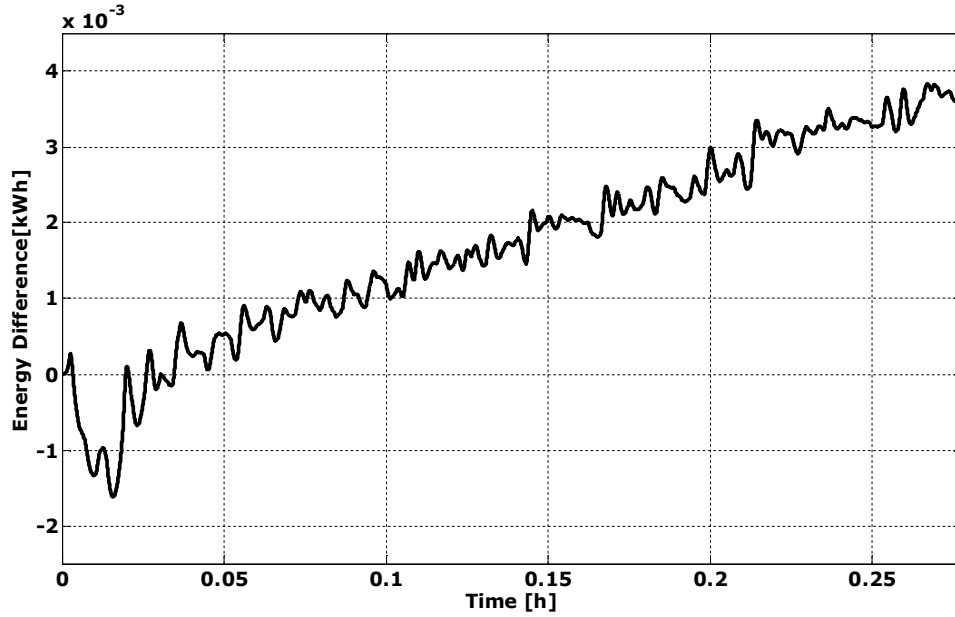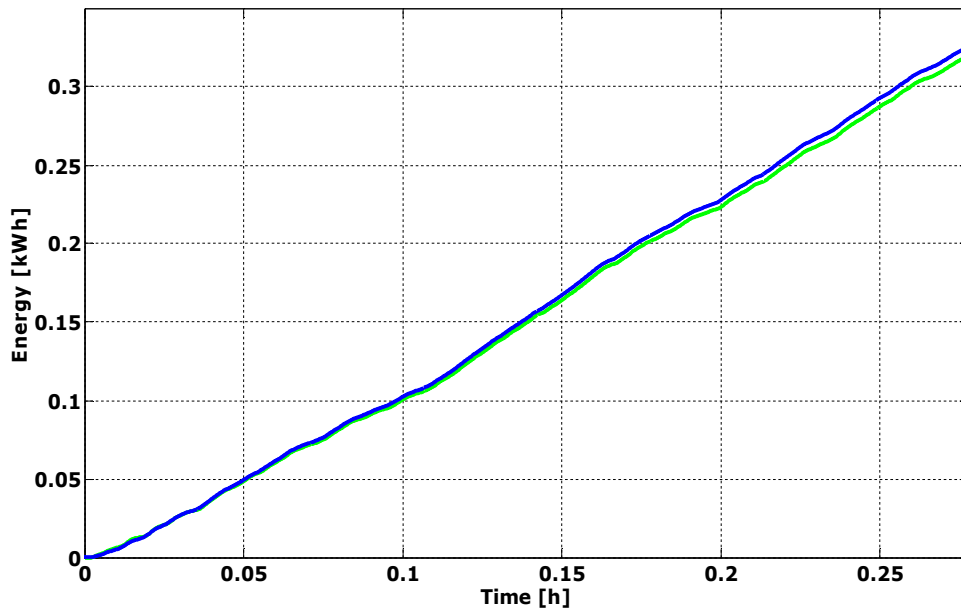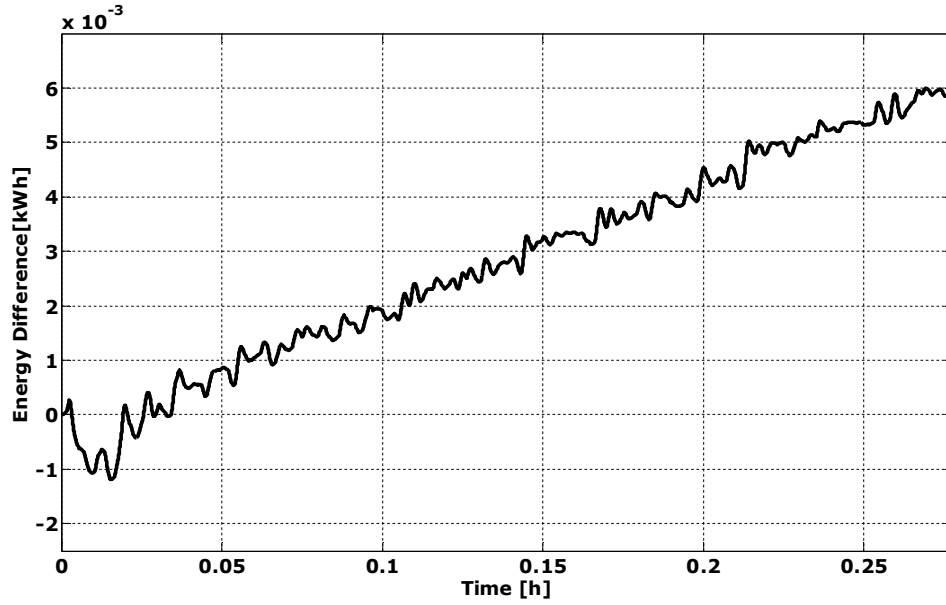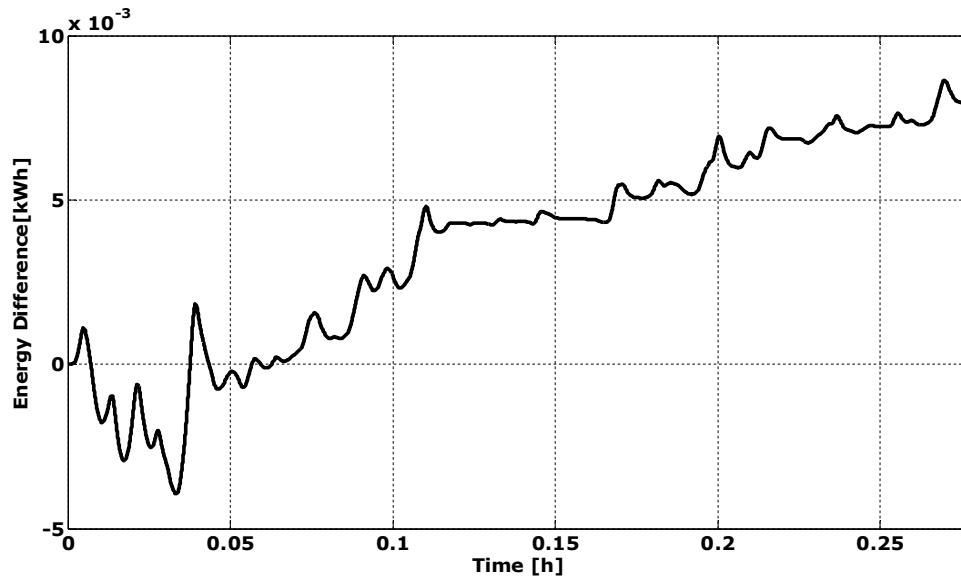Fig.4.53. Energy difference simulation results for real wind speed profile with three blades wind turbine and ρ=1.3413.

4.5. Conclusion

For SWECS, a MPP control algorithm is a key component necessary to extract the maximum available power from the wind speed. Two MPP control strategies, with transient regimes compensation were described, simulated and tested. They were validated by simulation and experimental results for steps wind speeds and a real wind speed profile for two types of wind turbines.

The advantage of the first MPP control strategy, using the wind turbine characteristics, is its simplicity in implementation, but is sensitive to the parameters variations.

The advantages of the implemented MPPT-FLC are the fast response and its robustness. This MPPT-FLC can be used even if the wind turbine systems parameters, wind turbine characteristics and air density are changed or unknown. Another advantage is the low computational effort of the FLC, designed just by the needed rules and the associated fuzzy operations.

It is also notable that the FLC does not require the knowledge of the wind speed.

It is concluded that the fuzzy logic is a valid tool for MPPT in SWECS.

Comparisons between the energies extracted with the two MPP controllers, in different cases, were presented and the MPPT–FLC was highlight to be the most energy conversion efficient and robust controller for SWECS.

A theoretical efficiency of SWECS was introduced in order to evaluate the global conversion and the control quality, having as reference the maximum obtainable mechanical energy from a specific wind turbine. Values closed to the global electrical part efficiency prove that the control strategies can extract the maximum available power. The smallest value was obtained for the three blades wind turbine for a real wind speed profile, due to the fact that for a continuous changing in wind speed the maximum power point operating point cannot be achieved, especially when the system has a relatively high inertia.

The first MPP control strategy was implemented on a full-scale, complete SWECS in real functioning conditions (described in the next chapter).

References

[1] Md. E. Haque, M. Negnevitsky and K. M. Muttaqi, "A novel control strategy for a variable-speed wind turbine with a permanent-magnet synchronous generator," *IEEE Trans. on Ind. Appl.,* vol. 46, no. 1, pp. 331-339, January/February 2010.
[2] M. G. Simoes, B. K. Bose and R. J. Spiegel, "Fuzzy logic based intelligent control of a variable speed cage machine wind generation system," *IEEE Trans. on Power Electronics,* vol. 12, no. 1, pp. 87-95, January 1997.
[3] M.A. Abdullah, A.H.M. Yatim, C.W. Tan, R. Saidur, "A review of maximum power point tracking algorithms for wind energy systems", *Renewable and Sustainable Energy Reviews,* vol. 16, 2012, pp. 3220-3227.
[4] M. Narayana, G.A. Putrus, M. Jovanovic, P.S. Leung, S. McDonald, "Generic maximum power point tracking controller for small-scale wind turbines", *Renewable Energy,* vol. 44, 2012, pp. 72-79.

[5]   C. Vlad, I. Munteanu, A.I. Bratcu, E. Creanga, "A peak Power tracker for low-power permanent-magnet-synchronous-generator-based wind energy conversion systems," *12th WSEAS International Conference on SYSTEMS*, Heraklion, Greece, July 22-24, 2008, pp. 407-412.

[6]   Q. Zeng, L. Chang and R. Shao, "Fuzzy-logic-based maximum power point tracking strategy for Pmsg variable-speed wind turbine generation system," *Canadian Conference on Electrical and Computer Engineering, CCECE 2008,* pp. 000405-000410, 4-7 May 2008.

[7]   C. Vlad, E. Ceanga, "MPPT Algorithm for Small Wind Systems based on Speed Control Strategy", *Annals of Dunarea de Jos Journal,* 2008, vol. 31, Issue 1, pp. 23-28.

[8]   J. Chen, J. Chen, C. Gong, "New Overall Power Control Strategy for Variable-Speed Fixed-Pitch Wind Turbines within the Whole Wind Velocity Range", *IEEE Transactions on Industrial Electronics,* Vol. PP, Issue: 99, 30 April 2012, pp. 1-9.

[9]   A. Mirecki, X. Roboam, F. Richardeau, "Architecture complexity and energy efficiency of small wind turbines", *IEEE Trans. on Power Electronics*, vol. 54, no. 1, pp. 660- 670, February 2007.

[10] R. Datta and V. T. Ranganatan, "A method of tracking the peak power points for a variable speed wind energy conversion system," *IEE Trans. on Energy Conversion,* vol. 18, No. 1, pp. 163-168, March 2003.

[11] A. Abo-Khalil, D. Lee and J. Seok, "Variable speed wind power generation system based on fuzzy logic control for maximum output power tracking," *35th Annual IEEE Power Electronics Specialist Conference,* Aachen Germany, 2004, pp. 2039-2043.

[12] M. Ors, "Maximum power point tracking for small scale wind turbine with self-excited induction generator", *Journal of Control Engineering and Applied Informatics, 2009*, vol. 11, No. 2, pp. 30-34.

[13] V. Lazarov, D. Roye, D. Spirov and Z. Zarkov, "New Control Strategy for Variable Speed Wind Turbine with DC – DC converters", *14th International Power Electronics and Motion Control Conference, EPE-PEMC 2010,* pp. T12-120-124.

[14] M. Godoy, K. Bose, J. Spiegel, "Design and Performance Evaluation of a Fuzzy-Logic-Based Variable-Speed Wind Generation System", *IEEE Trans. on Industry Applications*, vol. 33, no. 4, July/August 1997, pp. 956-965.

[15] C.C. Lee, "Fuzzy logic in control systems: fuzzy logic controller. I," *IEEE Transactions on Systems, Man and Cybernetics,* Vol. 20, Issue 2, March/April 1990, pp. 404-418.

[16] R. M. Hillowala and A. M. Sharaf, "A rule-based fuzzy logic controller for a PWM inverter in a stand alone wind energy conversion scheme," *Industry Applications, IEEE Transactions on,* Vol. 32, Issue 2, Jan/Feb 1996, pp. 57-65.

[17] V. Lazarov, D. Roye, D. Spirov and Z. Zarkov, "Study of Control Strategies for Variable Speed Wind Turbine under Limited Power Conditions", *14th International Power Electronics and Motion Control Conference, EPE-PEMC 2010,* pp. T12-125-130.

[18] C. Patsios, A. Chaniotis, M. Rotas and A.G. Kladas, "A comparison of maximum-power-point tracking control techniques for low-power variable-speed wind generators", *8th International Symposium on Advanced Electromechanical Motion Systems & Electric Drives Joint Symposium, ELECTROMOTION 2009,* Lille, France, 1-3 July 2009, pp. 1-6.

[19] A. Mesemanolis, C. Mademlis and I. Kioskeridis, "A fuzzy-logic based control strategy for maximum efficiency of a Wind Energy Conversion System", *2012 International Symposium on Power Electronics, Electrical Drives, Automation and Motion (SPEEDAM),* Sorrento, Italy, 20-22 June 2012, pp. 7-12.

[20] B. Neammanaee, K. Krajangpan, S. Sirisumrannukul and S. Chatrattana, "Maximum peak power tracking-based control algorithm with stall regulation for optimal wind energy capture," *Power Conversion Conference, PCC' 07,* 2 - 5 april, Nagoya, pp. 1424-1430.

[21] Q. Wang and L. Chang, "An Intelligent Maximum Power Extraction Algorithm for Inverter-Based Variable Speed Wind Turbine Systems," *IEEE Transaction on Power Electronics*, vol. 19, no. 5, September 2004, pp.1242-1249.

[22] I. Munteanu, A. I. Bratcu, N. A. Cutululis, E. Ceanga, "Optimal Control of Wind Energy Systems", Springer, 2008.

[23] P. Novak, T. Ekelund, I. Jovik, and B. Schmidtbauer, "Modeling and Control of Variable-Speed Wind-Turbine Drive-System Dynamics", *Control Systems, IEEE*, vol. 15, issue 4, August 1995, pp. 28-38.

[24] I. Munteanu, N. A. Cutululis, A. I. Bratcu, E. Ceangă, "Optimization of variable speed wind power systems based on a LQG approach", *Control Engineering Practice,* vol. 13, Issue 7, July 2005, pp. 903–912.

[25] B. Axelrod, Y. Berkovich, A. Ioinovici, "Switched-capacitor/switched-inductor structures for getting transformerless hybrid dc-dc PWM converters," *IEEE Trans. Circuits and Systems,* vol.55, no. 2, March 2008, pp. 687-696.

[26] N. Muntean, O. Cornea and D. Petrila, "A new conversion and control system for a small off – grid wind turbine," *Optim 2010 - 12th International Conference of Electrical and Electronic Equipment,* 20-22 may, Romania, pp. 1167-1173.

[27] N. Muntean, L. Tutelea, D. Petrila, O. Pelan, "Hardware in the loop wind turbine emulator," *ACEMP 2011 – International Aegean Conference on Electric and Power Electronics & Electromotion Joint Conference,* 8-10 September 2011, Istanbul, Turkey.

[28] "Fuzzy logic toolbox-User's guide", The MathWorks, Inc.

5. RESULTS OBTAINED IN AN EXPERIMENTAL PLATFORM

The proposed SWECS described and modeled in Chapter 2, and tested with MPP control strategy presented in Chapter 4, was installed on-site.

The proposed SWECS was studied and built within a research project [1]. The installed SWECS was monitored and the results were acquired with SCADA software. Also WECS control parameters can be changed with SCADA.

A five blades wind turbine was initially mounted in the field (Fig.5.1) and then it was changed with a three blades wind turbine. The change was made due to the bad wind speed prediction in the area. The PMSG is shaft connected with the turbine (direct drive).

The energy conversion and storage equipment presented in Fig.5.2 is equivalent with the laboratory experimental model. It consists of:

- a 6 diodes DBR;
- HDC;
- one SC;
- one inverter
- one charge controller;
- a battery bank;
- 3x10 Ω three phase resistor, connected at the PMSG output for protection and also a 2 Ω resistor in parallel with the SC.

The dSPACE system (used in laboratory) was changed with an industrial PLC configuration for all control and monitoring aspects.

Fig.5.1. Five blades wind turbine.

Fig.5.2. Energy conversion and storage equipment.
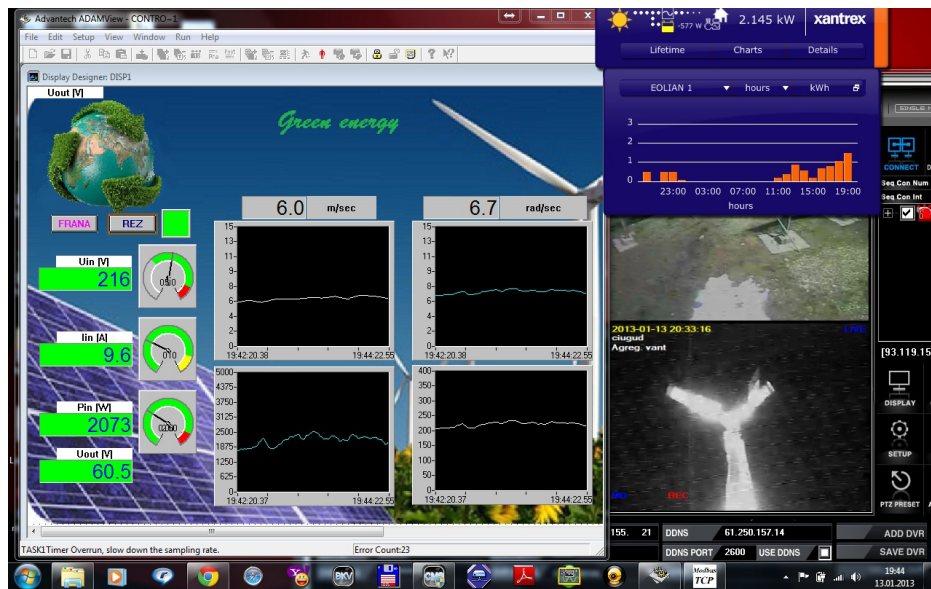
Fig.5.3. SCADA acquisition interface.

5.1. Results from the Test Site

Figs 5.4-5.10 show real time results acquired from the site, with the three blades wind turbine. In Fig. 5.9 it can be seen that when no AC loads are connected in the system and the battery bank is fully charged, the SC voltage reaches the 90 V

level, the 2 Ω protection resistor is connected and when the SC voltage decreases to 70 V, the protection resistor is disconnected. The SC voltage level is always maintained at min. 60 V by the charge controller, in order that the batteries to be supplied.

The first MPP control strategy described in Chapter 4 was implemented here. In fig.5.10 it can be seen that the PMSG electrical power (in red) is maintained at an optimum level and is between the blue and green curves, which are the optimum power versus rotating speed curves, provided by the turbine designers.

It can be concluded that the propose SWECS is a functional wind energy conversion system and works according to the described parameters and simulation results presented on Chapter 2.
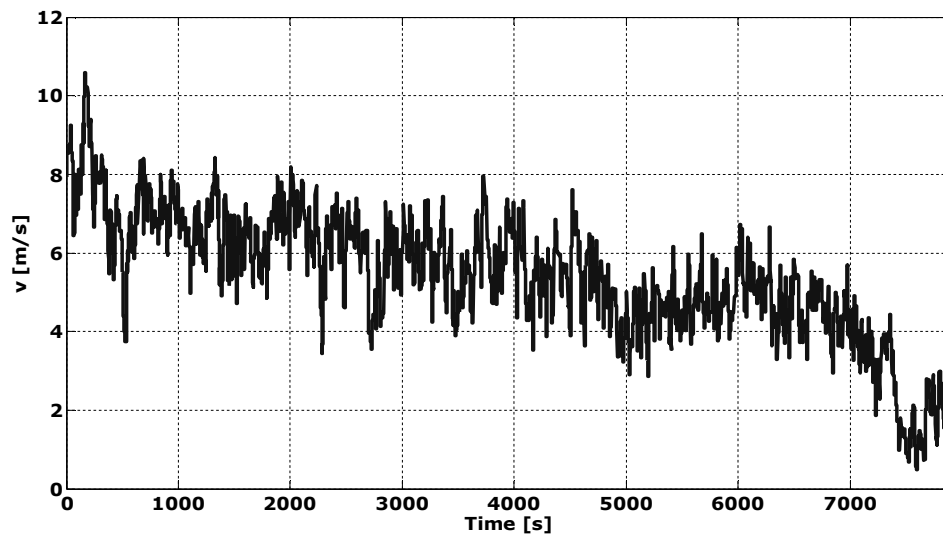
Fig.5.4. Real wind speed.
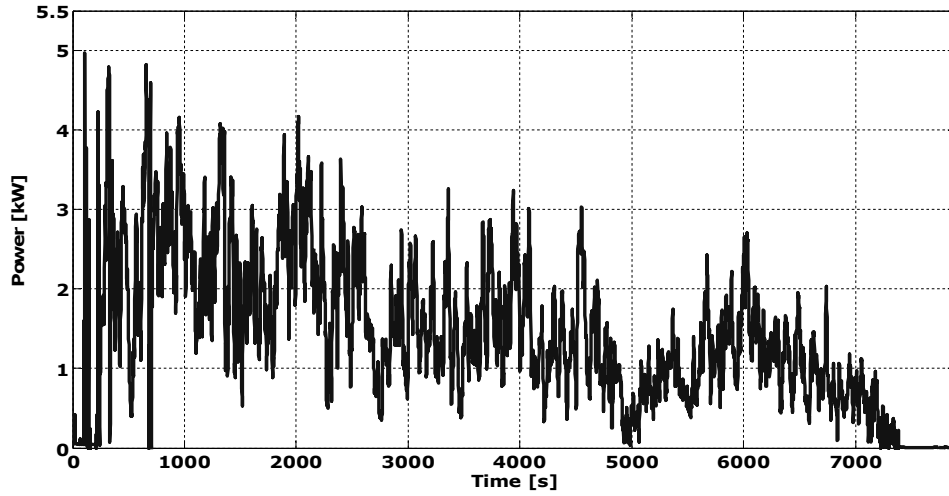
Fig.5.5. SWECS power.
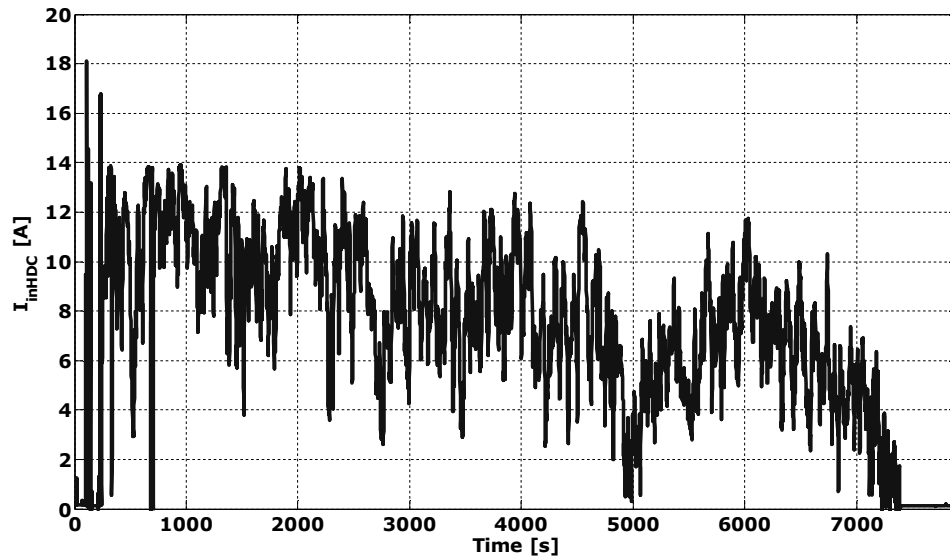
Fig.5.6 HDC input current.
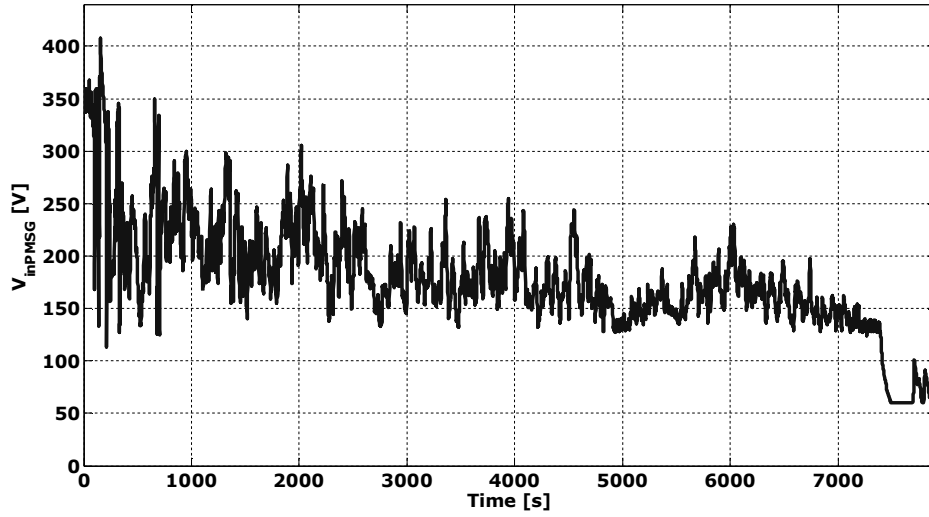
Fig.5.7 PMSG input voltage.
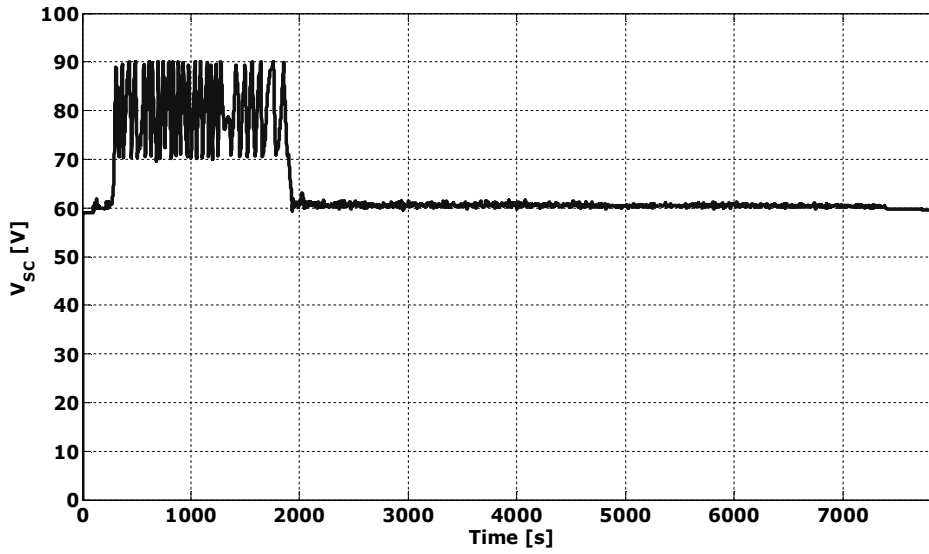
Fig.5.8. SC voltage.
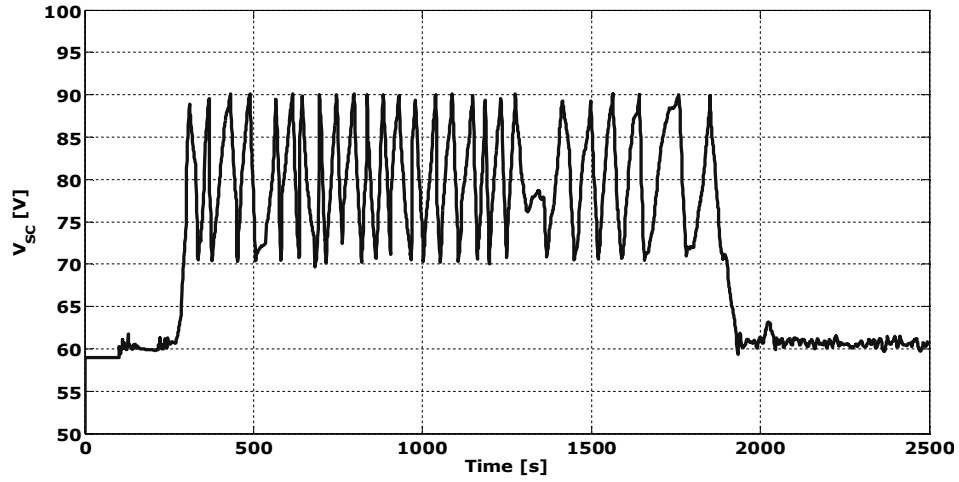
Fig.5.9. SC voltage with zoom.
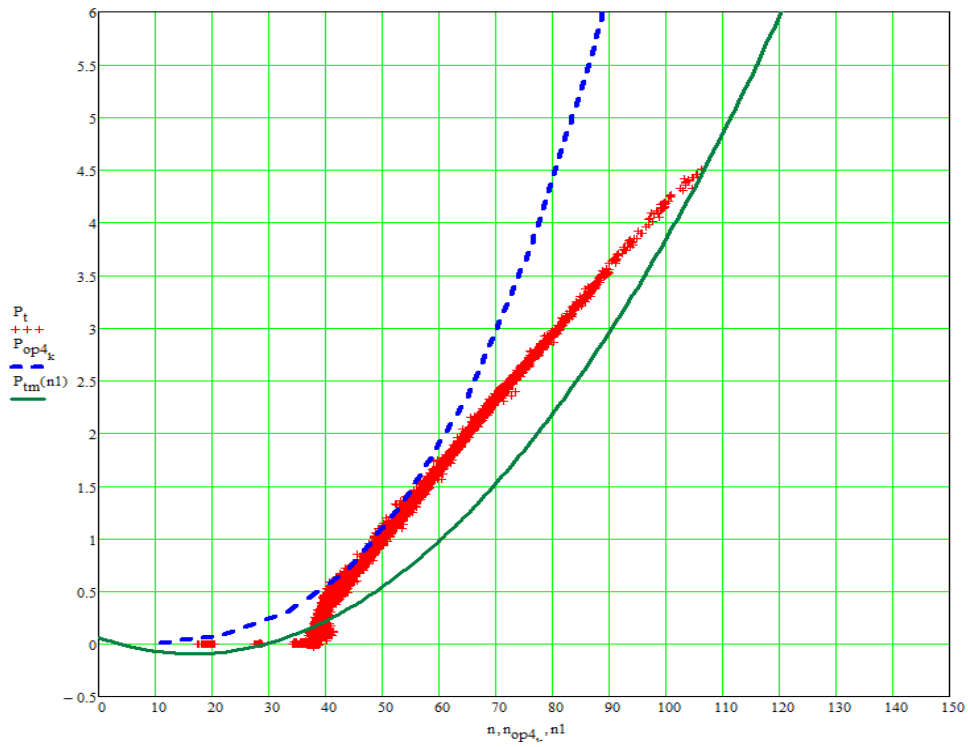
Fig.5.10. Power versus rotating speed experimentally results.

5.2. Conclusion

Experimentally results obtained in the laboratory, needed to be confirmed in real conditions tests to fully confirm the theory. This was the role of the site implemented system.

All main components (power electronics and storage) are the same as in laboratory, but some hardware control systems, including SCADA support, and the specific implementation were made in respect to industrial standards.

The first MPP control strategy, knowing the wind turbine characteristics, was implemented and experimental results, in good correspondence with simulations were presented.

The platform was built by a multidisciplinary research team from University "POLITEHNICA" Timişoara. Together with the laboratory setup, the on-site platform offers very good conditions for testing industrial equipment in the field of wind energy conversion systems, as a final test before industrial implementation.

References

[1] "Improvement of the Structures and Efficiency of Small Horizontal Axis Wind Generators with Non-Regulated Blades", no. RO018 EEA Grants.

6. EXPERIMENTAL SETUP DESCRIPTION

This chapter presents the laboratory setup, used to test and validate the proposed SWECS and MPP developed controls.

Parts of this chapter are found also in the previous sections, where they were placed for a better consistency.

The implementation of the laboratory platform started with the "hardware in the loop" wind turbine emulator, presented in Chapter 3.

Next, the emulator was completed with the components presented in the proposed SWECS structure, in Chapter 2. The complete wind energy conversion laboratory setup contains:

- dSPACE control board;
- voltage source inverter with direct torque control (DTC);
- IM with GB – the wind turbine equivalent;
- PMSG;
- 6 diodes bridge rectifier (DBR);
- HDC;
- SC;
- inverter and charge controller;
- 4x12V/100Ah batteries;
- 3x10 Ω three phase resistor, and a 2 Ω resistor.
- additional equipment (transducers, signal conditioners etc.)

Fig. 6.1 gives a complete image of the laboratory experimental platform (including the protective resistors R_1 and R_2 presented in Chapter 2).

Fig.6.1. The complete laboratory setup.

6.1. dSPACE Control Board

DS1104 R&D Controller Board is a standard board that can be plugged into a PCI slot or a PC. It is specially designed for the development of high-speed multivariable digital controllers and real-time simulations in various fields. For advance I/O purposes, the board includes a slave-DSP subsystem based on the TMS320F240 DSP microcontroller. For rapid control prototyping (RCP), specific interface connector panels provide easy access to all input and output signals on the board. Thus, the DS1103 R&D Controller Board is the ideal hardware for the dSPACE Prototyper development system for cost-sensitive RCP applications [1].

Specific interface connector panels, provides easy-to-use connections between the DS1104 R&D Controller Board and devices to be connected to it. Devices can be individually connected, disconnected or interchanged without soldering via BNC connectors and Sub-D connectors. This simplifies system construction, testing and troubleshooting. The Connector/Led Combi Panel provides an array of LEDs indicating the states of the digital signals [1].

Real-Time Interface (RTI) provides Simulink® blocks for graphical I/O configuration. It is easy to run function models on the DS1104 R&D Controller Board. All I/O can be configured graphically by inserting the blocks into a Simulink block diagram, and generate the model code via Simulink Coder® (formerly Real-

Time Workshop®). The real-time model is compiled, downloaded, and started automatically. This reduces the implementation time to a minimum [2].

6 BNC Connectors from the DS1104 R&D Controller Board have been used (Fig.6.2), 4 for input (estimated) signals and 2 for output (prescribed) signals. Also a digital I/O Connector was used in order to open/close 2 relays, which transmit commands to HDC: Run/Stop and Reset.

The experiment interface was designed with Control Desk ® software (Fig. 6.3), which is suitable for real-time and Simulink experiments. The interface enables changing parameter values interactively with input instruments, changing data connections, observing signals with data acquisition instruments, capturing data and saving the results to disk. Multiple data acquisitions can be synchronized to the global time, defined relative to the start of Control Desk's animation mode.
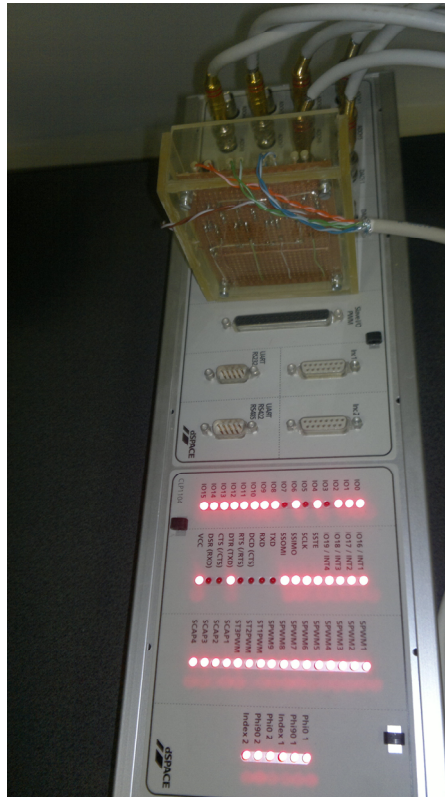
Fig.6.2. DS1104 R&D Controller Board.
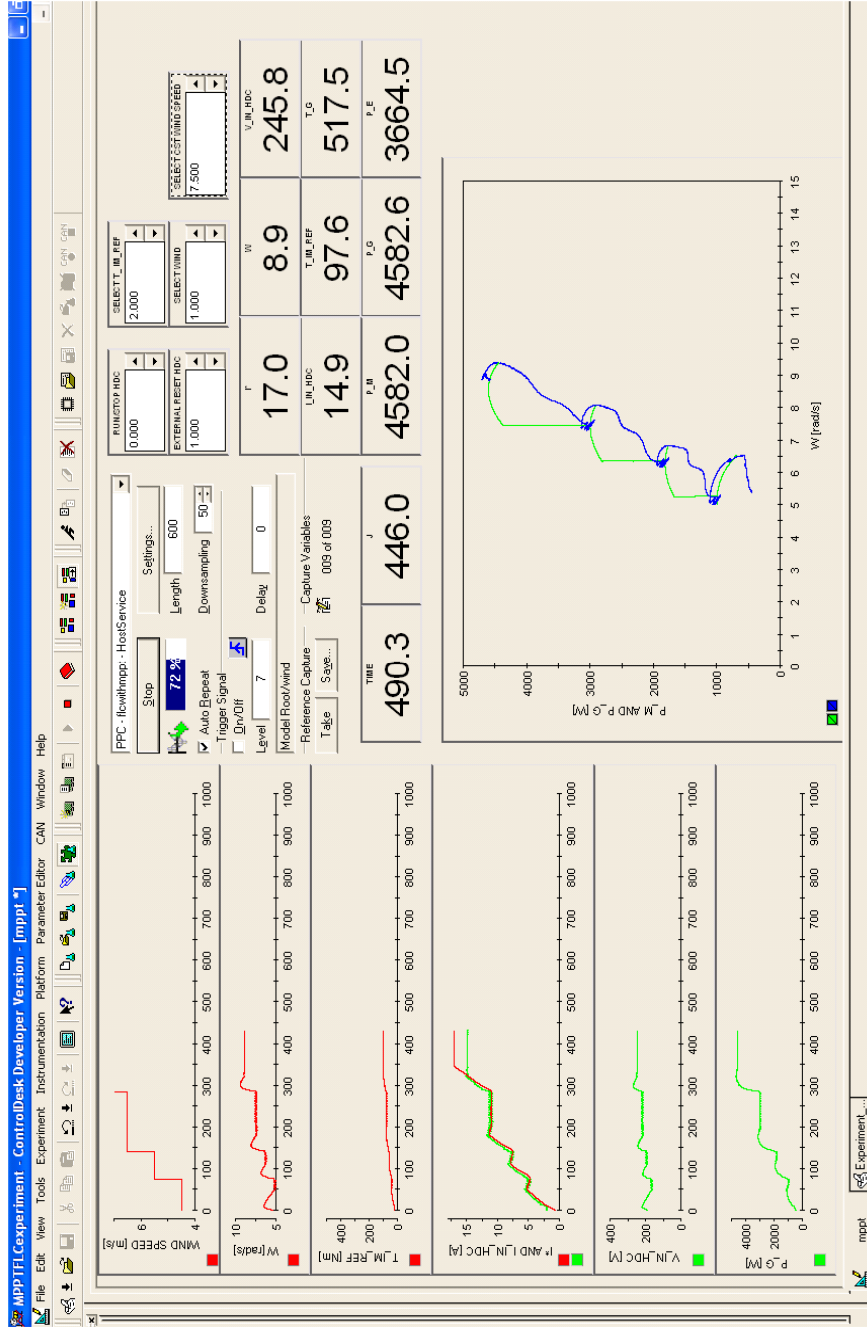
Fig.6.3. Control Desk experiment interface.

6.2. Direct Torque Control Drive

The voltage source inverter was chosen to be an ABB ACS800-04-0011-03+E200+J400 model. The inverter is an IP20 drive module for controlling AC motors. The voltage range (nominal rating in bold) is 380/**400**/415 V AC. The meaning of J400 parameter is that the control panel CDP312R is assembled on the drive module. The E200 EMC/RFI filter is for the second environment TN (grounded) system [3].

The ACS 800 achieves the ultimate in AC motor control performance, using Direct Torque Control. ACS 800 performs accurate speed and torque control of any standard squirrel cage motor - without encoder or tachometer feedback [3].

ACS 800 series features a multi-lingual, alphanumeric control panel that also provides an intelligent start-up assistant that will greatly simplify set-up, operation, and fault diagnostics. The control panel can be mounted on the cover of the drive, or remotely, and can upload, store, and download parameters [3].

ACS 800 can be used for the simplest application, or the most complex application. Three integral option slots can be configured with additional analog and digital inputs and outputs, encoder feedback, as well as a host of different communication bus adapters. An integral brake chopper is provided on all frame size drives as standard while an integral brake chopper is an option [3].

The motor control is based on the Direct Torque Control (DTC) method. Two phase currents and DC link voltage are measured and used for the control. The third phase current is measured for earth fault protection.

Other technical specifications of the ACS800-04-0011-03+E200+J400 model [3]:

- Nominal ratings, $I_{cont\ max}$= 19 [A], I_{max}= 24 [A];
- No-overload use, $P_{cont\ max}$= 7.5 [kW];
- Light-overload use, I_{2N}=18 [A], P_N=7.5 [kW];
- Heavy duty use, I_{2hd}=14 [A], P_{hd}=5.5 [kW];
- Air flow, 69 [m^3/h];
- Heat dissipation, 250 [W];
- Efficiency, approximately 98% at nominal power level.

Also, in the cabinet were the ABB Inverter was mounted, 6 Zelio analog interface modules were mounted and 2 Finder Relays with 24 V DC (Fig.6.4).

The Zelio Analog is designed to convert signals emitted by sensors or electrical measurement devices, into standard electrical signals that are compatible with automation platforms and controllers (thermal processes, speed, etc.). They also allow the connection distance between a sensor and a measurement acquisition device to be increased, for example, between a thermocouple and a programmable controller [4].

It is difficult to transmit low level signals over long electric lines without encountering problems of interference, signal reduction, or errors.

Connecting Zelio analog converters close to the sensors resolves problems like [4]:

- 4–20 mA current loops transmitted over a long distance are less sensitive to interference than low level voltage signals from sensors;
- signal reductions during transmission (resistance) of voltages do not occur;
- the cables used to connect the converters to process equipment (programmable controllers) are standard cables, which are more cost effective than extension cables or compensation cables suitable for low level signals for Pt100 probes or thermocouples.

Six Universal Voltage/Current Zelio Converters were used (to convert 0-10 V signal into 4-20 mA signal and reverse):

- inputs: a voltage/current range: 0–10 V, ± 10 V, 0–20 mA, 4–20 mA;
- outputs: a switchable voltage/current range: 0–10 V, ± 10 V, 0–20 mA, 4–20 mA.
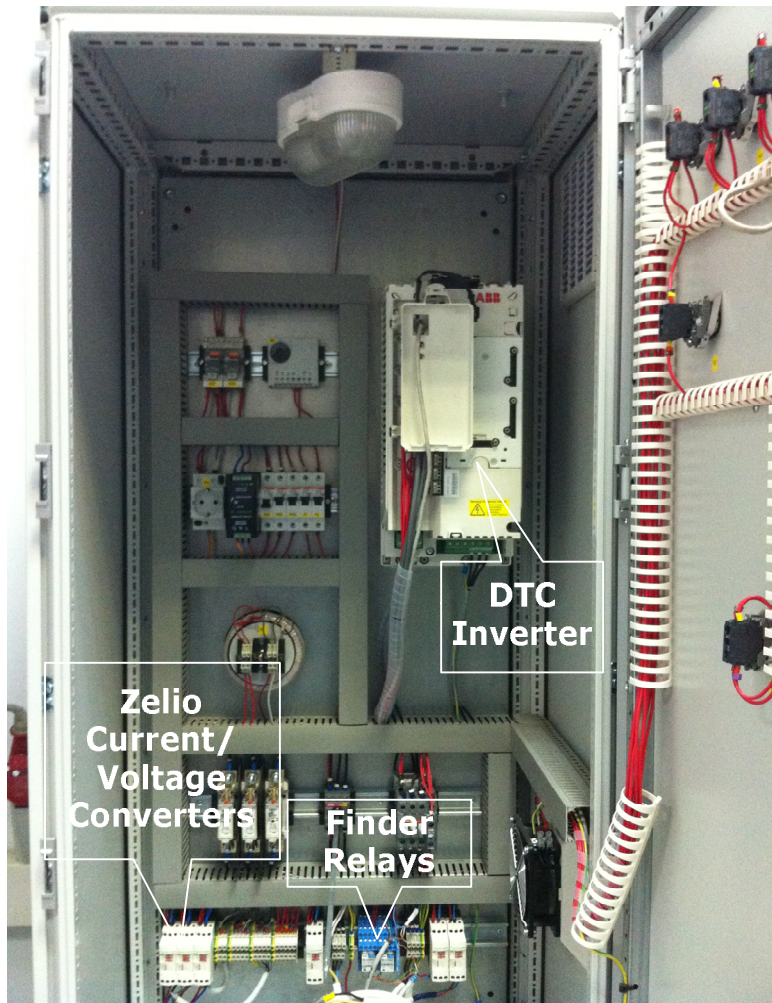
Fig.6.4. Cabinet with DTC Inverter, current/voltage converters and relays.

The three phases IM with GB – the wind turbine equivalent, and PMSG have been presented in Chapter 3, because they have been part of the hardware in the loop wind turbine emulator. Their electrical specifications have been also given there.

6.3. Hybrid Buck DC-DC Converter

The electrical specifications of the HDC have been presented in Chapter 2.

Table 1 presents the voltage values for the HDC prescribed input current and the HDC input current. In Fig.6.5 is presented the control HDC characteristic.

The HDC is presented in Fig.6.6.

Table 6.1. HDC prescribed input current and HDC input current

Nr.crt.	Prescribed Voltage for the HDC Current	Input HDC current (diode bridge output current)
	V_I*_IN [V]	I_DB [A]
1	-	0.50
2	-	1.00
3	-	1.50
4	1.10	2.00
5	1.40	2.50
6	1.70	3.00
7	2.00	3.50
8	2.30	4.00
9	2.62	4.50
10	2.92	5.00
11	3.20	5.50
12	3.50	6.00
13	3.80	6.50
14	4.00	7.00
15	4.30	7.50
16	4.60	8.00
17	4.90	8.50
18	5.20	9.00
19	5.50	9.50
20	5.80	10.00
21	6.10	10.50
22	6.40	11.00
23	6.70	11.50
24	7.00	12.00
25	7.30	12.50
26	7.60	13.00
27	7.90	13.50
28	8.20	14.00
29	8.50	14.50
30	8.80	15.00
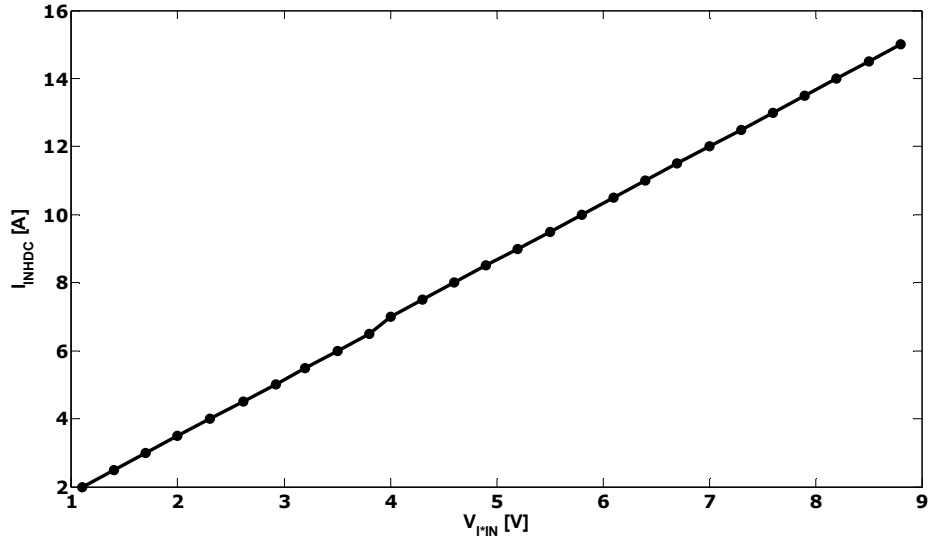
Fig.6.5. HDC control characteristic.
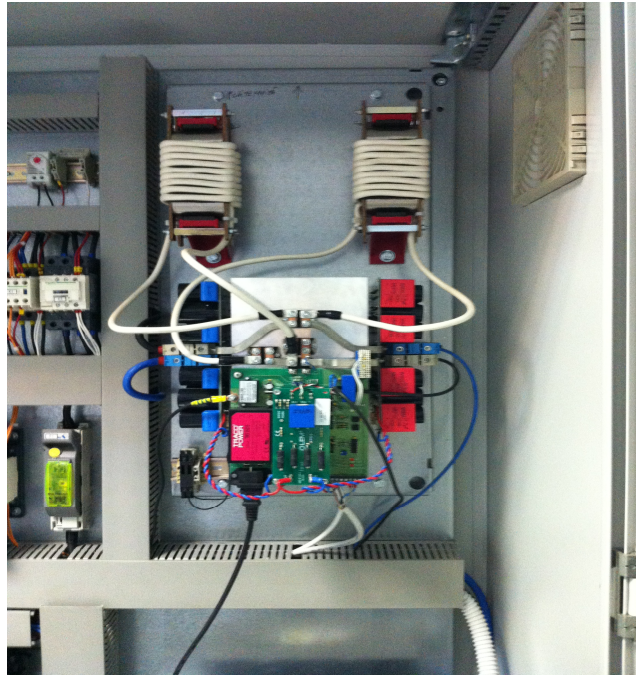
Fig.6.6. HDC prototype built for this application.

6.4. Supercapacitor

Maxwell Technologies' 125V Heavy Transportation series of supercapacitor modules (Fig.6.7) is a high performance energy storage product line for hybrid buses, trucks, trolleys, light rail, mining, construction and seaport cranes. Each model incorporates balancing, monitoring and thermal management capabilities to ensure industry-leading charge/discharge performance, high reliability and long operational life [5].
Features:
- Over 1 million charge/discharge cycles;
- IP 65 environmental protection;
- Operating temperature -40° C to +65° C;
- CAN bus digital monitoring and communications;
- Highest power performance available;
- Temperature and voltage monitoring;
- Series connection up to 1500V.
Benefits:
- Highest performance hybrid power systems;
- Survive in nearly any weather/environmental conditions;
- All in one solution with digital monitoring and built-in forced air cooling;
- Digital feedback enables optimized hybrid control algorithms.

Fig.6.7. Maxwell SC.

6.5. Charge Controller with Inverter and Batteries

The inverter used in the proposed WECS was chosen to be a 6 [kW] Xantrex Inverter/Charger XW6048 (Fig.6.8). The XW Inverter/Charger is one of the finest inverter/charges on the market today, incorporating state-of-the-art technology, high reliability and convenient control feature [6].

XW Inverter/Charger electrical specifications [6]:
- Continuous output power, 6000 [W];
- Surge rating, 12000 [W];
- Surge current, 53 [A_{rms}];
- Peak efficiency, 95.4%;
- Full load efficiency, 92 %;
- Waveform: true sine wave;
- Idle consumption – invert mode, no load 28 [W];
- Idle consumption – search mode < 7 [W];
- AC output voltage, 230 [V] ±3%;
- AC input voltage range (bypass/charge mode), 165-280 [V];
- AC input frequency range (bypass/charge mode), 45-55 [Hz] (default), 40-68 [Hz] (allowable);
- AC output continuous current, 26.1 [A];
- AC output frequency, 50±0.1 [Hz];
- Total harmonic distortion <5% at rated power;
- Automatic transfer relay, 56 [A];
- Auxiliary relay output 0-12 [V], maximum 250 [mA] DC;
- DC input voltage (nominal), 50.4 [V];
- DC input voltage range, 44-64 [V];
- DC current at nominal power, 131 [A];
- Continuous charge rate at nominal voltage, 100 [A];
- Power factor corrected charging PF (0.99);
  XW Inverter/Charger mechanical specifications:
- Supported battery types: flooded (default), gel, AGM, custom;
- Battery bank size, 100-2000 [A];
- Nonvolatile memory;
- System network, Xanbus;
- Enclosure type, IP 20, indoor, unheated;
- Rated temperature range, 0-40 °C;
- Operational temperature range, -25-70 °C;
- Storage temperature range, -40-85 °C;
- Inverter dimensions, (H x W x D) 580 x 410 x230 [mm];
- Inverter weight, 55.2 [kg].

The inverter/charger operation can be monitored with the Inverter Information Panel, which displays basic information or with the System Control Panel, with which the inverter can also be configured. Also the batteries connected to the system can be monitored with the two panels [7].

The Xantrex Solar Charge Controller (Fig.6.8) is a photovoltaic (PV) charge controller that tracks the maximum power point of a PV array to deliver the maximum available current for charging the batteries. The charge controller can be used with 12-, 24-, 36-, 48- and 60-volt DC battery system. The solar charge controller is designed to regulate PV input, but will also work with other DC sources. It can be installed with an Xantrex Inverter/Charger or in stand-alone installation [8].

Standard features [8]:

- Two or three stage charging process, with manual equalization to maximize system performance and maintain expected battery life;
- True dynamic Maximum Power Point Tracking to deliver the maximum available power from the DC source to the battery bank;
- Integrated PV Ground Fault Protection;
- 60 Amp Capacity;
- 150 volt open circuit input voltage;
- Input over-voltage and under-voltage protection, output over-current protection and reverse current protection;
- Over temperature protection and power derating when output power and ambient temperature are high;
- Battery temperature sensor to provide automatically temperature compensated battery charging;
- Xanbus-enabled. Xanbus is a network communication protocol developed by Xantrex. The charge controller is able to communicate its settings and activity to other Xanbus-enabled devices, such as the XW Series Inverter/Charger, the XW System Control Panel or other XW Charge Controllers.

Electrical Specifications:

- Maximum PV Array Voltage (operating): 140 [Vdc];
- Maximum PV Array Open Circuit Voltage: 150 [Vdc];
- Array Short Circuit Current: 60 [Adc] maximum;
- Nominal Battery Voltage: 12, 24, 36, 48, 60 [Vdc];
- Battery Voltage Range (operating): 10 [Vdc] to 80 [Vdc];
- Maximum Output Current: 60 [A];
- Maximum Output Power: 3500 [W];
- Auxiliary Output: 5-13 V, up to 200 [mA];
- Tare Loss/Nighttime Power Consumption: 2.5 [W];
- Charger regulation mode: Three-stage (bulk, absorption, float), two-stage (bulk, absorption).

Mechanical Specifications:

- Operating temperature range: -10 to +45°C;
- Storage temperature: -40 to +80 °C;
- Dimensions (H x W x D): 368 x 146 x 138 [mm];
- Mounting: Vertical wall mount;
- Weight: 4.8 [kg].

4 Ritar Valve regulated rechargeable batteries have been chosen with 12V/100AH/10AH specifications (Fig.6.8).
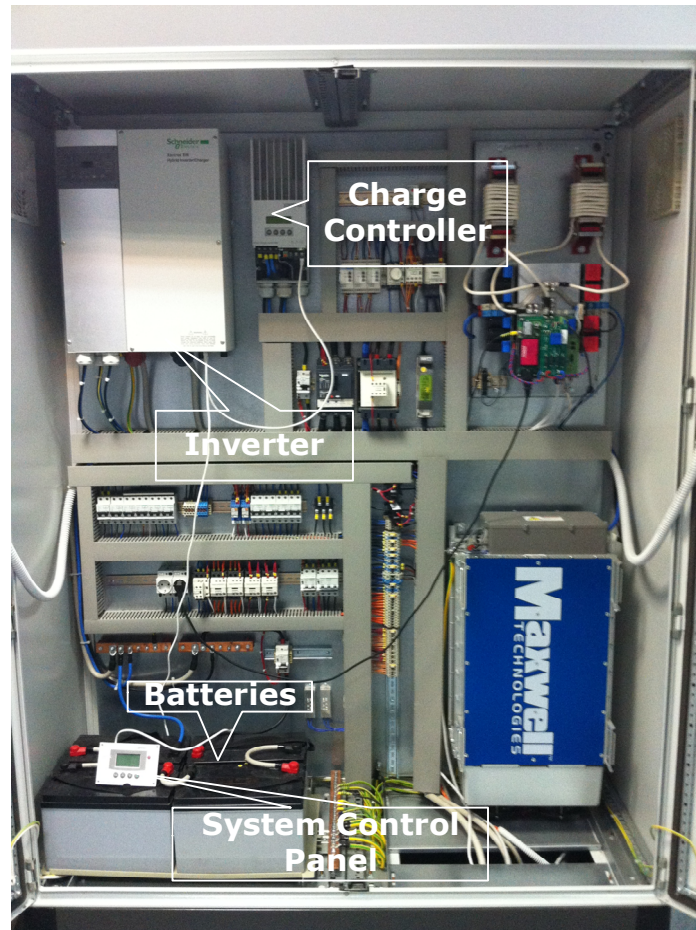
Fig.6.8. Xantrex inverter with charge controller, system control panel and batteries.

6.6. Conclusion

The experimental platform is one of the major parts of this work, because all main theoretical considerations were validated through experiments. It can be said that this platform is a complete laboratory setup possible to be used in wind energy conversion systems study, for teaching and research activities.

This chapter presented detailed information for all components. Some of them (HDC, PMSG, auxiliary devices etc.) were built as prototypes. The others were industrial equipment put together in this special, application oriented, designed system.

The setup implementation started with the "hardware in the loop" wind turbine emulator, built around a direct torque control AC drive, assisted with a dSPACE control system.

Then, the conversion and storage equipment were connected: the PM synchronous generator, the power electronics, the supercapacitor and the rechargeable batteries.

The system was completed with the corresponding transducers and signal conditioning devices.

Based on the previous experimental results obtained with the platform, an industrial designed system was built in order to be implemented in real conditions. This system is similar, in terms of operation principles, with the laboratory platform. Some specific details related to this implementation were presented in the previous chapter.

The author does not claim the full realization of these platforms. The design was made by a research, multidisciplinary team, and the concrete construction of the equipment was implemented by specialized companies.

The main contributions of the author are the software implementations, the design of the transducers system and the experimental obtained results.

References

[1] "DS1104 R&D Controller Board Hardware Installation and Configuration"
[2] www.dspace.com
[3] "ACS800 Hardware Manual"
[4] "Zelio Analog Interface Modules Catalog 2006"
[5] www.maxwell.com
[6] "XW Hybrid Inverter/Charger- Operation Guide".
[7] "XW System Control Panel- Owner's Guide".
[8] "XW Charge Controller Series Solar- Owner's Manual".

7. CONCLUSIONS AND CONTRIBUTIONS

7.1. Conclusions

In order to be targeted in this thesis, a literature research was done first, and the state of the art of WECS was studied. Different structures, generators types, power electronics topologies, and storage elements used in WECS were presented. Also some common control methods that are being used in most commercial available wind turbines in the market were presented. SWECS and their integration in hybrid energy generation systems were described. Finally, some components have been highlighted as the most suitable for a SWECS: VAWT, PMSG with DBR, and a DC-DC converter that can regulate the power and can charge the storage elements, followed by a PWM-VSI (connected or not to the grid).

A new structure of conversion and storage energy for a small off-grid wind turbine system was proposed and built. All main components were described in detail and modeled. Also a speed estimator for the PMSG was elaborated. The proposed SWECS was simulated in a simplified way, to better explain and motivate the role of a SC, as storage element for transients.

In order to study, test and implement SWECS and some control strategies for it, a direct torque control "hardware in the loop" wind turbine emulator was proposed, simulated, built, and tested.

Due to wind's unpredictable nature, MPP control algorithm is the key component, necessary to extract the maximum available power from WECS.

Two MPP controls have been developed and validated by simulation and experimental results on the real time "hardware in the loop" wind turbine emulator. The first MPP strategy is based on wind turbine known characteristics, memorized in the control system. The second is a P&O, MPPT-FLC algorithm.

Both strategies were tested under steps and real wind speed profile and were applied for two wind turbine types.

The main advantage of the first strategy s is its simplicity in implementation and commissioning, but it is sensitive to the parameters variation.

The MPPT-FLC proved its robustness. It can be used even if the wind turbine system parameters, wind turbine characteristics, air density or the wind speed are changing or unknown. Another attribute is the simplicity and low computational cost of the FLC, designed just by the needed rules and the associated fuzzy operations.

A comparison between the two MPP controllers was presented, to highlight the most efficient energy conversion strategy. It was concluded, for all studied cases, that MPPT–FLC is superior.

Some results from the site, where a similar system was installed, were presented to prove that in real conditions the system works properly.

Finally, the experimental setup details were presented as a part of the work.

This thesis has paid particular attention to the implementation, in a full-scale way, of all proposed solutions. Each theoretical consideration has been validated through simulations and experiments. These aspects can facilitate the transfer of the research results to industry.

7.2. Contributions

The main contributions of this thesis are summarized as follows:
– An overview of state of the art regarding the generators, power electronic converters, some common control strategies and storage elements used in WECS was presented.
– A SWECS structure using a hybrid DC-DC converter, a mixing (SC + batteries) storage elements was proposed and modeled.
– A speed estimator was elaborated.
– A simplified simulations of SWECS was presented in order to analyze the SC role, as storage element for transients;
– A "hardware in the loop" wind turbine emulator was proposed, built and validated by simulation and experimental results.
– Two MPP controllers were designed, simulated and tested in real time on the "hardware in the loop" wind turbine emulator. They were validated by simulation and experimental results for steps and real wind speed profile, using two types of wind turbines;
– Comparisons between the energies extracted with the two MPP controllers, in different cases, were presented and the MPPT–FLC was found to be the most efficient in terms of energy conversion and robustness;
– The first MPP control strategy was implemented on a full-scale, complete SWECS in real functioning conditions, and experimental results have been presented;
– A complete, full scale laboratory installation was built, and all necessaries software parts for simulations and control were developed.

The research results were disseminated at international conferences, during the doctoral study period. Five papers (four ISI Proceedings and one IEEEXplore) related to the thesis subject have been presented and published.

7.3. Future work

Future work related to the thesis subject could be summarized as follows:
❖ To implement MPPT-FLC control strategy on the site, in order to analyze its performance in real conditions.
❖ To redesign/improve the MPPT-FLC in order to limit the maximum extracted power to a desired/imposed value for over wind speeds.
❖ To study and propose control strategies for on-grid SWECS operation;
❖ To study an alternative energy conversion structure, based on new types of power converters, with improved efficiency.
❖ To analyze the economic aspects, in terms of the implementation costs, of the proposed structure.

APPENDICES

Appendix 1: Wind Turbines Characteristics

```matlab
%Five blades wind turbine characteristics, for lamda0=3.
Ct0=0.0222;   %wind turbine constant initial torque coefficient
a=0.0986;     %wind turbine constant coefficient
b=0.0113;     %wind turbine constant coefficient
R=2.5;        %wind turbine radius blade
ro=1.225;     %air density for 15 degreeC
ro1=1.1455;   %air density for 35 degreeC
ro2=1.3413;   %air density for -10 degreeC
A=19.6;       %wind turbine blade swept area
v=11;         %rated wind speed
n=0:1:126;    %rated rotating speed [rpm]
k=2.98;       %wind turbine constant coefficient
lam=(n*pi*R)/(v*30);      %tip-speed ratio
Cpmax=0.42;               %wind turbine maximum power conversion
coefficient
Ct= Ct0+a*lam-b*lam.^2.5;   %wind turbine torque coefficient
T= Ct*ro*A*R*(v^2)/2;       %wind turbine torque
P= Cp*ro*A*(v.^3)/2;        %wind turbine power
figure('Color','white')
hold on
set(gca,'FontName','Verdana','FontWeight','b','FontSize',14);
axis([0 13.18 0 6000])
axis([0 4.5 0 0.5])
%xlabel('v [m/s]')
%ylabel('P_w_t [kW]')
%xlabel('w [rad/s]')
%ylabel('T_w_t [Nm]')
xlabel('Tip-Speed Ratio')
ylabel(' Power Coefficient C_P')
for v =10;
n=0:1:126;
lam=(n*pi*R)/(v*30);
Ct= Ct0+a*lam-b*lam.^2.5;
T= Ct*ro*A*R*(v^2)/2;
P=T.*(n*pi/30);
w=n*pi/30;                    %rotating speed [rad/s]
Pmax=(2.98*(n*pi/30).^3);    %optimal regime characteristic for
ro (ORC)
T1= Ct*ro1*A*R*(v^2)/2;
P1=T1.*(n*pi/30);
```

```
Pmax1=(2.8*(n*pi/30).^3);    %optimal regime characteristic for
ro1 (ORC)
T2= Ct*ro2*A*R*(v^2)/2;
P2=T2.*(n*pi/30);
Pmax2=(3.2*(n*pi/30).^3);    %optimal regime characteristic for
ro2 (ORC)
Cp=Ct.*lam;
%P= 0.42*ro*A*(v.^3)/2
%plot(w, T,'b','LineWidth',3);
%plot(v,P,'b','LineWidth',10000);
%plot(w, P,'b','LineWidth',3);
%plot(w, Pmax,'b','LineWidth',3);
plot(w,
P,'g',w,P1,'r',w,P2,'b',w,Pmax,'g',w,Pmax1,'r',w,Pmax2,'b','Line
Width',3);
%plot(lam,Cp,'LineWidth',3);
end
%for v =10.3:0.001:15;
%Pm= 5500;
%plot(v,Pm,'b','LineWidth',10000);
%end


%Three blades wind turbine characteristics, for lamda0=4.
Ct0=0.0125;  %wind turbine constant initial torque coefficient
a=0.0626;     %wind turbine constant coefficient
b=0.0046;     %wind turbine constant coefficient
R=3.5;        %wind turbine radius blade
ro=1.225;     %air density for 15 degreeC
A=38.4845;    %wind turbine blade swept area
n=0:1:150;    %rated rotating speed [rpm]
v=8.8;        %rated wind speed
k=7.43;       %wind turbine constant coefficient
lam=(n*pi*R)/(v*30);      %tip-speed ratio
Ct= Ct0+a*lam-b*lam.^2.5  %wind turbine torque coefficient
T= Ct*ro*A*R*(v^2)/2;     %wind turbine torque
figure('Color','white')
hold on
%axis([0 15 0 1200])
axis([0 6 0 0.5])
set(gca,'FontName','Verdana','FontWeight','b','FontSize',14);
%xlabel('w [rad/s]')
%ylabel('P_w_t [kW]')
xlabel('Tip-Speed Ratio')
ylabel('Power Coefficient C_P')
for v =5;
n=0:1:150;
lam=(n*pi*R)/(v*30);
Ct= Ct0+a*lam-b*lam.^2.5
```

```
T= Ct*ro*A*R*(v^2)/2;
P=T.*(n*pi/30)              %wind turbine power
w=n*pi/30;                  %rotating speed [rad/s]
Pmax=(k*(n*pi/30).^3);     %optimal regime characteristic for ro
(ORC)
Cp=Ct.*lam;
%plot(w, T,'black','LineWidth',3);
%plot(w, P,'LineWidth',3);
%plot(w, Pmax, 'g','LineWidth',3);
plot(lam,Cp,'LineWidth',3);
end
```

Appendix 2: Speed Estimator

```
%Speed estimator coefficient kdc was found with the minimum
square deviation method,using the experimental results presented
in Table 2.8.
d_min=10;
k1=0;
for kddc=30:0.1:35;
Vdc1=kdc.*10;
Vdc2=kdc.*7.5;
Vdc3=kdc.*5;
d=sqrt( (((Vdc1-325).^2) + ((Vdc2-245).^2) + ((Vdc3-169).^2))
/3)
if d<d_min
    d_min=d
    k1=kdc
end
end


%Speed estimator parameters: Rdc and Ldc, were found with the
minimum square deviation method,using the experimental results
presented in Table 2.8.
d_min=10;
kdc=32.7;
R1=0;
L1=0;
e=0;
for Rdc=1:0.1:3; Ldc=0.02:0.001:0.04;

Vdc1=kdc*10 - sqrt((Rdc.^2)+ (Ldc.^2*(16*10)^2))*2;
Vdc2=kdc*7.5 - sqrt((Rdc.^2)+ (Ldc.^2*(16*7.5)^2))*2;
Vdc3=kdc*5 - sqrt((Rdc.^2)+ (Ldc.^2*(16*5)^2))*2;
Vdc4=kdc*10 - sqrt((Rdc.^2)+ (Ldc.^2*(16*10)^2))*3;
Vdc5=kdc*7.5 - sqrt((Rdc.^2)+ (Ldc.^2*(16*7.5)^2))*3;
```

```
Vdc6=kdc*5 - sqrt((Rdc.^2)+ (Ldc.^2*(16*5)^2))*3;


Vdc7=kdc*10 - sqrt((Rdc.^2)+ (Ldc.^2*(16*10)^2))*4;
Vdc8=kdc*7.5 - sqrt((Rdc.^2)+ (Ldc.^2*(16*7.5)^2))*4;
Vdc9=kdc*5 - sqrt((Rdc.^2)+ (Ldc.^2*(16*5)^2))*4;


Vdc10=kdc*10 - sqrt((Rdc.^2)+ (Ldc.^2*(16*10)^2))*5;
Vdc11=kdc*7.5 - sqrt((Rdc.^2)+ (Ldc.^2*(16*7.5)^2))*5;
Vdc12=kdc*5 - sqrt((Rdc.^2)+ (Ldc.^2*(16*5)^2))*5;


Vdc13=kdc*10 - sqrt(Rdc.^2+ (Ldc.^2*(16*10).^2))*6;
Vdc14=kdc*7.5 - sqrt((Rdc.^2)+ (Ldc.^2*(16*7.5)^2))*6;
Vdc15=kdc*5 - sqrt((Rdc.^2)+ (Ldc.^2*(16*5)^2))*6;


Vdc16=kdc*10 - sqrt((Rdc.^2)+ (Ldc.^2*(16*10)^2))*7;
Vdc17=kdc*7.5 - sqrt((Rdc.^2)+ (Ldc.^2*(16*7.5)^2))*7;
Vdc18=kdc*5 - sqrt((Rdc.^2)+ (Ldc.^2*(16*5)^2))*7;


Vdc19=kdc*10 - sqrt((Rdc.^2)+ (Ldc.^2*(16*10)^2))*8;
Vdc20=kdc*7.5 - sqrt((Rdc.^2)+ (Ldc.^2*(16*7.5)^2))*8;
Vdc21=kdc*5 - sqrt((Rdc.^2)+ (Ldc.^2*(16*5)^2))*8;


Vdc22=kdc*10 - sqrt((Rdc.^2)+ (Ldc.^2*(16*10)^2))*9;
Vdc23=kdc*7.5 - sqrt((Rdc.^2)+ (Ldc.^2*(16*7.5)^2))*9;
Vdc24=kdc*5 - sqrt((Rdc.^2)+ (Ldc.^2*(16*5)^2))*9;


Vdc25=kdc*10 - sqrt((Rdc.^2)+ (Ldc.^2*(16*10)^2))*10;
Vdc26=kdc*7.5 - sqrt((Rdc.^2)+ (Ldc.^2*(16*7.5)^2))*10;
Vdc27=kdc*5 - sqrt((Rdc.^2)+ (Ldc.^2*(16*5)^2))*10;


d=(sqrt( ( ((Vdc1-316).^2) + ((Vdc2-238).^2) + ((Vdc3-163).^2) +
((Vdc4-311).^2) + ((Vdc5-234).^2) + ((Vdc6-160).^2) + ((Vdc7-
307).^2) + ((Vdc8-230).^2) + ((Vdc9-157).^2) + ((Vdc10-302).^2)
+ ((Vdc11-226).^2) + ((Vdc12-154).^2) +  ((Vdc13-298).^2) +
((Vdc14-223).^2) + ((Vdc15-151).^2) + ((Vdc16-293).^2) +
((Vdc17-219).^2) + ((Vdc18-148).^2) + ((Vdc19-288).^2) +
((Vdc20-215).^2) + ((Vdc21-145).^2) + ((Vdc22-284).^2) +
((Vdc23-212).^2) + ((Vdc24-142).^2) +((Vdc25-279).^2) + ((Vdc26-
208).^2) + ((Vdc27-139).^2) ) /27));
e=min(d)
if d<d_min
    d_min=d
    R1=Rdc
    L1=Ldc
end
end
```

Appendix 3: Fuzzy Inference System (Fis File)

Fig.A3.1. Fis Editor: FLC.

1. If (DP is n) and (Dw is n) and (DP/Dw is p) then (DP* is n) (1)
2. If (DP is n) and (Dw is ns) and (DP/Dw is p) then (DP* is n) (1)
3. If (DP is n) and (Dw is z) and (DP/Dw is p) then (DP* is n) (1)
4. If (DP is ns) and (Dw is n) and (DP/Dw is p) then (DP* is n) (1)
5. If (DP is ns) and (Dw is ns) and (DP/Dw is p) then (DP* is ns) (1)
6. If (DP is ns) and (Dw is z) and (DP/Dw is p) then (DP* is ns) (1)
7. If (DP is z) and (Dw is n) and (DP/Dw is p) then (DP* is n) (1)
8. If (DP is z) and (Dw is ns) and (DP/Dw is p) then (DP* is n) (1)
9. If (DP is z) and (Dw is ns) and (DP/Dw is p) then (DP* is ns) (1)
10. If (DP is z) and (Dw is ps) and (DP/Dw is p) then (DP* is p) (1)
11. If (DP is z) and (Dw is z) and (DP/Dw is p) then (DP* is p) (1)
12. If (DP is z) and (Dw is z) and (DP/Dw is p) then (DP* is p) (1)
13. If (DP is ps) and (Dw is ps) and (DP/Dw is p) then (DP* is p) (1)
14. If (DP is ps) and (Dw is p) and (DP/Dw is p) then (DP* is p) (1)
15. If (DP is p) and (Dw is z) and (DP/Dw is p) then (DP* is p) (1)
16. If (DP is p) and (Dw is ps) and (DP/Dw is p) then (DP* is p) (1)
17. If (DP is p) and (Dw is p) and (DP/Dw is p) then (DP* is p) (1)
18. If (DP is n) and (Dw is z) and (DP/Dw is p) then (DP* is n) (1)

If   and   and   Then

DP is   Dw is   DP/Dw is   DP* is

p   p   n   p
n   n   p   n
z   z   none   z
ns   ns   ns
ps   ps   ps
none   none   none

□ not   □ not   □ not   □ not

Connection   Weight:

○ or   1

● and

Delete rule   Add rule   Change rule   >>   <<

Renamed FIS to "FLC"
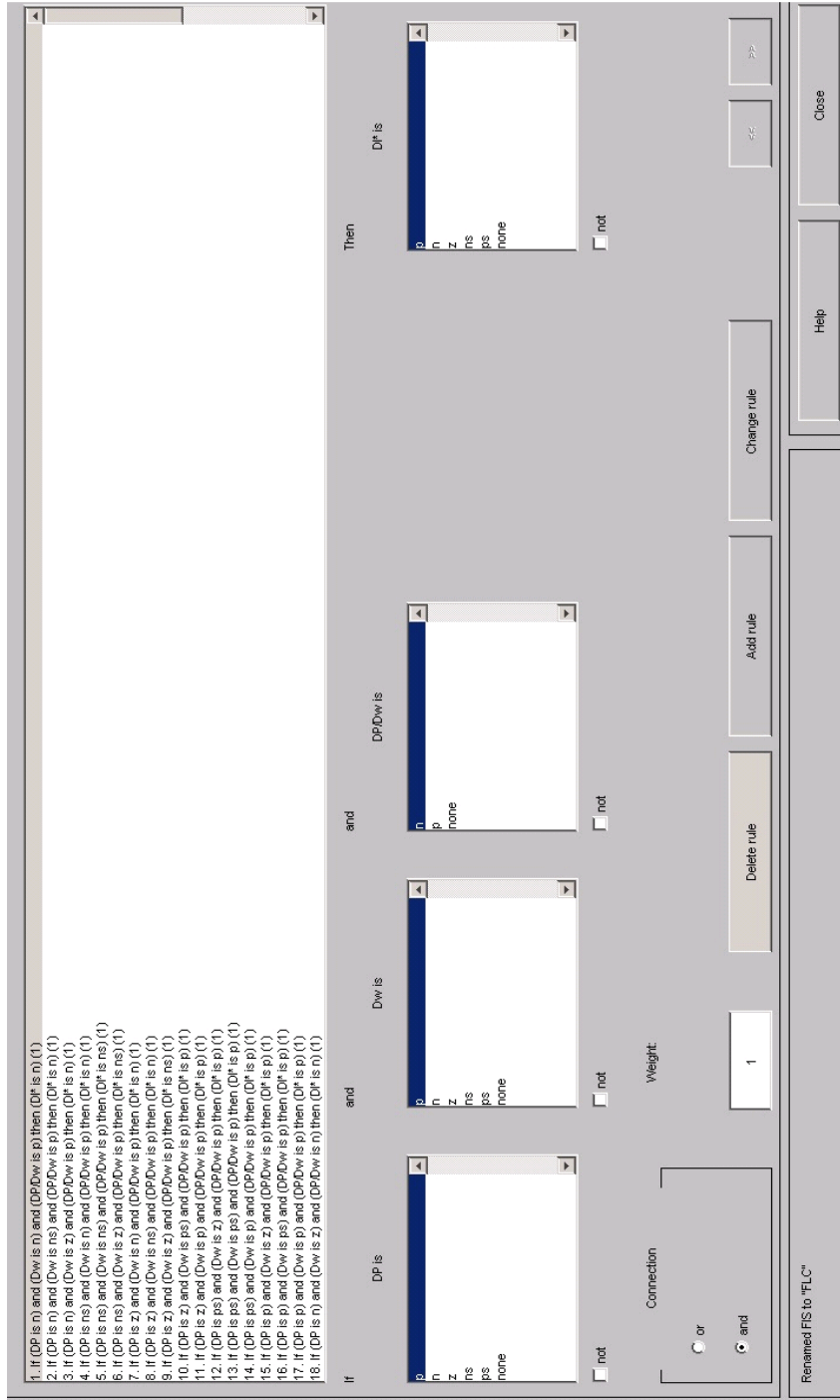
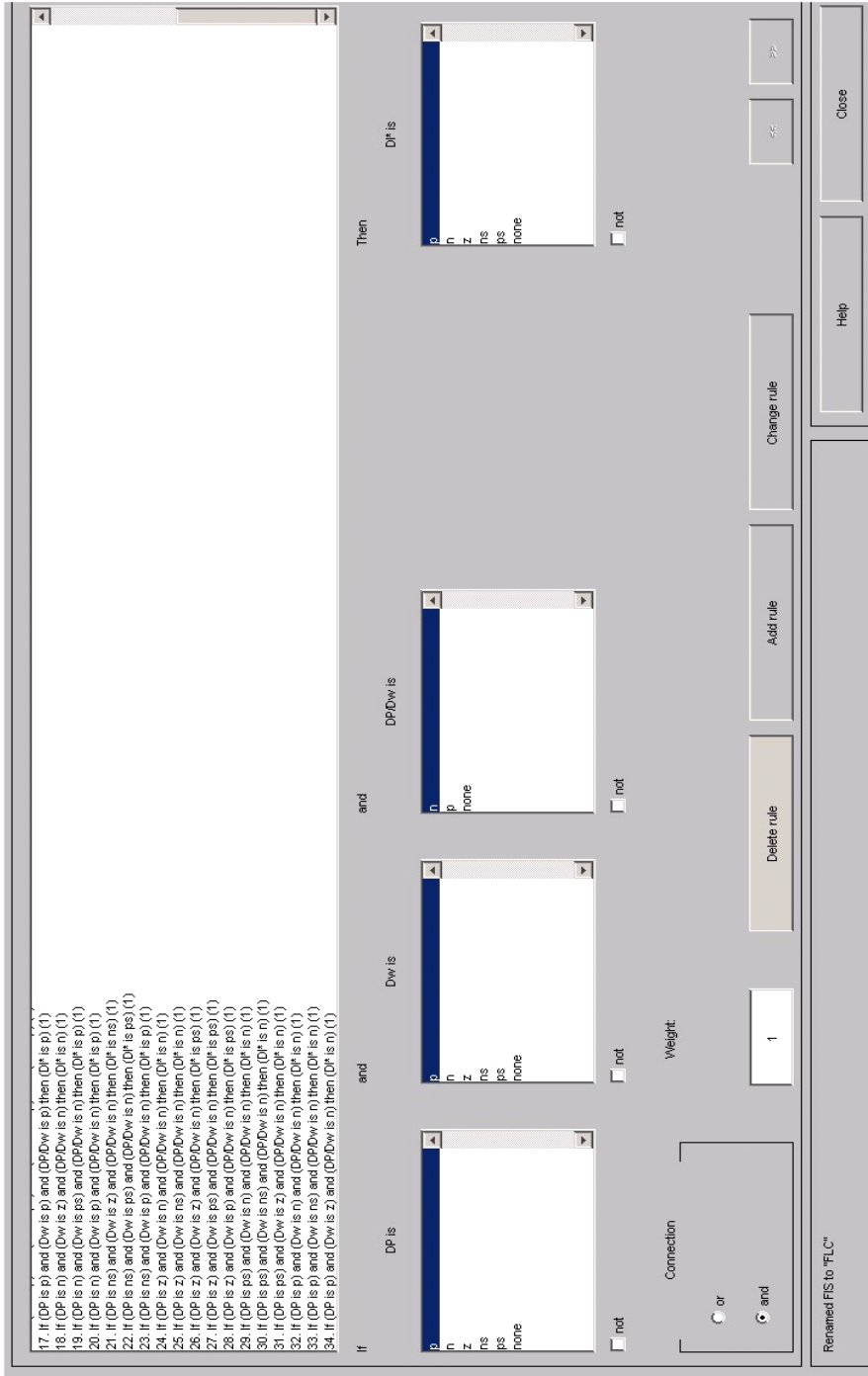Help   Close

Fig.A3.2. Rule Editor: FLC.

Fig.A3.3. Rule Editor: FLC.

Appendix 4: Electrical Wiring Diagram of ECS Equipment Installed on Site
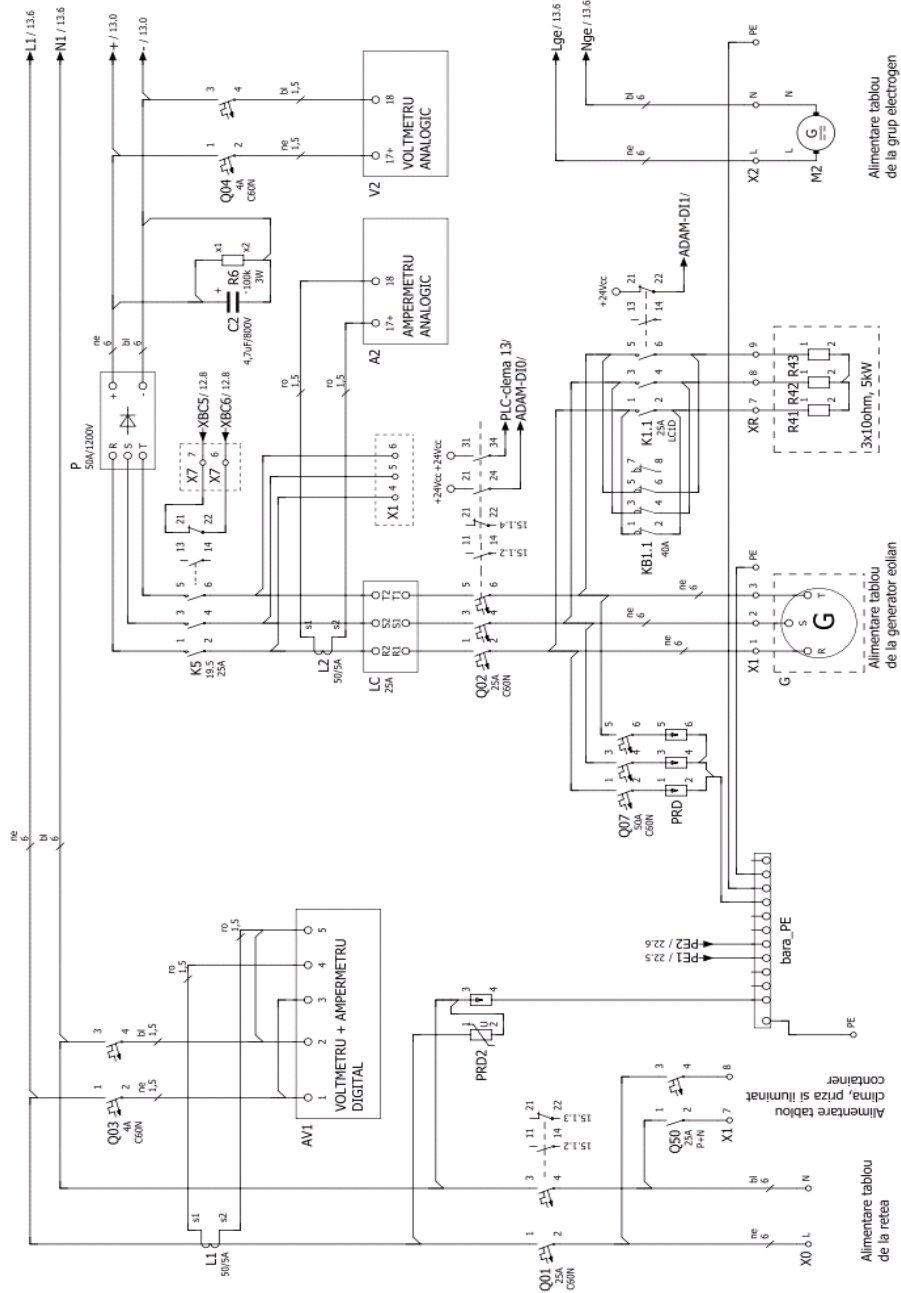

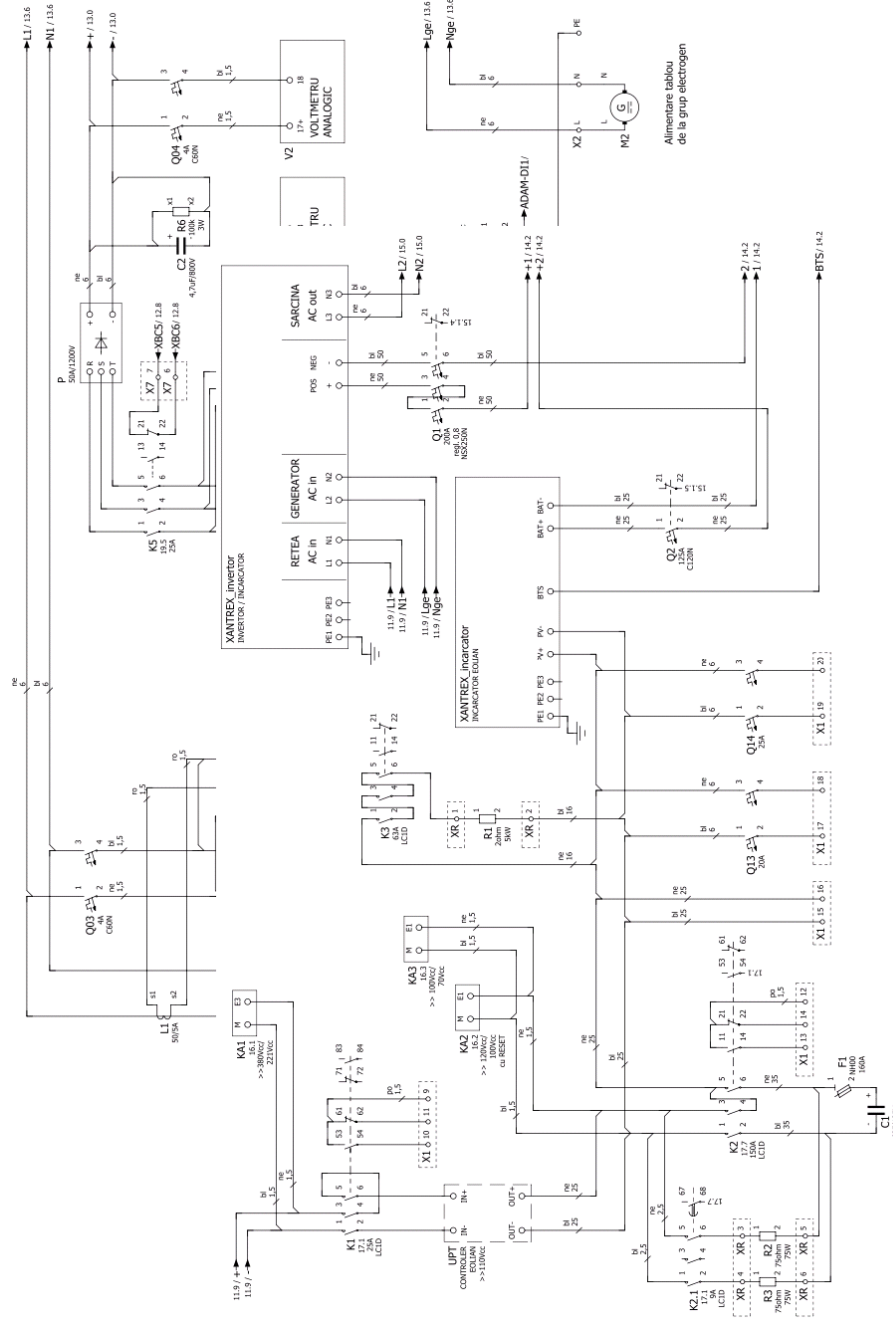Fig.A4.1. Grid and generator supply.
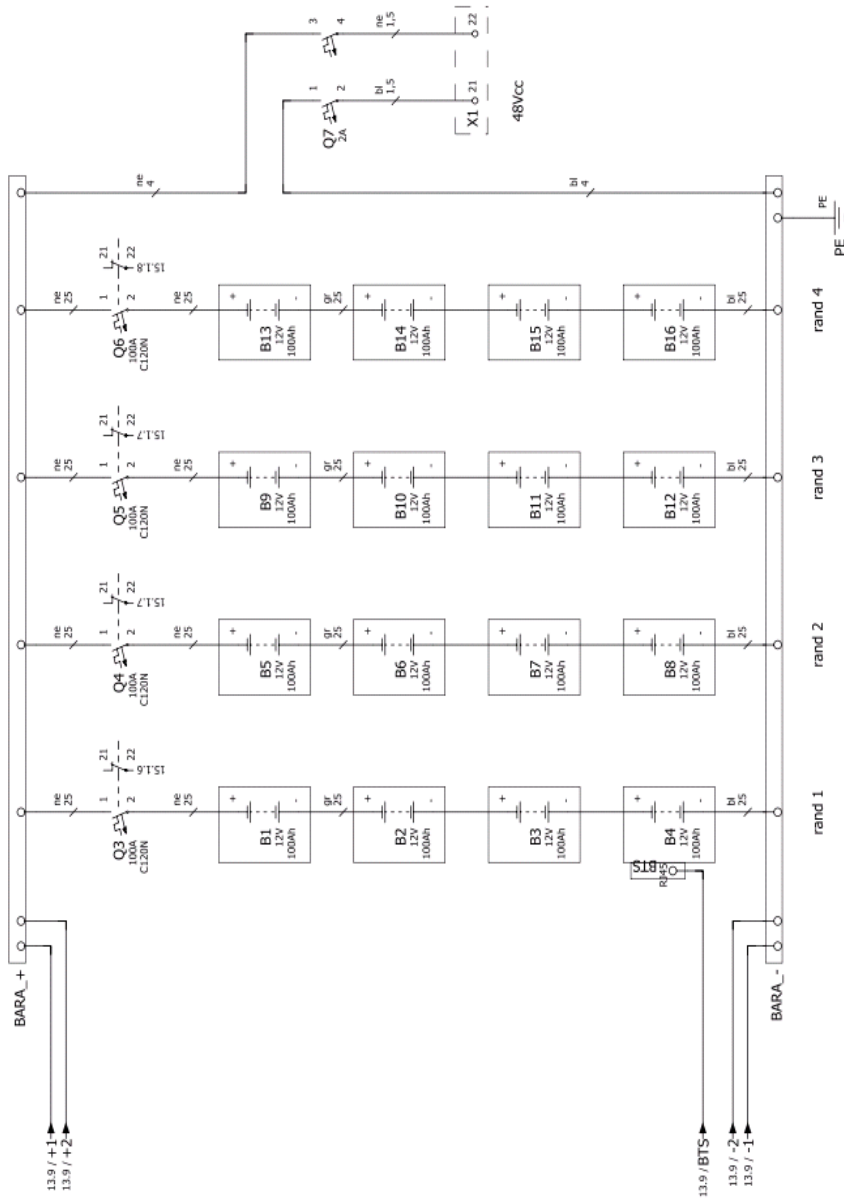
Fig.A4.2. Grid monitoring.

Fig.A4.3. Charging battery bank.

AUTHOR'S PAPERS RELATED TO THE PHD THESIS

[1] N. Muntean, O. Cornea and D. Petrila, "A new conversion and control system for a small off – grid wind turbine", *12th International Conference of Electrical and Electronic Equipment, OPTIM 2010,* 20-22 May, Brasov, Romania, pp. 1167-1173 (indexed ISI Proceedings, IEEEXplore and Scopus).

[2] N. Budisan, N. Muntean, R. Boraci, O. Cornea, C. Koch-Ciobotaru, D. Petrila, "Electronic conversion system and speed-control strategy for small wind generators*", IEEE International Joint Conferences on Computational Cybernetics and Technical Informatics, ICCC-CONTI 2010*, May 27-29, 2010, Timisora, Romania, pp. 455-458 (indexed IEEEXplore and Scopus).

[3] N. Muntean, L. Tutelea, D. Petrila, O. Pelan, "Hardware in the loop wind turbine emulator", *International Aegean Conference on Electric Machines and Power Electronics&Electromotion Joint Conference, ACEMP 2011,* 8-10 September 2011, Istanbul, Turkey (pending for ISI Proceedings indexing).

[4] D. Petrila, F. Blaabjerg, N. Muntean, C. Lascu, "Fuzzy logic based MPPT controller for a small wind turbine system", *13th International Conference of Electrical and Electronic Equipment, OPTIM 2012,* 24-26 May, Romania, pp. 993-999 (indexed IEEEXplore and Scopus, pending for ISI Proceedings indexing).

[5] D. Petrila, N. Muntean, "Simulation and experiment of a fuzzy logic based MPPT controller for a small wind turbine system", *10th International Conference of Numerical Analysis and Applied Mathematics*, *ICNAAM 2012*, Kos, Greece, 19-25 September 2012, pp.1619-1622 (indexed ISI Proceedings).

AUTHOR'S CV

First name/Surname:	Diana Paula Petrila
Address:	205/12, 47 No., Mioritei Street, 310287, Arad, Romania
Phone:	+407 65429071
E-mail:	diana5petrila@yahoo.com
Nationality:	Romanian
Date of birth:	December 27, 1985
Gender:	Female
Education:	
2009-2013	Ph.D. student at "Politehnica" University of Timisoara, Faculty of Electrical and Power Engineering;
2009	B.E. degree in electrical engineering;
2004-2009	"Politehnica" University of Timisoara, Faculty of Electrical and Power Engineering Timisoara, Romania;
2000-2004	"Elena Ghiba Birta" High School, Arad, Romania.
Professional experience:	
July-October 2011	Guest Ph.D. student at Institute of Energy Technology, Aalborg University, Denmark;
2010-2011	Assistant Researcher at "Politehnica" University of Timisoara, Faculty of Electrical and Power Engineering Timisoara, Romania; Project name: "Improvement of the Structures and Efficiency of Small Horizontal Axis Wind Generators with Non-Regulated Blades", no. RO018 EEA Grants.

Courses, certifications and awards:	Pedagogical course and certificate; English certificate; Assistant programmer certificate.
Drive license:	B Category.